NASA CR-134827
AiResearch 74-310862

SMALL AXIAL COMPRESSOR TECHNOLOGY PROGRAM

(VOLUME I)

by F.F. Holman, J.R. Kidwell and T.C. Ware

AIRESEARCH MANUFACTURING COMPANY OF ARIZONA
A DIVISION OF
THE GARRETT CORPORATION
Phoenix, Arizona

Prepared for

NATIONAL AERONAUTICS AND SPACE ADMINISTRATION
AND
U.S. ARMY AIR MOBILITY RESEARCH AND DEVELOPMENT LABORATORY

Lewis Research Center
Contract NAS 3-17846

1. Report No.	2. Government Accession No.	3. Recipient's Catalog No.
NASA CR-134827		

4. Title and Subtitle	5. Report Date
Small Axial Compressor Technology Volumes I and II	June 1976
	6. Performing Organization Code
7. Author(s)	8. Performing Organization Report No.
F. F. Holman, J. R. Kidwell, and T. C. Ware	74-310862
	10. Work Unit No.
9. Performing Organization Name and Address	11. Contract or Grant No.
AiResearch Manufacturing Company of Arizona Phoenix, Arizona 85010	NAS3-17846
	13. Type of Report and Period Covered
12. Sponsoring Agency Name and Address	Contractor Report
U.S. Army Air Mobility Research & Development Lab Moffitt Field, California	14. Sponsoring Agency Code

15. Supplementary Notes

Program Manager, Everett Bailey, Fluid Systems, NASA-Lewis Research Center, Cleveland, Ohio

16. Abstract

This final report covers the aerodynamic design and test of a scaled single-stage, highly-loaded, axial-flow transonic compressor. The compressor stage was tested at speeds from 70 to 110 percent design equivalent speed to evaluate the effects of scaling compromises and the individual and combined effects of rotor tip running clearance and rotor shroud casing treatment on the overall and blade element performance. At design speed and 1 percent tip clearance the stage demonstrated an efficiency of 83.2 percent at 96.4 percent design flow and a pressure ratio of 1.865. Casing treatment increased design speed surge margin 2.0 points to 12.8 percent. Overall performance was essentially unchanged. An increase in rotor running clearance to 2.2 percent with smooth casing, reduced design speed peak efficiency 5.7 points, flow by 7.4 percent, pressure ratio to 1.740, and surge margin to 5.4 percent. Re-installing casing treatment regained 3.5 points in design speed peak efficiency, 4.7 percent flow, increased pressure ratio to 1.800 and surge margin to 8.7 percent.

17. Key Words (Suggested by Author(s))	18. Distribution Statement
Compressor/Small Axial Transonic Scaling Technology Casing Treatment Tip Clearance	Unclassified - Unlimited

19. Security Classif. (of this report)	20. Security Classif. (of this page)	21. No. of Pages	22. Price*
Unclassified	Unclassified	Vol. I -185 Vol. II-329	

TABLE OF CONTENTS

TABLE OF CONTENTS (Continued)

LIST OF ILLUSTRATIONS

LIST OF ILLUSTRATIONS (Continued)

LIST OF ILLUSTRATIONS (Continued)

LIST OF ILLUSTRATIONS (Continued)

LIST OF ILLUSTRATIONS (Continued)

LIST OF ILLUSTRATIONS (Continued)

LIST OF ILLUSTRATIONS (Continued)

LIST OF ILLUSTRATIONS (Continued)

SUMMARY

A scaled, single-stage, highly-loaded, axial-flow transonic compressor was tested at speeds from 70 to 110 percent of design equivalent speed to evaluate the effects of scaling to a small size, and the individual and combined effects of rotor running clearance, and rotor shroud casing treatment, on the overall and blade element performance.

This compressor stage, essentially a 0.1445 scale (approximately 50:1 flow scale) of the stage designed and tested under NASA Contract NAS3-10492, was predicted to operate at a flow rate of 1.662 kg/sec (3.663 lb/sec), pressure ratio of 1.837 and stage adiabatic efficiency of 82.6 percent at a corrected speed of 76,718 rpm.

At design speed, with smooth outer shroud and close running clearance of 0.020 cm (0.008 in.), the stage obtained an efficiency of 83.2 percent at a flow rate 96.4 percent of design and a pressure ratio of 1.865. At this close running clearance, casing treatment increased the design speed surge margin to 12.8 percent from the 10.8 percent obtained with the untreated casing. Overall performance was essentially unchanged.

An increase of rotor running clearance to 0.056 cm (0.022 in.) with the smooth casing, reduced design speed peak efficiency by 5.7 points, flow by 7.4 percent, and pressure ratio to 1.74. Design speed surge margin was similarly reduced to 5.4 percent. Reinstalling the casing treatment at this large running clearance regained 3.5 points in design speed peak efficiency, 4.7 percent in flow, increased pressure ratio to 1.8, and surge margin to 8.7 percent.

This test series clearly indicates performance penalties associated with scaling to small size, especially with large running clearances over a small transonic rotor. But moreover, it demonstrated that a large portion of the performance lost, due to increased tip clearance, can be regained with casing treatment.

This volume, the first of two, presents details of the test equipment, test procedures, data reduction methods, overall performance data, and blade element data plots. Plots of total pressure profiles in the casing endwall boundary layers at the rotor inlet, rotor exit, and downstream of the stator are also presented. Volume II contains tabulations of all overall performance and blade element data.

INTRODUCTION

Small, single-stage, axial compressors for use in small gas turbines are of increasing importance in military and civil applications as primary propulsion units for helicopters, light aircraft, tanks, and trucks, and as auxiliary power units for larger aircraft. The present body of design rules for loss, incidence, deviation, aspect ratio, and solidity has been developed as a result of extensive research and development efforts over the years on large size components. To utilize this knowledge effectively when dealing with small components, the compromises required as a result of scaling, and effects of scaling, must be identified. These compromises result from the inability to scale dimensions such as leading and trailing edge radii directly, and from the fact that tolerances cannot be scaled directly while maintaining low costs. These considerations introduce an element of uncertainty in performance predictions for small stages. Therefore, the manner in which attractive larger stages are scaled is important.

Rotor casing treatment has produced beneficial results in improving the operational flow range of large axial-flow compressors. Results presented in Reference 1 indicate that a significant improvement in rotor stall margin was obtained when a porous casing was present over the rotor blade tip region. This improvement, during testing of a rotor only configuration, was most pronounced when the rotor was tested with inlet flow distortion. Further research, under a NASA contract, evaluated the effects of a porous honeycomb casing over the rotor tip of a moderately loaded transonic stage, both with and without radial inlet distortion. These results, presented in Reference 2, again indicated an improvement in stall margin with the porous honeycomb casing relative to that obtained with a conventional solid casing. However, losses of five points in peak rotor efficiency at design speed were sustained for the improvement in surge margin. Additional evaluations of this concept, i.e., casing treatment, such as skewed slots and blade angle grooves (References 3 and 4) indicated improvement in operating flow range, both with and without inlet flow distortion. However, in most cases there was an accompanying loss in rotor and stage efficiency. One configuration (Reference 4) indicated an improvement in stall margin without a significant performance penalty. A screening program was initiated to evaluate use of circumferential grooves in the casing. Results of that study, presented in Reference 5, indicated the greatest improvement in surge margin was found among the configurations utilizing circumferential grooves. This was obtained with the grooves over the rotor blade tip mid-chord region only, and was accomplished without a decrease in stage efficiency.

To increase the understanding of scaling methodologies, and to evaluate the potential of casing treatment to provide benefits similar to those already demonstrated in large compressors, a modified scale of the high-tip-speed compressor reported in References 6 and 7 was selected for testing.

This report presents test results demonstrating the effects of scaling compromises and the effectiveness of casing treatment, especially in the presence of large running clearance over the rotor and compares these results to performance achieved in the larger size component. Complete tabulations of all test data and computed performance parameters are presented in Reference 8. Definition of symbols and performance parameters used in this report appear in Appendix A, and the procedure used for momentum averaging of data is described in Appendix B.

APPARATUS AND PROCEDURES

Aerodynamic Design

An existing AiResearch axial-flow compressor rotor was selected for this investigation. This compressor rotor is of a high-tip-speed, high-pressure-ratio design with relatively high specific-flow; typical of the compressor type that would be selected for advanced, small engine concepts. The compressor stage, essentially a 0.1445 scale of the stage designed and tested under NASA Contract NAS3-10482 and reported in References 6 and 7, was designed to operate at a flow rate of 1.662 kg/sec (3.663 lb/sec), a pressure ratio of 1.837, and a stage adiabatic efficiency of 82.6 percent at a corrected speed of 76,718 rpm.

Application constraints made it necessary to alter the original stage design when scaled to the small flow size. At engine design speed and total pressure ratio, the flow scaled from the tested stage map of Reference 7 was greater than required. Sufficient detailed data was available from Reference 6 to identify a three percent flow streamline measured from the casing. This streamline was selected as the casing line for the stage. The rotor tip diameter was reduced to this dimension. Radial location of the design stator sections was defined by locating the scaled stator hub section at the hub radius, while moving the scaled stator casing section inward to the three percent flow streamline. All intermediate sections were proportionately spaced between the resulting hub and casing sections.

Blade definition. - Certain manufacturing compromises precluded a direct scale of blade dimensions in proportion to scaling ratios. The scaled rotor chord was increased 25 percent over a direct scale to obtain more practical dimensions for manufacturing. This rotor chord increase was accommodated by a decrease in the number of blades to maintain the same solidity. Therefore, a 25-percent reduction in blade aspect ratio resulted.

An examination of directly scaled leading- and trailing-edge thicknesses indicated that an unreasonably small thickness would result on some rotor blade sections, especially in the tip region. Therefore, each blade section was individually examined and a reasonable edge thickness determined. Table I summarizes the scaled and modified blade edge dimensions.

The leading-edge thickness alteration was applied to the pressure surface, while the trailing-edge thickness alteration was distributed on both the pressure and suction surfaces. Both surfaces were faired to the scaled blade section in a manner consistent with minimum chord-wise change and maintenance of monotonically changing surface curvature. The maximum thickness and applicable location were retained.

TABLE I

ROTOR EDGE THICKNESS

Hub		Tip		Remarks
Leading Edge	Trailing Edge	Leading Edge	Trailing Edge	
0.0925 cm (0.0364 in.)	0.1052 cm (0.0414 in.)	0.0615 cm (0.0242 in.)	0.0320 cm (0.0126 in.)	Original Configuration (Reference 6)
0.0135 cm (0.0053 in.)	0.0152 cm (0.0060 in.)	0.0089 cm (0.0035 in.)	0.0046 cm (0.0018 in.)	Exact scale to 0.1445 size
0.0168 cm (0.0066 in.)	0.0191 cm (0.0075 in.)	0.0112 cm (0.0044 in.)	0.0058 cm (0.0023 in.)	Exact scale adjusted for 25 percent chord increase
0.0168 cm (0.0066 in.)	0.0191 cm (0.0075 in.)	0.0127 cm (0.0050 in.)	0.0127 cm (0.0050 in.)	Modified for manufacturing

An optical comparison at 10 times size was made between the finished rotor and design configuration. Figure 1 presents results of such a comparison near mid-span for a sample blade on the finished rotor. A similar inspection of several additional blades indicated that the quality of all blades was represented by the sample. Figure 2 presents a view of the finished rotor from the inlet side.

The scaled stator chord and thickness were increased by 47 percent over a direct scale of the Reference 6 stator to again obtain more practical dimensions for manufacture. This stator chord increase was accompanied by a decrease in the number of vanes from 44 to 30 to maintain the same solidity as the reference design. These changes resulted in a 47-percent reduction in stator aspect ratio.

A sample optical inspection for a typical stator vane near mid-span is shown in Figure 3. As noted, the leading edge region was thicker than design, and a hand finish operation utilizing an electro-optical comparator was employed to correct this condition. The final stator assembly had a leading edge region within acceptable tolerances. A view looking aft of the finished stator assembly is shown in Figure 4.

Flow path definition. - The 25-percent increase in rotor chord required a 25-percent increase in blade axial projection. At the end walls, this was accommodated by axially shifting, at constant radius, points on the surfaces of revolution 25 percent away from a base point, i.e., the rotor trailing-edge/hub intersection. The resulting surface slopes and curvatures were less than initial values. Similar minor flow-path alterations were undertaken to accommodate the stator chord increase; however, axial space between the rotor and stator was retained at the scaled dimension. Reductions in hub-wall slope and curvature and retention of the scaled axial space made it inconvenient to retain the exact stator leading-edge/hub-wall intersection point. It was judged that a small reduction in hub radius at the stator leading edge would not substantially alter the flow field. The resulting meridional flow path and exact scale are presented in Figure 5 for comparison.

An axial inlet designed for the Reference 6 axial compressor was representative of aircraft power plant usage, where higher values of inlet flow per unit frontal area are more desirable because of weight and envelope considerations. In the size range being investigated in this program, this requirement was not paramount. Therefore, an axial-flow-compressor radial inlet was judged more representative of that which could be expected when a gas turbine engine of this small size is used in an application where accessibility is given priority. To ensure that the flow conditions into the rotor were not distorted by the change from

axial to radial inlet, an analytical model was established and an appropriate inlet shape designed to minimize wall boundary-layer thickness and duplicate the inlet velocity gradients that existed for the original compressor.

Table II presents a summary of pertinent aerodynamic and geometric parameters for this design.

Velocity diagrams. - Once the scaling approach was determined, the meridional flowpath and recomputed blade geometry parameters were integrated into an axisymmetric compressible-flow analysis program. The stage geometry, together with radial variations of rotor exit total pressure and total temperature, as given in Reference 7 for the stage test near design point operating conditions, were input to this program to define the design rotor blade edge velocity diagrams and rotor blade element performance. Stator velocity diagrams were similarly determined by using the measured stator loss coefficients presented in Reference 7. These computed velocity diagrams served as a basis for subsequent comparison with experimental data and are indicated as design values on subsequent figures. The design blade element parameters are listed in Figures 6 and 7 for the rotor and Figures 8 and 9 for the stator. All values are referenced to NASA sea level standard day conditions as defined in Appendix A.

The level of agreement between the synthesized design blade element parameters and test data from Reference 7 is indicated in Figures 10 through 14. Rotor and stator diffusion factors are compared to test data in Figure 10. The rotor and stator incidence and deviation angles are similarly compared in Figures 11 through 14. The radial variation of rotor and stage efficiency are compared to Reference 7 test data in Figures 15 and 16, respectively. These comparisons provide a good replica of the original compressor demonstrated performance into the present small compressor design intent.

TABLE II

ROTOR

(24 BLADES)

Average Streamline Radius		Solidity	Blade Camber (Deg.)	Streamline Slope	
cm	in.			Inlet (Deg.)	Exit (Deg.)
3.277	1.290	2.350	53.7	14.98	14.98
3.637	1.432	2.120	42.3	9.4	10.4
4.232	1.666	1.825	22.5	1.5	4.4
4.732	1.863	1.633	14.04	- 4.6	- 0.6
5.184	2.041	1.491	8.95	-11.0	- 6.4
5.639	2.220	1.371	6.94	-14.7	-12.0
5.885	2.317	1.314	6.2	-14.58	-14.58

Tip Radius	Rotor Inlet	Rotor Exit
cm	5.999	5.770
in.	2.362	2.272
Hub Radius		
cm	3.035	3.518
in.	1.195	1.385

Rotor Inlet Hub-Tip Ratio = 0.506

TABLE II (Contd)

STATOR

(30 VANES)

Average Streamline Radius		Solidity	Vane Camber (Deg.)	Streamline Slope	
cm	in.			Inlet (Deg.)	Exit (Deg.)
3.744	1.474	2.067	57.7	13.5	0.0
3.957	1.558	1.952	53.25	9.4	4.9
4.359	1.716	1.774	50.5	4.9	1.9
4.717	1.857	1.639	49.48	2.2	2.6
5.050	1.988	1.580	49.83	- 0.3	1.7
5.395	2.124	1.432	52.95	- 3.3	0.9
5.583	2.198	1.388	58.14	- 8.5	0.0

	Tip Radius	Stator Inlet	Stator Exit
	cm	5.603	5.563
	in.	2.206	2.190
	Hub Radius		
	cm	3.625	3.862
	in.	1.427	1.521

Stator Inlet Hub-Tip Ratio = 0.647

Compressor Test Rig

The test vehicle was capable of achieving speeds up to and including 85,000 rpm, approximately 112 percent of design equivalent speed. As shown in Figure 17, the test vehicle design incorporated a radial inlet, rotor, stator, and a constant-area discharge section followed by an annular diffuser.

To facilitate test-vehicle configuration changes, removable casing inserts were designed. The solid casing incorporated an abradable plasma coating extending over the blade tip. Grooves were assembled into the casing treatment hardware. The casing had five grooves extending over the mid 60-percent of the blade-tip projected chord. A land-to-groove width ratio of approximately 1:3 was selected. The grooved casing geometry details are shown in Figure 18. This configuration was a reasonable geometric scale of configuration (f), Figure 3, of Reference 5 [I], and was selected because performance improvements had been demonstrated at 70 and 100 percent speed. The grooved casing prior to installation is shown in Figure 19.

Instrumentation. - Aerodynamic evaluation of overall performance, rotor performance, blade element data, and stator vane element data required the use of small, highly accurate sensing elements and utilized a computer-controlled data-acquisition system. Design, selection, and distribution of both fixed and traversable instrumentation were carefully controlled to provide the necessary accuracy while minimizing blockage effects. Circumferential location and identity of instrumentation are shown in Figures 20 and 21 for the shroud and hub, respectively. A test flowpath schematic identifying the location of the instrumentation stations is provided in Figure 22. A summary of these stations is listed below.

Station Number	Location
0	Inlet bellmouth
0.9	Rotor shroud boundary layer survey plane
1	Rotor inlet
1.5	Rotor shroud
2	Rotor exit
3	Stator inlet
4	Stator exit
4.5	Blade element survey plane
5	Stage discharge

Airflow was measured using a standard ASME long radius 9.525 cm (3.750 in.) diameter bellmouth for 70 percent design equivalent speed and a 14.745 cm (5.805 in.) diameter bellmouth for all higher speeds. These calibrated bellmouths, in conjunction with a 0.25 percent full-scale accuracy low-pressure transducer insured airflow measurement accuracy to within one percent during all compressor mapping.

Compressor speed was monitored using an electromagnetic pick-up. Measurement of speeds between 40,000 and 85,000 rpm was accurate within $\pm$10 rpm.

Inlet total temperature was measured at the compressor inlet (Station 0) by eight chromel-alumel thermocouples. Stage discharge total temperatures (Station 5) were measured with four fixed radial rakes using shielded high-recovery thermocouples. These five-element rakes, shown in Figure 23, were circumferentially located to obtain readings evenly distributed across a stator vane passage and radially positioned at the design location of 10, 30, 50, 70, and 90 percent streamlines. Both inlet and discharge fixed thermocouples were constructed with stainless steel sheathed chromel-alumel wire of 0.051 cm (0.020 in.) outer diameter. The internal thermocouple wires were 0.006 cm (0.0025 in.) diameter, insulated from each other and the outer sheath with magnesium oxide. All thermocouple junctions were calibrated against a standard reference at two points within the affected range. Overall rms temperature accuracy was estimated at $\pm$1 degree.

Blade-element temperature data was obtained by using an 11-element, radially-traversable wake rake located at Station 4.5 and shown in Figure 24. Thermocouple elements were made of 0.0025 cm (0.001 in.) chromel-alumel wire, with magnesium oxide insulation and stainless steel sheaths having an outside diameter of 0.025 cm (0.010 in.). These 11 elements were shielded and circumferentially positioned to cover in excess of one stator passage.

In conjunction with the temperature wake rake, a similar 11-element pressure wake rake was utilized to obtain blade element pressure data. This wake rake was constructed of 0.071 cm (0.028 in.) OD tubing with 0.015 cm (0.006 in.) wall thickness and internally chamfered edges. Calibration of the rake over a range of Mach numbers indicated that negligible correction was required over the performance mapping range. As shown in Figure 25, the wake rake stem was streamlined and swept in the aft direction to minimize blockage effects.

These two circumferential wake rakes, plus a stator discharge angle sensing cobra probe, shown in Figure 26, radially traversed the stator discharge passage. An incremental stepping system immersed the probes to discrete radial positions, corresponding to design location of the 10, 20, 30, 50, 70, and 90 percent flow streamlines measured from the casing. Stepping system calibration, using the digital computer data acquisition system, indicated repeatable positioning of probes within $\pm$0.3 percent of the radii being considered.

Stage discharge total pressure measurements were obtained at Station 5 with four circumferentially positioned radial pressure rakes. These five-element rakes, shown in Figure 23, were identical in radial positioning and circumferential indexing to the fixed temperature rakes previously described.

Traversable survey probes, utilized in obtaining rotor inlet and rotor exit boundary layer data, are shown in Figure 27. Again, these probes were selected over fixed instrumentation methods to minimize blockage. The two probes differed in one respect; the rotor inlet probe was internally chamfered to reduce pitch and yaw sensitivity, whereas, the rotor exit probe was externally chamfered to increase pitch and yaw sensitivity. This configuration was selected to enable determination of rotor exit total pressure while minimizing blockage associated with a large, automatically nulled, probe. During data acquisition, the rotor exit probe was immersed and manually rotated until maximum pressure was located. The locus of maximum pressure was then assumed to be the boundary layer profile.

Boundary layer data at the stator exit was obtained using the previously described cobra probe. The side port static pressures were allowed to balance prior to data recording.

Static pressure taps were located on the hub and shroud surfaces along the flowpath, and at the leading and trailing edges of blade rows as shown in Figures 20 and 21.

All probe, rake, and static tap pressures were recorded digitally through 48 port scannivalves utilizing a transducer appropriate for the range of pressures being recorded. These transducers had an accuracy of 0.25 percent of full scale. A series of calibration pressures, compatible with each transducer, were recorded during each data scan from ports reserved on the scannivalve unit for this purpose. The positive reference calibration pressures were maintained by utilizing deadweight precision-pressure standards. The pressure reading combined accuracy from the digital data acquisition system was estimated at $\pm$0.5 percent of full scale value. However, utilization of standard reference pressures in the data reduction program to calibrate each transducer for each data scan reduced the ultimate

inaccuracy in pressure measurement to approximately ±0.1 percent of value.

Audible detection of compressor instability was facilitated by using a high response inlet microphone upstream of the rotor inlet station. Visual and permanent recordings of surge were obtained by using a bare-wire thermocouple located immediately forward of the rotor leading edge. The thermocouple was placed at 10-percent of the rotor inlet span, measured from the casing. Thermocouple output was recorded on an eight-channel recorder to indicate the presence of reverse flow.

All aerodynamic and mechanical instrumentation was recorded on a digital computer. Critical performance parameters, such as pressure and temperature, were sampled at a rate of 200 times per second; and the final recorded value of each parameter was obtained by averaging 16 successive samplings. This procedure reduced the error potential due to random electrical signal noise. On-line cathode-ray-tubes were located at the test console and provided a display of selected raw data and computed performance parameters. Thus, by utilizing the CRT, which was updated every 30 seconds, test conditions were monitored continuously during testing.

Four calibrated, capacitance type, clearance probes were installed in the solid casing over the rotor midchord at four equally spaced circumferential locations. These probes were flush mounted in the casing, and contoured to maintain the desired casing surface shape. The system was calibrated using the actual rotor and casing in a rotating bench fixture. The clearance measuring system accuracy is approximately ±10 percent of the clearance recorded. Clearance measurements were not made during casing treatment tests. However, since casing shape was identical for both the solid casing and casing treatment hardware, and each part occupied the same axial position in the vehicle, it was judged (and later verified) that the rotating group axial stacking could vary by ±0.0127 cm (0.005 in.), which was equivalent to ±0.0025 cm (0.001 in.) radial tip clearance variation. This variance was checked, and verified, utilizing feeler gauge stock between the rotor tips and casing.

Facility

The compressor test facility utilized during this study was designed to accommodate compressors with flow rates to 4.54 kg/sec (10 lb/sec) and speeds to 90,000 rpm. The compressor test area, inlet air, and compressor test vehicle were isolated from the high temperature drive turbine, thereby eliminating undesirable thermal effects on performance measurements.

Compressor inlet air temperature was controlled using refrigeration units and/or evaporative coolers as required. An inlet plenum was used to establish uniform compressor inlet test conditions. A flow straightening section in the plenum, forward of the rotor inlet station, maintained a uniform flow field with a minimum of turbulence. An appropriate bellmouth was installed at the plenum inlet to measure compressor airflow.

Flow rate was varied with a set of motor driven throttle valves located approximately 30 cm (12 in.) downstream of the compressor exhaust diffuser.

Test Procedure

Prior to aerodynamic evaluation of each stage configuration, a series of comprehensive checkouts were accomplished as follows:

(1) Establish the test vehicle mechanical integrity.

(2) Thoroughly check all instrumentation connections and mechanical systems as required.

(3) Thoroughly check data reduction programs.

During mechanical integrity testing, the test vehicle was accelerated to 110 percent of design equivalent speed with wide-open throttle valves. The unit was then decelerated to design equivalent speed and the throttle valves slowly closed, familiarizing test personnel with unit response to aerodynamic test conditions. Upon reaching the surge limit, rotor tip clearance was checked and the throttle valves opened. The unit was then shut down and all instrumentation connected. Pressure and vacuum leakage checks were conducted and adjustments made as required. Upon completion of all mechanical checks, the unit was accelerated to design equivalent speed, throttled to near peak efficiency, and several data scans recorded. Traversable wake rakes were immersed and again several data scans recorded. Following completion of these test scans, the unit was shut down and a thorough check of the data reduction programs conducted. This concluded the shakedown phase prior to each test series.

It shall be emphasized that the stability limit for all testing reported herein was determined by a system surge. This surge was readily identified by a series of loud reports and an abrupt discontinuity in mass flow rate and stage discharge pressure. The unit was not instrumented to identify rotating stall.

Test 1: Smooth casing with close clearance. - The basic compressor stage, with smooth casing and nominal rotor running tip clearance of 0.020 cm (0.008 in.), was subjected to overall and blade element performance testing at four selected speeds between 70 and 110 percent of design equivalent speed. Discharge valves were closed, throttling the stage at each speed to obtain performance data over a range of pressure ratios from wide open throttle to the surge limit. At each data point, a set of eight data scans was recorded; one scan with the wake rakes fully retracted into the casing, one scan for each radial position of the traversable wake rakes, and one scan with the wake rakes again retracted.

The rakes were not immersed at surge to preserve both the rig and rakes. Overall performance and blade element data were obtained for 24 data points within the operating range. Surge flow rate was measured for each speed. Outer wall boundary layer surveys were obtained at the rotor inlet, rotor exit, and stator exit for ten selected data points.

Test 2: Casing treatment with close clearance. - The unit remained on the test stand while the removable casing inserts were interchanged. The stage was then subjected to overall and blade element performance testing at three selected speeds between 70 and 100 percent of design equivalent speed. Discharge valves were closed, throttling the stage at each selected speed, to obtain performance data over a range of pressure ratios and flow rates from wide open throttle to the surge limit. At each selected data point a set of eight data scans was recorded in a manner identical to that described for Test 1. Overall performance and blade element data were obtained for 18 data points within the operating range. Outer wall boundary layer surveys were obtained at the rotor inlet, rotor exit, and stator exit for nine selected data points.

Test 3: Smooth casing with open clearance. - Prior to initiation of Test 3, a rear bearing failure was incurred during mechanical integrity testing. Rotor inspection, following this failure, revealed severe damage in the rotor blade tip region. A second rotor was fabricated in accordance with identical drawings, thoroughly inspected, and substituted into the test program. The second rotor was then machined so that the tip diameter was 0.071 cm (0.028 in.) less than the original Test 1 and 2 rotor. Following mechanical integrity testing, the compressor stage with smooth casing and an average rotor running tip clearance of 0.056

cm (0.022 in.) was subjected to overall and blade element performance testing at three selected speeds between 70 and 100 percent of design equivalent speed. Discharge valves were closed, throttling the stage at each selected speed to obtain performance data over a range of pressure ratios and flow rates from wide open throttle to surge limit. As before, at each selected data point a set of eight data scans was recorded. Overall performance and blade element data were obtained for 18 data points within the operating range and the surge flow rate, was determined for each speed. Outer wall boundary layer surveys were obtained at the rotor inlet, rotor exit and stator exit for nine selected data points.

Test 4: Casing treatment with open clearance. - The unit remained on the test stand while the removable casing inserts were interchanged. The stage was then subjected to overall and blade element performance testing at three selected speeds between 70 and 100 percent design equivalent speed. Discharge valves were closed, throttling the stage at each selected speed to obtain performance data over a range of pressure ratios and flow rates from wide open throttle to the surge limit. Again, at each selected data point a set of eight data scans was recorded. Overall performance and blade element data were obtained for 17 data points within the operating range and the surge flow rate was determined for each speed. Outer wall boundary layer surveys were obtained at the rotor inlet, rotor exit, and stator exit for six selected data points.

Data Reduction Procedure

Rotor and stage overall performance. - A flow chart depicting the various phases of data reduction is shown in Figure 28.

Prior to testing each day, and during testing, an electronic calibration was performed on all data sensors. This calibration provided the basis for converting raw data to engineering units.

The test cell raw data was transmitted from a multiplexing unit, via cable, to a data acquisition computer and stored on magnetic tape. Simultaneously, these data were selectively processed by the computer and communicated to the cell site as pertinent overall performance parameters, and were displayed to permit verification of recorded data.

Following completion of an individual test, a composite magnetic tape was generated. This tape contained the raw data, along with calibration and bias parameters required to convert the raw data to engineering units.

Data was processed by first converting raw data to a form the general data reduction program could accept. This was accomplished during Step 3 as illustrated in Figure 28. The general data reduction program was then executed as indicated in Step 4. The purpose of this program was to convert data to absolute engineering units and compensate for any non-linearity in presesure transducers.

Due to an observed discrepancy between wake rake temperature and downstream multi element fixed rakes, approval was obtained for dual prccessing of performance data. Downstream fixed temperature instrumentation was used in all calculations involving stage and rotor performance, while the temperature wake rake data was used only to compute the efficiency profile across the stator spacing.

By using the 11-element temperature rake and the 11-element pressure rake, circumferential variation in efficiency was obtained at each radial immersion. The rotor total pressure analysis assumed that rotor efficiency could be detected in this plot of efficiency versus stator vane spacing. It was assumed that a portion of this plot was a reflection of rotor efficiency unaffected by stator wakes or secondary flows. The method for selecting the region to be used to compute rotor total pressure was determined by selecting a minimum efficiency level below which the data was not considered to be representative of rotor performance. This process is illustrated in Figure 29. As indicated in Step 4 of Figure 28, the general data reduction program was processed once for wake rake temperatures and once for fixed downstream temperatures. Output from this process was combined in Step 5 prior to further data analysis.

Overall performance was based on an averaging technique that; (1) calculated pressure of an equivalent uniform flow field with total momentum identical to the test field and, (2) calculated temperature of an equivalent uniform flow field with total energy the same as the test field. The latter is equivalent to a mass-averaged temperature. Compressor inlet temperatures and pressures were simple arithmetic averages since negligible radial and circumferential gradients were observed to exist at this location.

Appendix B presents a detailed mathematical summary of the procedure used to momentum average the total pressure. This procedure was repeated for each immersion and results were numerically integrated radially to obtain the momentum averaged stagnation pressure of the equivalent uniform flow field for the entire annulus area. The average compressor efficiency was obtained from enthalpy values of temperature and momentum averaged pressure.

Blade element performance. - Certain selected parameters for each data point were preserved for processing by an axisymmetric compressible flow analysis program. This program generated velocity diagrams at the inlet and exit of each blade row using the full radial equilibrium equation.

The derivation and applicability of this equation closely follows that of Reference 9. This analysis has been generalized, however, to allow use along station lines that are other than radial lines in the meridional (r-z) plane, as shown in Figure 30.

The basic equation that results from combining the momentum, continuity, energy, and state equations is;

$$\frac{1}{\rho}\frac{\partial P}{\partial n} = \frac{V_\theta^2}{r}\frac{[\cos\xi - M_m^2\cos(\alpha-\xi)\cos\alpha]}{(1-M_m^2)} - \frac{V_m^2[1-M_m^2\cos^2(\alpha-\xi)]}{r_c(1-M_m^2)\cos(\alpha-\xi)}$$

$$+ \frac{V_m^2\sin(\alpha-\xi)\cos(\alpha-\xi)}{(1-M_m^2)r}\left\{\frac{\partial[r\tan(\alpha-\xi)]}{\partial n} + \frac{\sin\alpha - \sin(\alpha-\xi)\cos\partial}{\cos(\alpha-\xi)}\right\}$$

$$+ \frac{V_m^2\sin(\alpha-\xi)}{(1-M_m^2)r}\left[\frac{(U-V_\theta)M_m^2}{rV_m^2}\frac{D(rV_\theta)}{D_m} - \frac{1}{R_g}\frac{DS}{Dm} - \frac{\cos\alpha}{r}\frac{\partial(\tan\beta_e)}{\partial\theta}\right]$$

$$+ \frac{V_m}{r}(\tan\varepsilon\cos\xi - \tan\beta^*\sin\xi)\frac{D(rV_\theta)}{Dm}$$

Definition of symbols used in this equation is presented in Appendix A.

As suggested by Smith in Reference 9, the computational form of this equation can be obtained by expressing the entropy derivative, DS/Dm, in terms of the local static pressure and temperature and integrating the definition of entropy from S = 0 at $P = P_o$ and $T = T_o$ to give:

$$Q = e^{-\Delta S/C_P} = \frac{(P/P_o)^{(\gamma-1)/\gamma}}{(T/T_o)} \quad \text{then;}$$

$$-\frac{DS}{Dm} = \frac{C_P}{Q}\frac{DQ}{Dm}$$

The circumferential derivative, $\frac{D(\tan\beta_e)}{d\theta}$, was approximated by assuming $\tan\beta_e$ to vary linearly in the circumferential direction and by introducing λ. The final approximate form was obtained as follows:

$$-\frac{\cos\alpha}{r}\frac{\partial\tan\beta_e}{\partial\theta}\frac{1}{\lambda}\frac{\rho\lambda}{Dm}$$

The last term on the right hand side of the radial equilibrium equation represents blade force effect on the flow field, and was not used since all calculation stations lay just outside the blades.

The data analysis process utilized the preceding radial equilibrium equation together with continuity and energy considerations to compute from the measured data, the vector diagram details at each measuring station. To effect closure of this set of equations, values of streamline slope, curvature, dQ/dm, and $d\lambda/dm$ were assumed constant at the values derived during the reference design point computation. This simplifying assumption is an obvious approximation devised to keep the extensive data reduction process economically manageable.

Measured values of casing static pressure, stator exit swirl angle, and radial distributions of total pressure and total temperature were utilized along with the measured flow rate. Through an iterative routine, the program computed at each station an annulus blockage factor, to simultaneously satisfy these measurements.

Since all measurements of total pressure and total temperature at the stage exit were made at fixed radial positions, namely the design location of specific streamlines, it was necessary to compute the total mass flow fraction contained between these fixed measurement positions for each data point. At the rotor inlet, rotor exit, and stator inlet stations, the radial locations of these streamlines were then determined through a continuity computation. Finally, the vector diagram and blade loading parameters were computed, at the blade and vane edges, for the flow along these deduced streamlines.

RESULTS AND DISCUSSION

Test 1

Smooth Casing With Close Clearance

The test compressor was configured with a smooth (untreated) casing over the rotor tips, and assembled so that the rotor tip running clearance was approximately 0.020 cm (0.008 in.). This clearance represents 0.78 percent of the mean rotor blade height. The clearance was measured in four casing quadrants and was continuously monitored throughout all smooth casing tests. Rig vibration problems were encountered during initial mechanical shakedown. Altering the rear bearing from a resilient mount to a hydraulically damped configuration eliminated this problem, and rig operation to the required 86,000 rpm was successful. Following instrumentation and leakage checks, baseline testing (Test 1) from 70 to 110 percent of design speed was completed.

Overall performance. - Rotor and stage overall performance is shown in Figures 31 and 32. For comparison, these data are superimposed on the performance obtained from Reference 7. At design speed, the rotor achieved a peak efficiency of 87.4 percent at a pressure ratio of 1.87 but at a flow three percent less than the design objective. A pressure ratio of 1.885 and an efficiency of 86.6 percent were the design objectives. At the design pressure ratio the rotor achieved design efficiency.

The pressure ratio produced by this rotor is at all speeds less than the corresponding value measured for the original compressor, and reported in Reference 7.

The maximum efficiency achieved by the stage at design speed was 83.3 percent and occurred at a pressure ratio of 1.865, whereas the design intent was 82.6 percent at a pressure ratio of 1.835. The design efficiency was met, or exceeded, over the stage pressure ratio range from approximately 1.78 to 1.91. A pressure ratio of 1.925 was developed at surge, which compares to a value of 1.96 obtained on the original compressor.

To permit a ready comparison of performance achieved in this and succeeding tests, a reference operating line was defined based on performance measured during Test 1. This reference operating line was defined as the locus of stage operating points along a fixed throttle line that passed through design pressure ratio at design speed. When compared to this reference operating line, the surge margin of this stage at design speed was 10.8 percent. Similarly, at 110 percent, 90 percent, and 70 percent speed the surge margin was 11.8 percent, 13.5 percent, and 18.1 percent, respectively. As can be seen in Figure 32, the demonstrated surge margin compares favorably to that reported in Reference 7.

Blade element performance. - Blade element performance for five radial positions (10, 30, 50, 70, and 90 percent span from the tip) is presented in Figures 33 through 37 for the rotor, and Figures 38 through 42 for the stator, in terms of total loss coefficient, diffusion factor, total loss parameter, and deviation angle versus suction surface incidence angle. Design values are indicated in these figures. At design pressure ratio, rotor incidence angles are seen to be approximately one degree higher than design. This results from the stage inability to obtain design equivalent flow.

Rotor diffusion factors were close to design estimates throughout the span with a peak value slightly in excess of 0.53 near the hub. This value compares to 0.6 reached on the Reference 7 rotor at 70 percent span from the tip. Loss coefficient and loss parameter, although satisfying design levels near the endwalls, were approximately two times the intent at mid-span. Contrary to the higher than design deviation angles obtained on the original rotor, deviation angles indicated for this rotor were generally lower than design estimates by approximately five degrees near the tip and two degrees at mid-span. Design levels were attained adjacent to the hub.

Stator incidence and deviation angles agreed well with design values. Vane diffusion factors at design speed did not exceed design levels; however, endwall values reached 0.54 at 110 percent speed. The stator loss coefficient and loss parameter were below design values near the tip and mid-span regions, but exceeded design values near the hub.

Boundary layer data. - Surveys of total pressure versus distance, measured from the outer wall, were obtained at the rotor inlet, rotor exit, and stator exit boundary layer survey locations described in the Instrumentation Section of this report. Figures 43 through 45 show data taken at 70 percent speed, Figures 46 through 48 show data for 90 percent speed, and Figures 49 through 51 show profiles at design speed. Figures 52 through 54 present data obtained at 110 percent speed. Data is shown at wide open throttle, peak efficiency, and near surge for all speeds except 70 percent where profiles were not obtained near surge. Peak efficiency and wide open throttle were coincident at 70 percent speed.

The momentum average rotor discharge and stage discharge pressure ratios, calculated from the downstream wake rake instrumentation, are presented in Figures 50 and 51 for comparison to the boundary layer data obtained at design speed near peak efficiency and surge. As can be seen, reasonable agreement between the two sets of data exists.

Test 2

Casing Treatment Close Clearance

The test compressor rotor outer casing was changed from solid to circumferentially grooved. This was facilitated by the removable casing inserts that were changed without removing the compressor from the test facility or uncoupling instrumentation. Rotor tip-to-casing running clearances were maintained at 0.020 cm (0.008 in.).

Overall performance. - Rotor and stage overall performance obtained with casing treatment and close radial clearance (Test 2) are shown in Figures 55 and 56 for 70, 90, and 100 percent of design speed. Superimposed on these figures is the performance previously determined during baseline testing with smooth casing (Test 1). Comparison of data from the stage with treated casing and that obtained with smooth casing show a two point improvement in rotor efficiency at design speed, with lesser improvements at part speed. The maximum stage efficiency at 90 and 100 percent speed is essentially unchanged. The surge margin showed significant increases at all speeds when casing treatment was added. The stage surge margin increased to 12.8, 17.3, and 21.0 percent at 100, 90, and 70 percent of design speed, respectively. Therefore, these results substantiate the basic conclusions reached in Reference 1 regarding surge margin improvement, with no penalty in stage performance for this casing treatment configuration.

Blade element performance. - Rotor blade element performance is presented in Figures 57 through 61 and stator blade element performance is presented in Figures 62 through 66.

Rotor incidence, deviation angles, and diffusion factor were similar to values obtained during Test 1. Losses near the casing remained at approximately the same level but, generally were reduced at all other positions. This was reflected in improved rotor efficiency. However, stator losses were increased, thereby resulting in similar stage efficiency for both tests. Stator loading was essentially unchanged, but stator deviation angles increased by approximately five degrees above the values from Test 1.

The above observations, regarding rotor losses and stator losses, are suggestive of an uncertainty in identifying a precise allocation of losses between rotor and stator. Little, or no judgement need be applied during computation of overall stage pressure ratio and efficiency. However, selection of the wake rake profile portion that is representative of rotor exit flow conditions is a matter of judgement and numerical technique.

The fact that the computed increase in rotor efficiency is located primarily near the hub, and is combined with the fact that stage performance is essentially unchanged, casts doubt on the automated rotor efficiency computation accuracy.

In addition, the swirl angle measurement downstream of a stator row, is subject to errors incurred because of total pressure gradients that exist in the stator wake area. Shifts in wake position, or character, are perhaps responsible for otherwise inexplicable changes in measured swirl angle downstream of stationary blade rows.

Boundary layer data. - Rotor inlet, rotor exit, and stator exit boundary layer survey data were obtained at 70, 90, and 100 percent of design speed and are presented in Figures 67 through 75. These data were taken at wide open throttle, peak efficiency, and near surge.

Local values of rotor discharge and stage discharge pressure ratio, determined from the downstream wake rake instrumentation, are also shown in Figures 74 and 75 for comparison to the boundary layer data obtained near peak efficiency and surge. Observe that the casing boundary layer profile thickness at the rotor exit has increased with casing treatment (compare Figures 50 and 74).

Test 3

Smooth Casing With Open Clearance

Various methods were considered to alter rotor tip clearance in order to investigate this effect on performance. The method used for this investigation consisted of machining rotor blade tips to reduce rotor diameter. Axial rotor displacement (within the sloping casing) appeared to offer certain economic advantages, but was considered undesirable since instrumentation station changes relative to the rotor would result.

Alternatively, the increased clearance could have been obtained by machining the casing locally to a larger diameter in the rotor tip region. This would have resulted in flowpath contour discontinuities and would require some new instrumentation. Therefore, blade tips were machined to remove 0.036 cm (0.014 in.) radially, which resulted in an average design speed running clearance of 0.056 cm (0.022 in.), as measured in the smooth casing. This represents an increase in clearance from 0.78 to 2.14 percent of the mean rotor blade span.

Overall performance. - Rotor and stage overall performance for this configuration are presented in Figures 76 and 77. These data are superimposed on performance obtained from Test 1 for comparison. Maximum efficiency achieved by the rotor at design speed was approximately three points below that obtained with close clearance. A large reduction in the maximum pressure ratio achieved by the rotor was observed at design speed. In addition, the rotor maximum flow capacity was reduced to about 91.2 percent of design with this enlarged clearance. All of these performance decrements are reduced in severity with decreasing speed; presumably as a consequence of lower blade loadings associated with the part speed operation.

Stage performance was greatly reduced at high speeds from that of the baseline configuration. Pressure ratio at surge was lower at all speeds with the greatest decay occurring at design speed, where 1.745 was obtained compared to 1.925 at the smaller clearance. A loss of 5.5 points in peak efficiency at design speed was a result of this large running clearance. Stage surge margins of only 5.4, 7.2, and 11.0 percent were obtained at 100, 90, and 70 percent of design speed, respectively, which are approximately 50 percent of values demonstrated during Test 1.

Blade element performance. - Blade element performance parameter summary plots are presented in Figures 78 through 82 for the rotor and in Figures 83 through 87 for the stator. As a result of flow reduction, rotor incidence was approximately four or five degrees higher than design. Rotor diffusion factors were well below corresponding values from Test 1, with maximum values of about 0.4 occurring in the tip region. For comparison maximum loading with close clearance occurred in the hub and exceeded 0.53. Higher than design losses were obtained in the rotor tip region, but losses approximated design levels near mid-span and hub. Deviation angles near the rotor tip were approximately four degrees below that obtained in Test 1, but again approximated design levels at the hub.

Stator incidence angles were generally less than the corresponding value during Test 1, particularly in proximity to the hub. This reduced incidence resulted in a severe increase in losses near the hub. Stator diffusion factors were reduced from Test 1.

Boundary layer data. - Measurements of total pressure versus distance from outer wall were obtained at rotor inlet, rotor exit, and stator exit survey locations as defined in the Instrumentation Section of this report. Figures 88 through 90 show data for 70 percent speed, Figures 91 through 93 for 90 percent speed, and Figures 94 through 96 for design speed. Surveys are shown for wide open throttle, peak efficiency, and near surge at all speeds.

Local values of rotor discharge and stage discharge pressure ratio determined from the downstream wake rake instrumentation are also presented in Figures 95 and 96 for comparison to the boundary layer data obtained at near peak efficiency and surge. The two data sources show the same agreement typical of data obtained during Tests 1 and 2. However, boundary layer data near the casing presented in Figures 89, 92, and 95 indicate a substantially different trend than previously obtained. Figure 97 presents a comparison between data from Tests 1 and 3 near peak efficiency for design speed. This figure clearly shows the rotor pressure ratio reduction due to the increase in rotor running clearance.

As indicated by the blade element data (Figures 78 through 82), this rotor pressure ratio reduction is in part attributable to increased losses near the rotor tip, but more generally is the consequence of rotor blade unloading at all spanwise positions.

Test 4

Casing Treatment With Open Clearance

The smooth casing insert was removed, and the insert incorporating casing treatment was installed in the test compressor. Rotor tip-to-casing running clearances were maintained at 0.056 cm (0.022 in.) as for Test 3.

Overall performance. - Rotor and stage overall performance obtained with casing treatment, and open radial clearance, are shown in Figures 98 and 99 for 70, 90, and 100 percent of design equivalent speed. Superimposed on these figures for comparison is the performance previously determined from both tests with smooth casing; i.e., Test 1 with close running clearance, and Test 3 with the same large clearance as Test 4.

A dramatic improvement in performance over that obtained with the smooth casing at the same open clearance was seen at all speeds tested. Approximately one-half of the performance lost as a result of increased clearance was regained with casing treatment. Rotor peak efficiency at 90 percent speed even exceeded the level achieved during baseline testing. Rotor maximum pressure ratio at design speed was increased from 1.81 with smooth casing to approximately 1.87 with casing treatment. Maximum flow at design speed was increased from 91.2 to 94.2 percent of design. At design speed, the stage maximum efficiency was improved from 77.5 percent with smooth casing to almost 81 percent with treated casing for this test. At 90 percent speed, the maximum stage efficiency was improved to essentially the same level obtained with close clearance. Stage surge margins at 100, 90, and 70

percent of design speed were significantly increased to 8.7, 10.6, and 16.7 percent, respectively, from the previously obtained values of 5.4, 7.2, and 11.0 percent with a smooth casing.

Blade element performance. - Blade element performance parameter summary plots are presented in Figures 100 through 104 for the rotor and Figures 105 through 109 for the stator.

When compared to Test 3 results, it is apparent the rotor was operating with a slightly reduced incidence because of increased flow rate. Regardless of this, rotor blade loading (D-factor) and deviation angle were slightly higher than during Test 3. Rotor loss coefficients were generally reduced from the levels observed for Test 3. Stator losses were substantially reduced in the hub region as a result of a less negative incidence. Near the casing, stator losses were unchanged and insensitive to incidence angle.

Boundary layer data. - As in all previous testing, measurements of total pressure versus distance from outer wall were obtained at rotor inlet, rotor exit, and stator exit survey locations. However, during post-test data analysis, it was determined that total pressure data obtained at the rotor exit position were in error. After extensive investigation, it was determined that these data were irretrievably lost. As a result, only the rotor inlet and stator exit survey data are shown. Figures 110 and 111 show 70 percent speed data; Figures 112 and 113, 90 percent speed; and Figures 114 and 115, 100 percent speed.

Local values of stator discharge pressure ratios, determined from the downstream wake rake instrumentation, are presented in Figure 115 for comparison to the boundary layer data obtained near peak efficiency and surge. The data obtained at stage discharge shows the same reasonable agreement obtained during previous tests.

SUMMARY OF RESULTS

As described in detail under Data Reduction Procedure, vector diagrams at the inlet and exit to each blade row were determined through an extensive computational procedure utilizing the measured flow conditions and the fluid dynamic equations. One parameter, necessarily determined during this computation to model the tested flow condition details, was the local annulus area blockage factor (λ). Historically, this parameter has been used to represent, in an axisymmetric flow analysis, the effects of endwall boundary layer blockage as well as circumferential (blade-to-blade) non-uniformities. Some significant results of this present test series can be more clearly visualized by observing the deduced changes in rotor exit blockage factor as presented in Figure 116. As shown, the rotor exit blockage factor has been normalized by the value at rotor inlet, because, it is the area-ratio across a rotor that is most significant in determining operation at a given flow-rate and rotating speed. The data in Figure 116 must be interpreted in recognition of assumptions inherent in the data analysis procedure. However, significant variations are observed that serve to clarify some performance changes between the four tests.

The addition of casing treatment to the close-clearance baseline configuration appears to have caused a slight decrease in blockage factor (more blockage). However, according to the data, there was a slight decrease in rotor deviation angle, particularly near the casing to the effect that overall stage performance was relatively unchanged.

Performance of the open-clearance configuration (Test 3), is dominated by a very large reduction in blockage factor at the rotor trailing edge. This reduction in blockage factor can be interpreted as an axisymmetric approximation to the complex three-dimensional flow process in the rotor tip region. As rotor running clearance increases, the tip leakage increases, giving rise to an increase in the rotor tip vortex magnitude and an associated increase in loss coefficient in the rotor tip region. When observed in the stationary coordinate system, these effects of increased clearance appear as reduced total pressure level and reduced blockage factor. The resultant effect on rotor operation is a general flow shift away from the casing and an increase of axial velocity, primarily near the hub and mid-span. This is evident in reduced rotor loading (lower D-factor) and higher axial velocity into the stator.

It should be noted that the computed blockage factor was distributed uniformly across the annulus (see Appendix B for detailed discussion). A more complex modeling that recognized variations in blockage as a function of radial position may have provided different vector diagram details.

The addition of circumferential grooves to the open-clearance configuration resulted in a blockage factor increase and, therefore, a significant recovery of rotor pressure rise and stage flow capacity.

Figure 117 illustrates blockage variation effects on axial velocity at the rotor discharge. Shown in this figure for comparison, is the computed axial velocity profile for the four tests near peak rotor efficiency at design speed. The comparison of Test 1 data and Reference 7 data illustrates the agreement between these velocity profiles.

The annulus blockage factor at the stator inlet, illustrated in Figure 118, showed surprisingly small changes between the four tests when compared to results obtained at the rotor exit. At the higher speeds, trends are similar but the magnitude of changes are a small fraction of changes shown in Figure 116. At 70 percent speed, no significant change is seen in blockage level between the various rotor configurations. This observation is consistent with the comparatively slight variations in stage performance at 70 percent speed.

Extreme variations of rotor exit blockage and relatively small variations of stator inlet blockage are difficult to accept. However, since the rotor exit blockage factor decreases (more distortion) with increasing flow and reduced rotor loadings, it would appear that the major contribution to area blockage at the rotor exit is related to some shock induced, or at least some Mach number dependent, process rather than being controlled by increasing diffusion on the endwalls or blade surfaces in the usual sense. It is not known whether this type of blockage might achieve a comparatively mixed state within the short axial distance between rotor exit and stator inlet.

Alternatively, it should be recognized that some approximation in the data interpretation or the axisymmetric modeling may have induced an unfavorable comparison.

Shown in Figure 119 are the radial distributions of stator incidence angle obtained from data points near peak rotor efficiency at design speed. The effect of variations in blockage factor on stator incidence is evident. Note that there are significant flow-rate differences between the selected data points.

Data in Figure 120 shows a large variation in stator loss coefficient between the same operating points as above. These stator losses are seen to increase rapidly at the low incidence angles.

The preceding data presentations and accompanying discussions clearly show that performance of this small transonic compressor was critically dependent on the effective annulus area available for flow at the rotor exit and stator inlet.

Flow deficiency of the close-clearance baseline configuration of Test 1 can be attributed, to a large degree, to a lower blockage factor than design. Whether this low blockage factor is a result of low rotor aspect-ratio or some other design consideration, remains to be determined. However, results of Test 1 clearly show that at design speed, rotor losses are limiting the performance attainable on the speed line low flow side, and stator losses are limiting the maximum flow capacity and performance on the speed line high flow end.

Since the rotor exit blockage factor and stator incidence are reduced, while the rotor incidence is increased with large clearances (Test 3), this mismatch between rotor and stator is amplified. Performance benefits realized by addition of casing treatment to the open-clearance configuration (Test 4), are largely the consequence of improved matching between the rotor and stator.

It appears clear that the basic stage performance could be improved by the incorporation of a design modification to increase the rotor exit area by an amount devised to optimize the match between the rotor and stator low loss operating ranges. Such a modification should also avoid some of the precipitous performance reduction associated with increased tip clearance, as observed in the present test series.

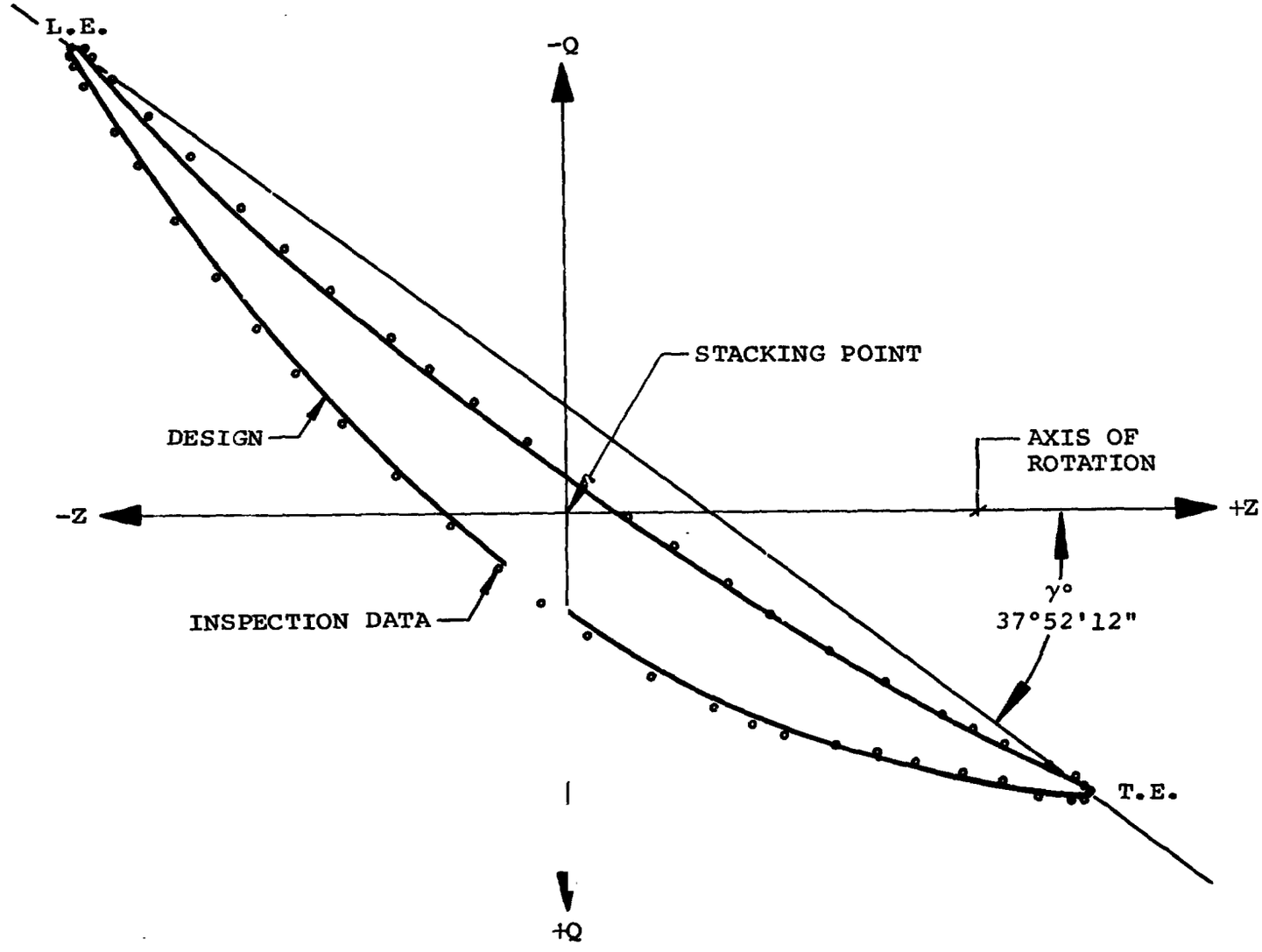

Figure 1. -Rotor optical comparison near mid-span.

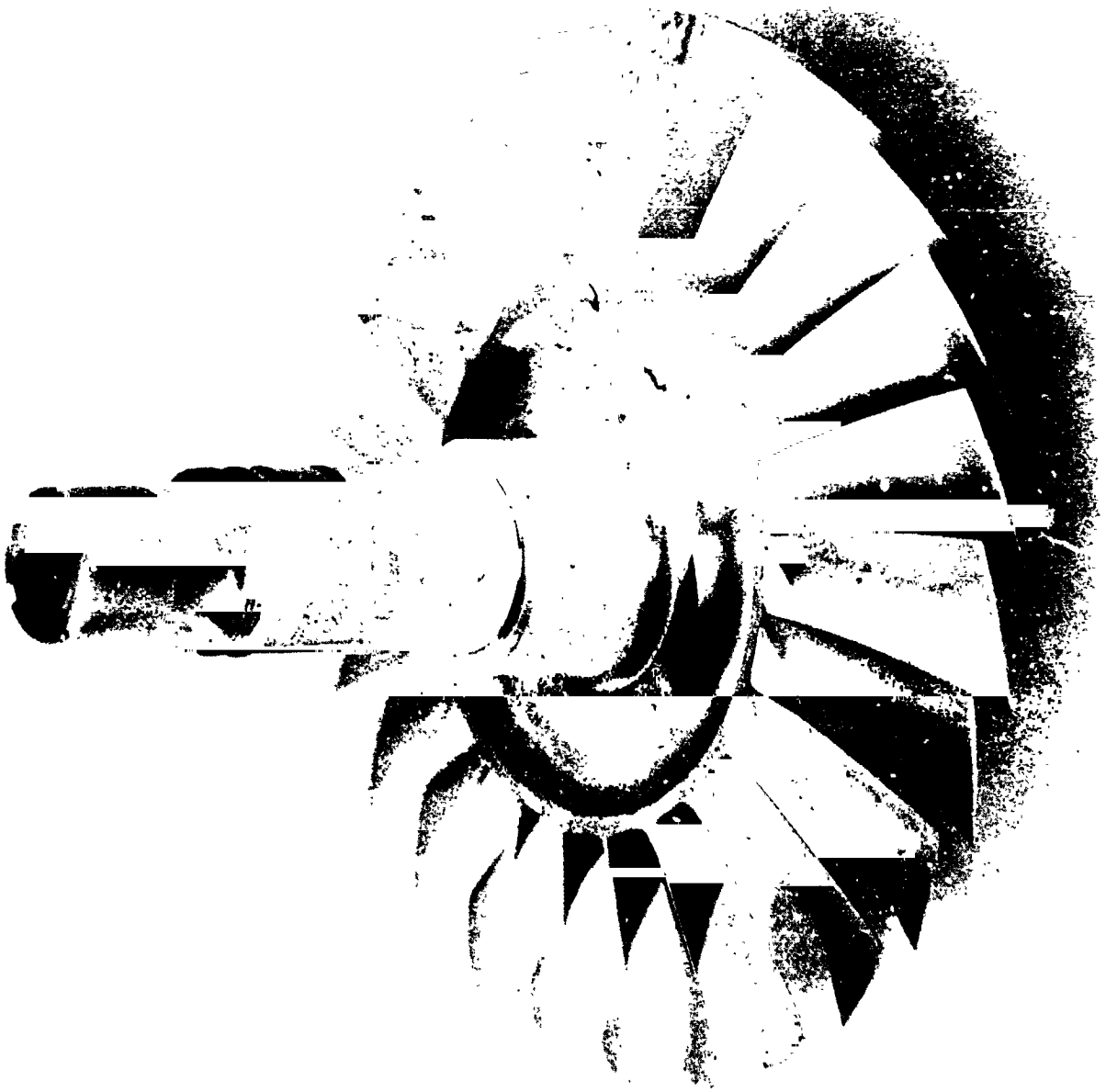

Figure 2. -View of rotor, looking aft.

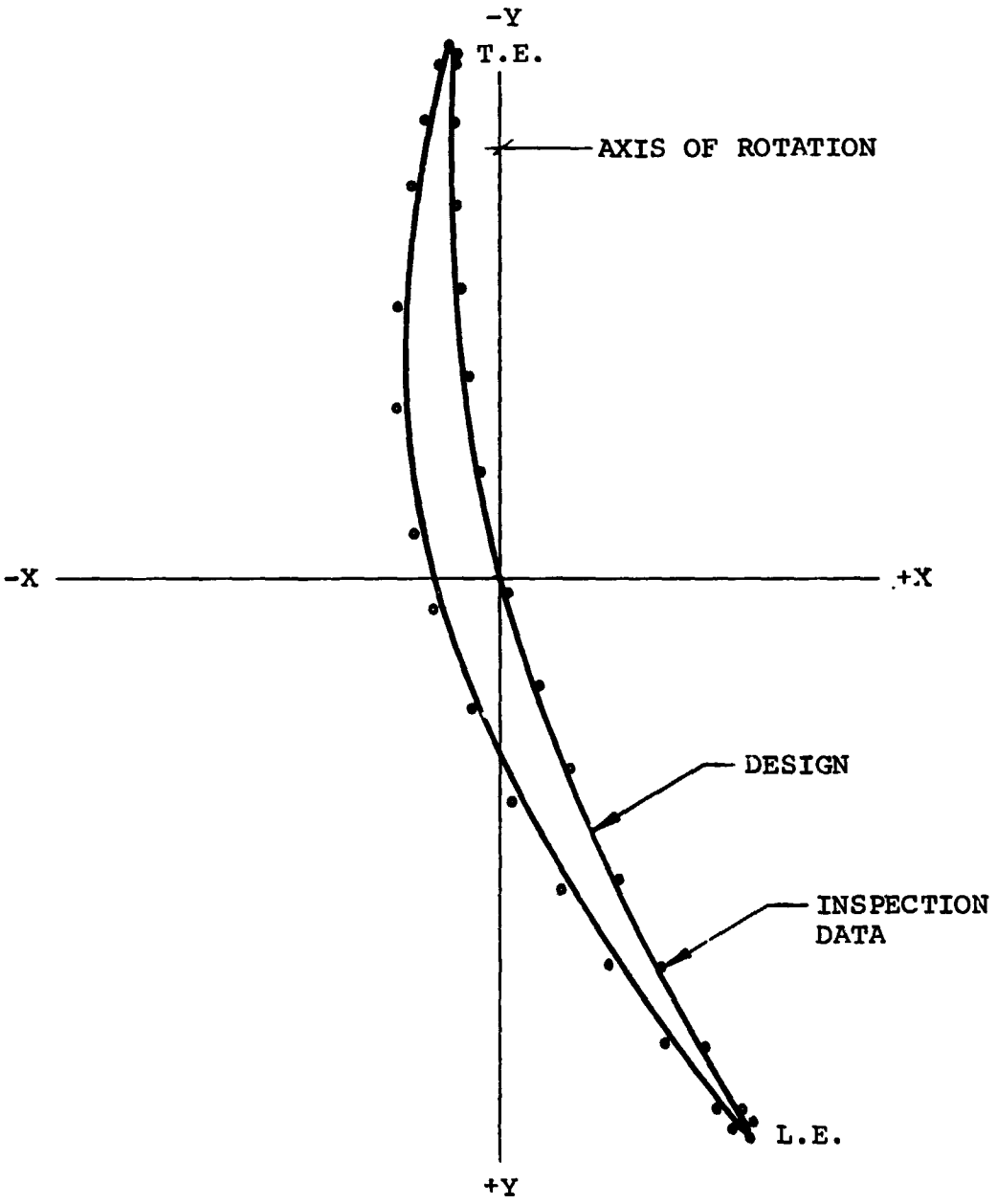

Figure 3. -Stator vane optical inspection near mid-span.

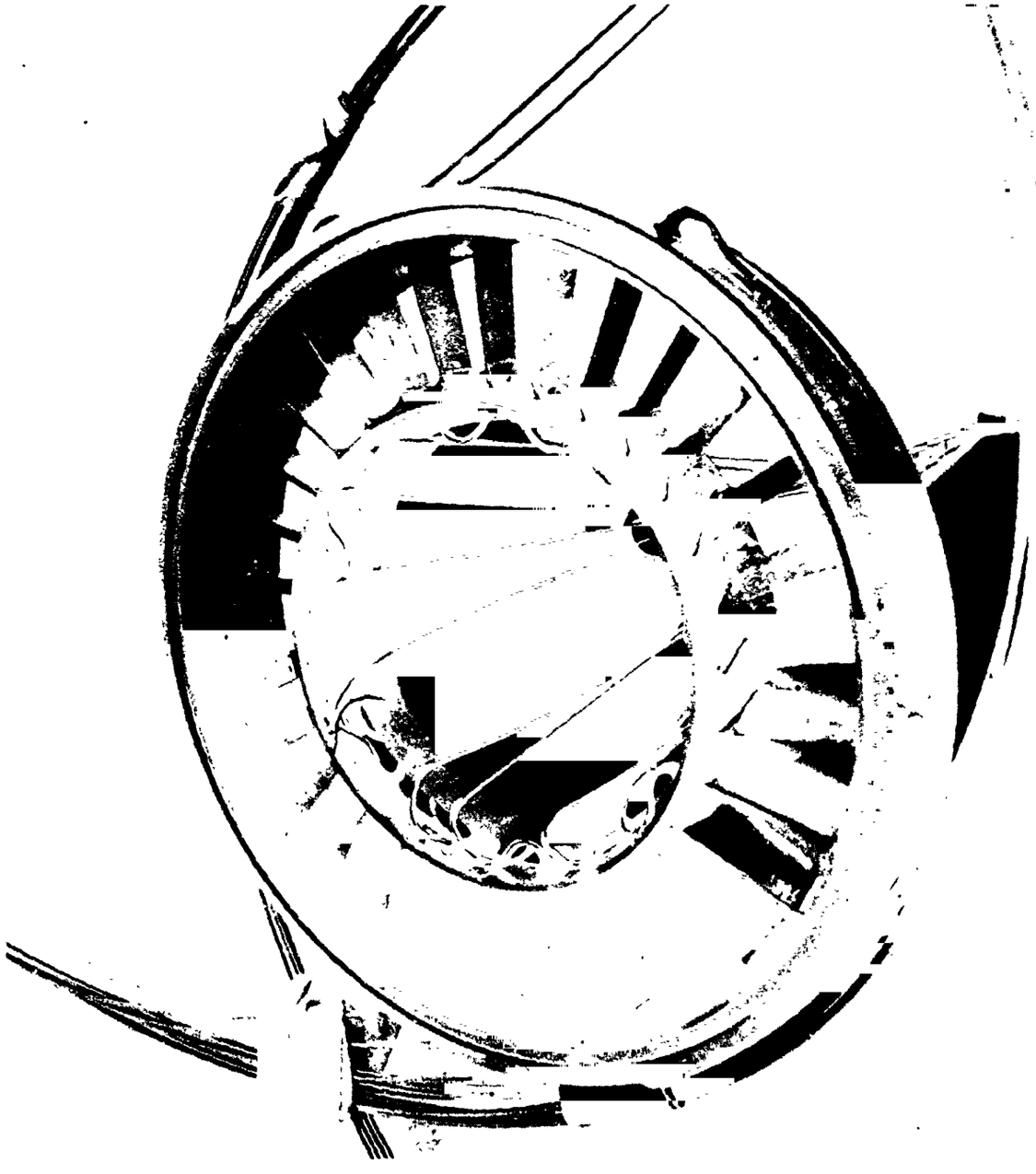

Figure 4. -View of finished stator assembly, looking aft.

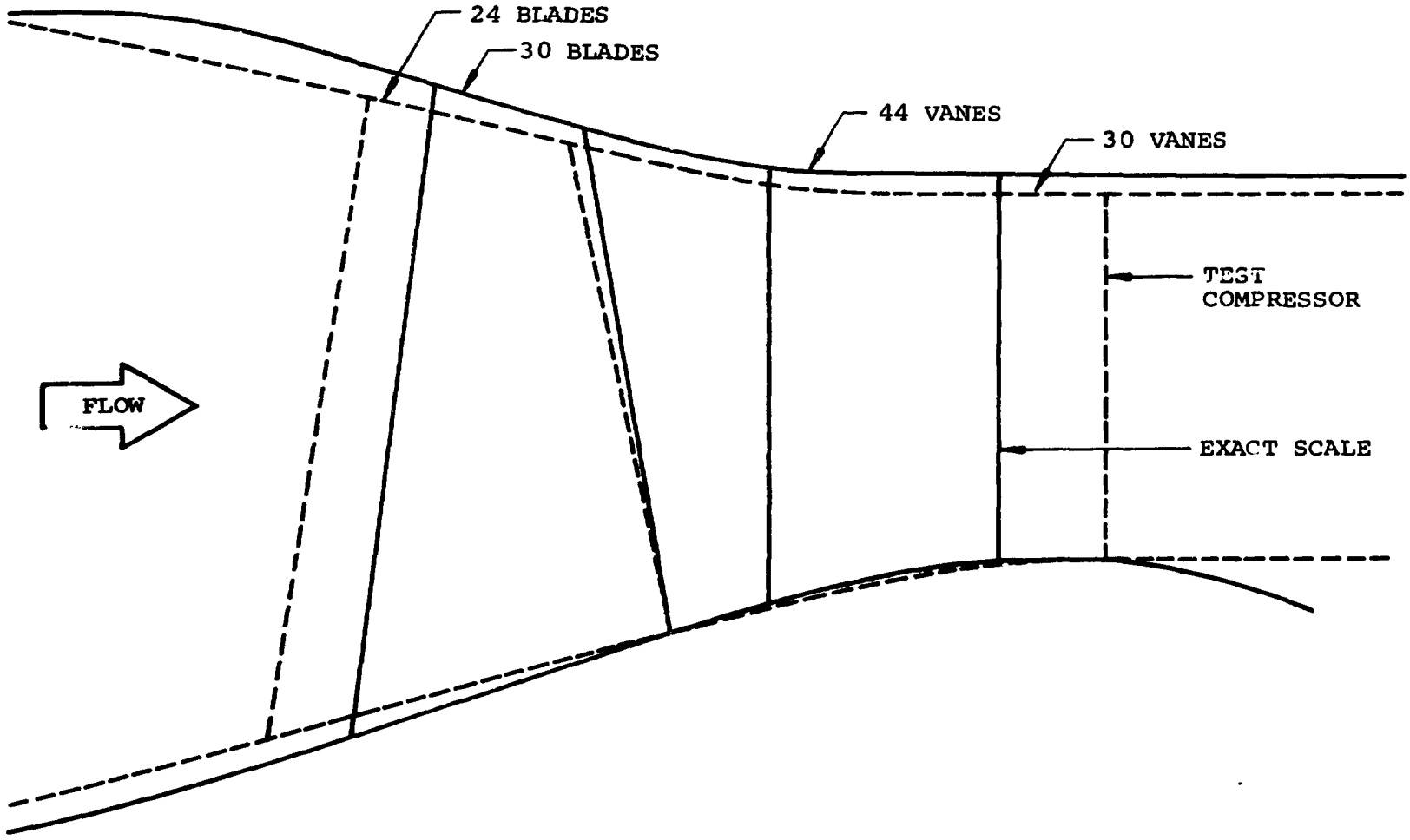

Figure 5. -Comparison of test compressor and exact scale of Reference 6.

100 PERCENT DESIGN SPEED - SCAN NO 0

EQUIVALENT WEIGHT FLOW = 1.6613 KG/SEC
PERCENT DESIGN EQUIVALENT FLOW = 100.0000
EQUIVALENT SPEED = 76719.825 R.P.M.
EQUIVALENT FLOW / INLET ANN AREA = 197.5068 KG/SEC-SQ M

INLET VELOCITY DIAGRAM DATA
CALCULATED AERODYNAMIC BLOCKAGE = 1.0045

PERCENT SPAN FROM TIP (L. E.)	BETA*1 (DEG)	V*1 (M/SEC)	VU*1 (M/SEC)	M*1	BETA1 (DEG)	V1 (M/SEC)	VU1 (M/SEC)	M1	VM1 (M/SEC)	VZ1 (M/SEC)	U1 (M/SEC)
0.00	69.87	513.32	481.94	1.551	0.00	176.69	0.00	.534	176.69	171.00	481.94
7.97	68.72	495.86	462.97	1.503	0.00	180.33	0.00	.546	180.33	174.42	462.97
24.20	65.21	467.62	424.33	1.422	0.00	195.99	0.00	.596	195.99	192.38	424.33
41.29	62.38	432.99	383.64	1.320	0.00	200.74	0.00	.612	200.73	200.09	383.64
60.63	60.10	389.28	337.46	1.183	0.00	194.03	0.00	.590	194.03	193.96	337.46
84.45	57.03	334.24	280.39	1.012	0.00	181.91	0.00	.551	181.91	179.46	280.39
100.00	54.24	300.52	243.85	.908	0.00	175.63	0.00	.531	175.63	169.66	243.85

EXIT VELOCITY DIAGRAM DATA
CALCULATED AERODYNAMIC BLOCKAGE = .9852

PERCENT SPAN FROM TIP (T. E.)	BETA*2 (DEG)	V*2 (M/SEC)	VU*2 (M/SEC)	M*2	BETA2 (DEG)	V2 (M/SEC)	VU2 (M/SEC)	M2	VM2 (M/SEC)	VZ2 (M/SEC)	U2 (M/SEC)
0.00	68.97	318.62	295.55	.857	54.68	205.86	167.97	.554	119.01	115.17	463.52
11.35	62.05	310.74	279.78	.863	47.71	220.62	163.19	.601	148.66	145.21	442.98
30.26	55.20	305.01	250.45	.844	42.29	235.31	158.33	.651	174.07	172.99	408.78
48.03	48.32	275.21	205.55	.767	43.07	250.52	171.08	.698	183.00	182.99	376.62
66.93	41.96	241.38	161.33	.676	45.25	255.03	181.12	.714	179.54	179.01	342.45
88.27	24.06	207.36	84.54	.585	49.20	289.73	219.30	.818	189.33	186.22	303.85
100.00	9.77	193.93	32.91	.550	52.57	314.45	249.71	.892	191.11	184.61	282.62

ROTOR PERFORMANCE DATA

PERCENT SPAN FROM TIP LEADING EDGE	TRAILING EDGE	MASS FLOW (PCT)	DELTA BETA* (DEG)	INCIDENCE MEAN (DEG)	ANGLE SUCT SUR (DEG)	D FACTOR	OMEGA* BAR	LOSS PARAMETER	DEVIATION ANGLE (DEG)	ROTOR PRESS RATIO	ROTOR ADIABATIC EFF	ROTOR POLYTROPIC EFF
0.00	0.00	0.00	1.80	6.030	5.562	.5039	.2836	.0403	11.076	1.776	.6629	.6888
7.97	11.35	10.00	6.67	6.466	5.270	.4818	.2142	.0364	7.058	1.813	.7418	.7623
24.20	30.26	30.00	10.01	5.927	3.944	.4605	.0947	.0180	4.955	1.885	.8879	.8974
41.29	48.03	50.00	14.08	5.477	2.698	.4847	.0602	.0121	5.775	1.940	.9363	.9419
60.63	66.93	70.00	18.16	5.678	1.860	.5067	.0555	.0113	10.916	1.911	.9484	.9529
84.45	88.27	90.00	32.96	5.695	.670	.5312	.0699	.0149	14.879	2.001	.9519	.9564
100.00	100.00	100.00	44.47	5.485	-.589	.5281	.0961	.0202	16.823	2.069	.9469	.9520

MOMENTUM AVERAGE MOTOR EFFICIENCY = .8879 (POLYTROPIC)
MOMENTUM AVERAGE ROTOR EFFICIENCY = .8773 (ADIABATIC)

MOMENTUM AVG. ROTOR PRESS RATIO = 1.9017
MASS AVERAGE TEMPERATURE RISE = 1.2293

Figure 6. -Design point rotor performance (metric units).

100 PERCENT DESIGN SPEED - SCAN NO 0

EQUIVALENT WEIGHT FLOW = 3.6626 LBM/SEC
PERCENT DESIGN EQUIVALENT FLOW = 100.0000
EQUIVALENT SPEED = 76719.825 R.P.M.
EQUIVALENT FLOW / INLET ANN AREA = 40.4526 LBM/SEC-SQ FT

INLET VELOCITY DIAGRAM DATA
CALCULATED AERODYNAMIC BLOCKAGE = 1.0045

PERCENT SPAN FROM TIP (L. E.)	BETA*1 (DEG)	V*1 (FT/SEC)	VU*1 (FT/SEC)	M*1	BETA1 (DEG)	V1 (FT/SEC)	VU1 (FT/SEC)	M1	VM1 (FT/SEC)	VZ1 (FT/SEC)	U1 (FT/SEC)
0.00	69.87	1644.13	1581.18	1.551	0.00	579.69	0.00	.534	579.69	561.01	1581.18
7.97	68.72	1630.12	1518.93	1.503	0.00	591.64	0.00	.546	591.64	572.26	1518.93
24.20	65.21	1533.53	1392.17	1.422	0.00	643.02	0.00	.596	643.00	631.18	1392.17
41.29	62.38	1420.59	1258.66	1.320	0.00	658.59	0.00	.612	658.57	656.45	1258.66
58.48	60.10	1277.16	1107.17	1.183	0.00	634.60	0.00	.590	634.58	636.36	1107.17
76.65	57.03	1096.59	919.93	1.012	0.00	596.82	0.00	.551	596.80	588.79	919.93
100.00	54.24	985.96	800.03	.908	0.00	576.22	0.00	.531	576.20	556.62	800.03

EXIT VELOCITY DIAGRAM DATA
CALCULATED AERODYNAMIC BLOCKAGE = .9852

PERCENT SPAN FROM TIP (L. E.)	BETA*2 (DEG)	V*2 (FT/SEC)	VU*2 (FT/SEC)	M*2.	BETA2 (DEG)	V2 (FT/SEC)	VU2 (FT/SEC)	M2	VM2 (FT/SEC)	VZ2 (FT/SEC)	U2 (FT/SEC)
0.00	58.07	1045.32	969.64	.857	54.68	675.40	551.09	.554	390.44	377.87	1520.72
11.35	52.05	1039.18	917.92	.863	47.71	723.83	535.41	.601	487.07	476.43	1453.33
34.24	55.20	1000.70	821.70	.844	42.29	772.02	519.45	.651	571.18	567.54	1341.15
44.33	44.32	902.93	674.37	.767	43.07	821.90	561.27	.698	600.38	600.35	1235.65
64.73	41.94	791.93	529.30	.676	45.25	836.73	594.23	.714	589.04	587.30	1123.52
84.27	24.06	680.30	277.38	.585	49.20	950.57	719.50	.818	621.14	610.96	996.88
100.00	9.77	636.24	107.98	.550	52.57	1031.67	819.25	.892	626.99	605.68	927.23

ROTOR PERFORMANCE DATA

PERCENT SPAN FROM TIP LEADING EDGE	TRAILING EDGE	MASS FLOW (PCT)	DELTA BETA* (DEG)	INCIDENCE MEAN (DEG)	ANGLE SUCT SUR (DEG)	D FACTOR	OMEGA* BAR	LOSS PARAMETER	DEVIATION ANGLE (DEG)	ROTOR PRESS RATIO	ROTOR ADIABATIC EFF	ROTOR POLYTROPIC EFF
0.00	0.00	0.00	1.80	6.030	5.562	.5039	.2836	.0403	11.076	1.776	.8629	.8888
7.97	11.35	10.00	6.47	6.466	5.270	.4818	.2142	.0364	7.058	1.813	.7418	.7623
24.20	30.26	30.00	10.01	5.927	3.944	.4605	.0947	.0180	4.935	1.895	.8879	.8974
41.29	48.03	50.00	14.06	5.477	2.698	.4847	.0602	.0121	5.775	1.940	.9363	.9419
58.68	66.93	70.00	18.16	5.678	1.860	.5067	.0555	.0113	10.916	1.911	.9484	.9529
76.65	88.27	90.00	32.96	5.695	.670	.5312	.0699	.0149	14.879	2.001	.9519	.9564
100.00	100.00	100.00	44.47	5.445	-.589	.5281	.0961	.0202	16.823	2.069	.9469	.9520

MOMENTUM AVERAGE ROTOR EFFICIENCY = .8879 (POLYTROPIC)
MOMENTUM AVERAGE ROTOR EFFICIENCY = .8773 (ADIABATIC)
MOMENTUM AVG. ROTOR PRESS RATIO = 1.9017
MASS AVERAGE TEMPERATURE RISE = 1.2293

Figure 7. -Design point rotor performance (English units).

100 PERCENT DESIGN SPEED - SCAN NO 0

INLET VELOCITY DIAGRAM DATA
CALCULATED AERODYNAMIC BLOCKAGE = .9854

PERCENT SPAN FROM TIP (L. E.)	BETA 3 (DEG)	V3 (M/SEC)	VU3 (M/SEC)	M3	VM3 (M/SEC)	VZ3 (M/SEC)	U3 (M/SEC)
0.00	46.72	237.60	172.96	.645	162.89	161.10	450.15
10.13	42.51	246.49	166.55	.677	181.71	181.40	434.05
28.37	37.75	260.94	159.78	.730	206.35	206.35	405.06
46.22	38.56	274.40	171.05	.772	214.56	214.40	376.68
65.61	40.63	275.41	179.33	.778	209.02	208.25	345.87
87.73	44.81	304.35	214.47	.865	215.92	213.02	310.70
100.00	47.44	328.96	242.28	.941	222.50	216.35	291.19

EXIT VELOCITY DIAGRAM DATA
CALCULATED AERODYNAMIC BLOCKAGE = .9881

PERCENT SPAN FROM TIP (T. E.)	BETA 4 (DEG)	V4 (M/SEC)	VU4 (M/SEC)	M4	VM4 (M/SEC)	VZ4 (M/SEC)	U4 (M/SEC)
0.00	0.00	178.77	0.00	.477	178.77	178.77	446.89
10.40	0.00	188.95	0.00	.510	188.94	188.92	432.68
29.81	0.00	213.59	0.00	.587	213.59	213.49	406.17
48.22	0.00	224.24	0.00	.619	224.23	224.00	381.02
67.74	0.00	216.20	0.00	.597	216.20	216.08	356.35
89.06	0.00	232.60	0.00	.641	232.60	231.75	325.23
100.00	0.00	232.95	0.00	.639	232.94	232.94	310.29

STATOR PERFORMANCE DATA

PERCENT SPAN FROM TIP LEADING EDGE	TRAILING EDGE	MASS FLOW (PCT)	DELTA BETA (DEG)	INCIDENCE MEAN (DEG)	ANGLE SUCT SUR (DEG)	D FACTOR	OMEGA BAR	LOSS PARAMETER	DEVIATION ANGLE (DEG)	STAGE PRESS RATIO	STAGE TEMP RATIO	STATOR POLYTROPIC EFF
0.00	0.00	0.00	46.72	10.398	6.476	.5120	.1278	.0460	22.180	1.721	1.2685	.7647
10.13	10.40	10.00	42.51	6.360	2.964	.4689	.1158	.0402	16.788	1.757	1.2493	.7507
28.37	29.81	30.00	37.75	1.641	-2.115	.3822	.0520	.0171	13.232	1.856	1.2232	.8707
46.22	48.22	50.00	38.56	1.009	-2.015	.3718	.0640	.0196	12.014	1.900	1.2222	.8451
65.61	67.74	70.00	40.63	1.310	-1.597	.3973	.0746	.0214	11.104	1.864	1.2139	.8435
87.73	89.06	90.00	44.81	2.545	-.364	.4139	.0950	.0251	11.680	1.928	1.2298	.8231
100.00	100.00	100.00	47.44	2.808	-.635	.4672	.1710	.0432	18.700	1.915	1.2434	.7390

MOMENTUM AVERAGE STAGE EFFICIENCY = .8602 (POLYTROPIC)
MOMENTUM AVERAGE STAGE EFFICIENCY = .8475 (ADIABATIC)

MOMENTUM AVG. STAGE PRESS RATIO = 1.8640
MASS AVERAGE TEMPERATURE RISE = 1.2293

Figure 8. -Design point stator performance (metric units).

100 PERCENT DESIGN SPEED - SCAN NO 0

INLET VELOCITY DIAGRAM DATA
CALCULATED AERODYNAMIC BLOCKAGE = .9854

PERCENT SPAN FROM TIP (L. E.)	BETA 3 (DEG)	V3 (FT/SEC)	VU3 (FT/SEC)	M3	VM3 (FT/SEC)	VZ3 (FT/SEC)	U3 (FT/SEC)
0.00	46.72	779.51	567.45	.645	534.43	528.55	1476.87
10.13	42.51	828.70	546.41	.677	596.15	595.16	1424.05
28.37	37.75	856.27	524.23	.730	677.01	677.00	1328.92
46.22	38.56	900.28	561.19	.772	703.94	703.42	1235.84
65.60	40.63	903.58	588.35	.778	685.75	683.24	1134.75
87.73	44.81	998.51	703.64	.865	708.41	698.90	1019.35
100.00	47.44	1079.26	794.90	.941	729.98	709.81	955.35

EXIT VELOCITY DIAGRAM DATA
CALCULATED AERODYNAMIC BLOCKAGE = .9881

PERCENT SPAN FROM TIP (T. E.)	BETA 4 (DEG)	V4 (FT/SEC)	VU4 (FT/SEC)	M4	VM4 (FT/SEC)	VZ4 (FT/SEC)	U4 (FT/SEC)
0.00	0.00	586.52	0.00	.477	586.50	586.50	1466.16
10.40	0.00	619.90	0.00	.510	619.89	619.81	1419.57
29.81	0.00	700.76	0.00	.587	700.74	700.43	1332.58
48.22	0.00	735.70	0.00	.619	735.68	734.92	1250.05
67.74	0.00	709.32	0.00	.597	709.30	708.91	1162.58
89.84	0.00	763.14	0.00	.641	763.11	760.32	1067.02
100.00	0.00	764.26	0.00	.639	764.24	764.24	1018.01

STATOR PERFORMANCE DATA

PERCENT SPAN FROM TIP LEADING EDGE	TRAILING EDGE	MASS FLOW (PCT)	DELTA BETA (DEG)	INCIDENCE ANGLE MEAN (DEG)	SUCT SUR (DEG)	D FACTOR	OMEGA BAR	LOSS PARAMETER	DEVIATION ANGLE (DEG)	STAGE PRESS RATIO	STAGE TEMP RATIO	STATOR POLYTROPIC EFF
0.00	0.00	0.00	46.72	10.398	6.476	.5120	.1278	.0460	22.180	1.721	1.2685	.7447
10.13	10.40	10.00	42.51	6.360	2.964	.4689	.1158	.0402	16.788	1.757	1.2493	.7607
28.37	29.81	30.00	37.75	1.241	-2.115	.3822	.0520	.0171	13.232	1.856	1.2232	.8707
46.22	48.22	50.00	38.56	1.009	-2.015	.3718	.0640	.0196	12.014	1.900	1.2222	.8451
65.60	67.	70.00	40.63	1.310	-1.597	.3973	.0746	.0214	11.104	1.864	1.2139	.8435
87.73	89.09	90.00	44.81	2.545	-.364	.4139	.0950	.0251	11.690	1.928	1.2298	.8231
100.00	100.00	100.00	47.44	2.806	-.635	.4672	.1710	.0432	18.700	1.915	1.2434	.7390

MOMENTUM AVERAGE STAGE EFFICIENCY = .8602 (POLYTROPIC)
MOMENTUM AVERAGE STAGE EFFICIENCY = .8475 (ADIABATIC)

MOMENTUM AVG. STAGE PRESS RATIO = 1.8640
MASS AVERAGE TEMPERATURE RISE = 1.2293

Figure 9. -Design point stator performance (English units).

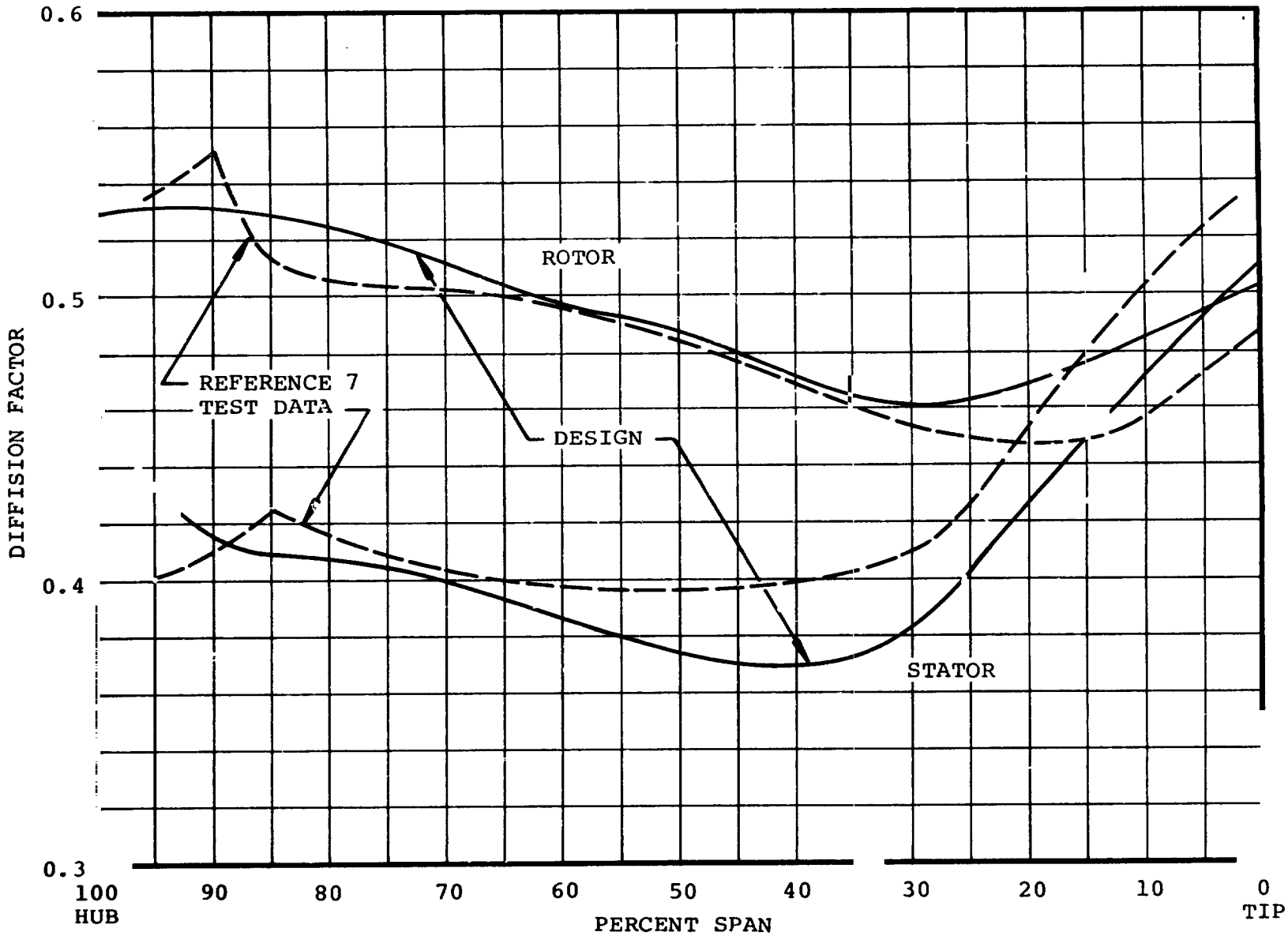

Figure 10. -Comparison of design point rotor and stator D-factor with Reference 7 test data.

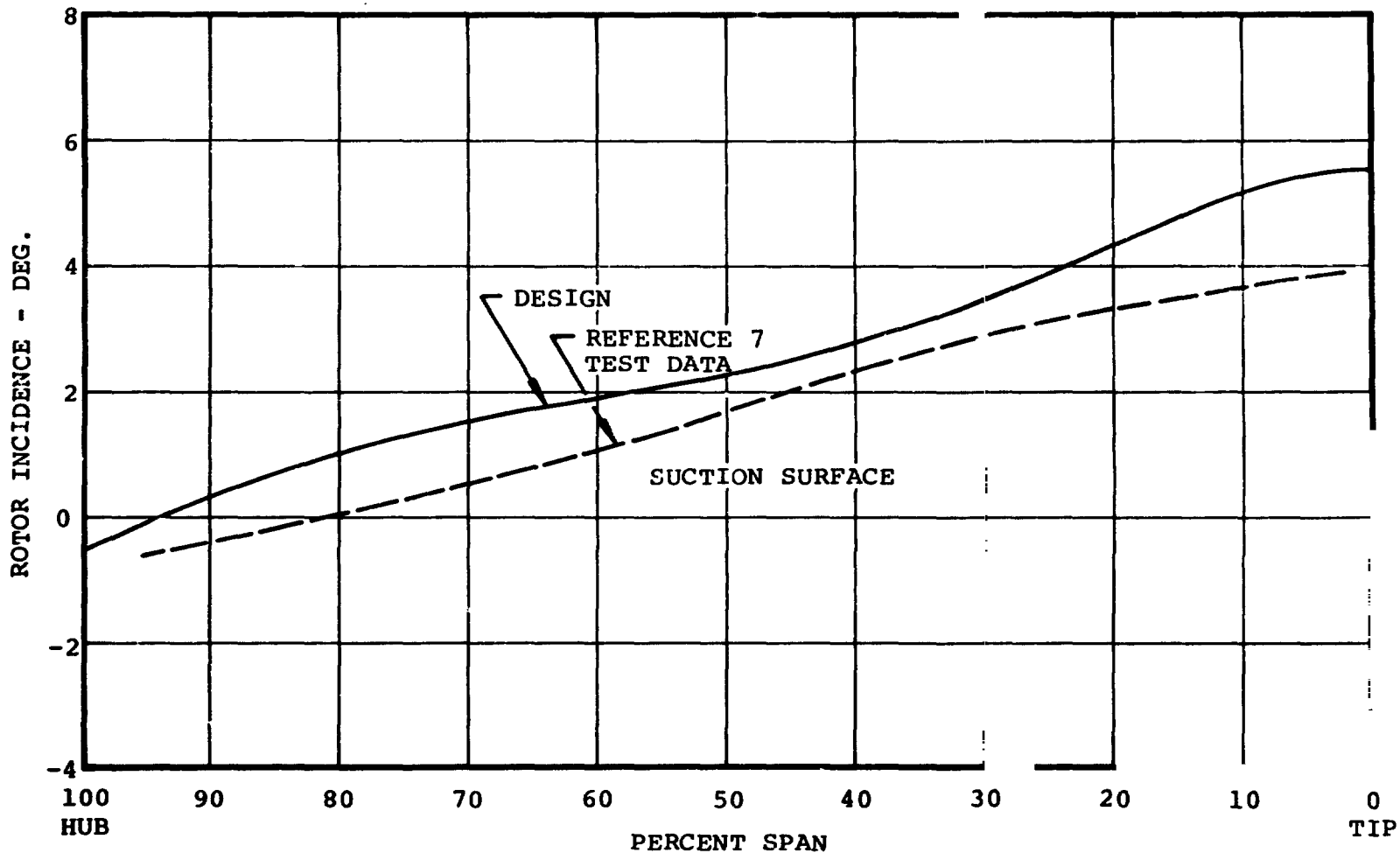

Figure 11. -Comparison of design point rotor suction surface incidence with Reference 7 test data.

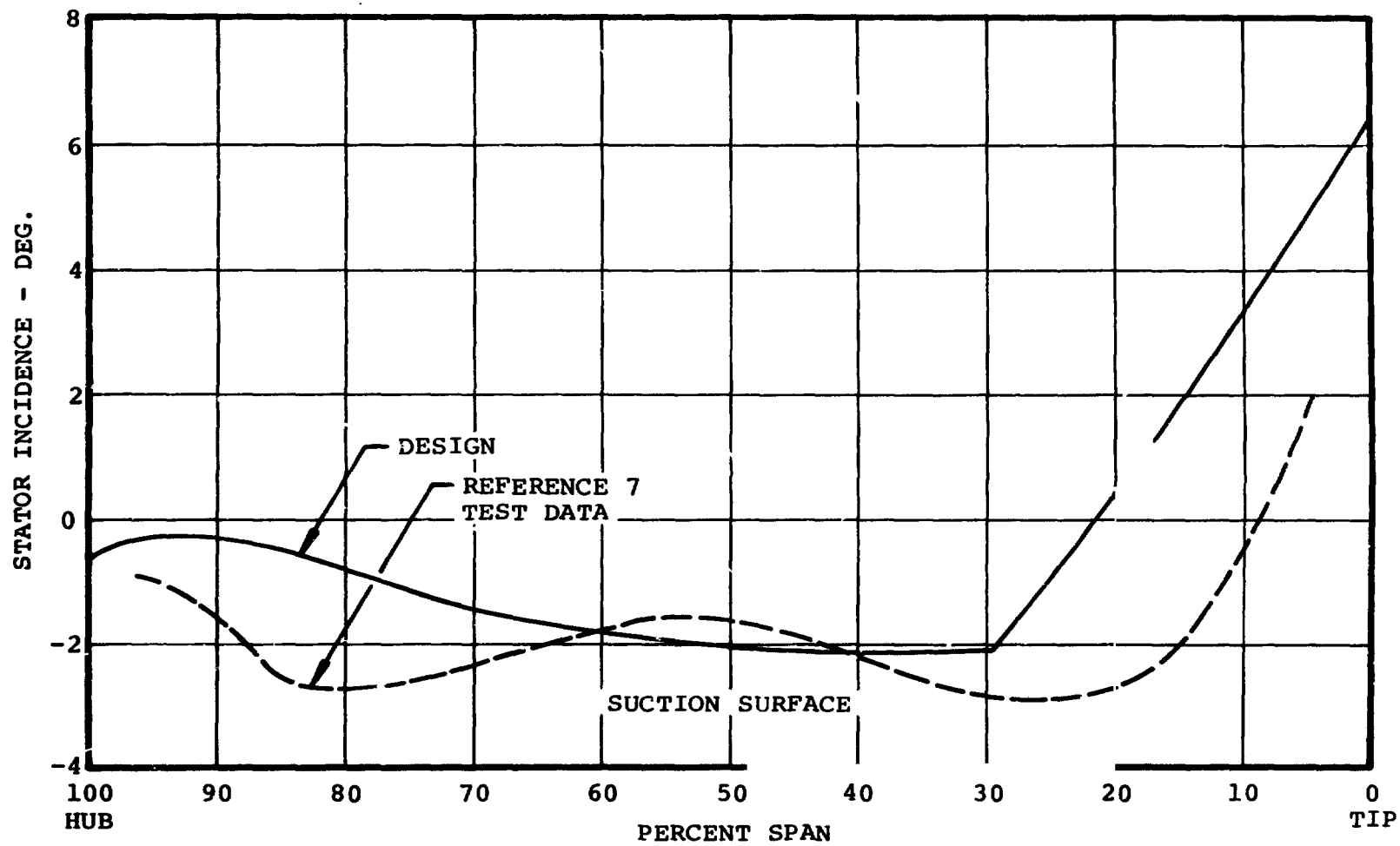

Figure 12. -Comparison of design point stator suction surface incidence with Reference 7 test data.

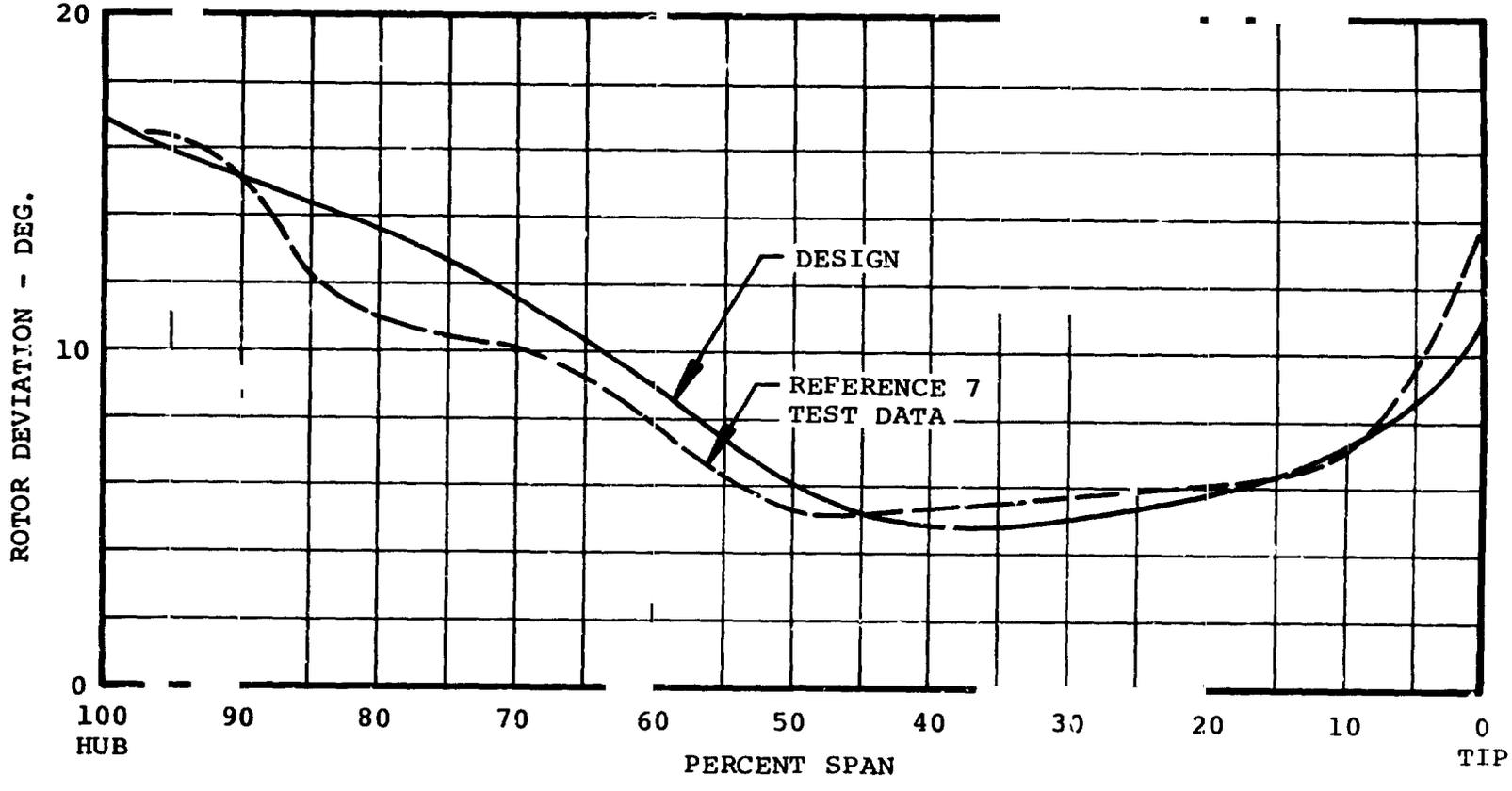

Figure 13. -Comparison of design point rotor deviation with Reference 7 test data.

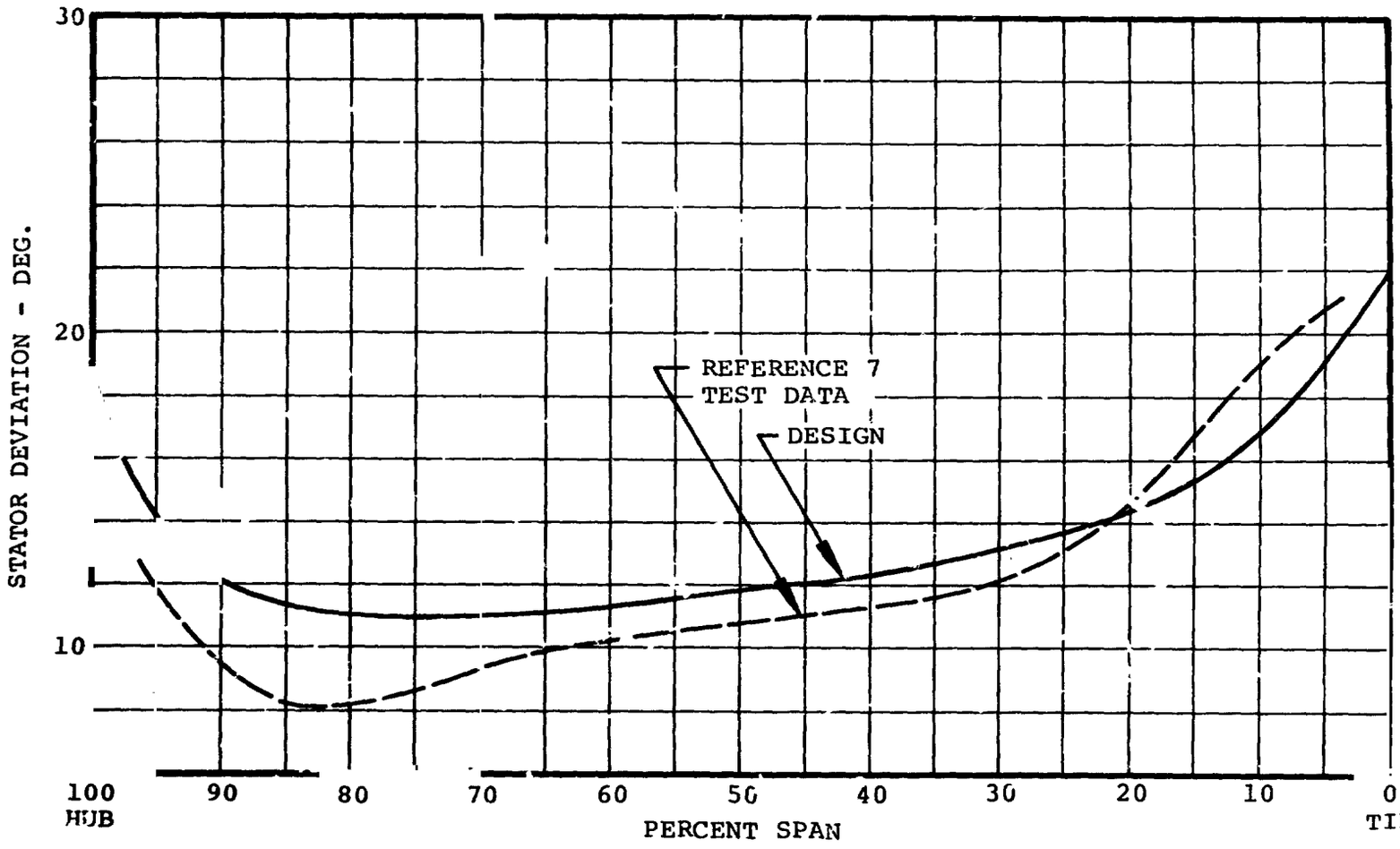

Figure 14. -Comparison of design point stator deviation with Reference 7 test data.

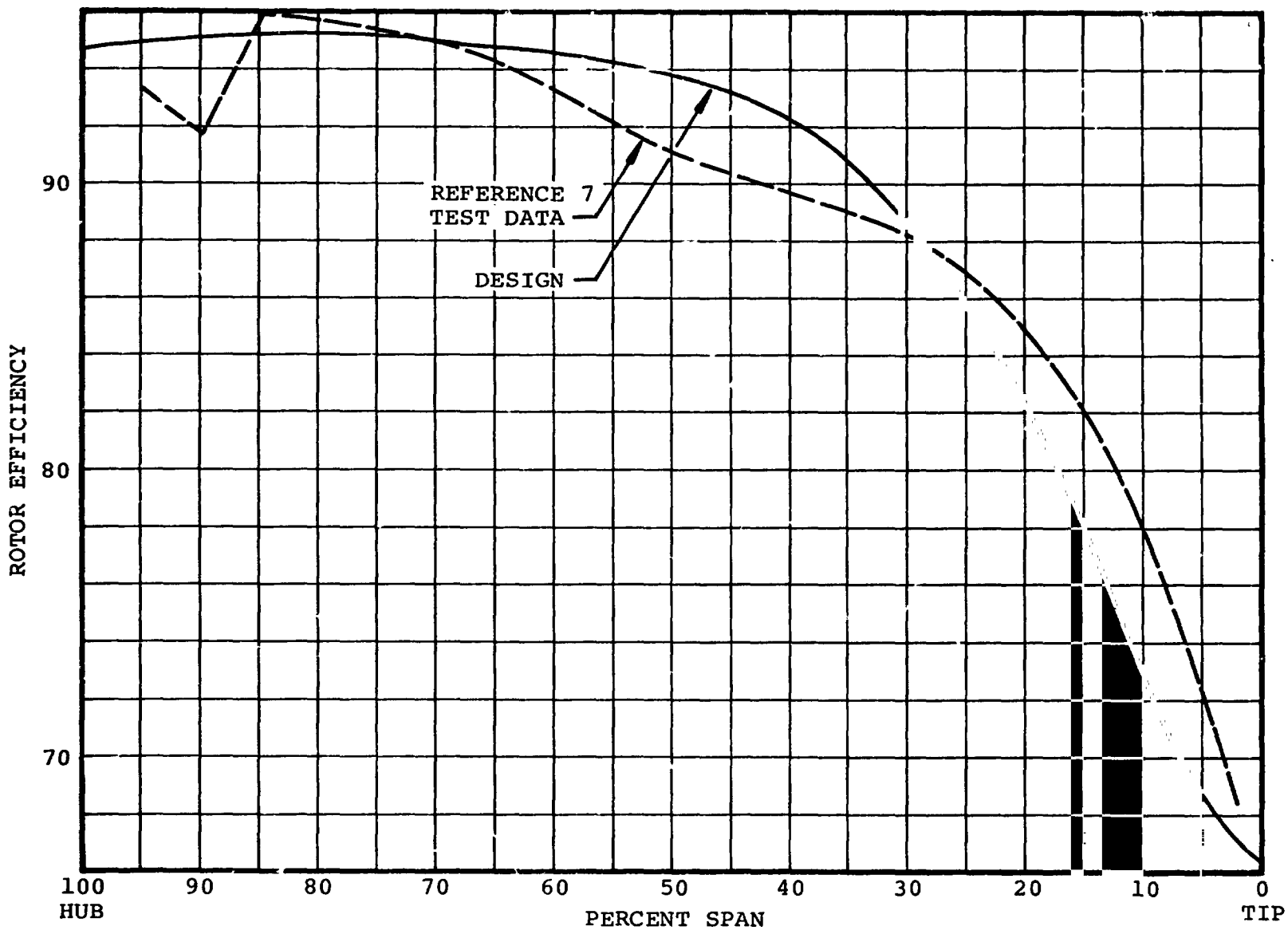

Figure 15. -Comparison of design point rotor efficiency with Reference 7 test data.

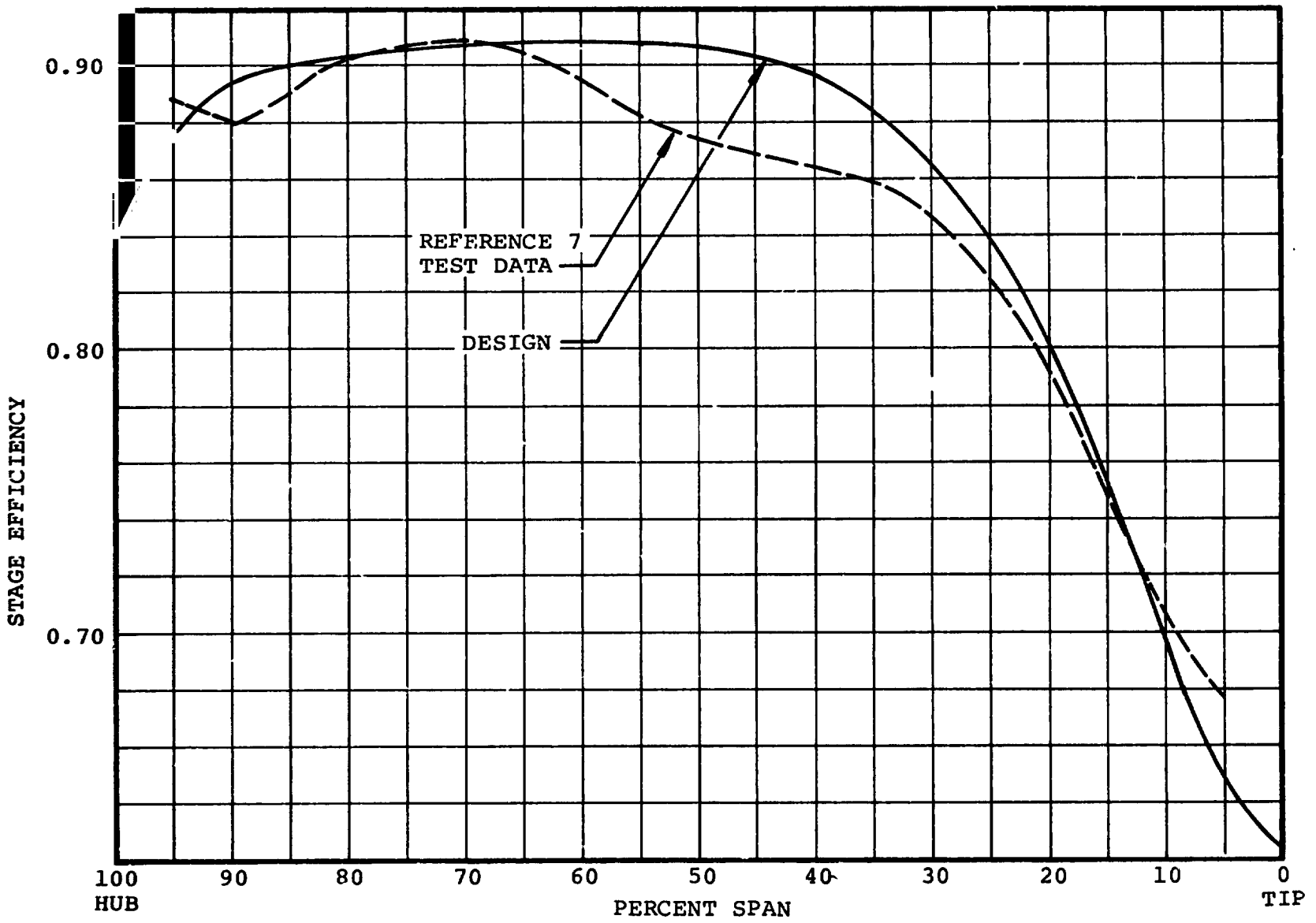

Figure 16. -Comparison of design point stage efficiency with Reference 7 test data.

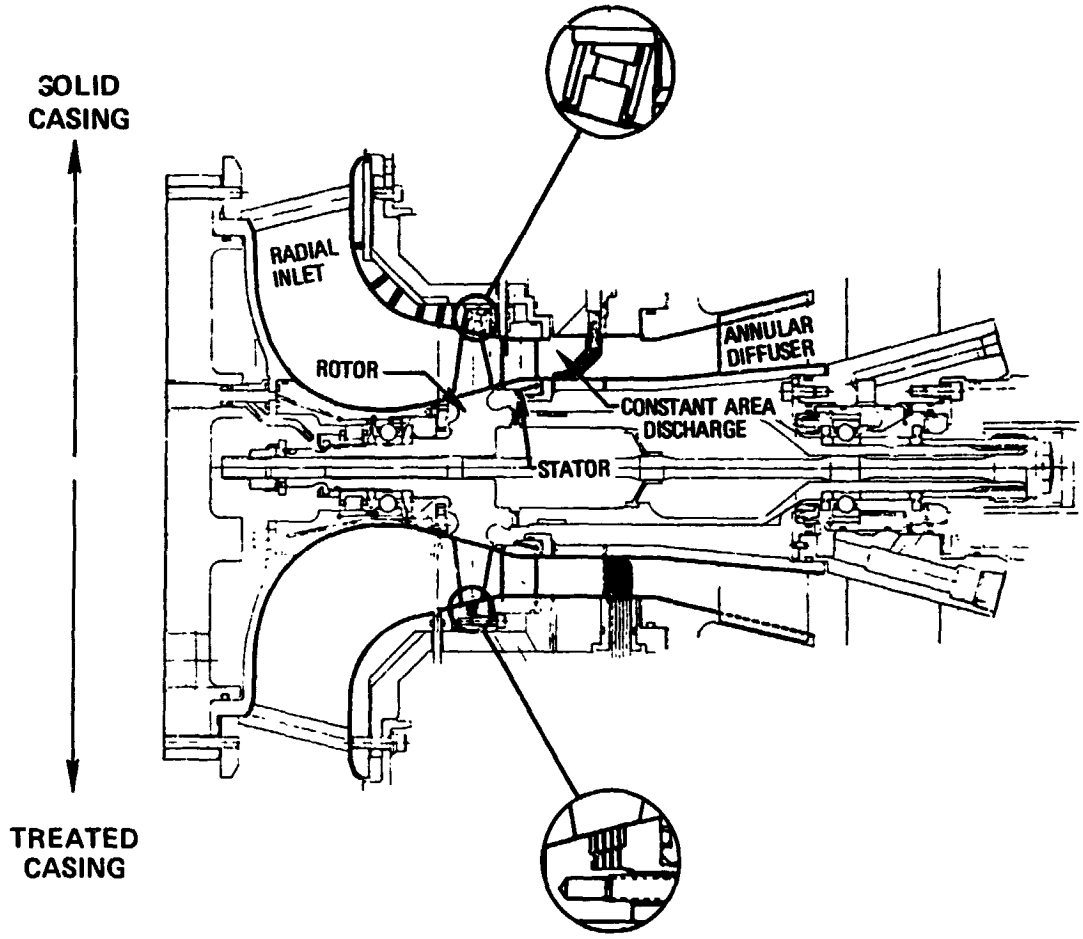

Figure 17. -Test rig layout.

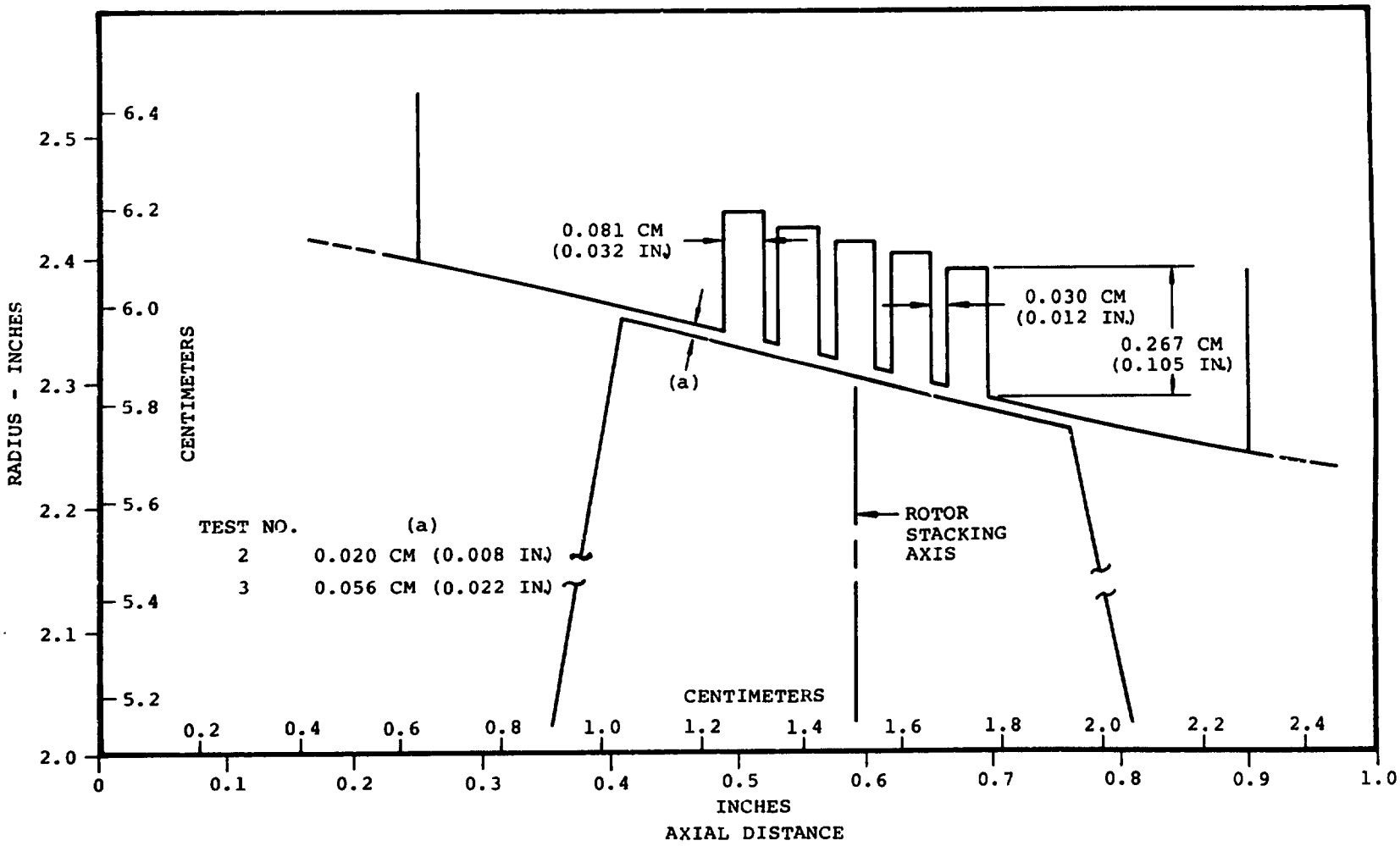

Figure 18. -Schematic of grooved casing insert.

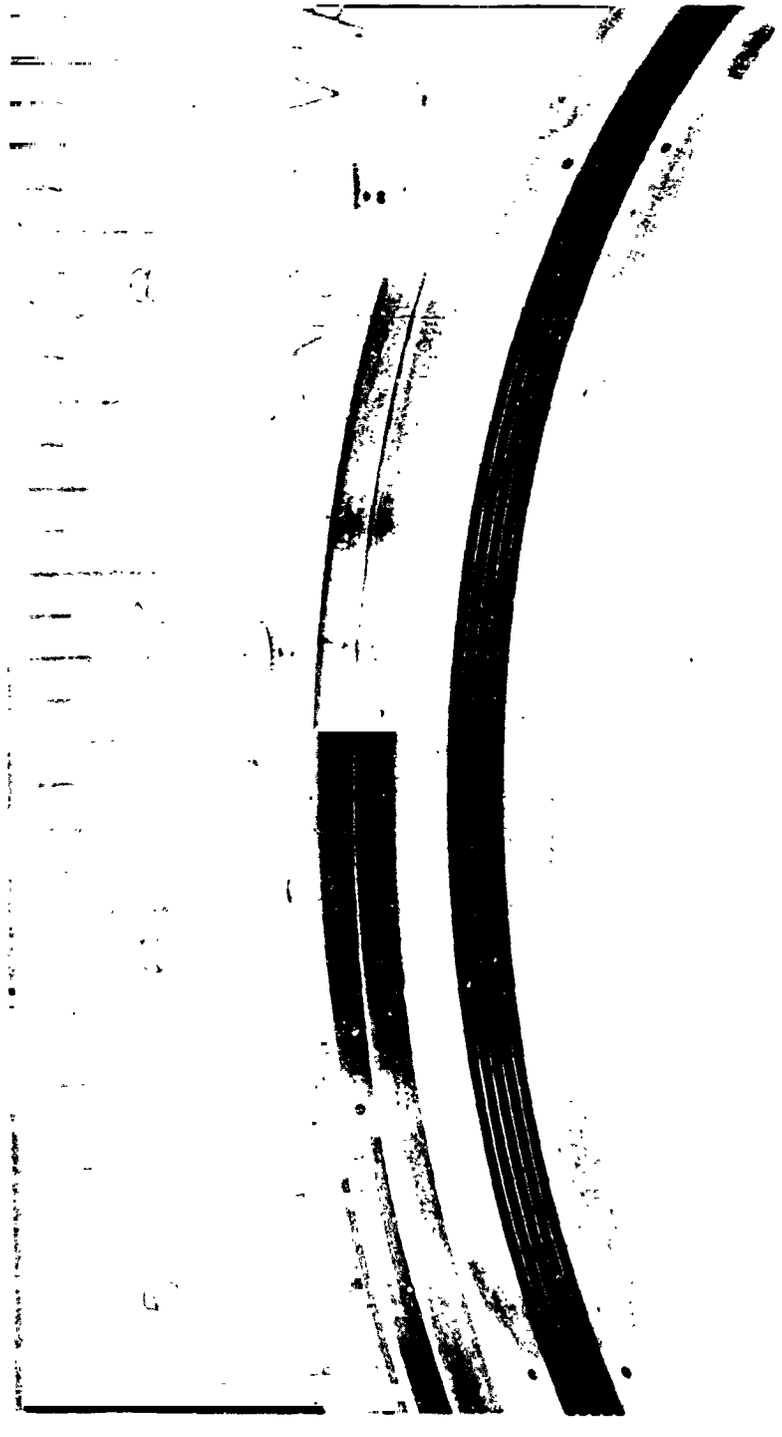

Figure 19. -Grooved casing insert.

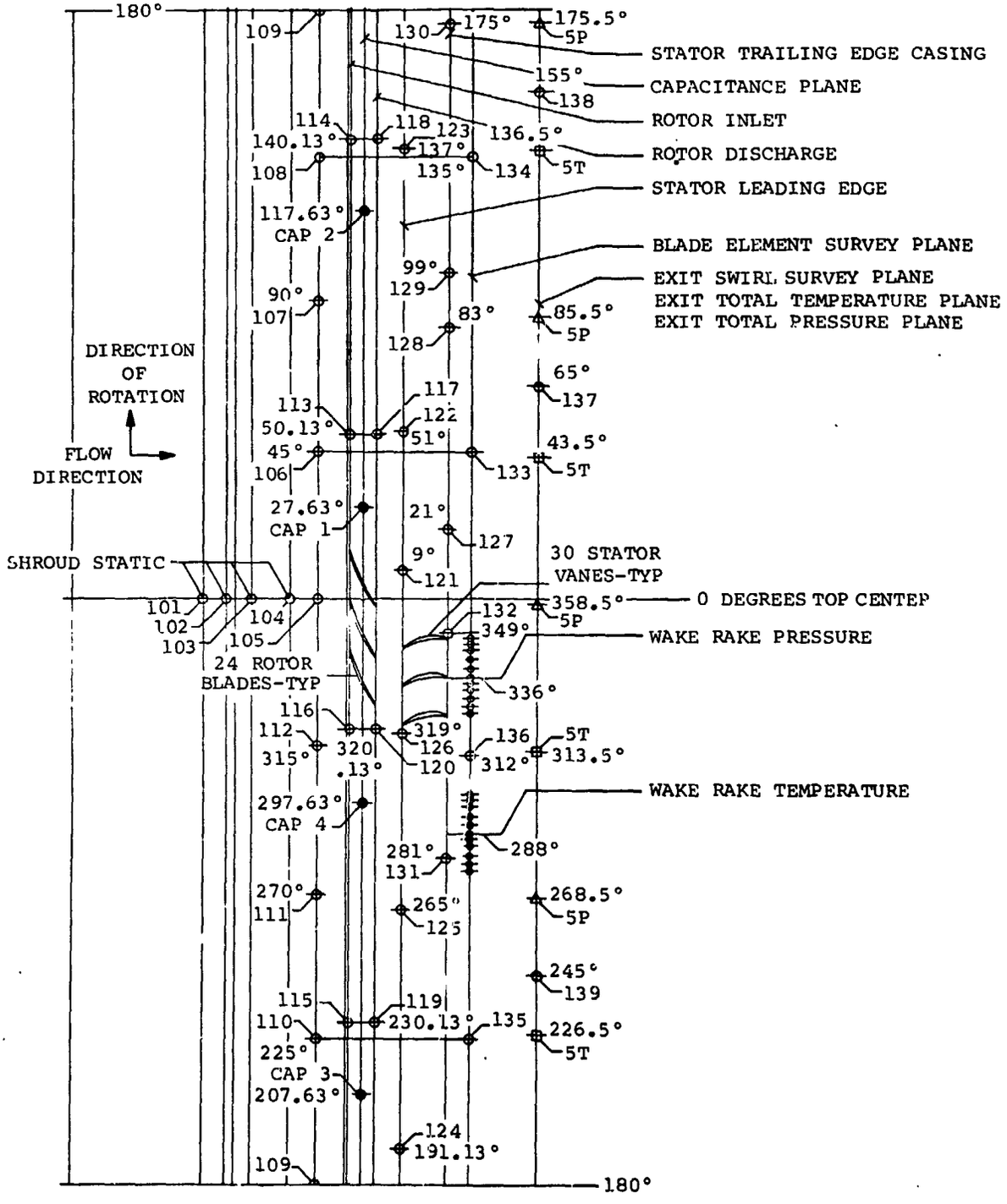

ORIGINAL PAGE IS
OF POOR QUALITY

Figure 20. -Shroud instrumentation layout.

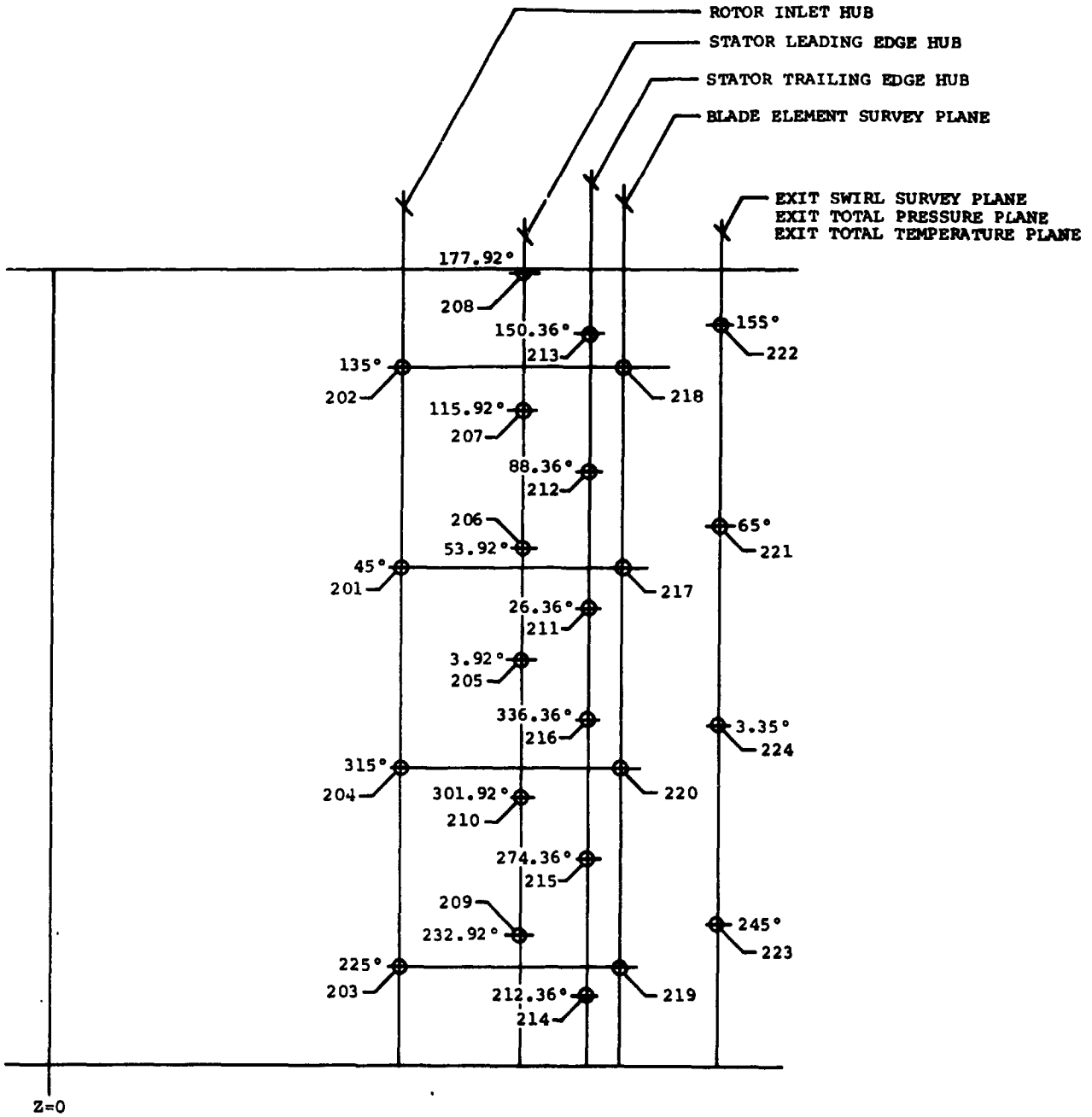

Figure 21. -Hub instrumentation layout.

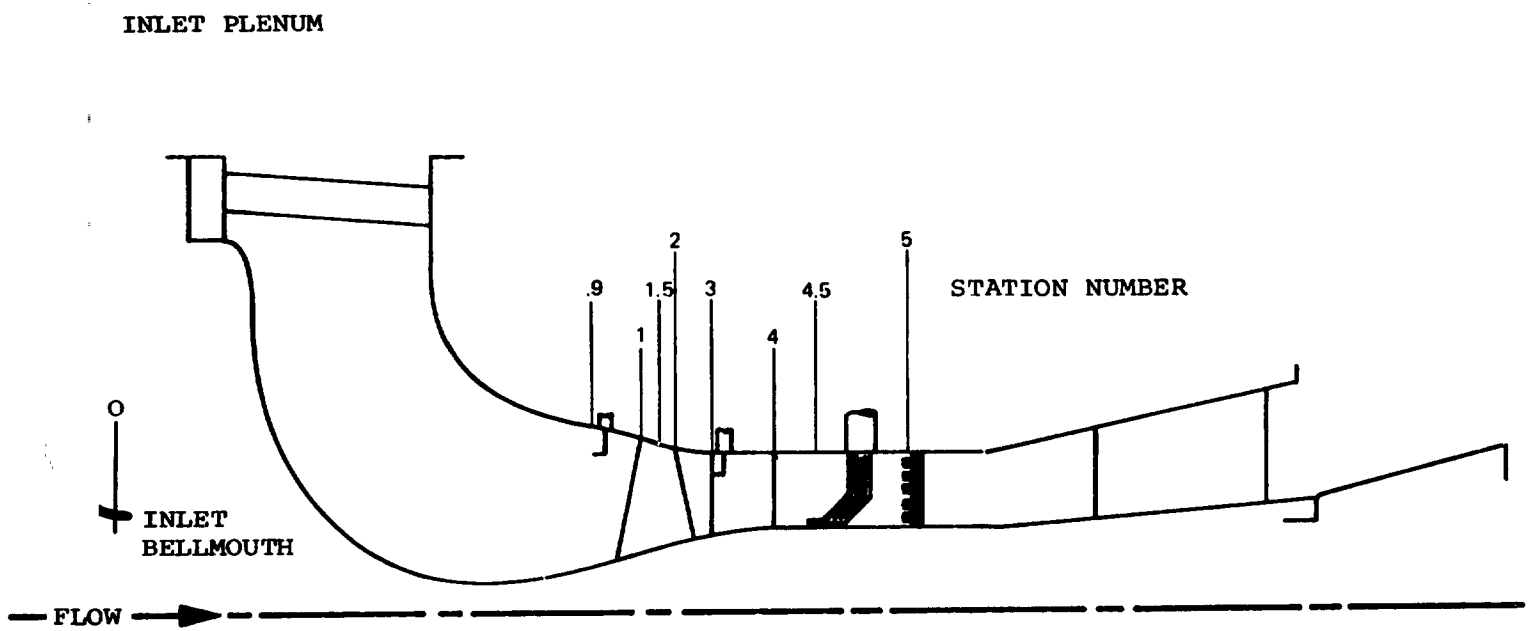

Figure 22. -Instrumentation station identity.

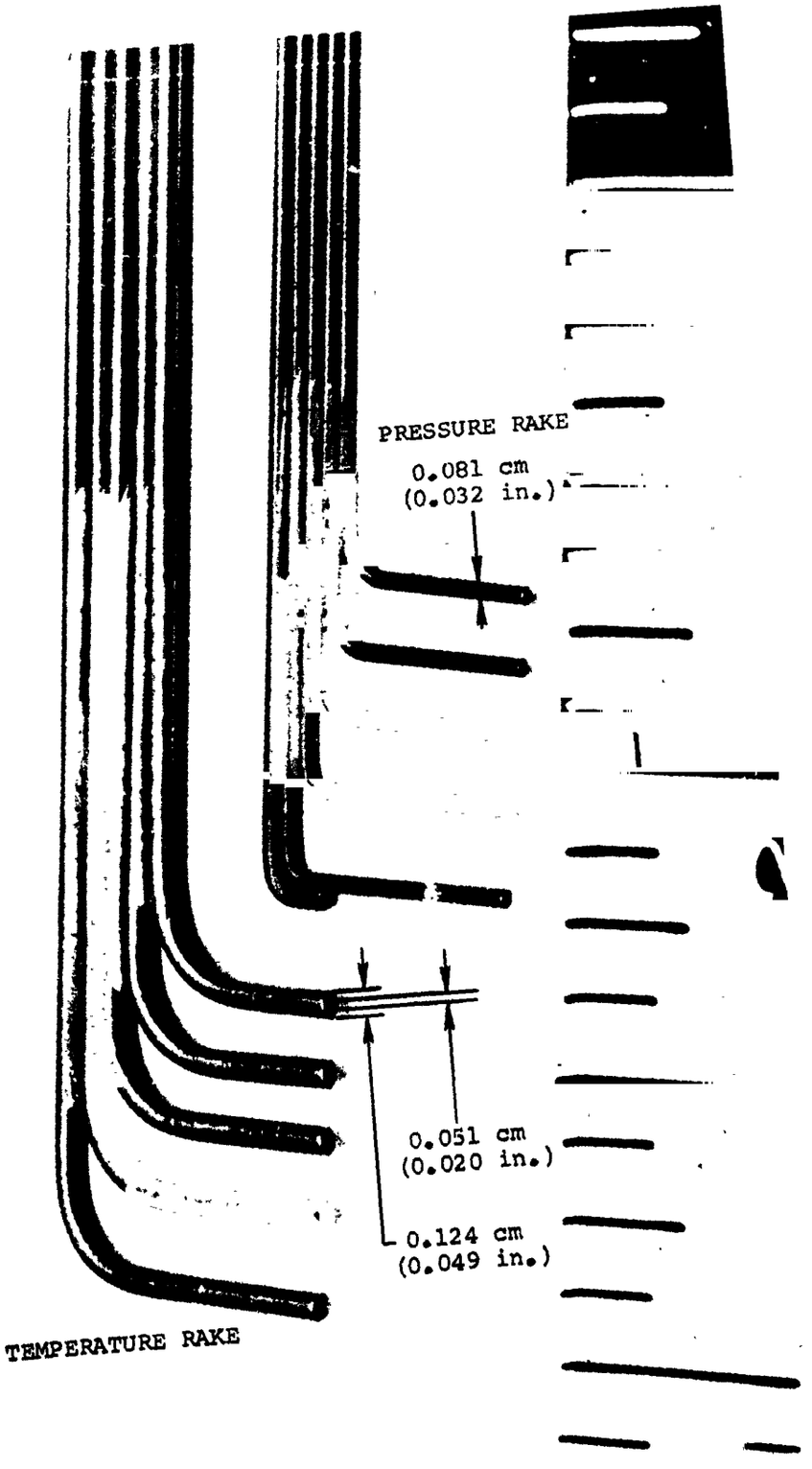

Figure 23. -Stage discharge radial rakes.

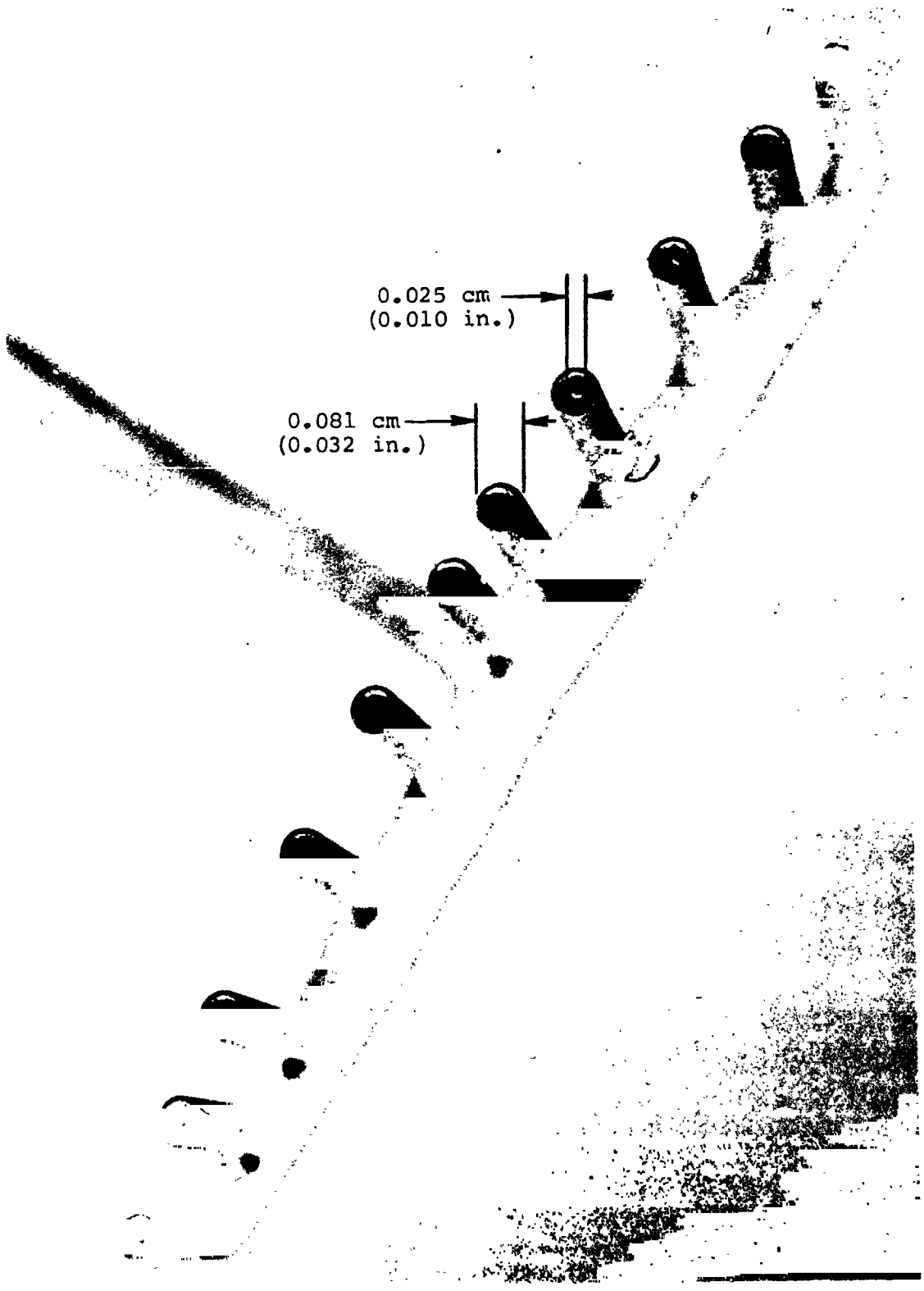

Figure 24. -Traversable temperature wake rake.

MP-55299

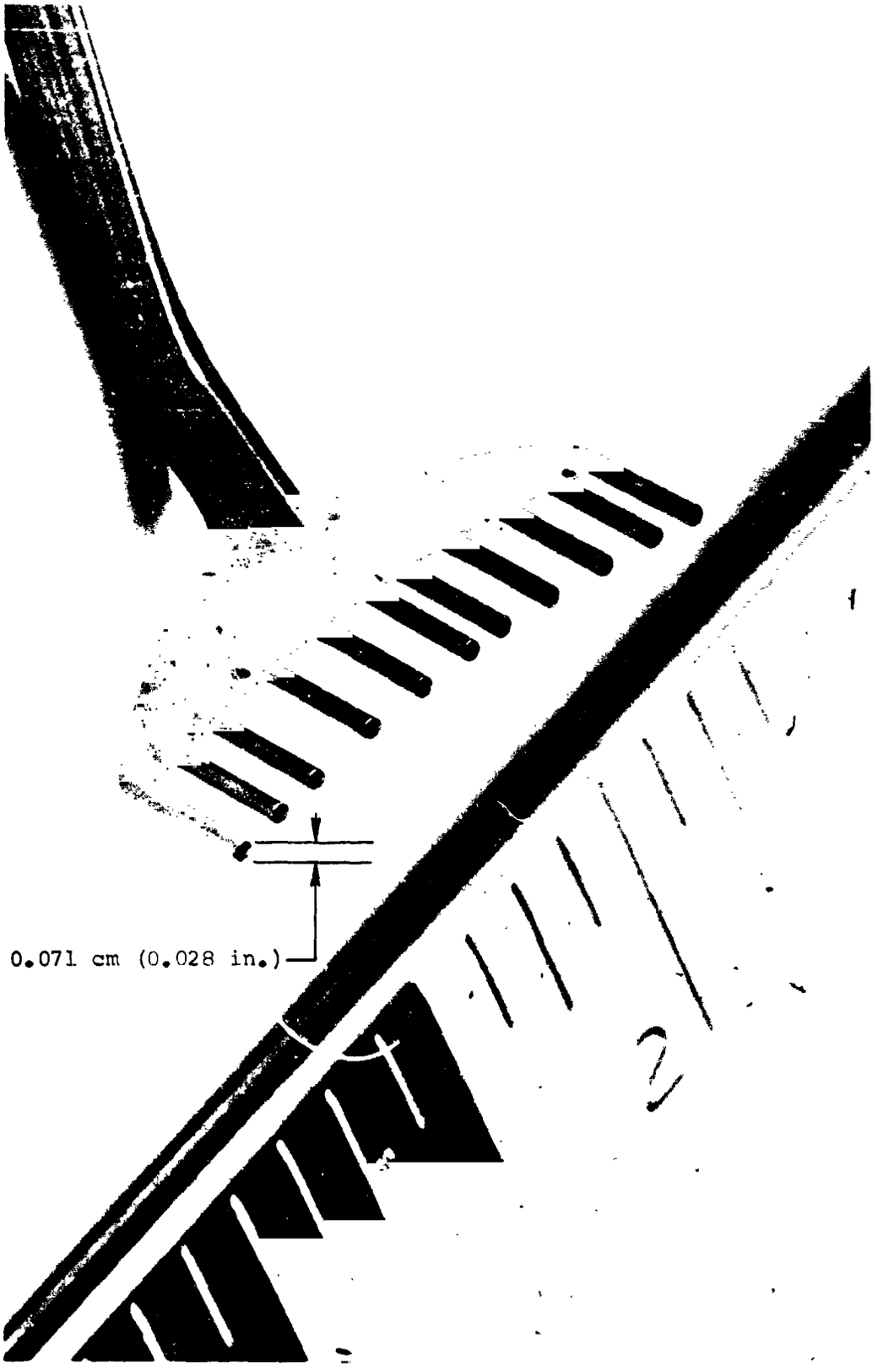

Figure 25. -Traversable pressure wake rake.

MP-55301

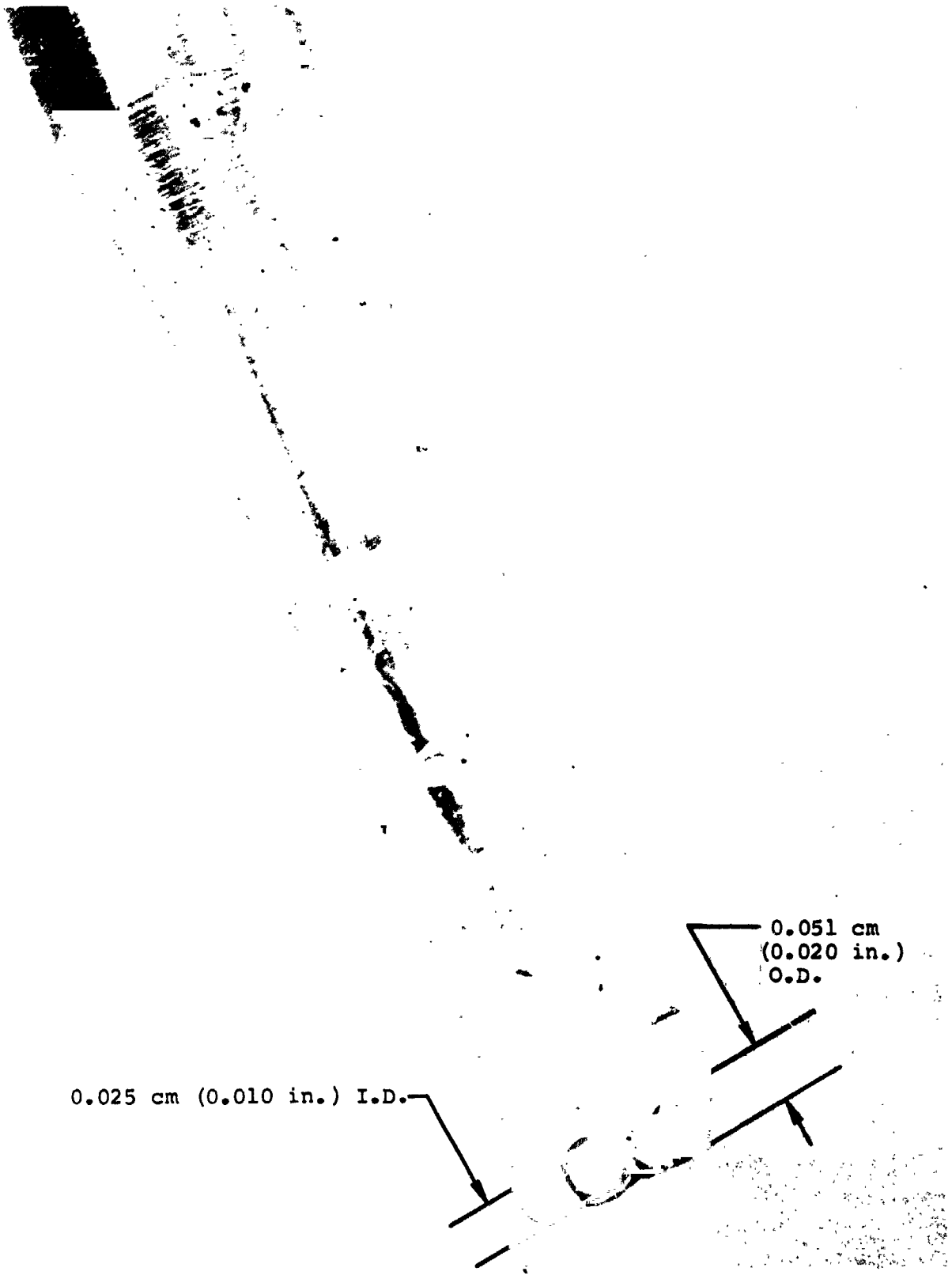

MP-55300

Figure 26. -Cobra probe.

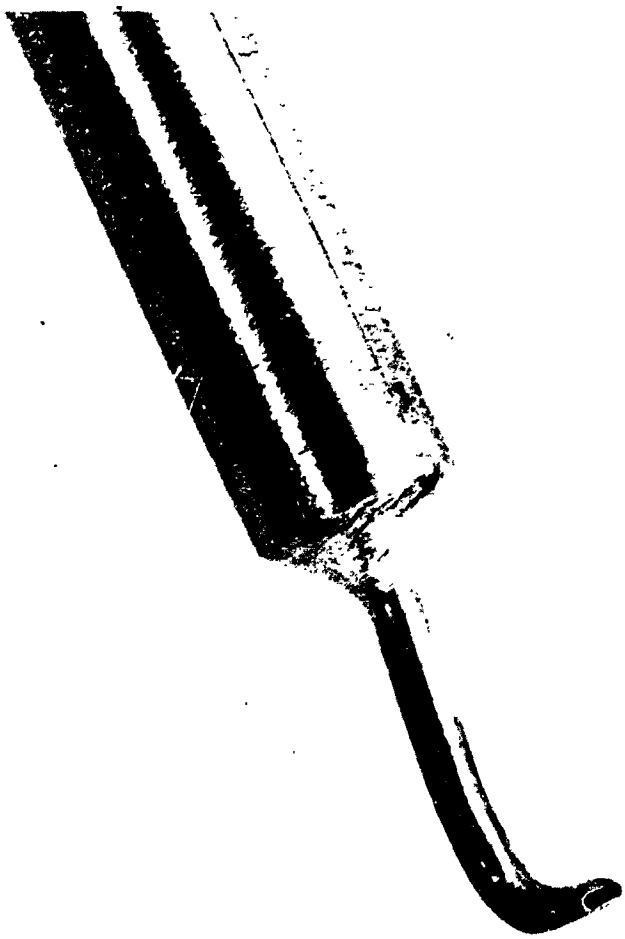

ROTOR INLET
B. L. PROBE

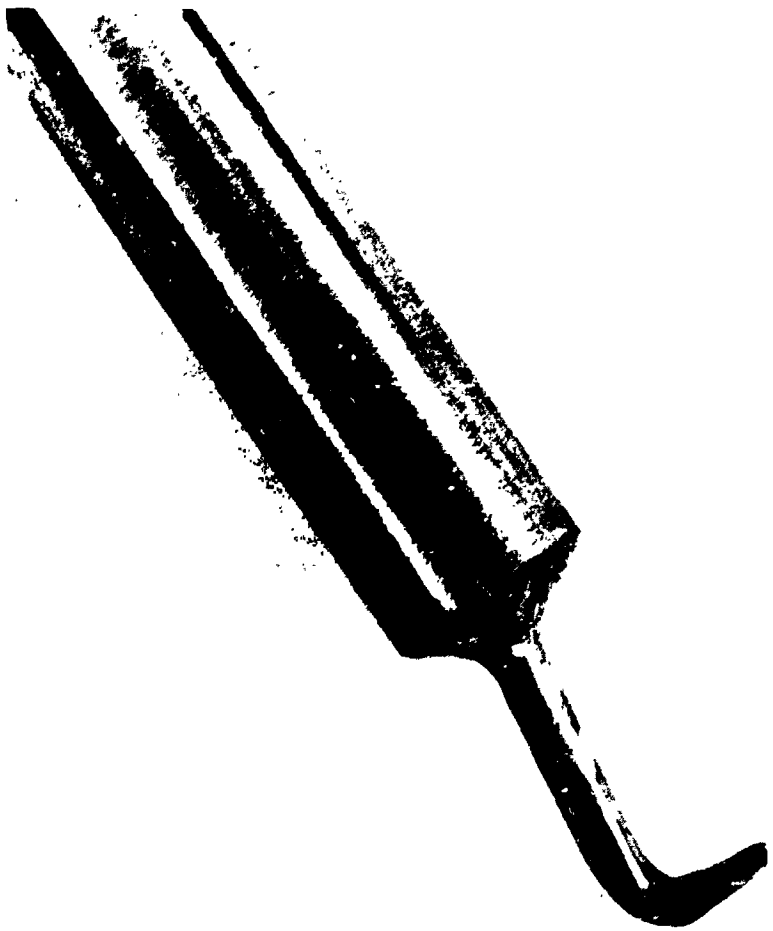

ROTOR EXIT
B. L. PROBE

Figure 27. -Rotor inlet and exit boundary layer survey probes.

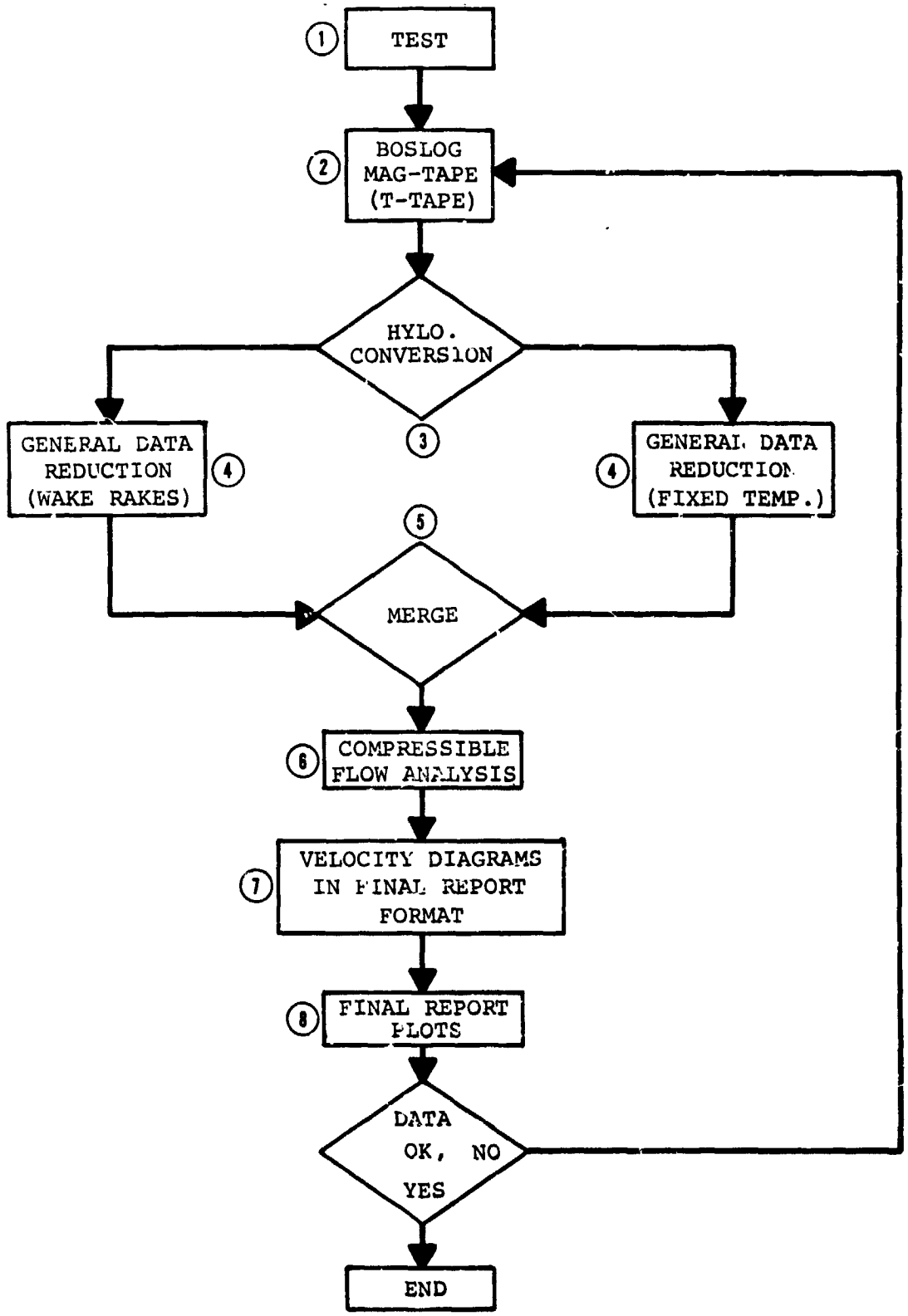

Figure 28. -Data reduction flow chart.

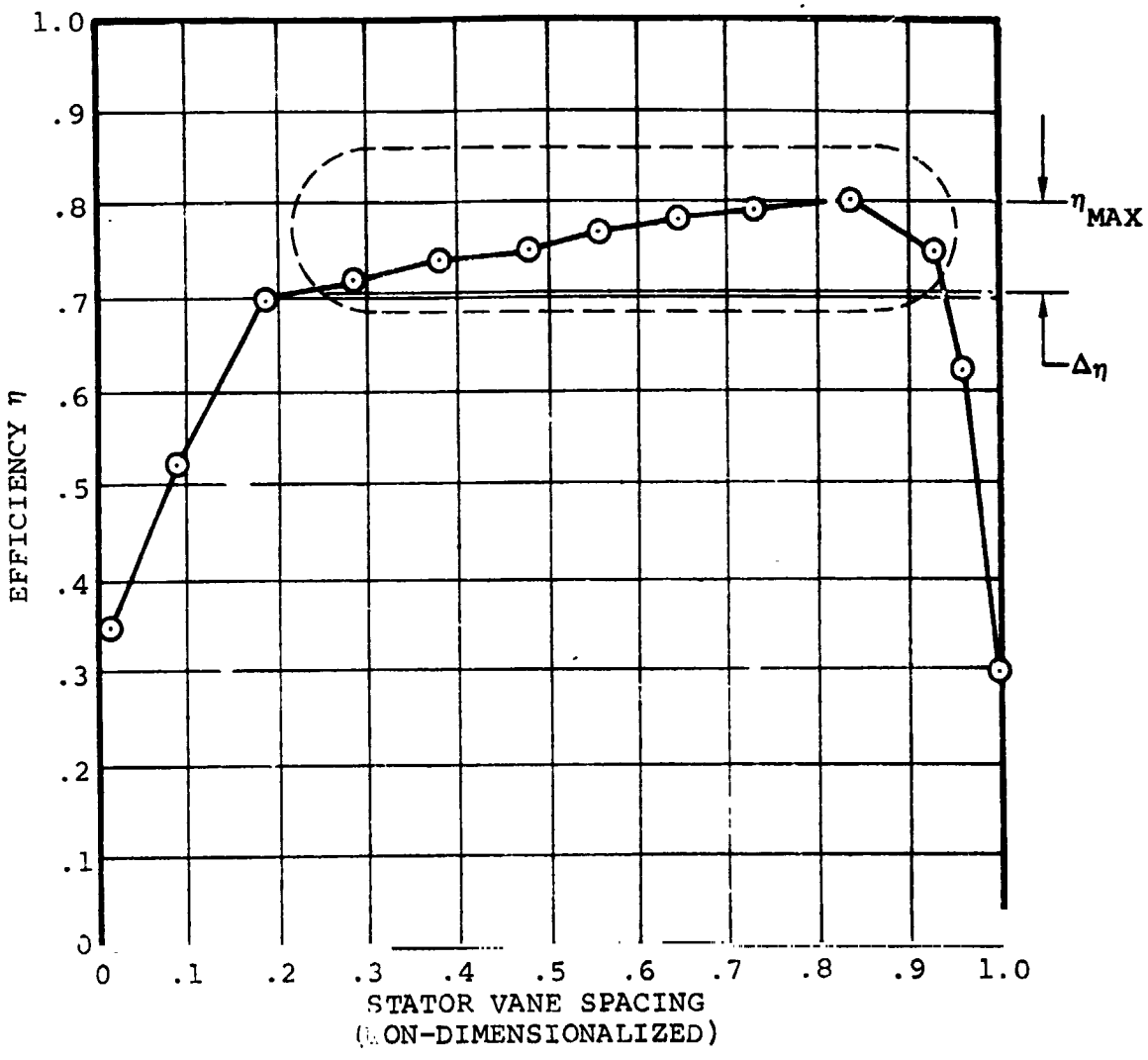

Figure 29. -Rotor efficiency estimate.

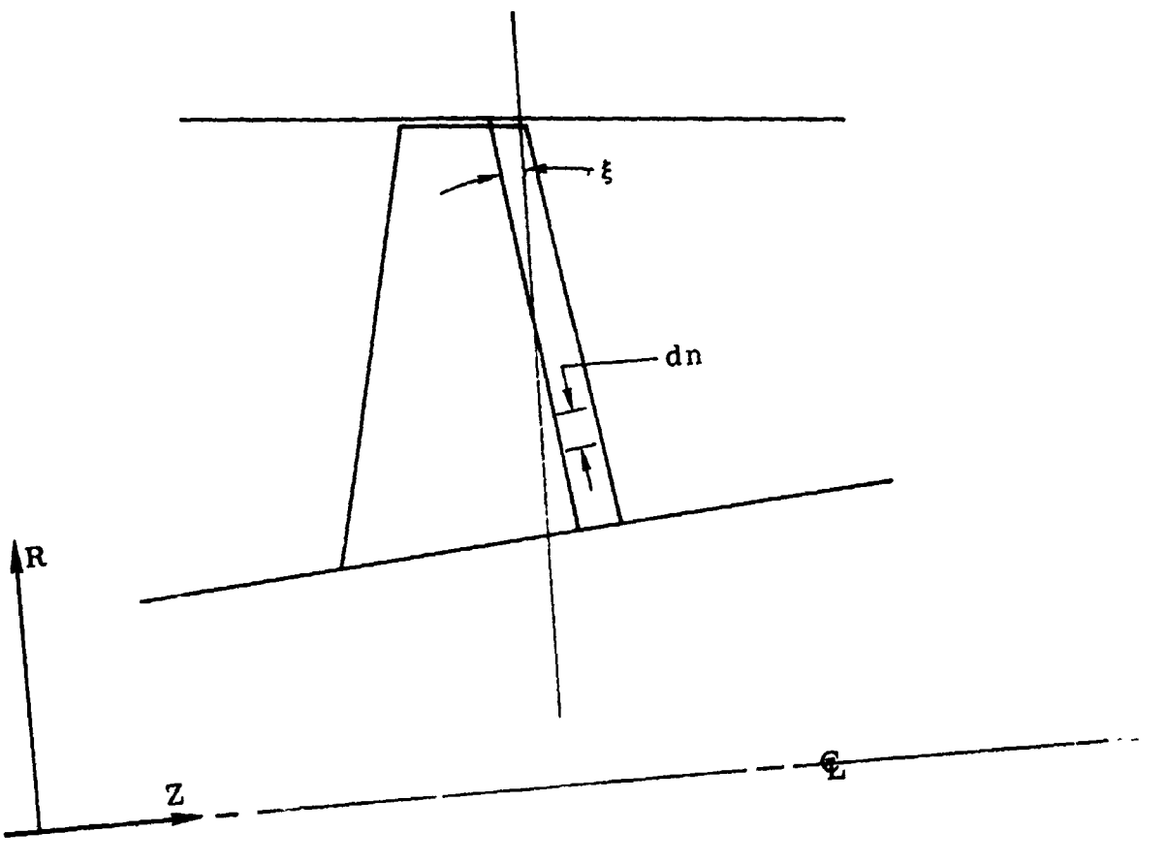

Figure 30. -Meridional view with projection of station line.

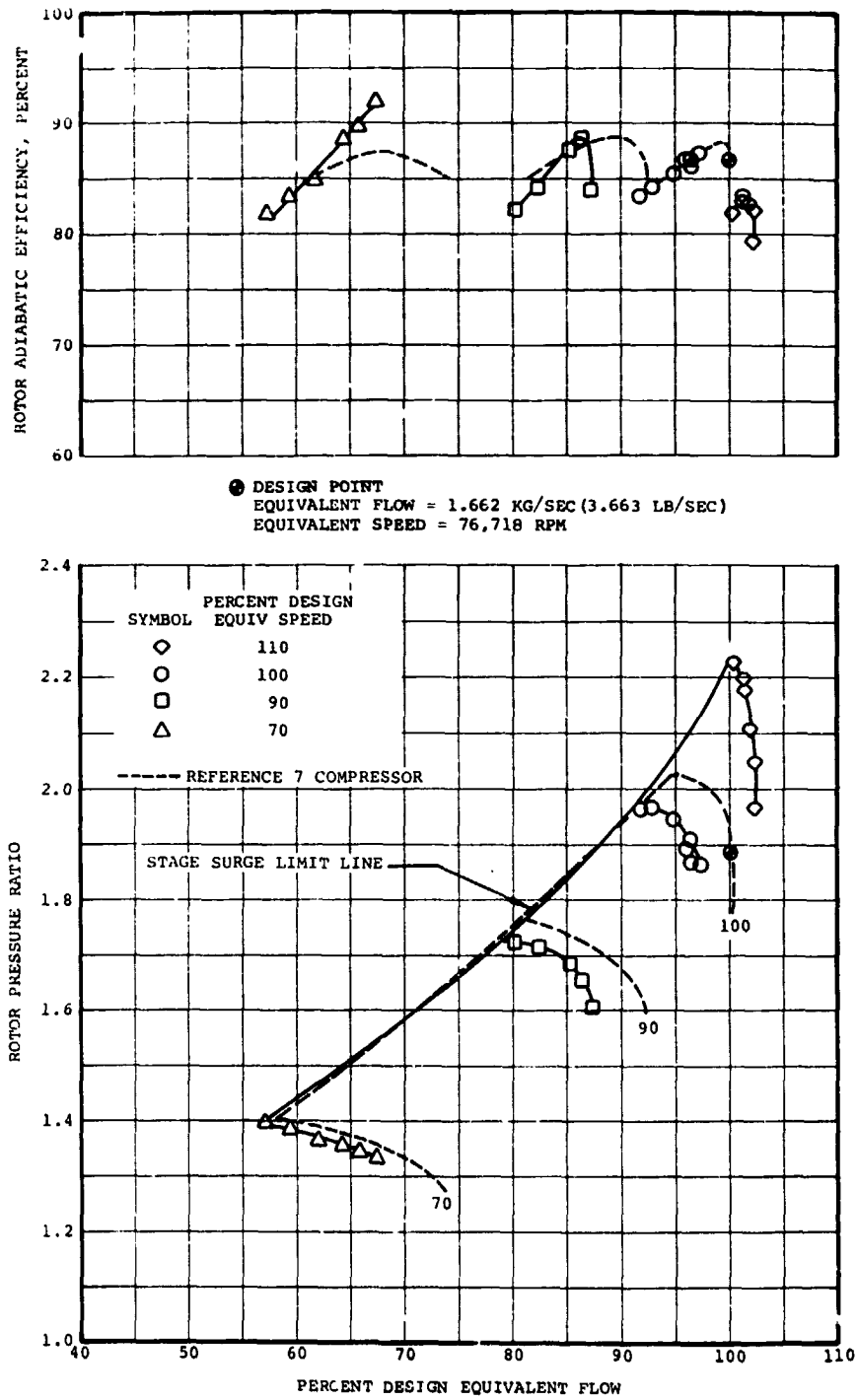

Figure 31. -Test 1 - rotor performance.

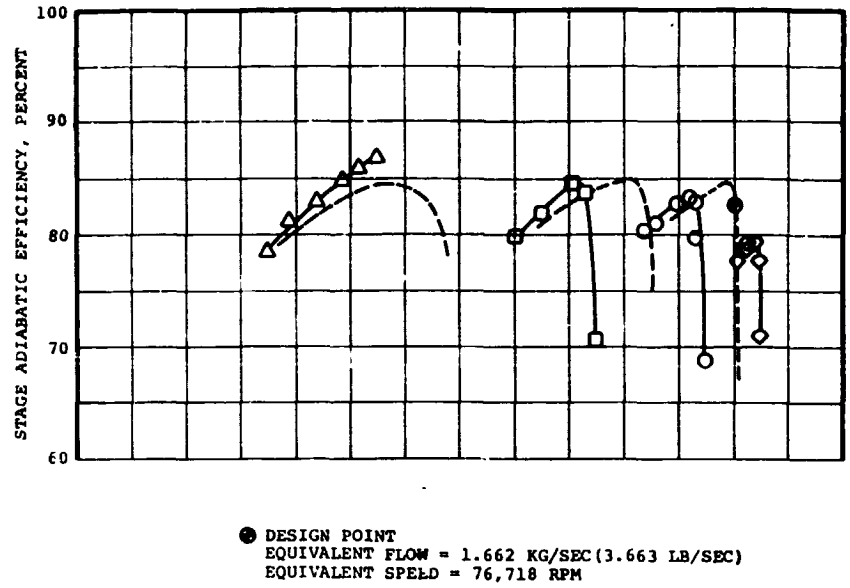

● DESIGN POINT
EQUIVALENT FLOW = 1.662 KG/SEC(3.663 LB/SEC)
EQUIVALENT SPEED = 76,718 RPM

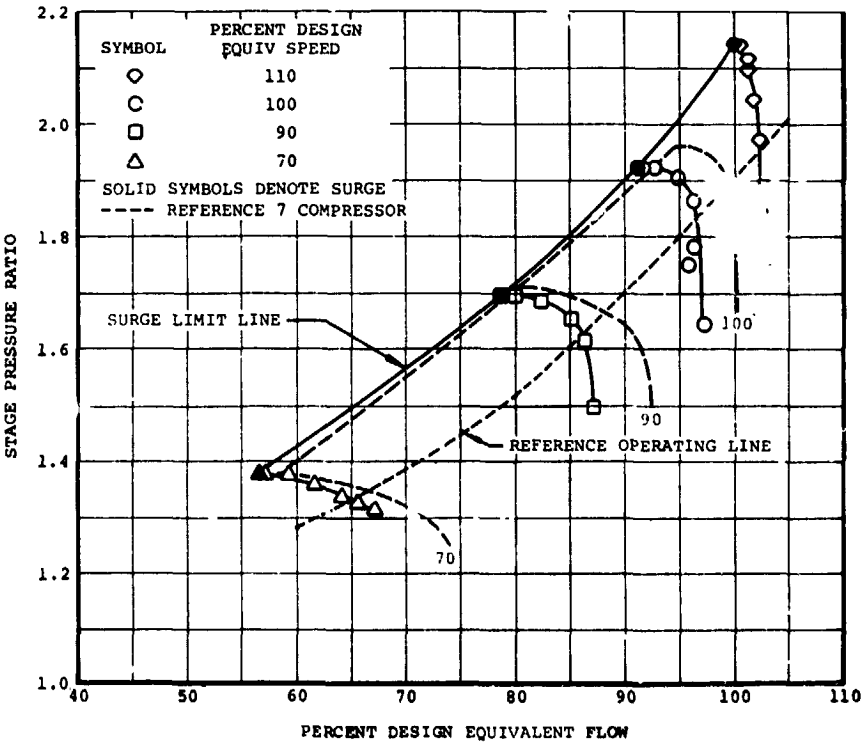

Figure 32. -Test 1 - stage performance.

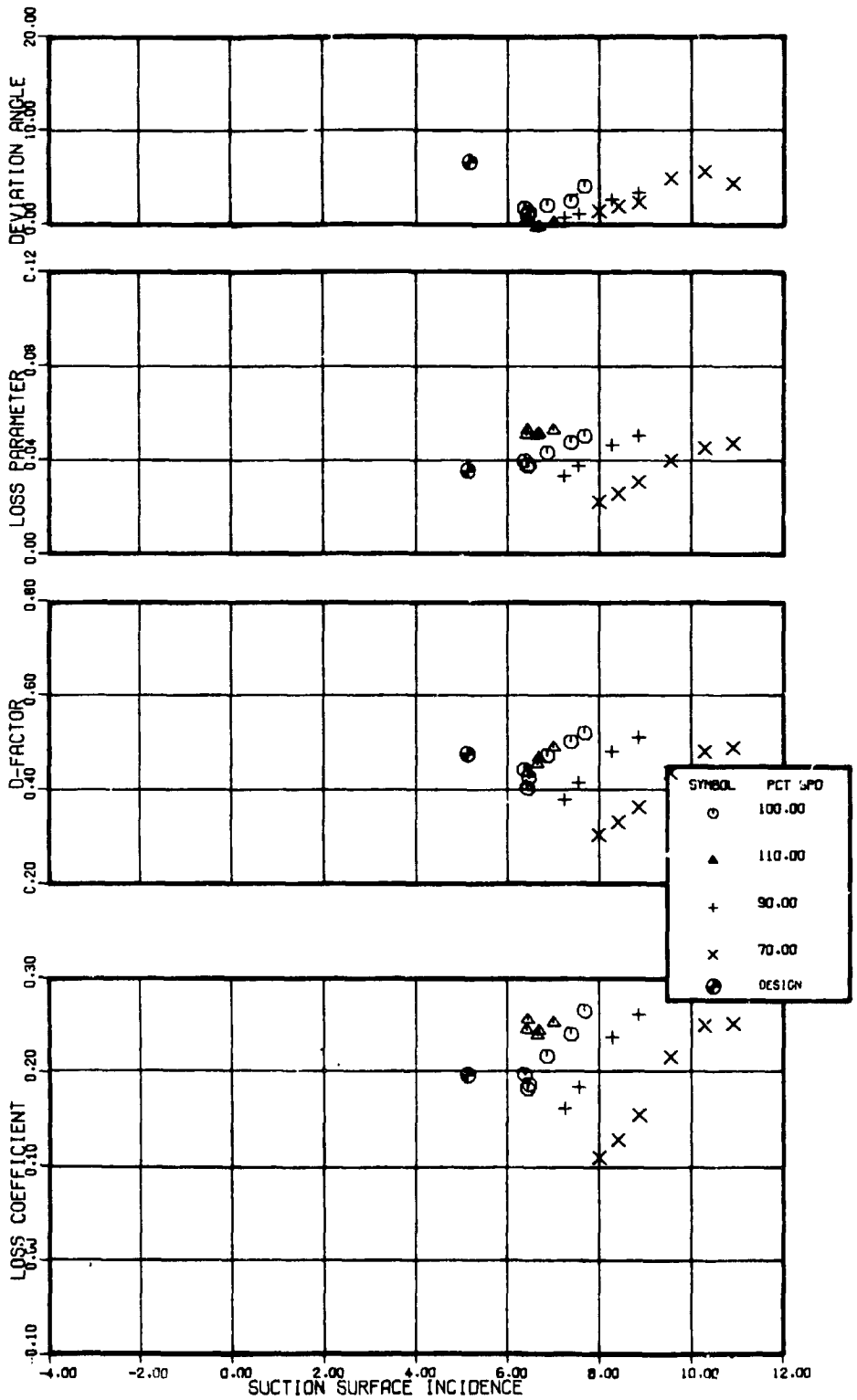

Figure 33. -Rotor blade element performance, 10 percent span from tip, Test 1.

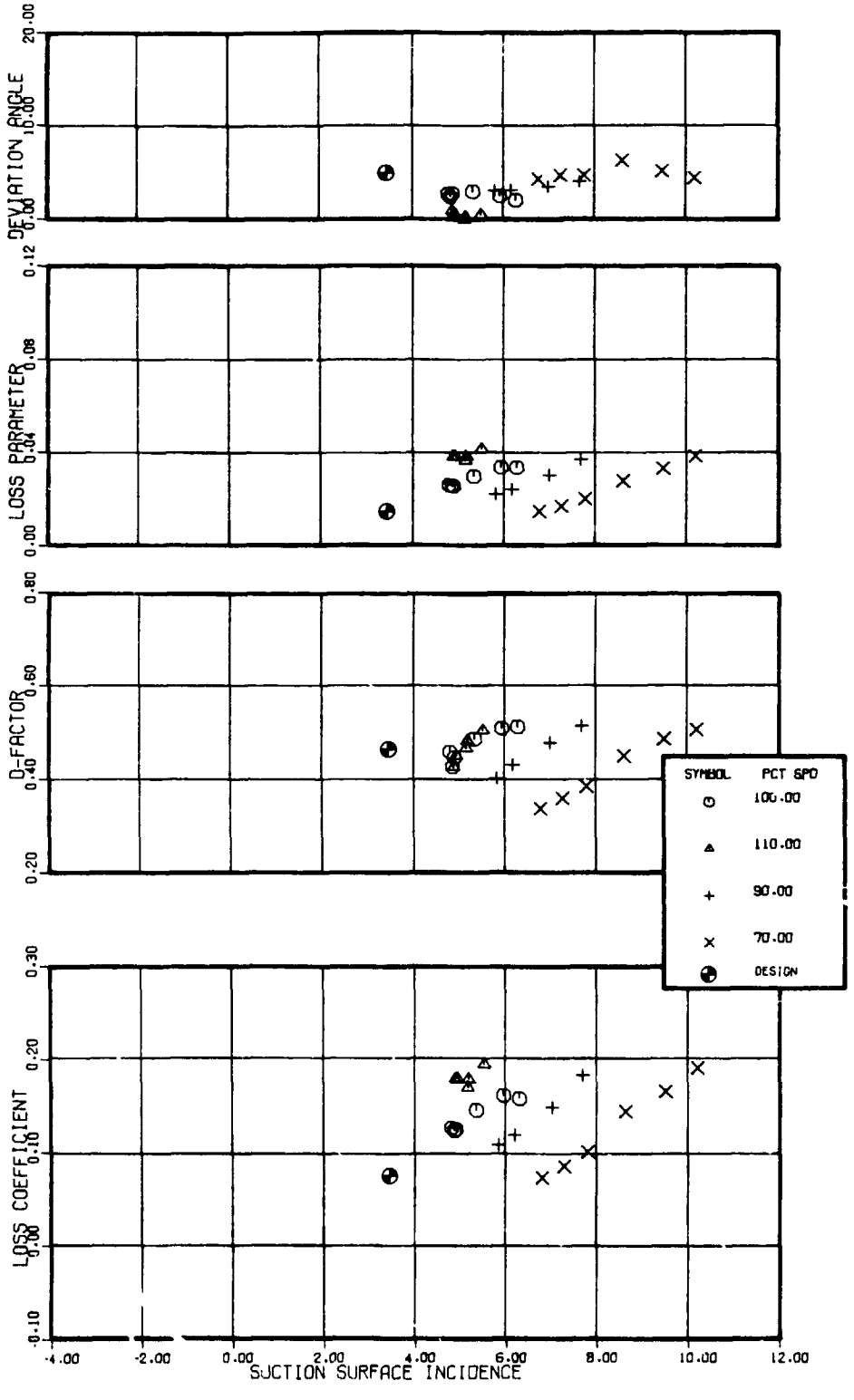

Figure 34. -Rotor blade element performance, 30 percent span from tip, Test 1.

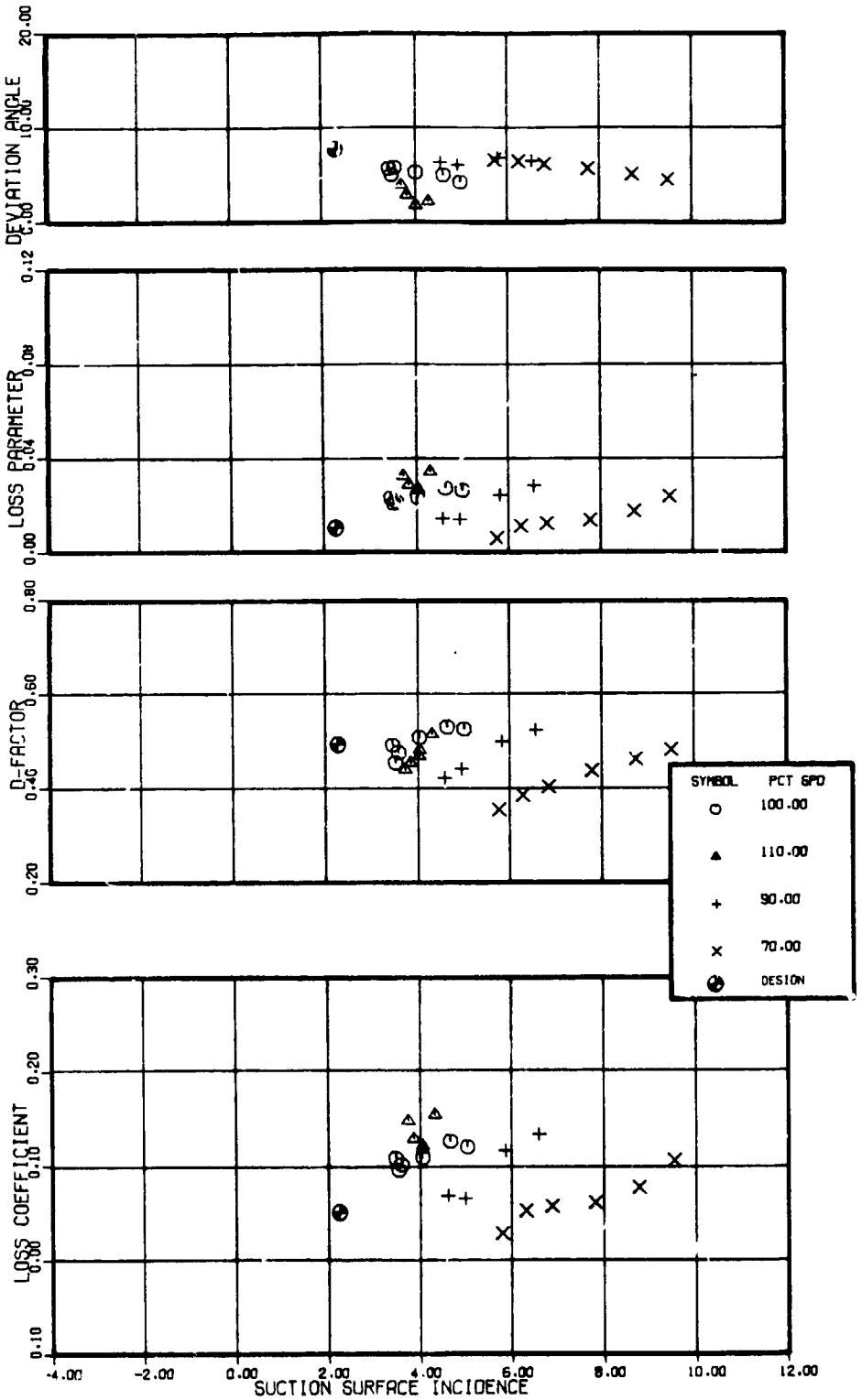

Figure 35. -Rotor blade element performance, 50 percent span from tip, Test 1.

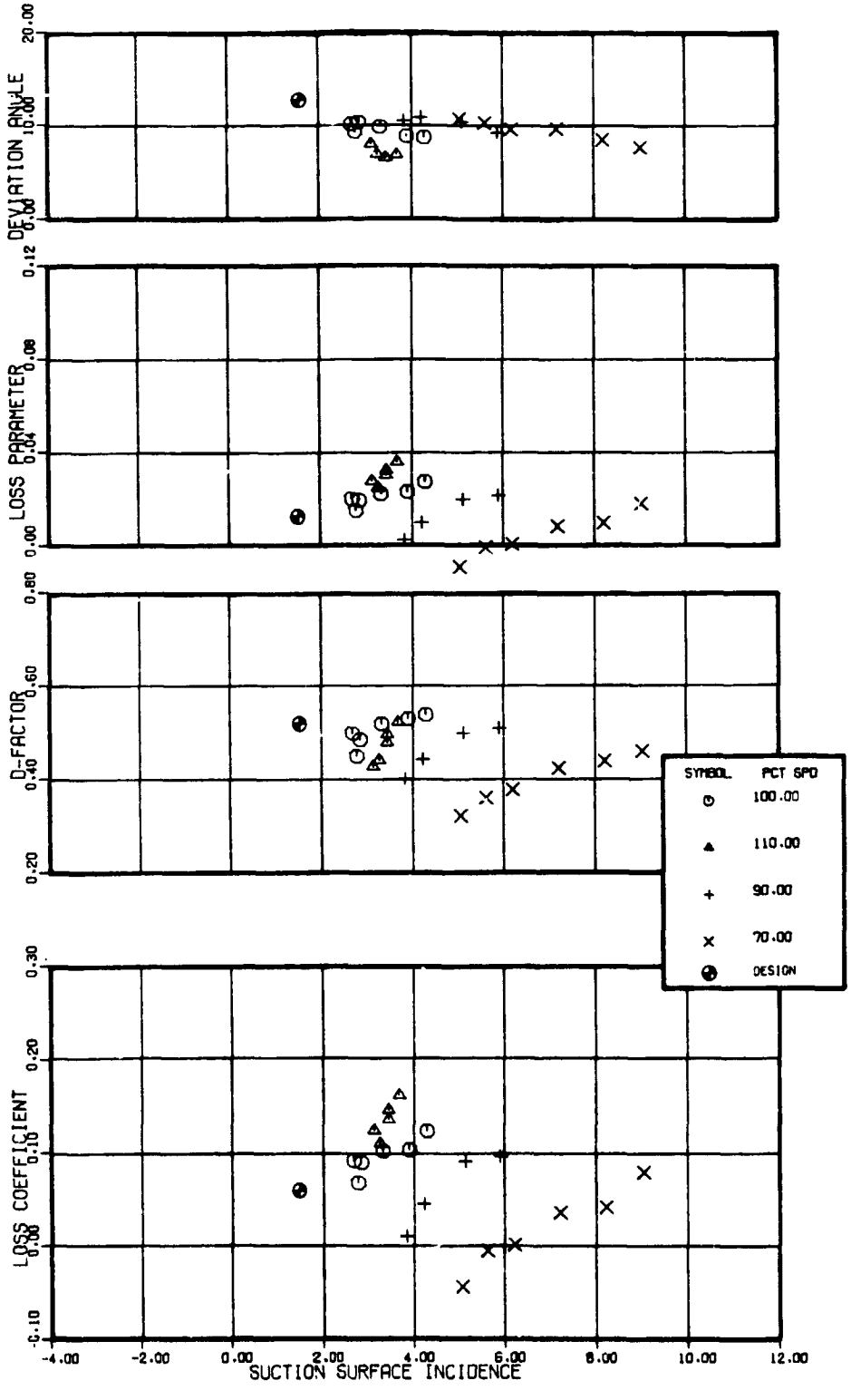

Figure 36. -Rotor blade element performance, 70 percent span from tip, Test 1.

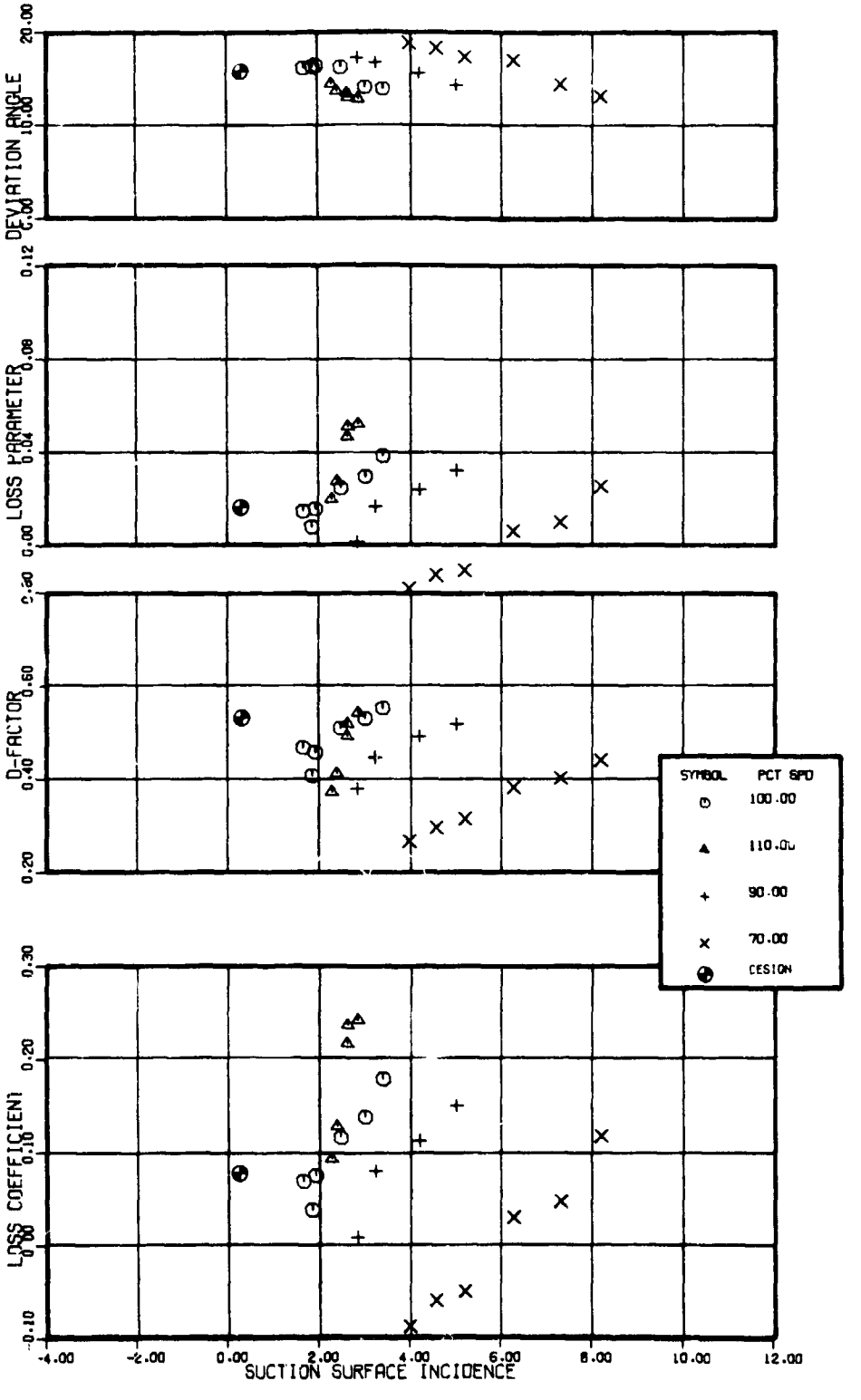

Figure 37. -Rotor blade element performance, 90 percent span from tip, Test 1.

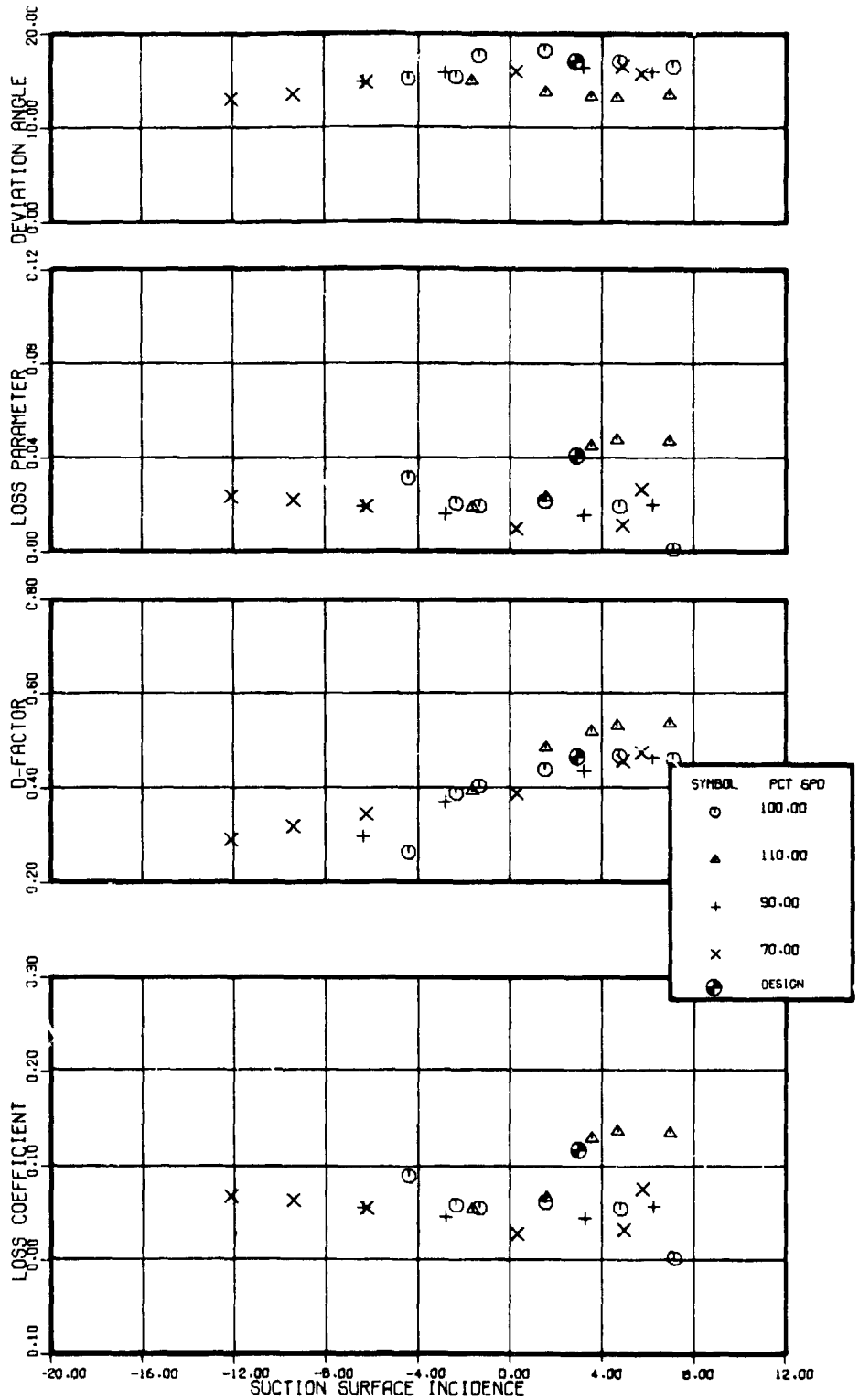

Figure 38. -Stator blade element performance, 10 percent span from tip, Test 1.

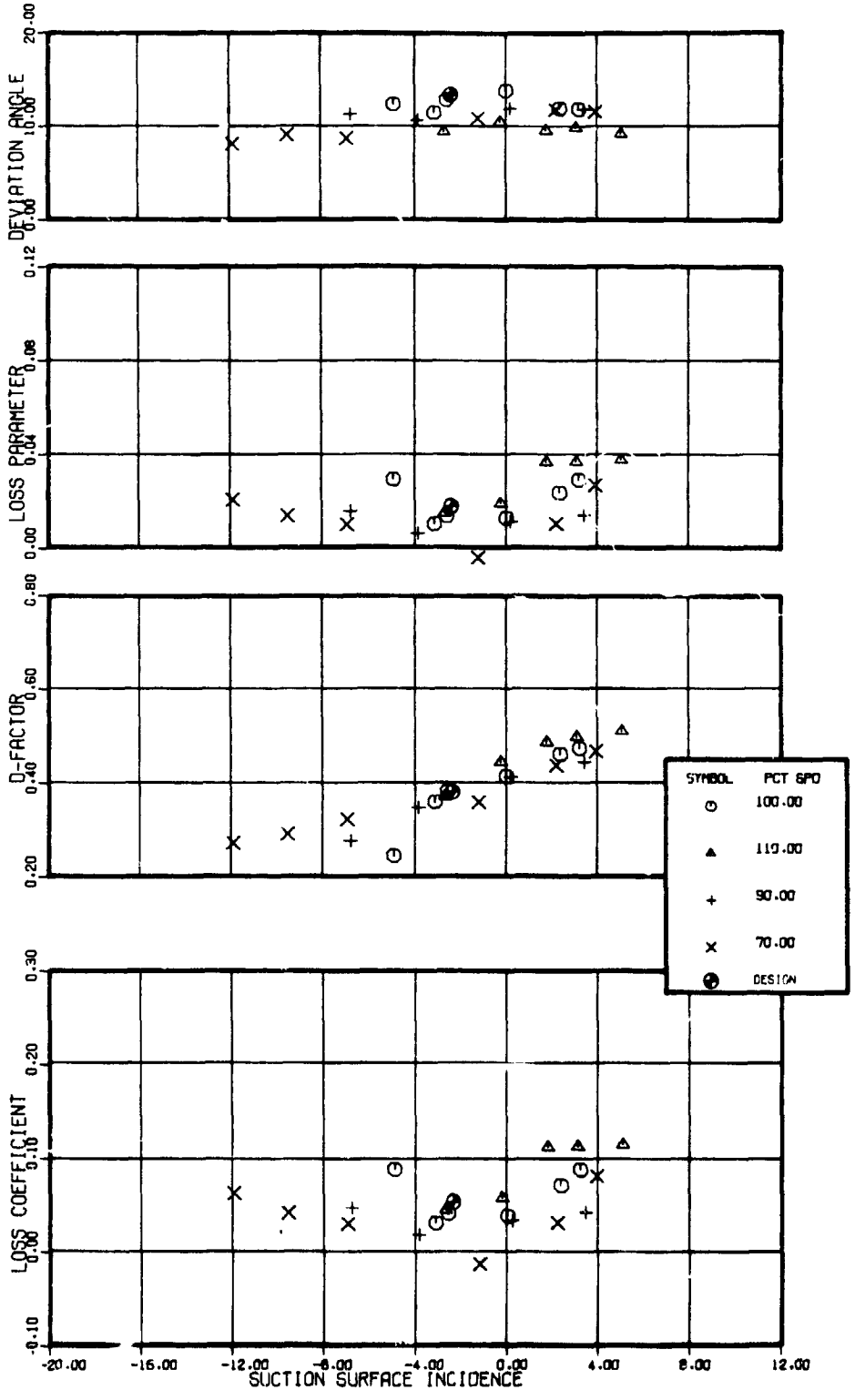

Figure 39. -Stator blade element performance, 30 percent span from tip, Test 1.

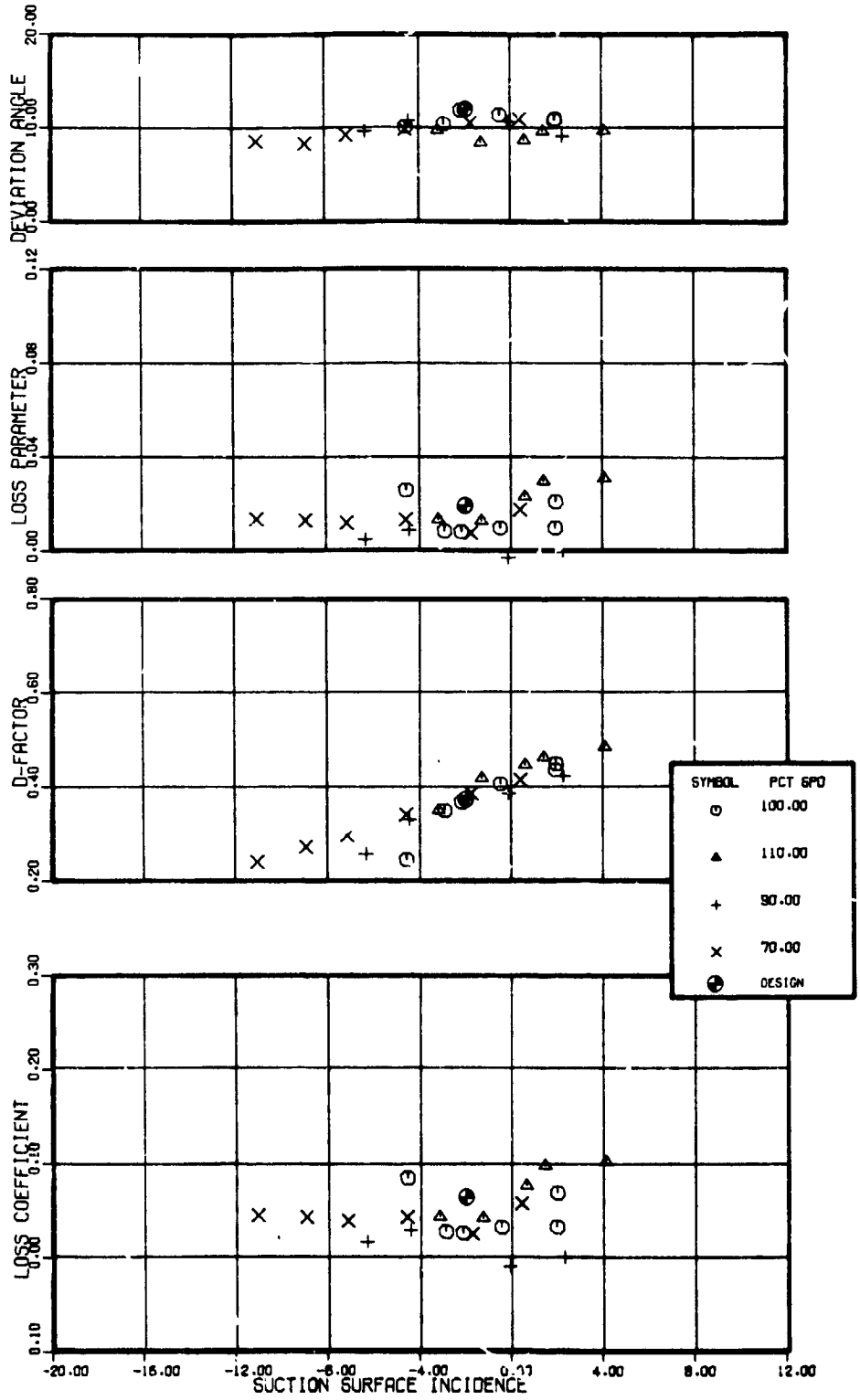

Figure 40. -Stator blade element performance, 50 percent span from tip, Test 1.

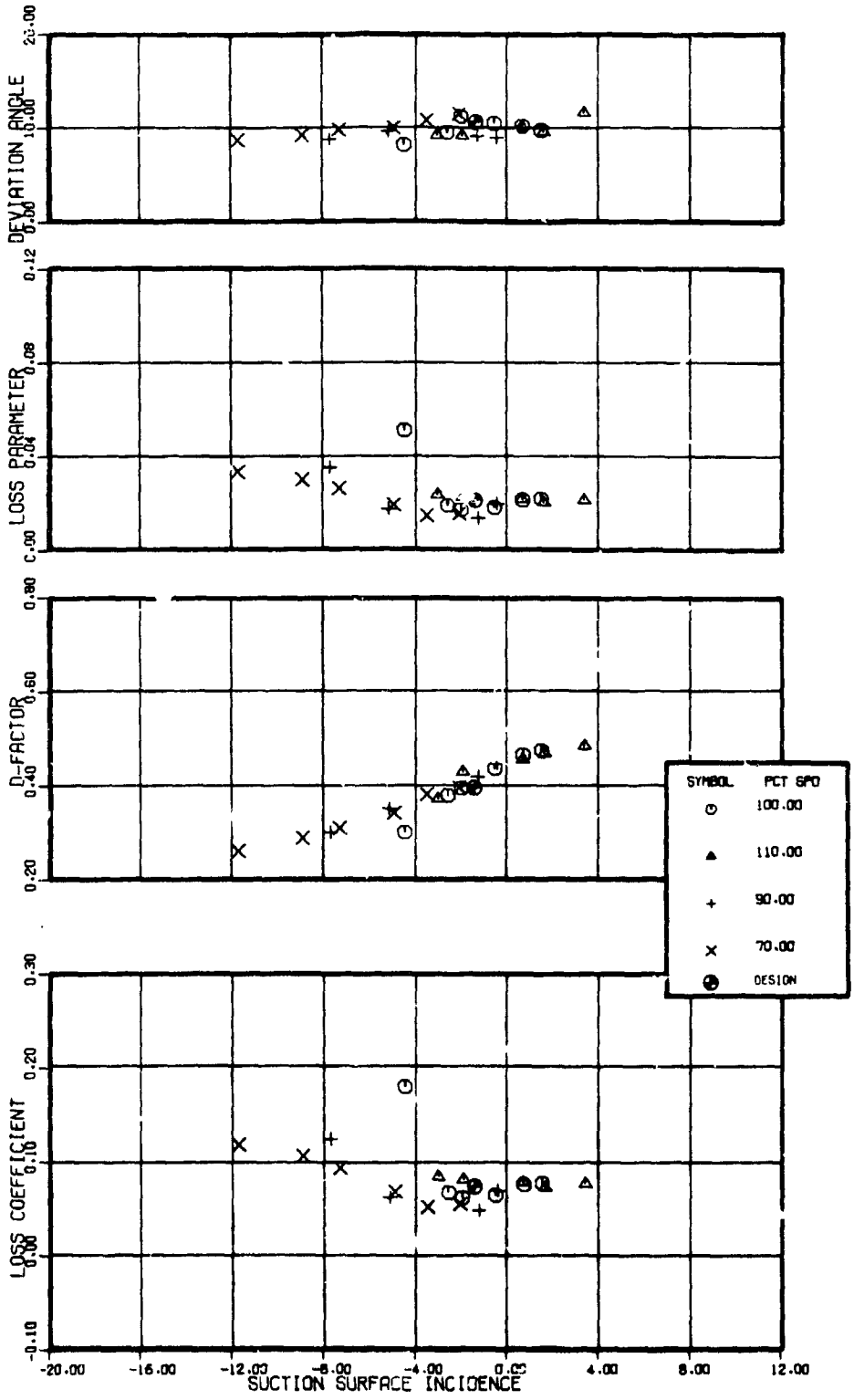

Figure 41. -Stator blade element performance, 70 percent span from tip, Test 1.

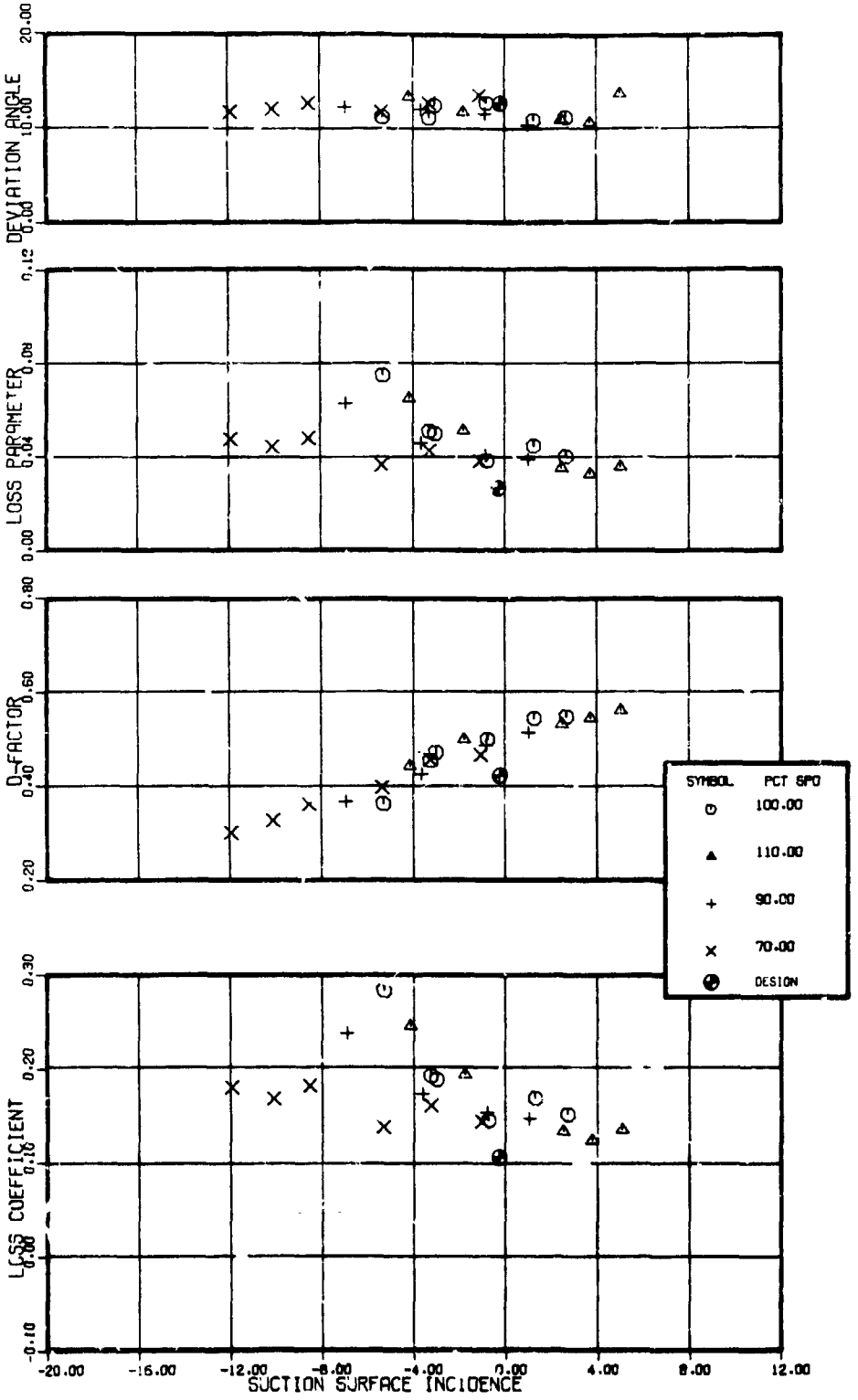

Figure 42. -Stator blade element performance, 90 percent span from tip, Test 1.

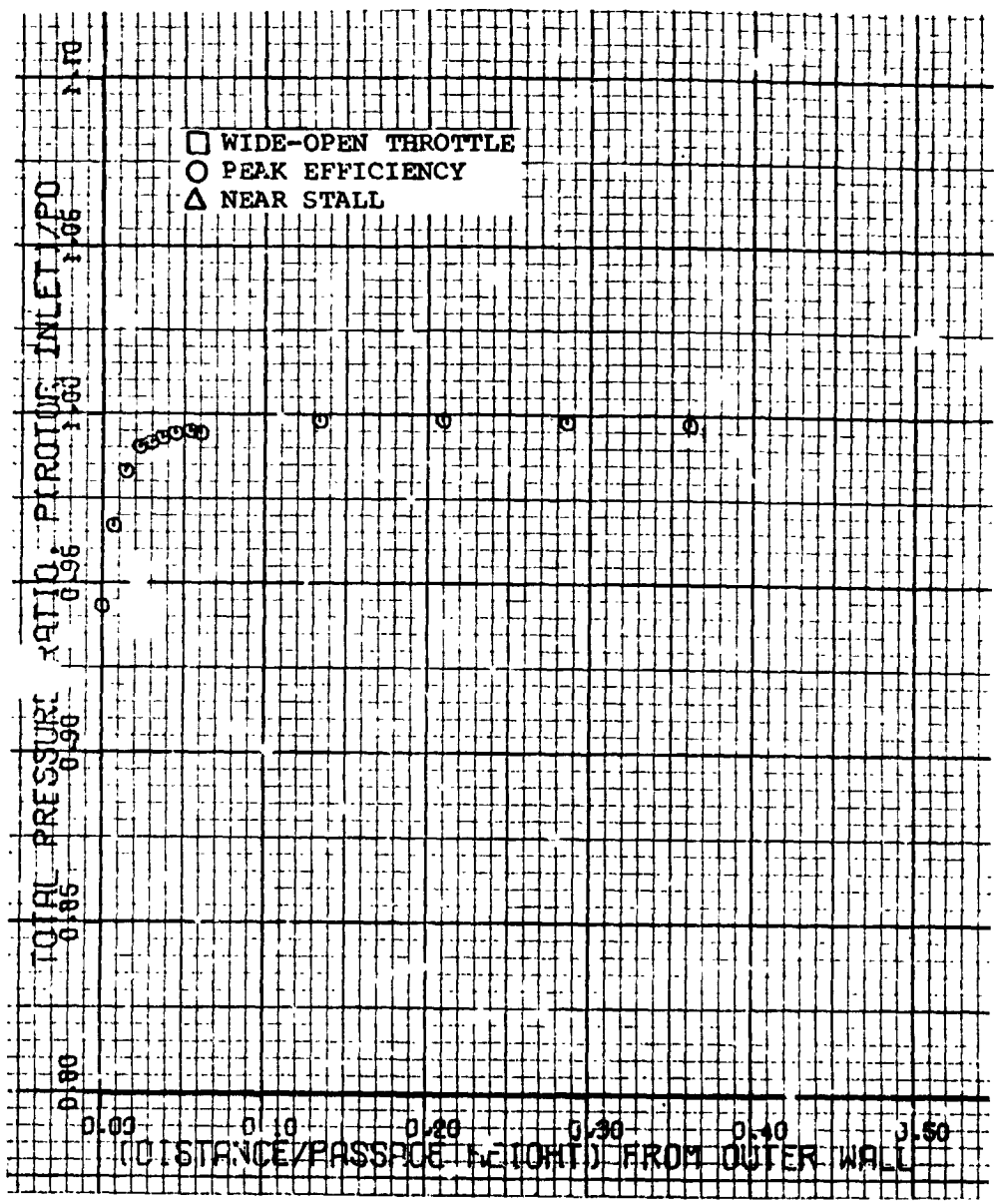

Figure 43. -Rotor inlet outerwall boundary layer total pressure profile, 70 percent design speed, Test 1.

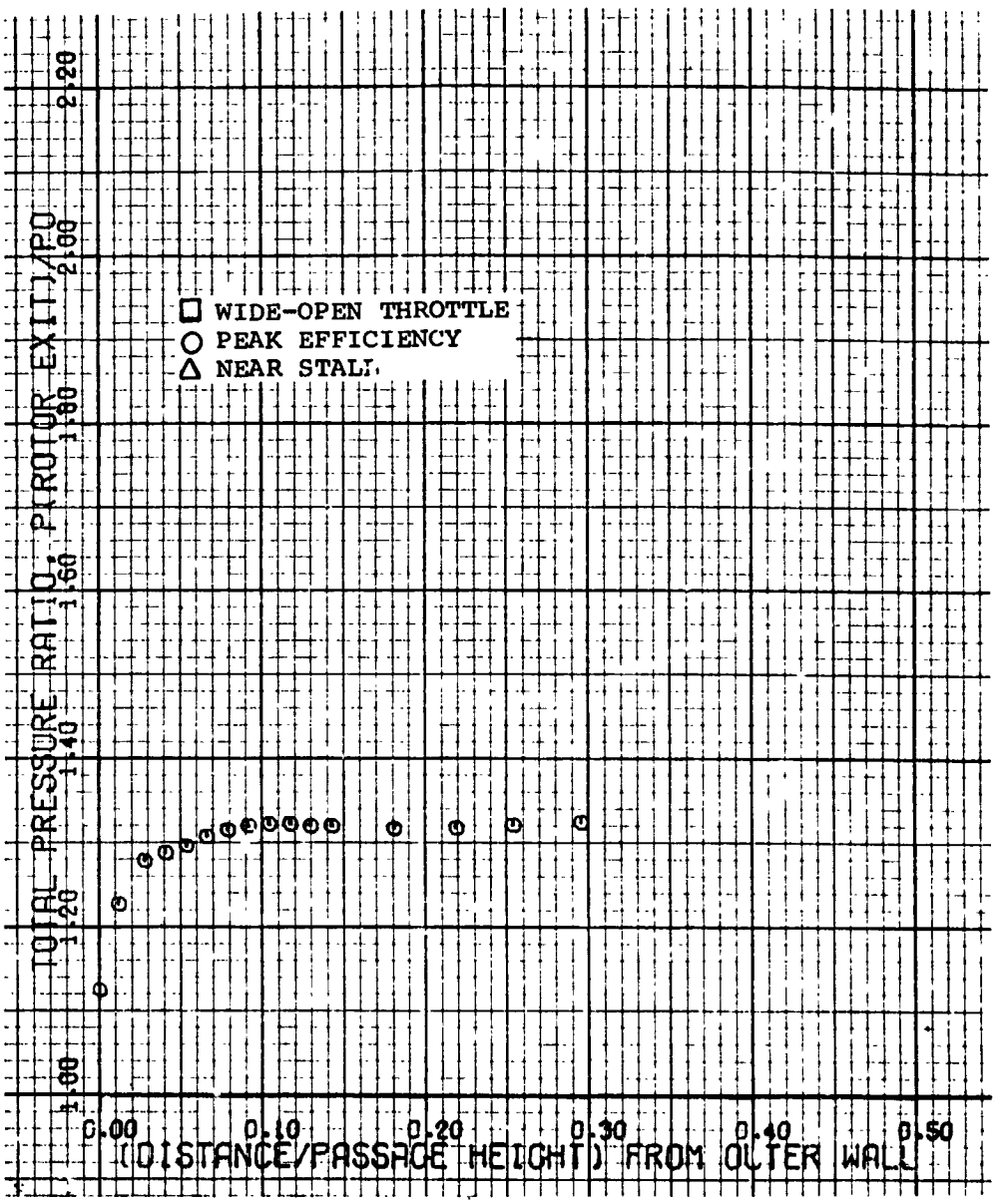

Figure 44. -Rotor exit outerwall boundary layer total pressure profile, 70 percent design speed, Test 1.

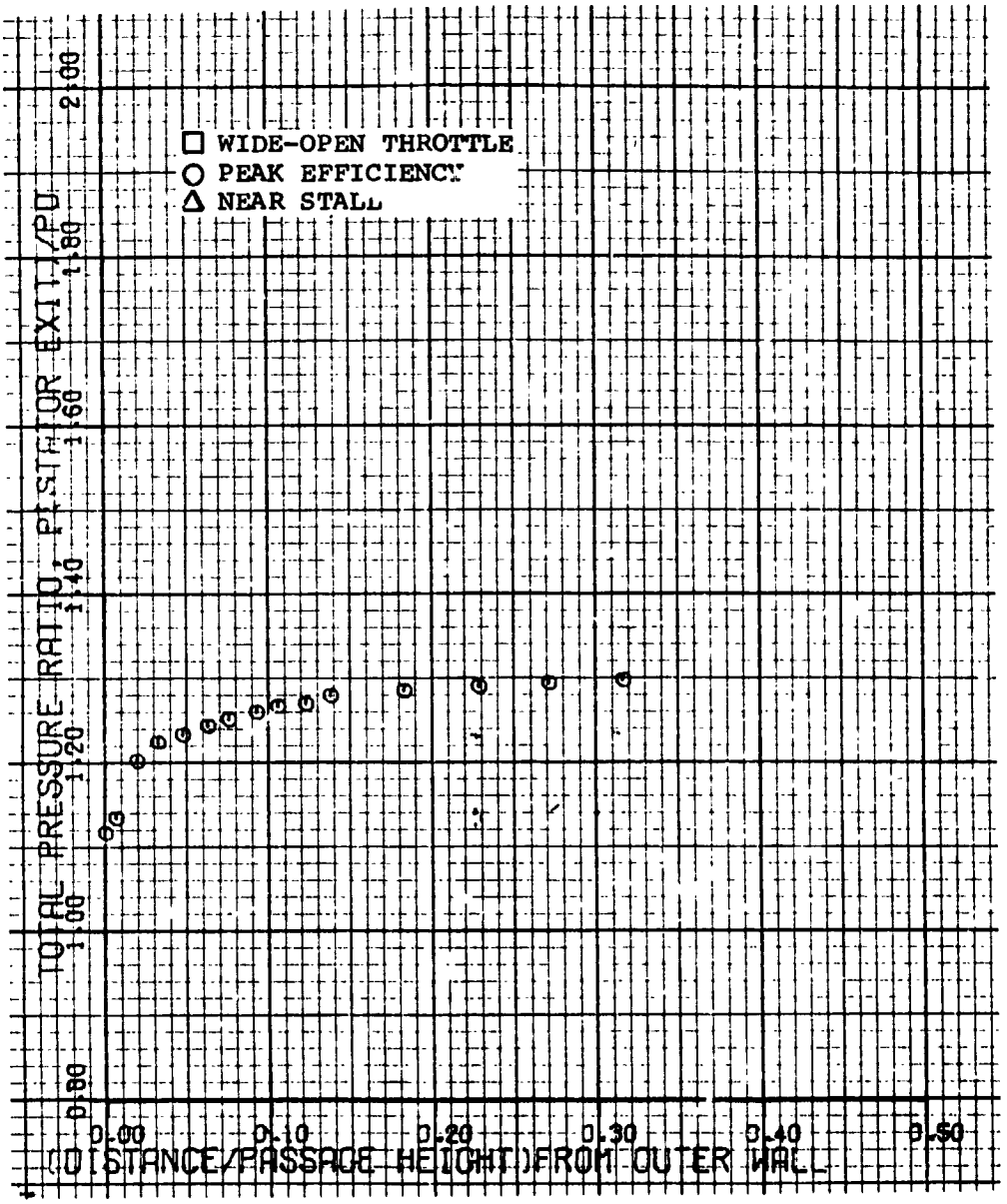

Figure 45. -Stator exit outerwall boundary layer total pressure profile, 70 percent design speed, Test 1.

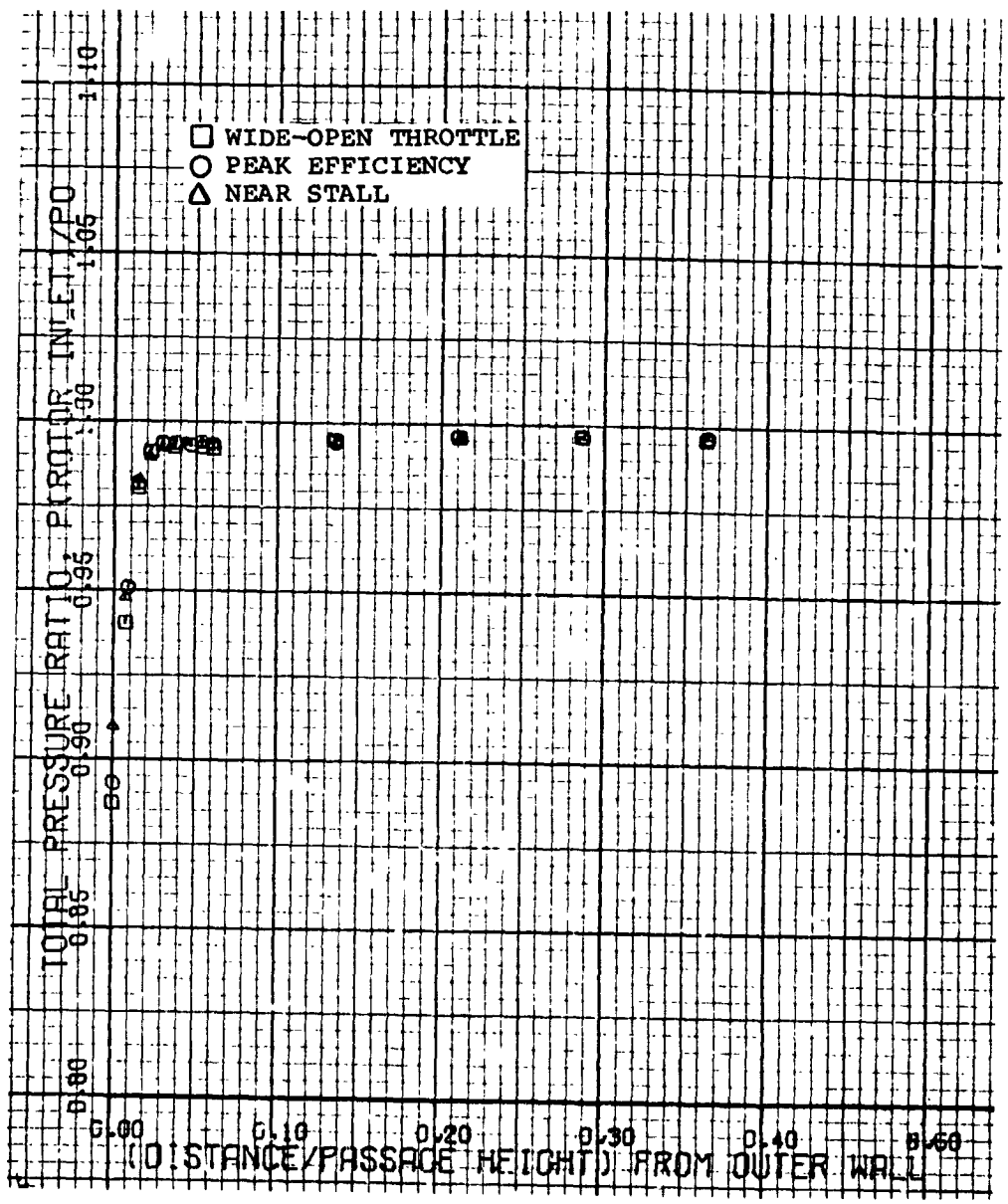

Figure 46. -Rotor inlet outerwall boundary layer total pressure profile, 90 percent design speed, Test 1.

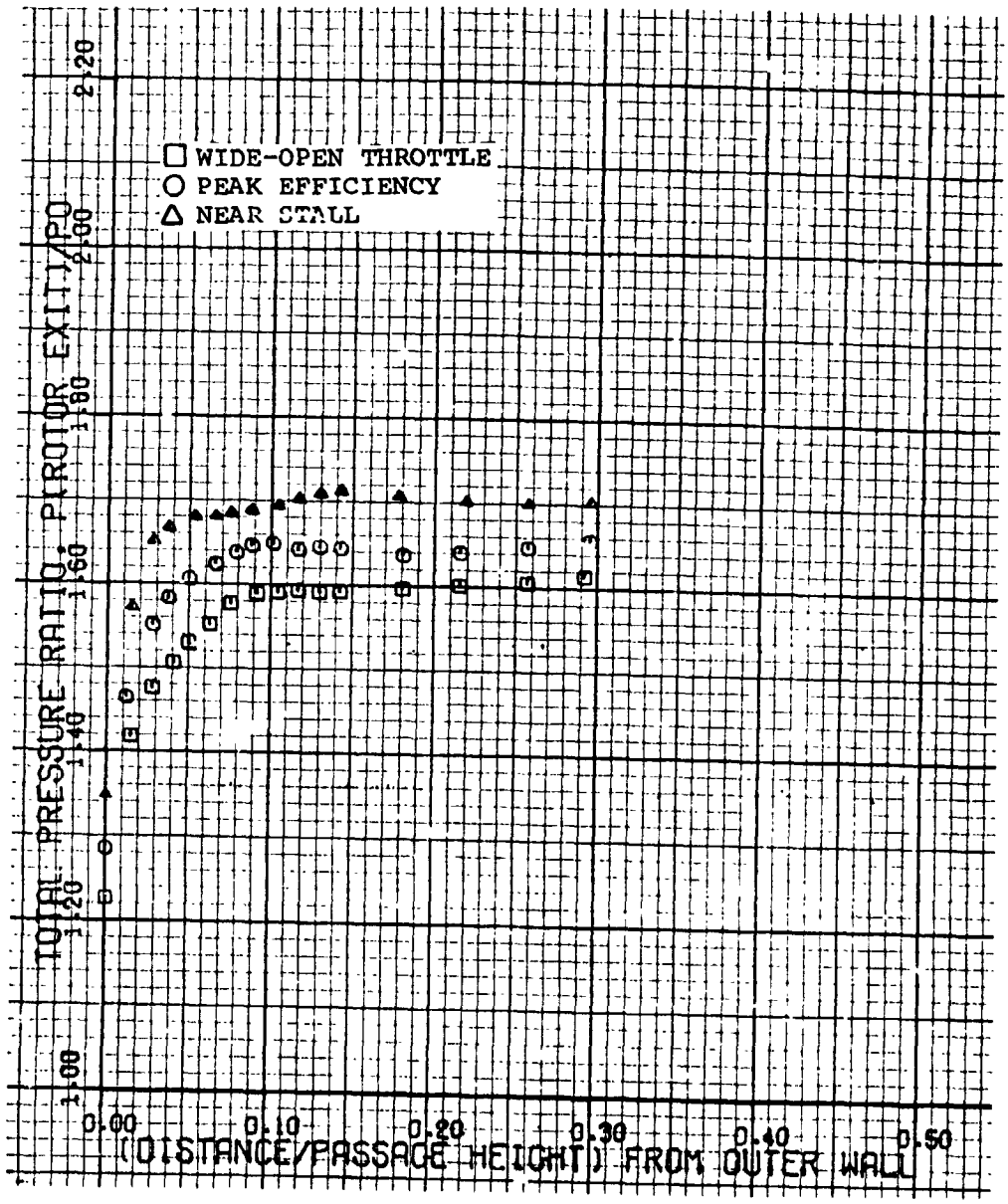

Figure 47. -Rotor exit outerwall boundary layer total pressure profile, 90 percent design speed, Test 1.

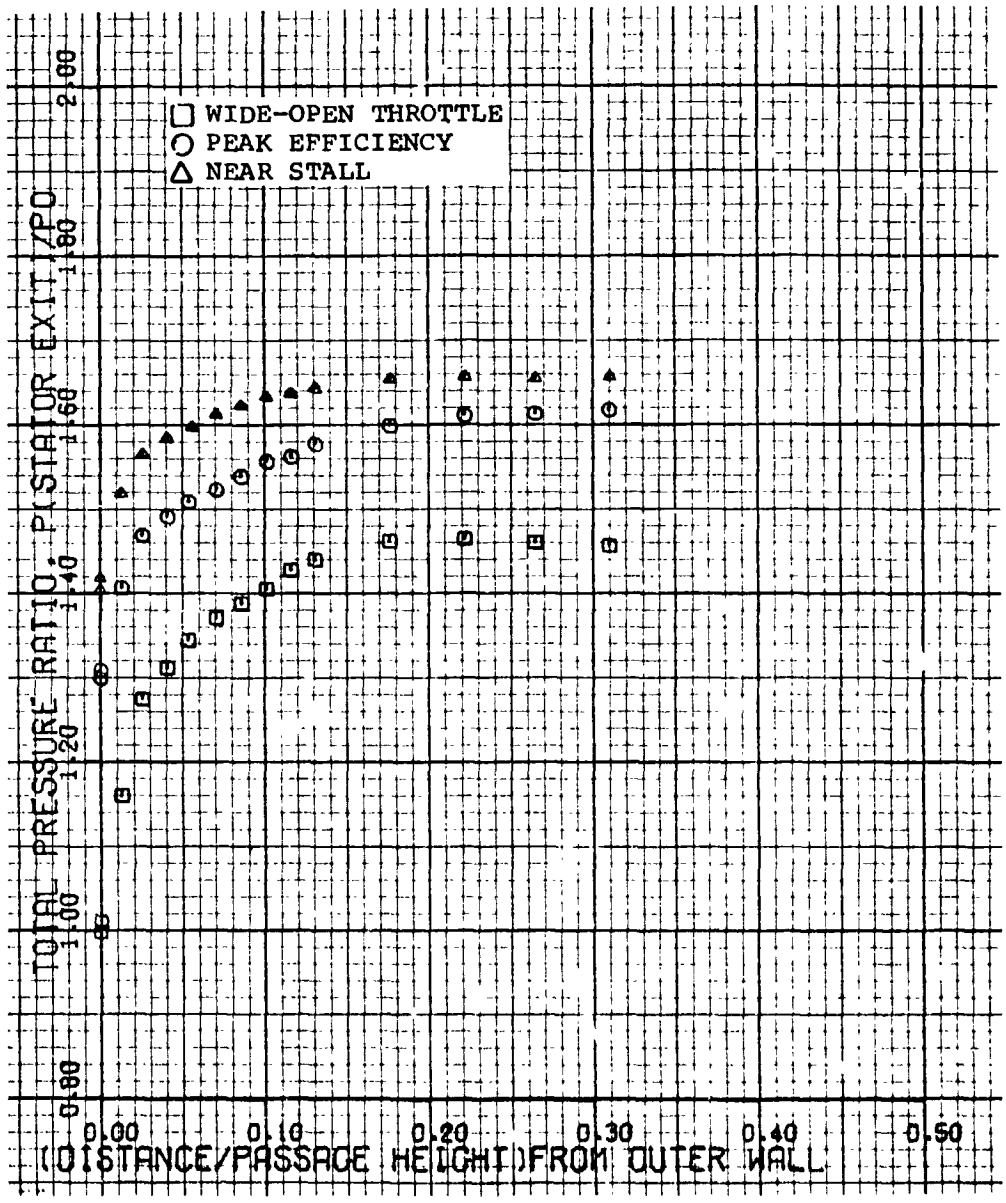

Figure 48. -Stator exit outerwall boundary layer total pressure profile, 90 percent design speed, Test 1.

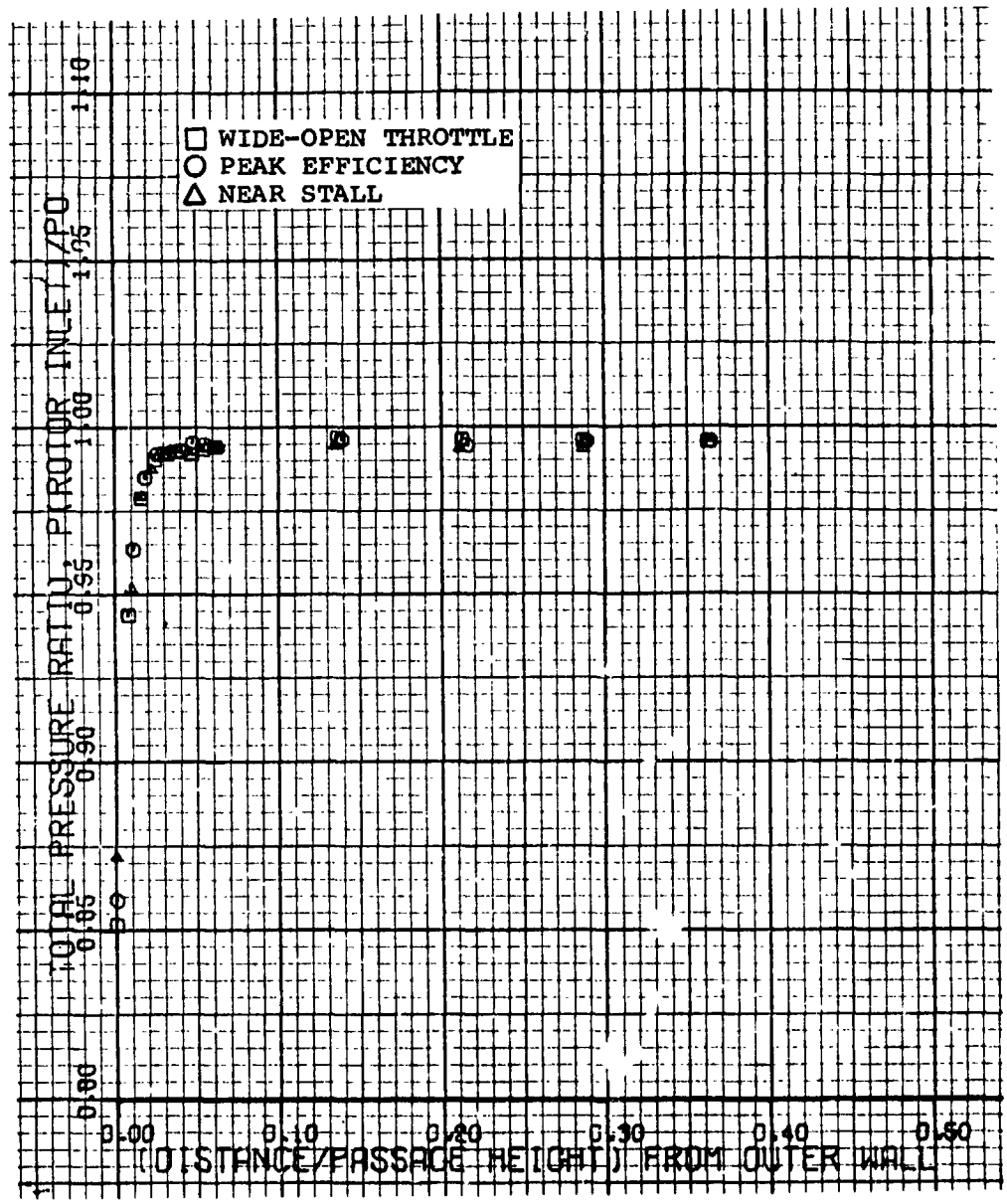

Figure 49. -Rotor inlet outerwall boundary layer total pressure profile, 100 percent design speed, Test 1.

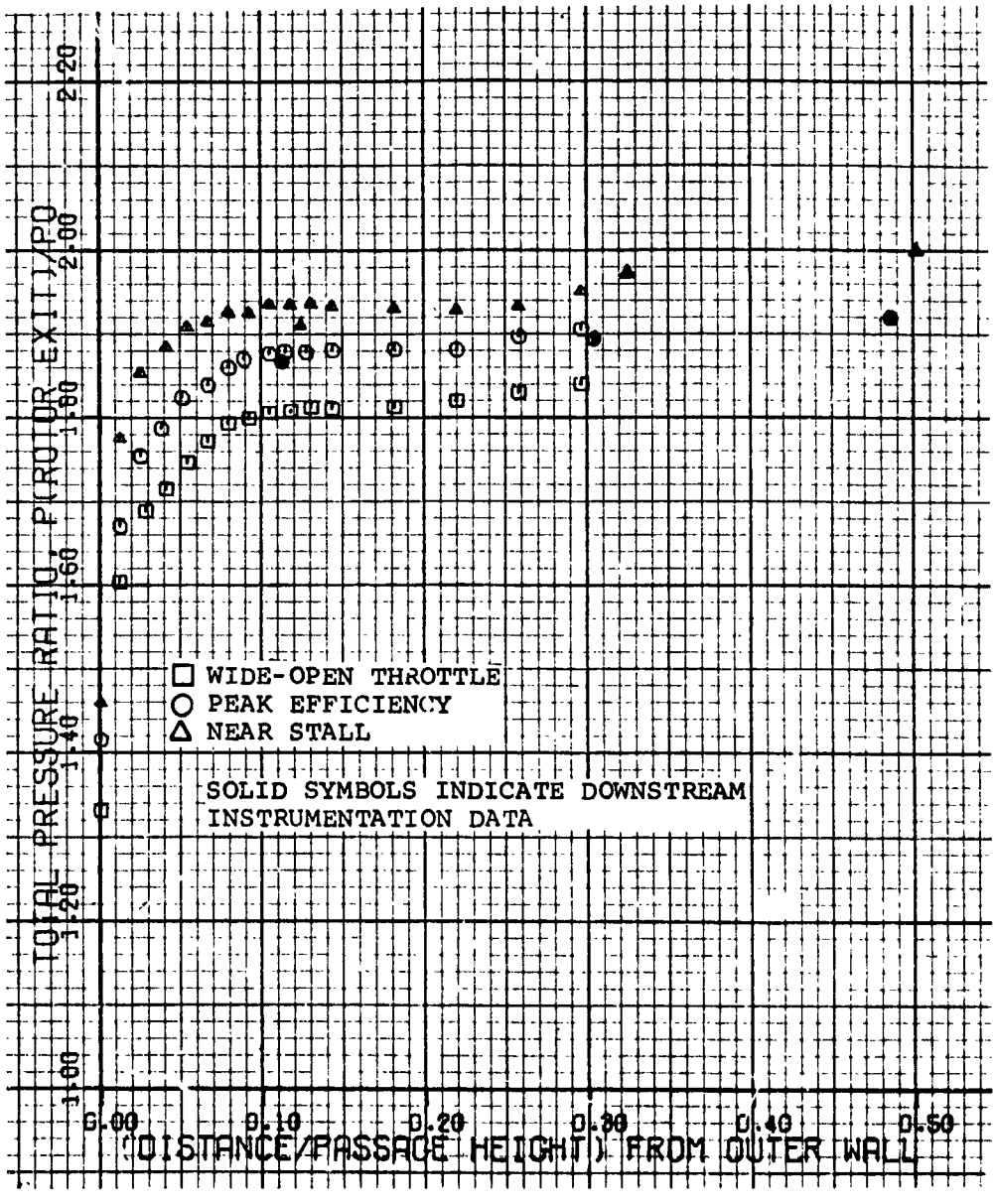

Figure 50. Rotor exit outerwall boundary layer total pressure profile 00 percent design speed, Test 1.

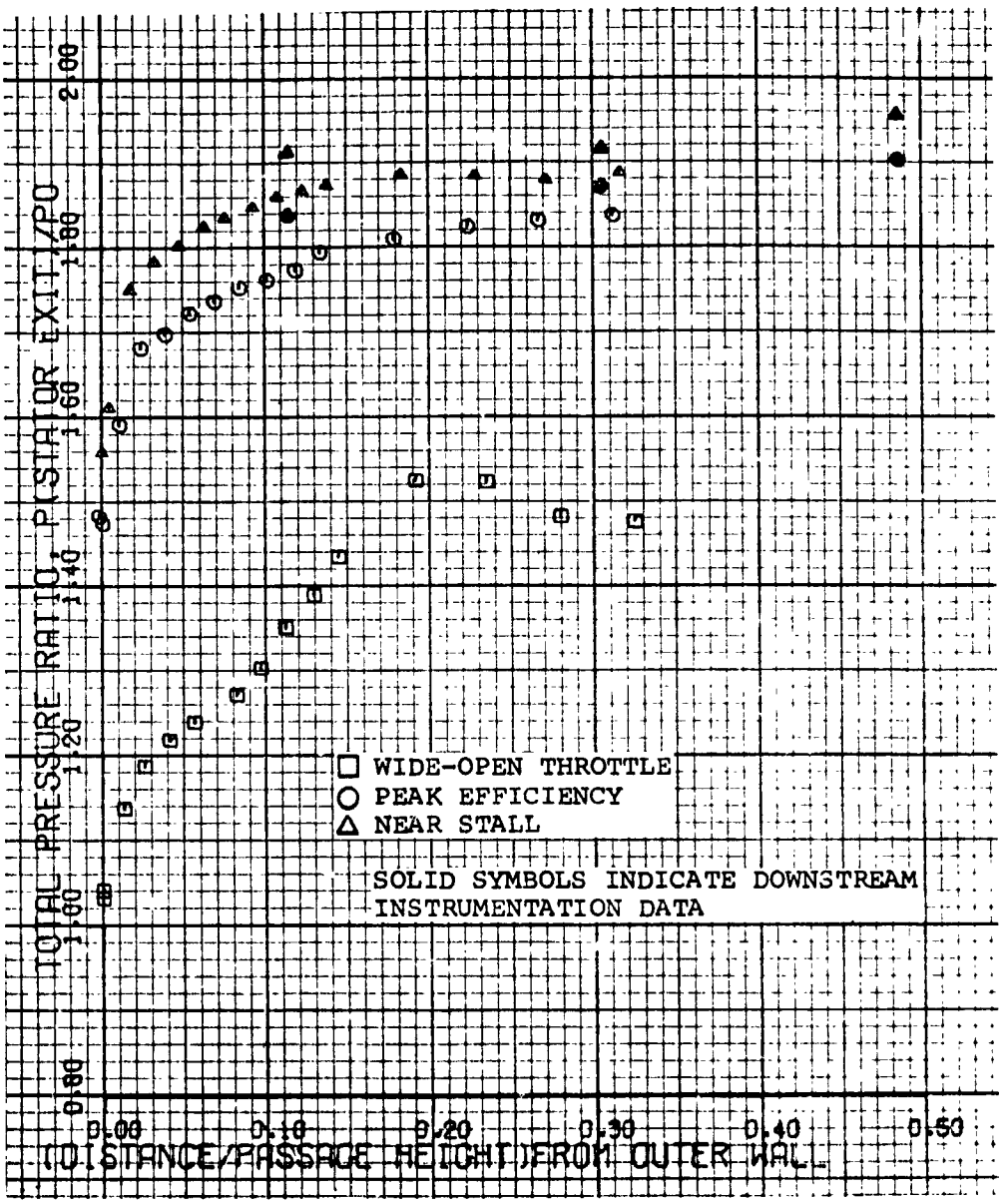

Figure 51. -Stator exit outerwall boundary layer total pressure profile, 100 percent design speed, Test 1.

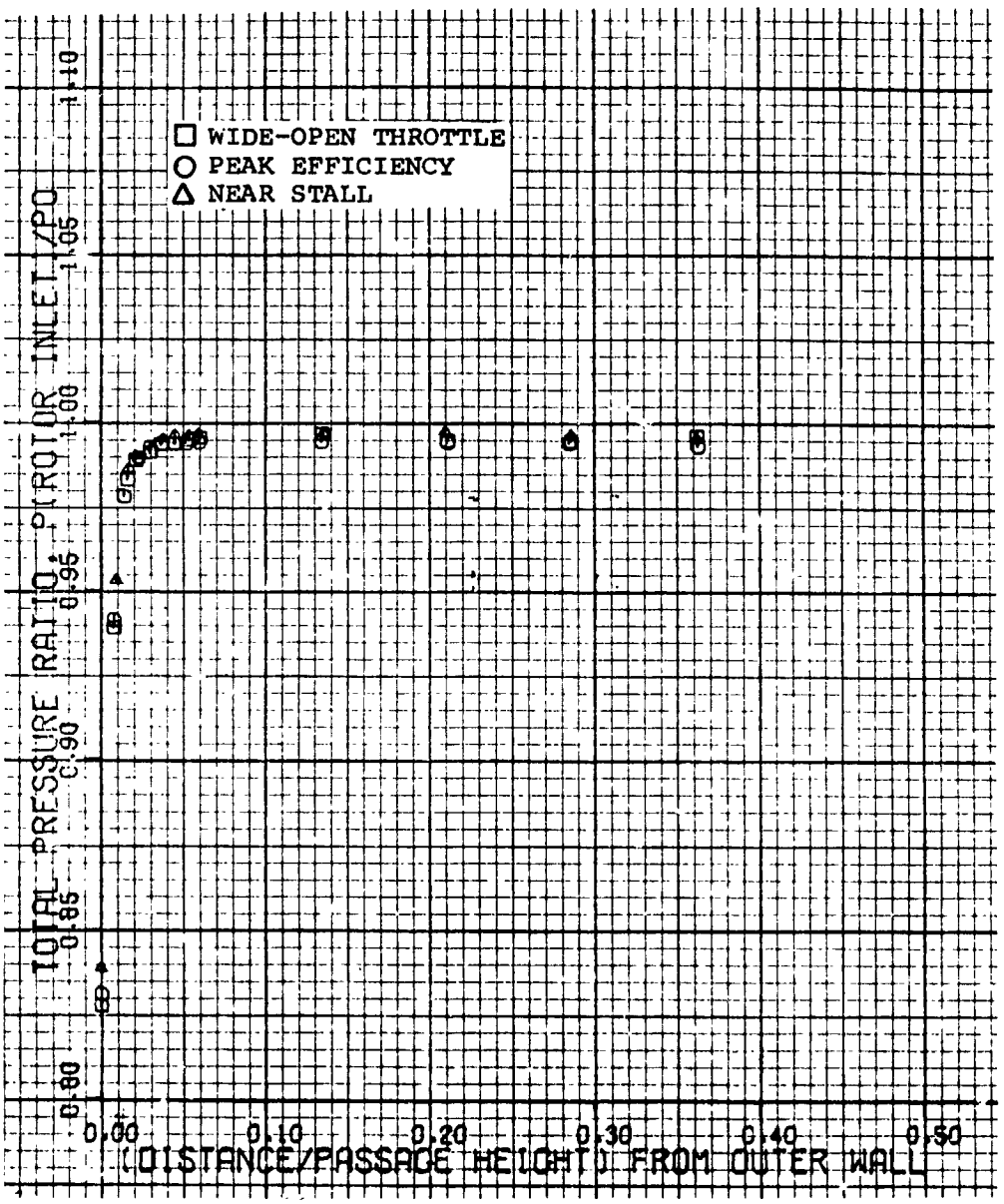

Figure 52. -Rotor inlet outerwall boundary layer total pressure profile, 110 percent design speed Test 1.

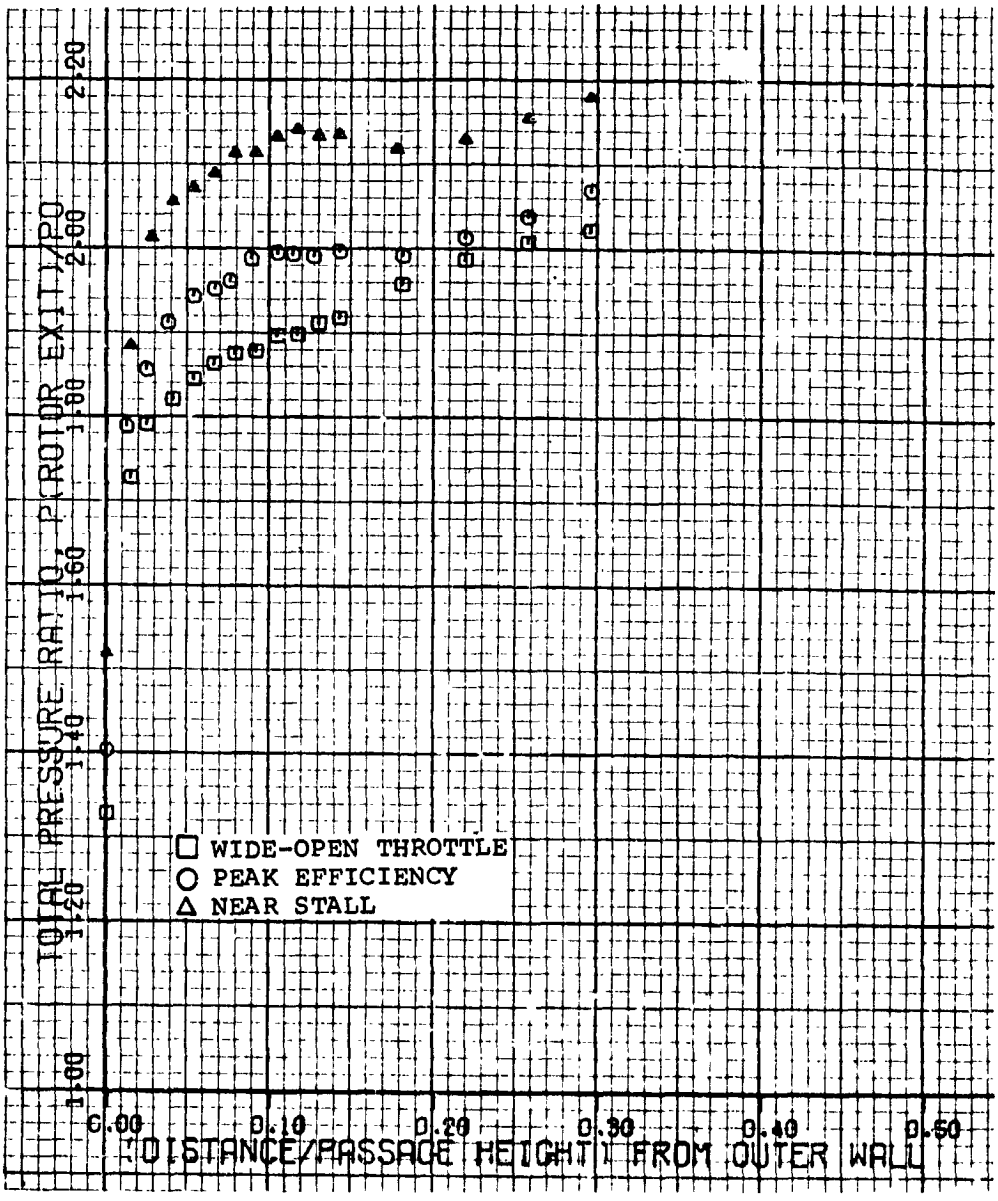

Figure 53. -Rotor exit outerwall boundary layer total pressure profile, 110 percent design speed, Test 1.

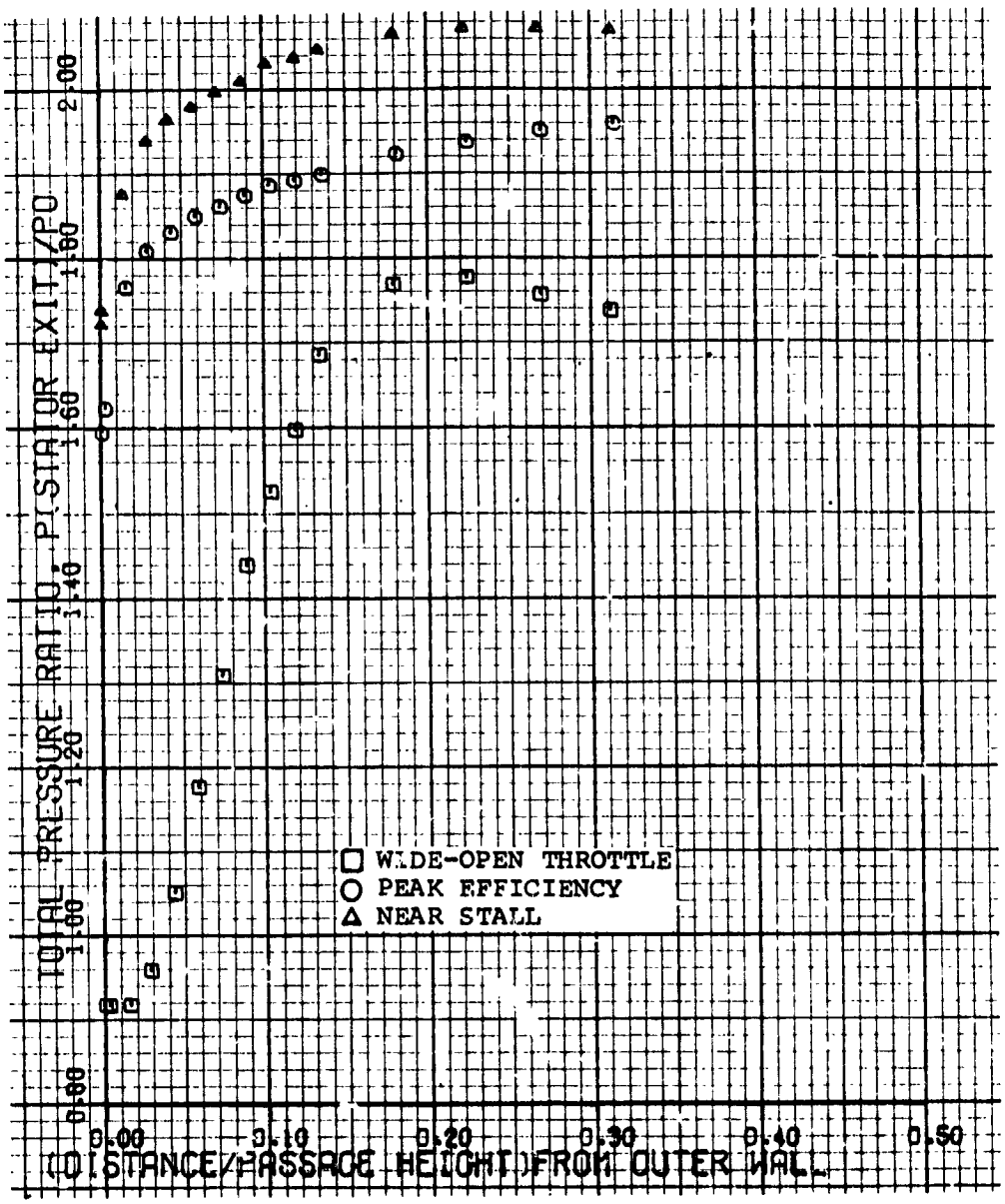

Figure 54. -Stator exit outerwall boundary layer total pressure profile, 110 percent design speed, Test 1.

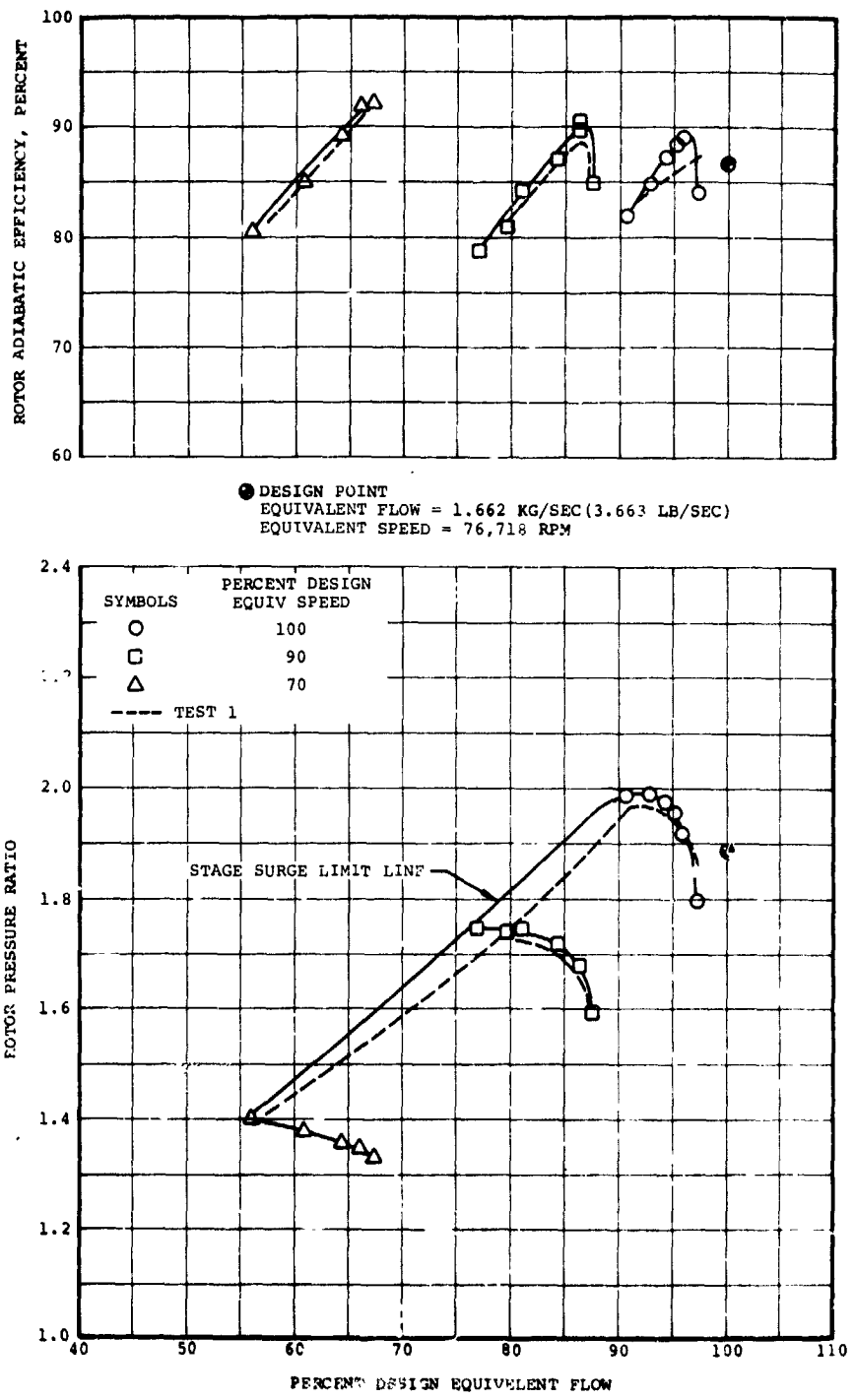

Figure 55. -Test 2 - rotor performance.

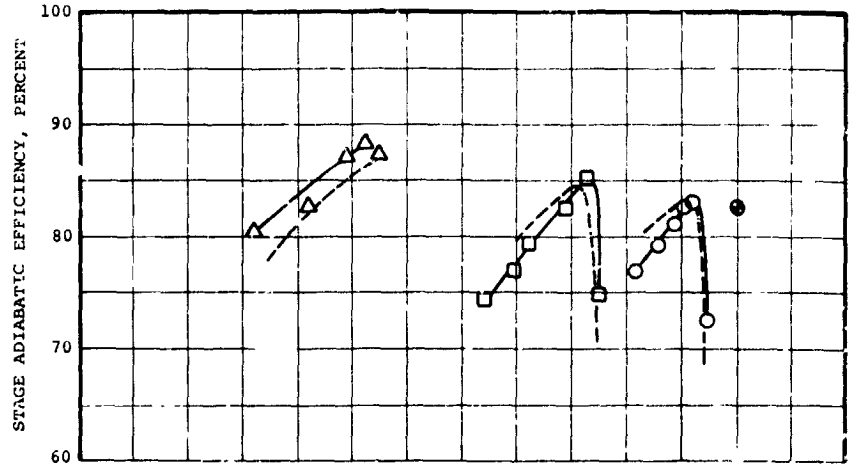

● DESIGN POINT
EQUIVALENT FLOW = 1.662 KG/SEC (3.663 LB/SEC)
EQUIVALENT SPEED = 26,718 RPM

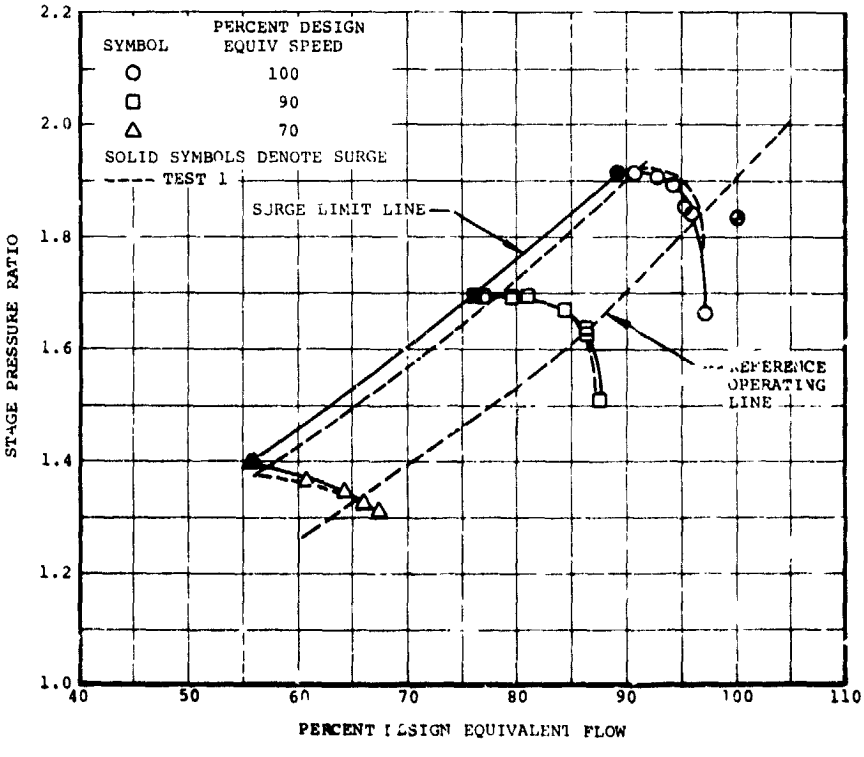

Figure 56. -Test 2 - Stage performance.

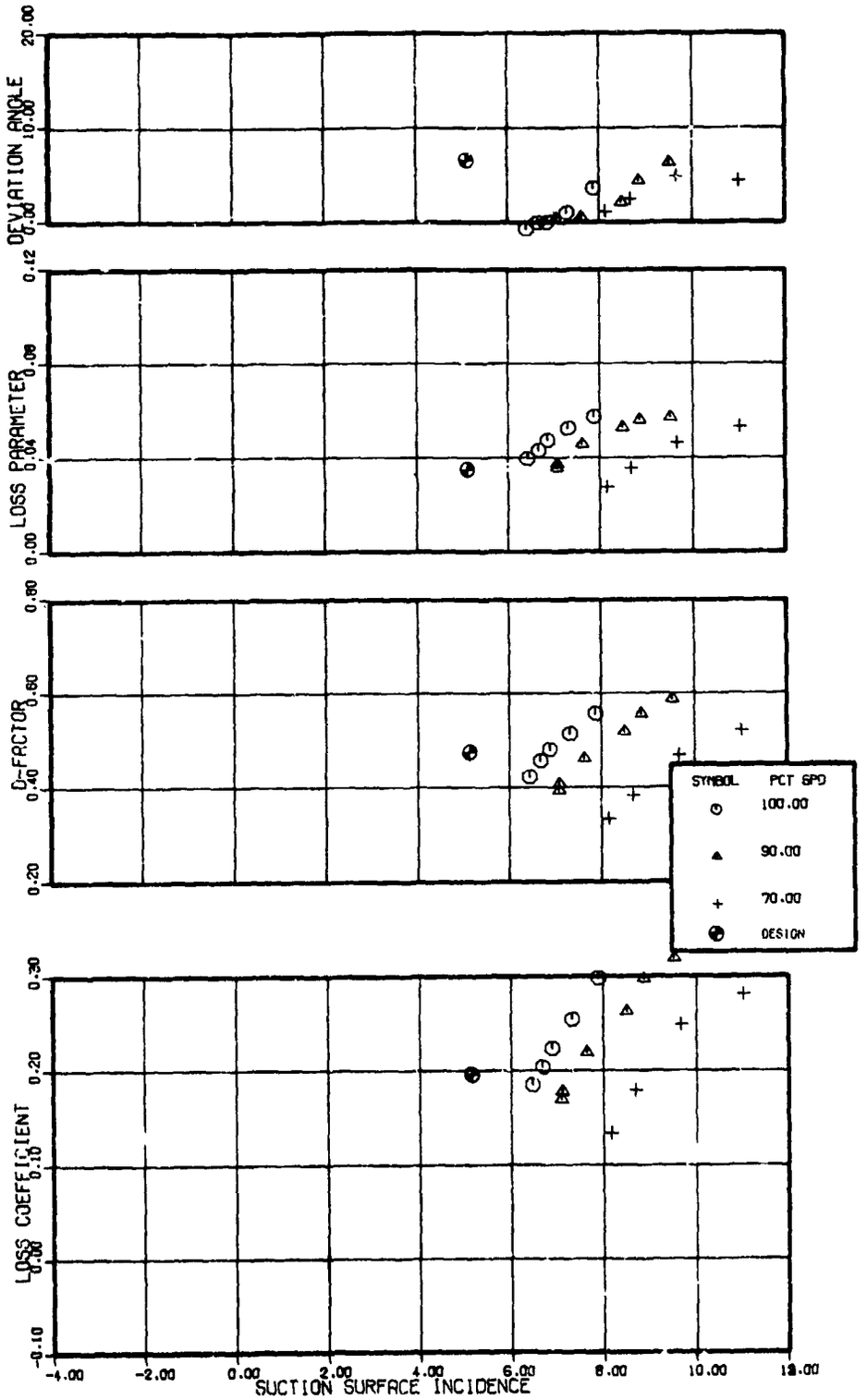

Figure 57. -Rotor blade element performance, 10 percent span from tip, Test 2.

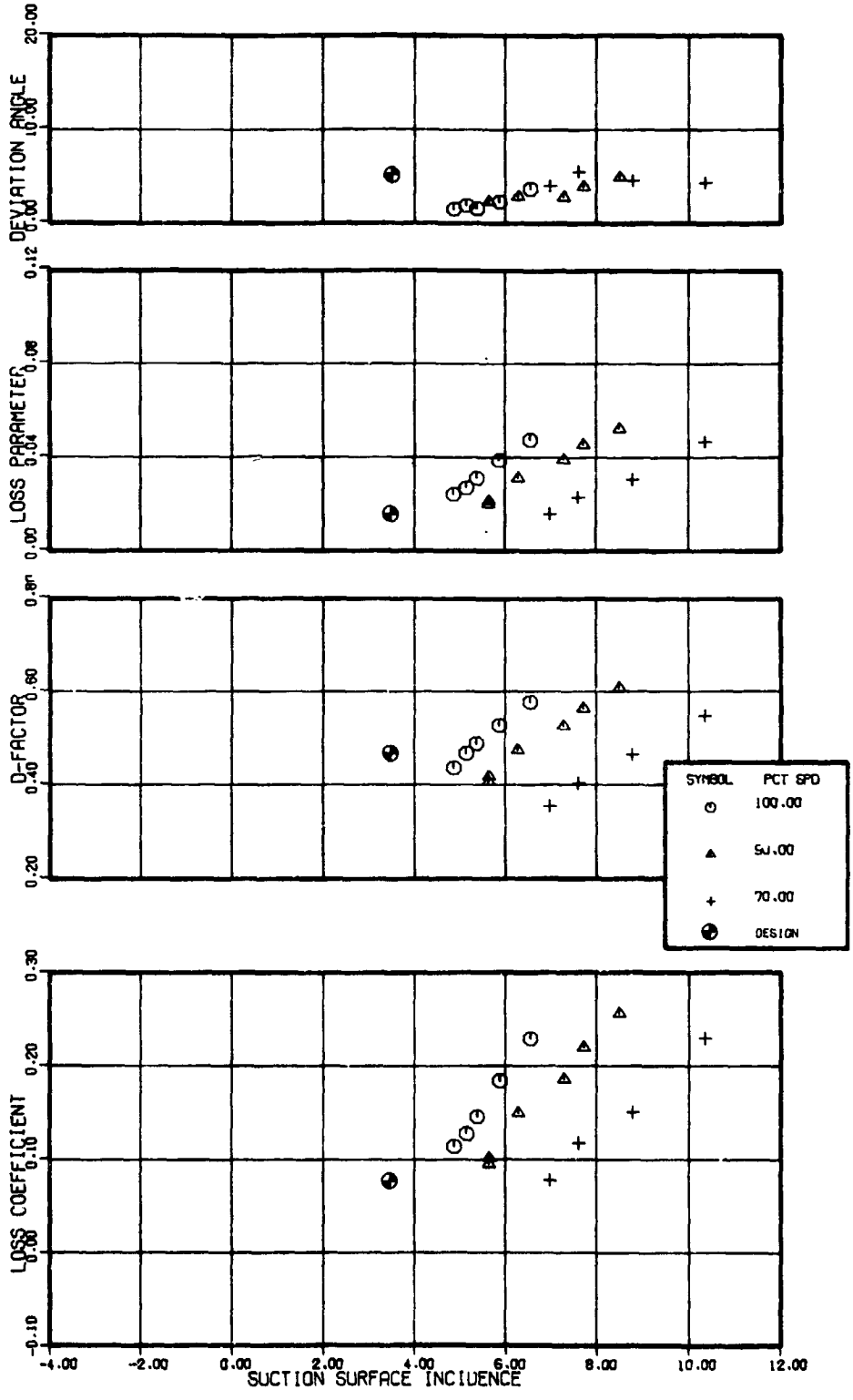

Figure 58. -Rotor blade element performance, 30 percent span from tip, Test 2.

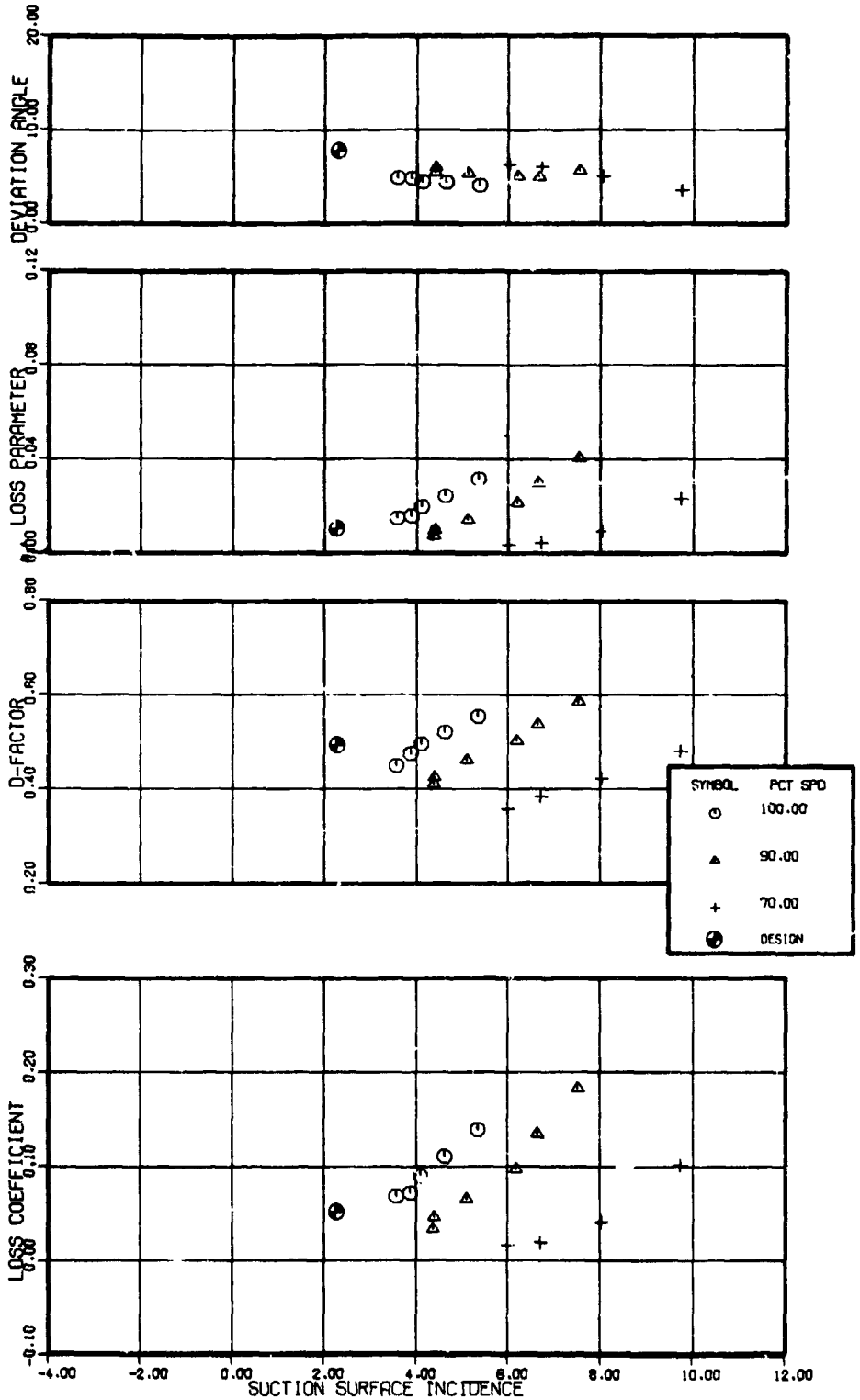

Figure 59. -Rotor blade element performance, 50 percent span from tip, Test 2.

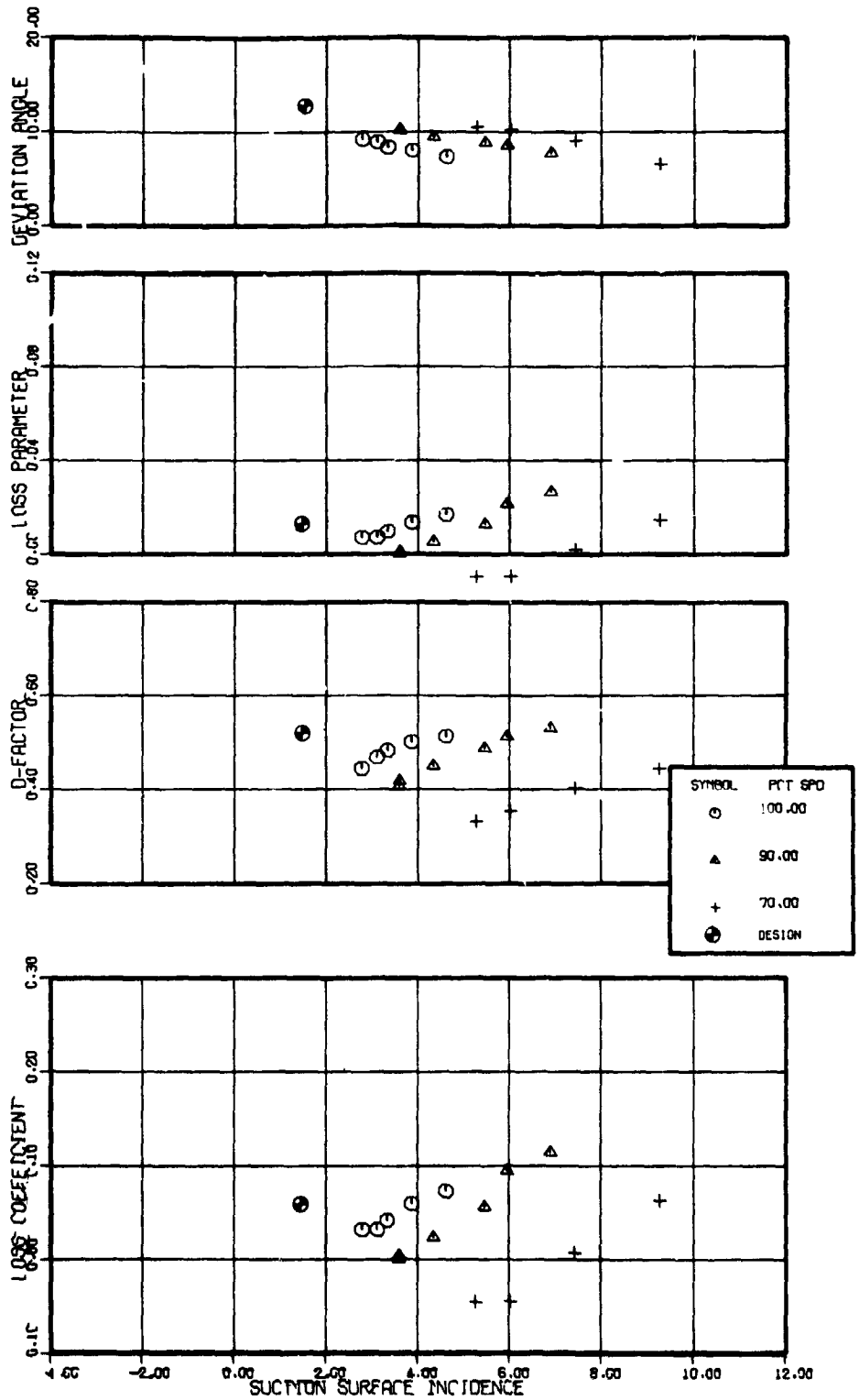

Figure 60. -Rotor blade element performance, 70 percent span from tip, Test 2.

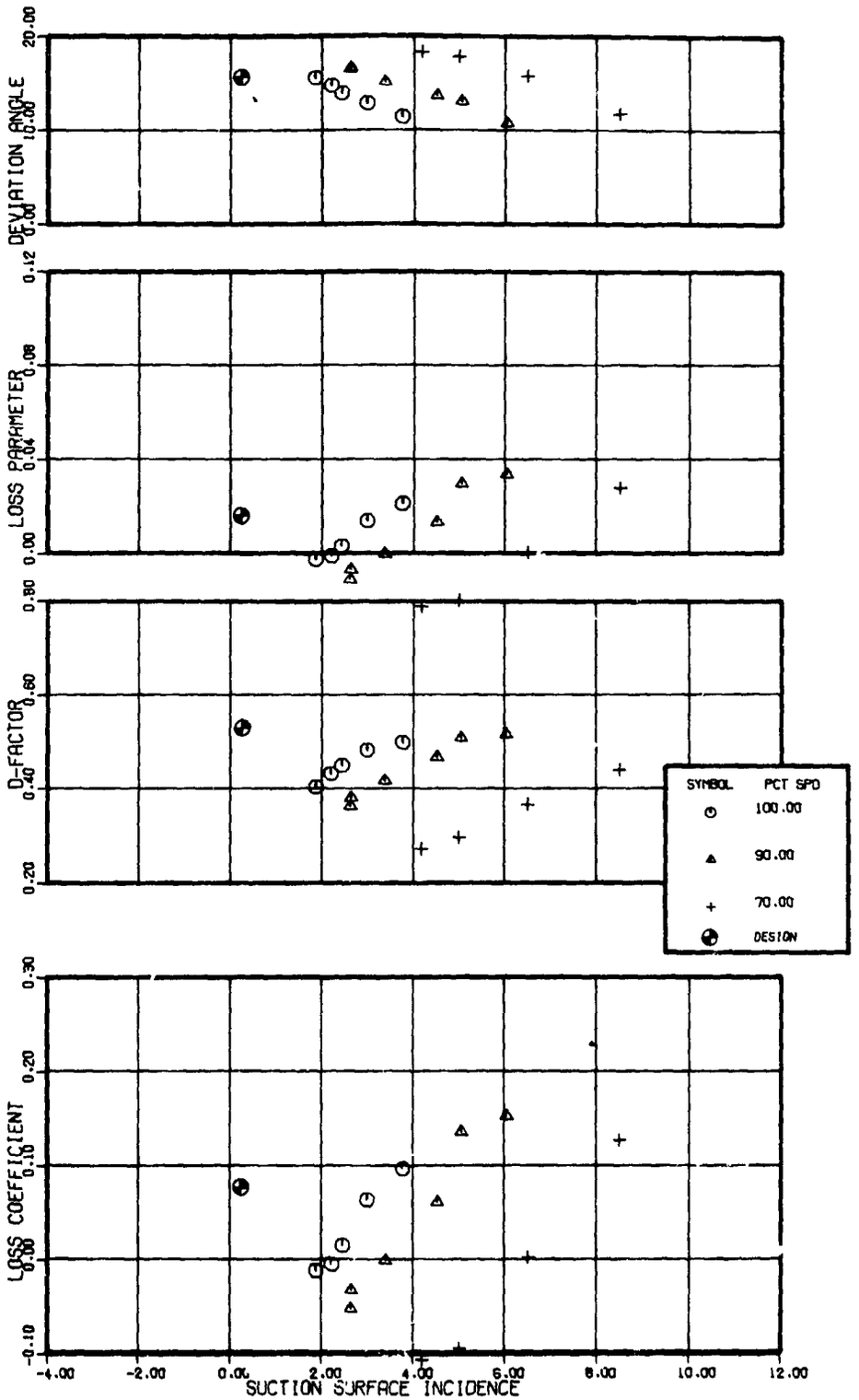

ORIGINAL PAGE IS OF POOR QUALITY

Figure 61. -Rotor blade element performance, 90 percent span from tip, Test 2.

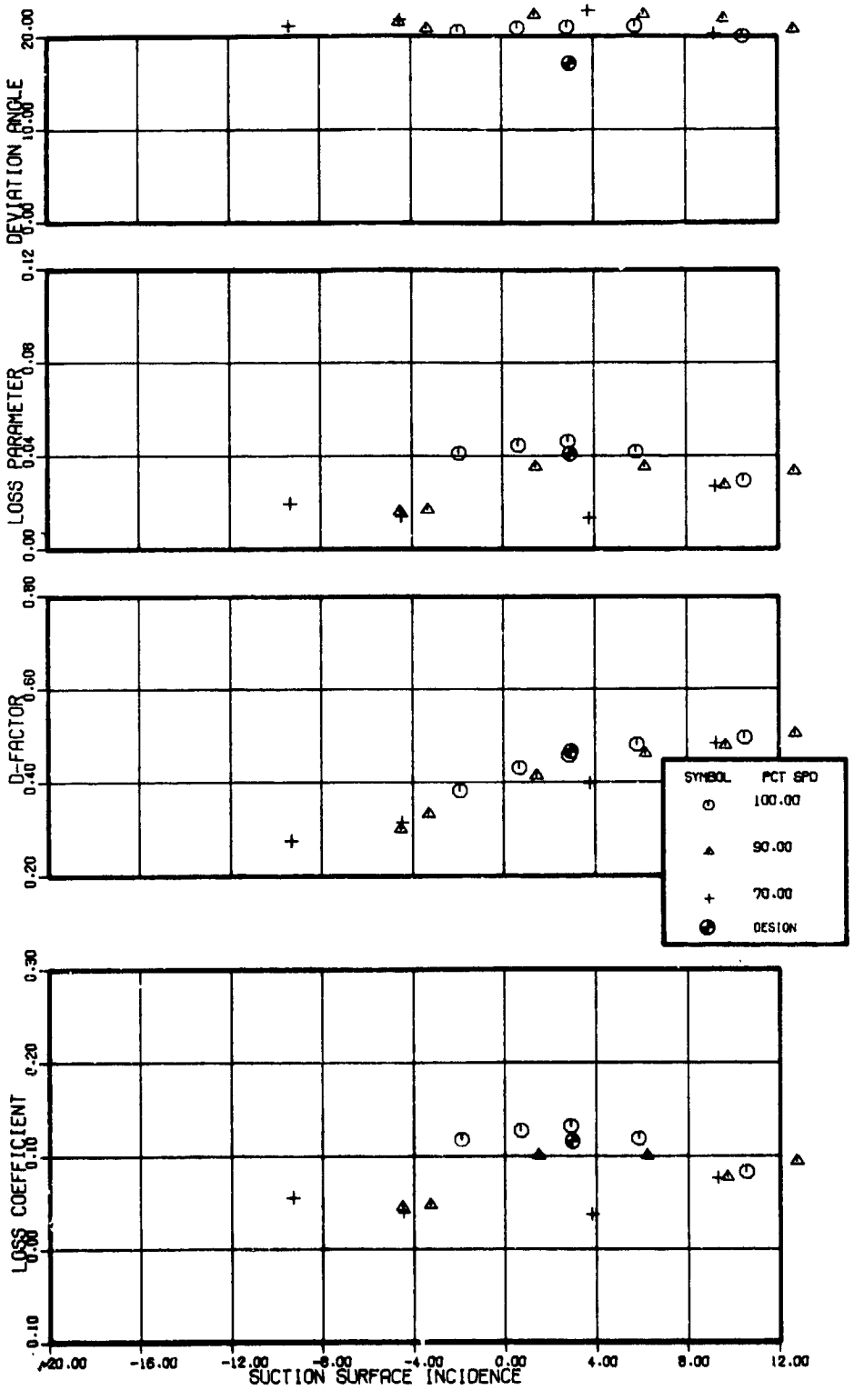

Figure 62. -Stator blade element performance, 10 percent span from tip, Test 2.

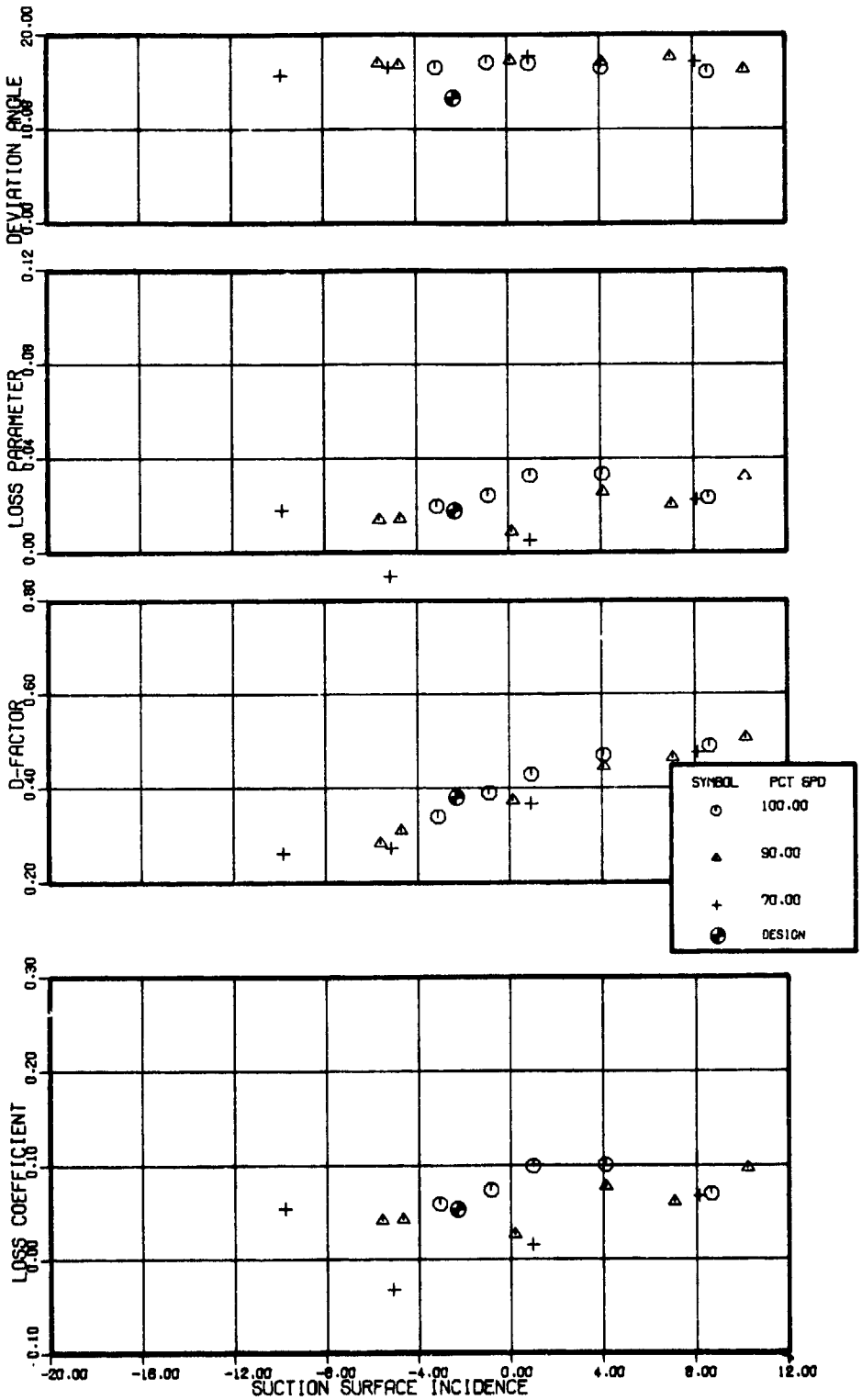

Figure 63. -Stator blade element performance, 30 percent span from tip, Test 2.

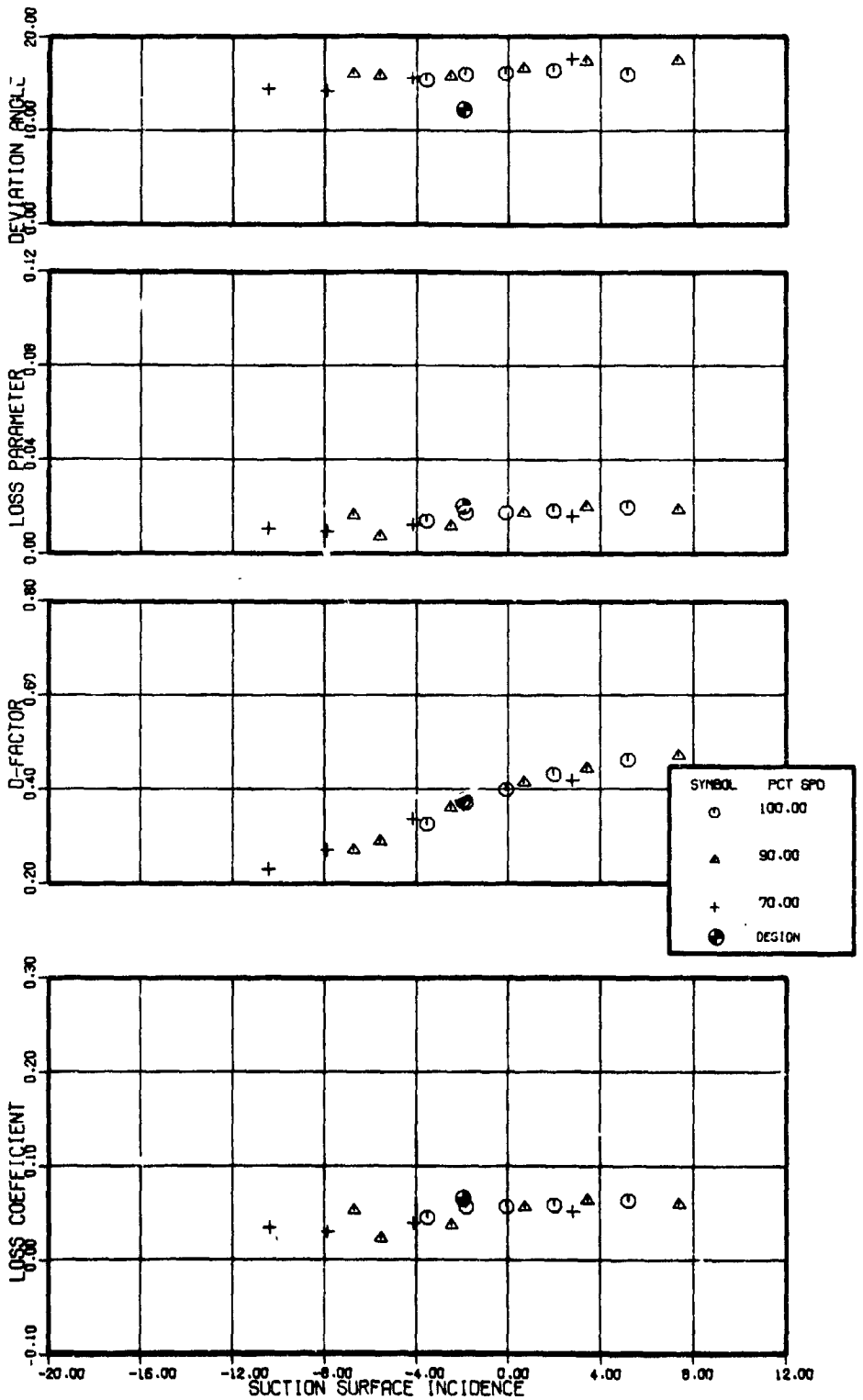

Figure 64. -Stator blade element performance, 50 percent span from tip, Test 2.

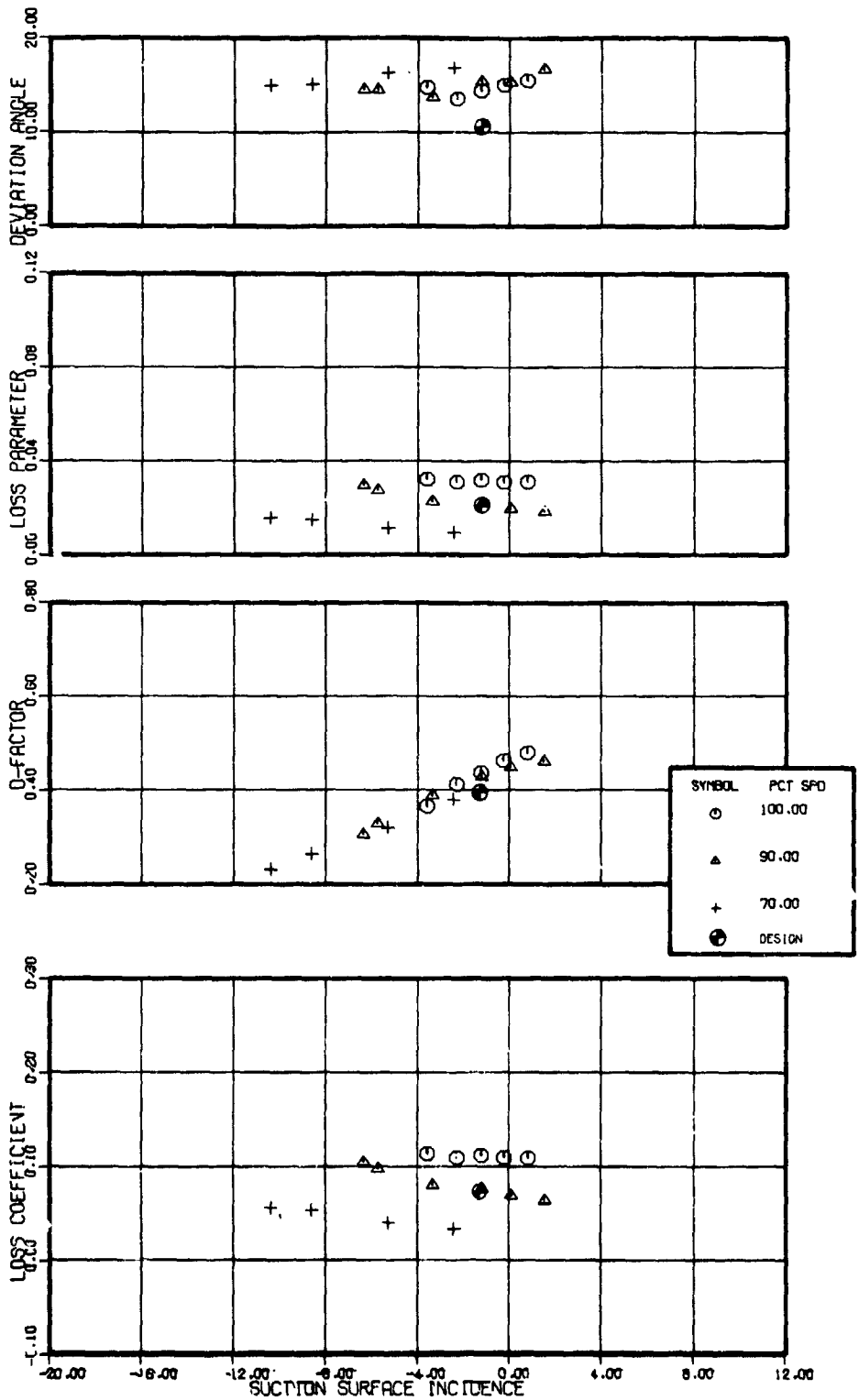

Figure 65. -Stator blade element performance, 70 percent span from tip, Test 2.

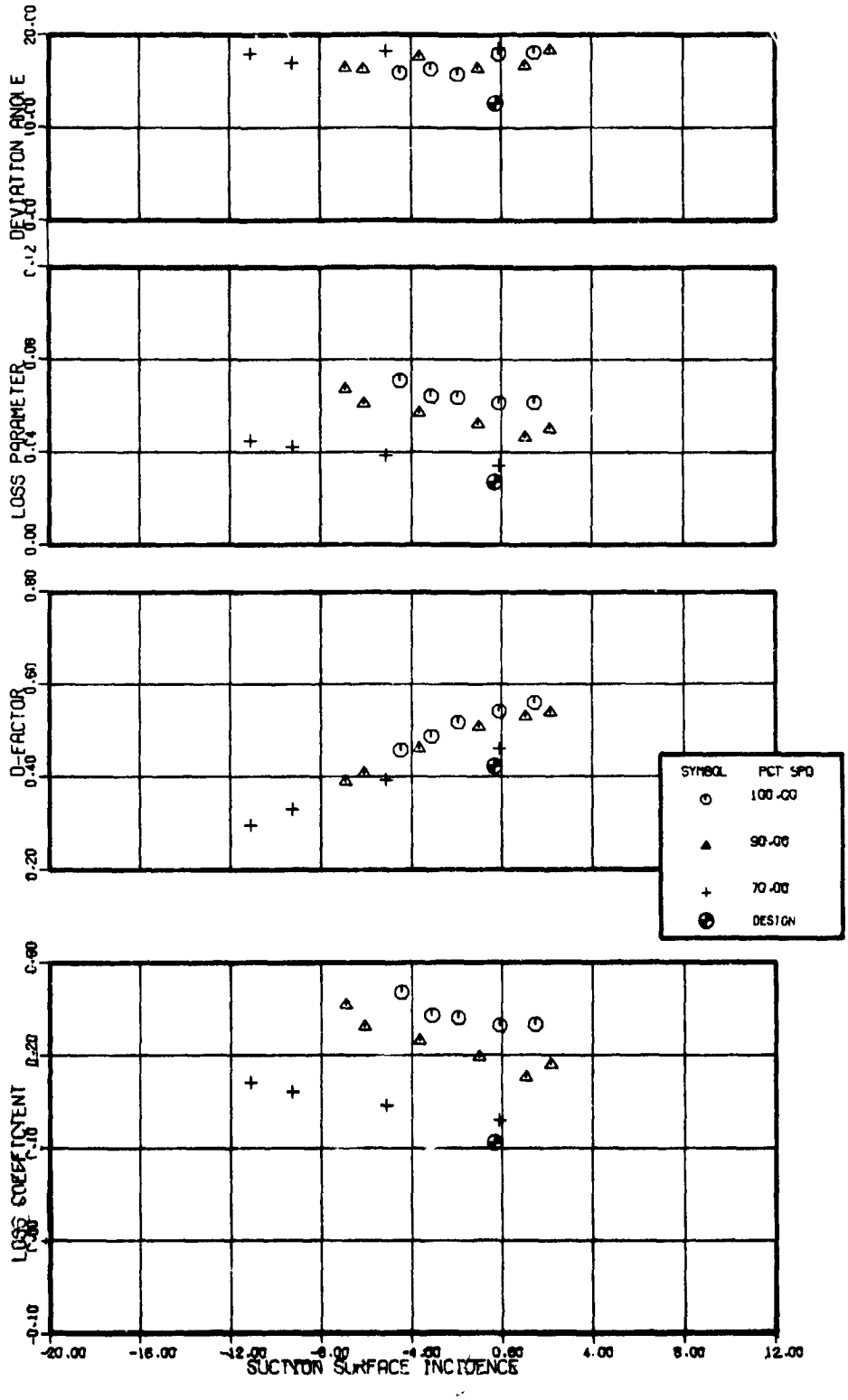

Figure 66. -Stator blade element performance, 90 percent span from tip, Test 2.

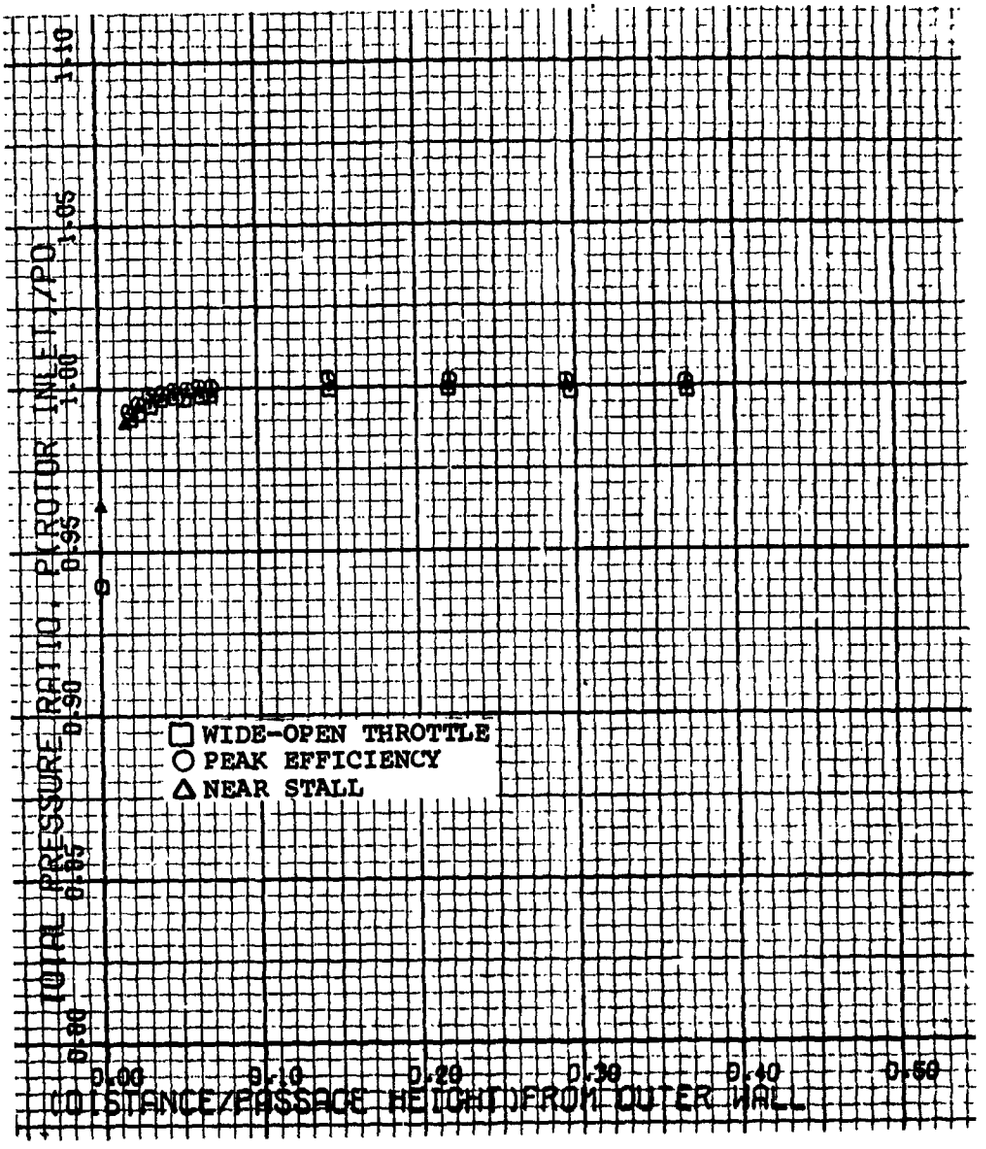

Figure 67. -Rotor inlet outerwall boundary layer total pressure profile, 70 percent design speed, Test 2.

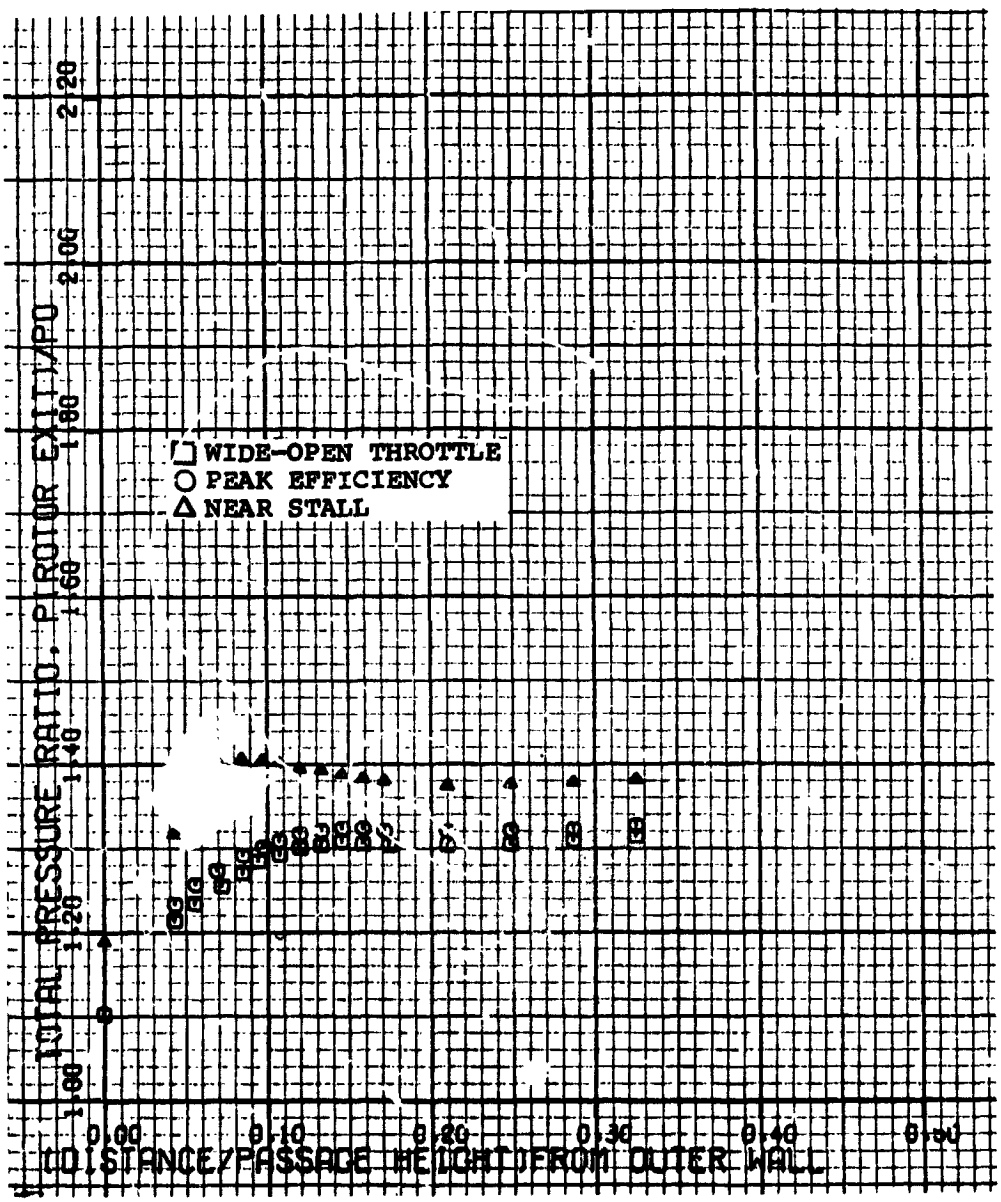

Figure 68. -Rotor exit outerwall boundary layer total pressure profile, 70 percent design speed, Test 2.

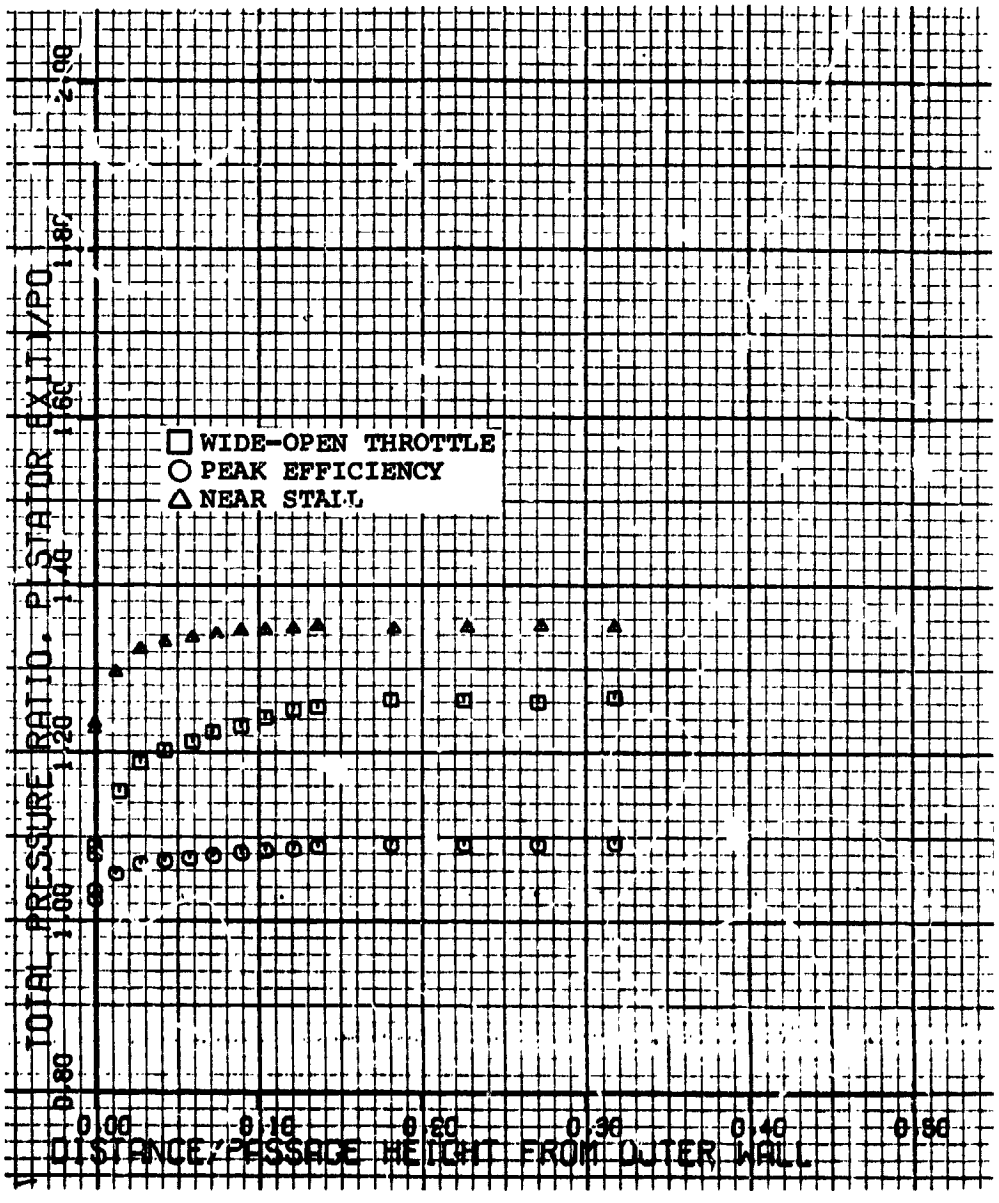

Figure 69. --Stator exit outerwall boundary layer total pressure profile, 70 percent design speed, Test 2.

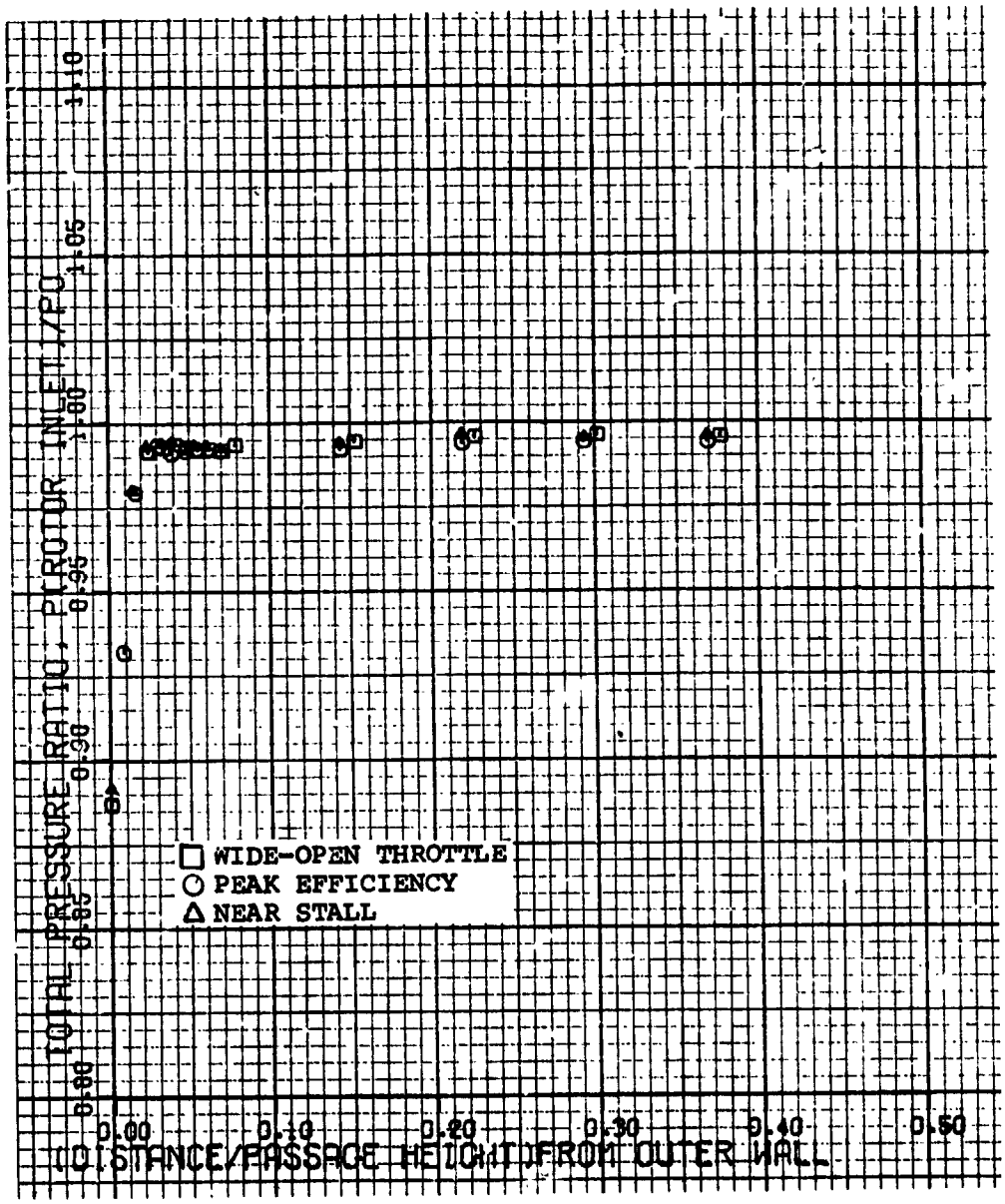

Figure 70. -Rotor inlet outerwall boundary layer total pressure profile, 90 percent design speed, Test 2.

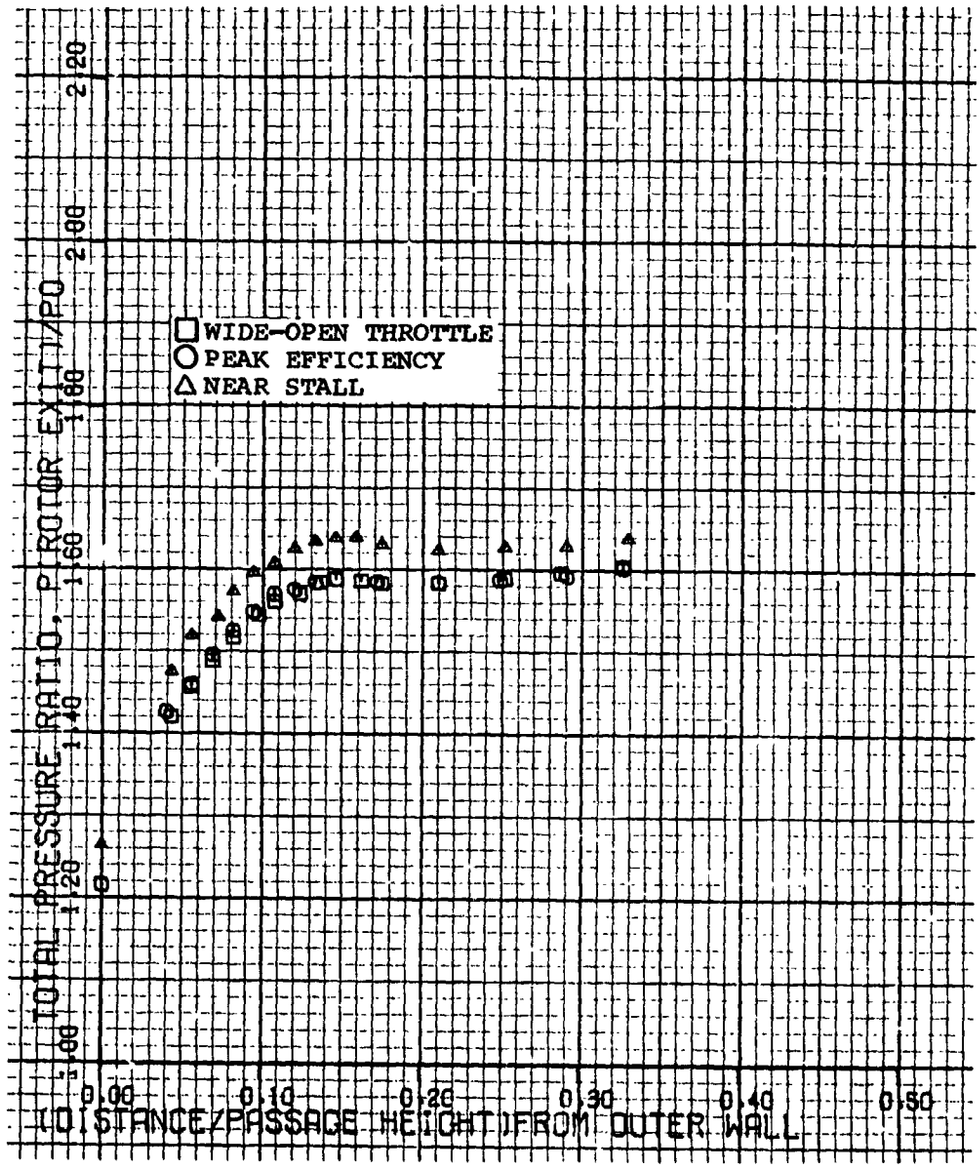

Figure 71. -Rotor exit outerwall boundary layer total pressure profile, 90 percent design speed, Test 2.

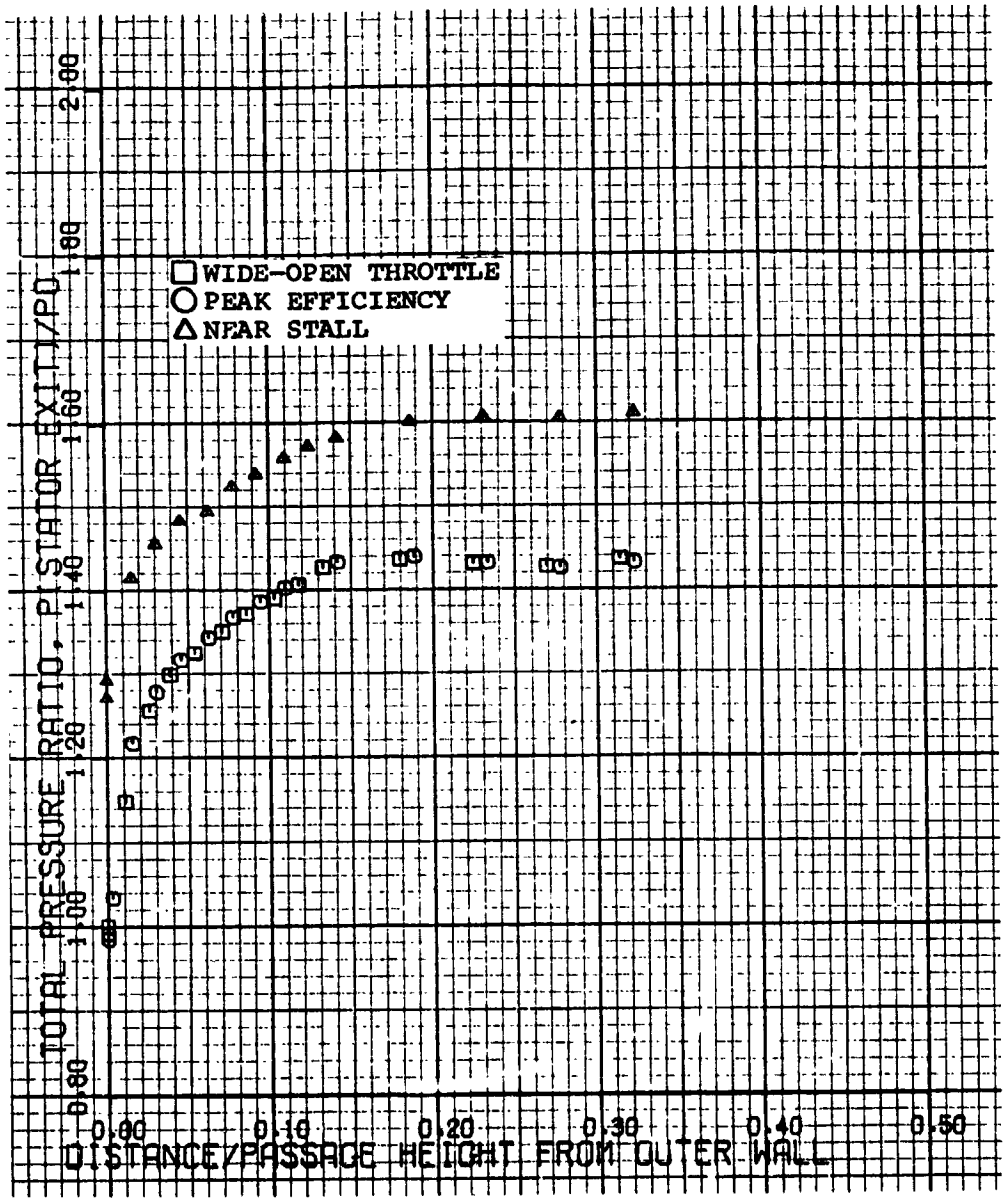

Figure 72. -Stator exit outerwall boundary layer total pressure profile, 90 percent design speed, Test 2.

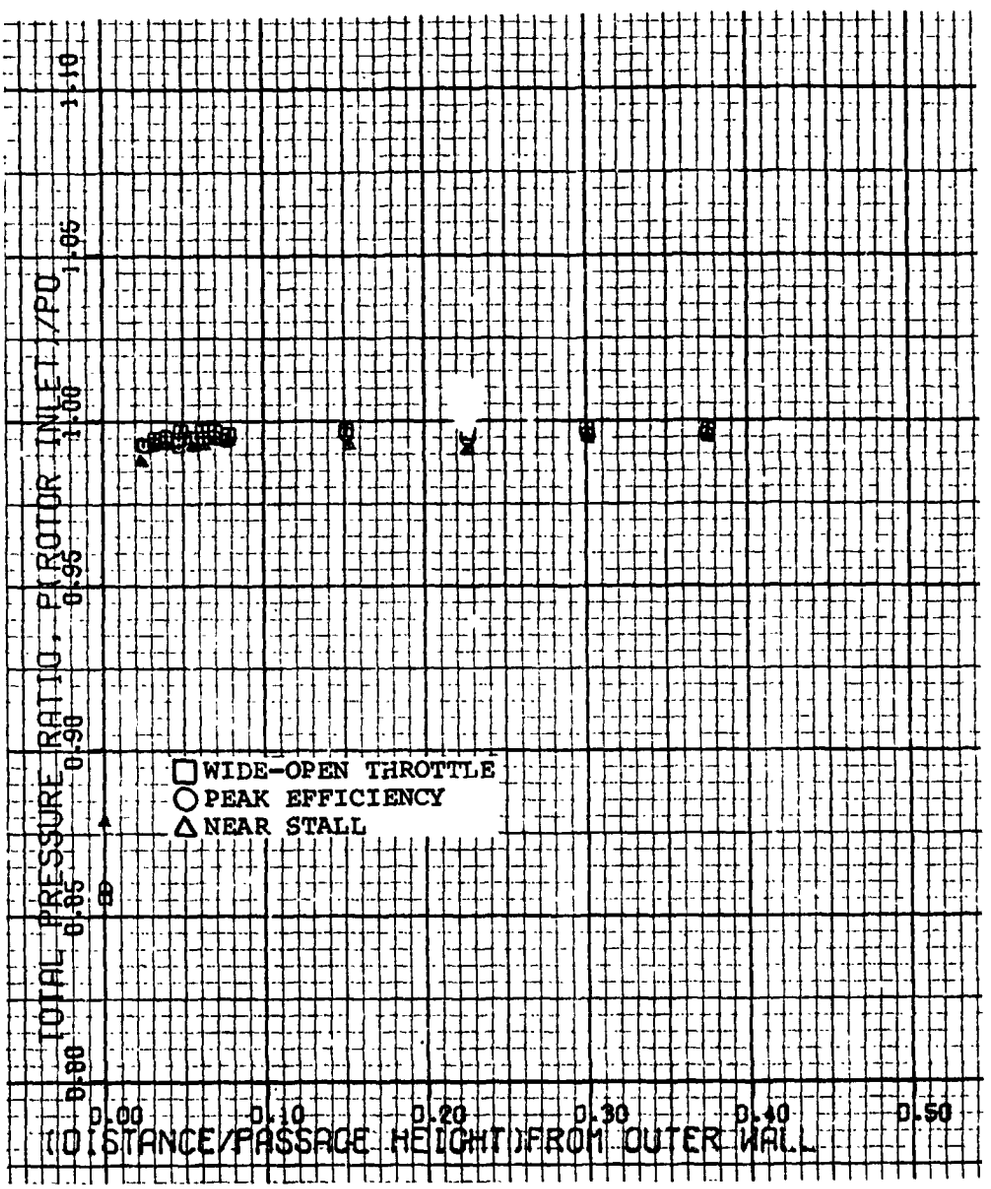

Figure 73. -Rotor inlet outerwall boundary layer total pressure profile, 100 percent design speed, Test 2.

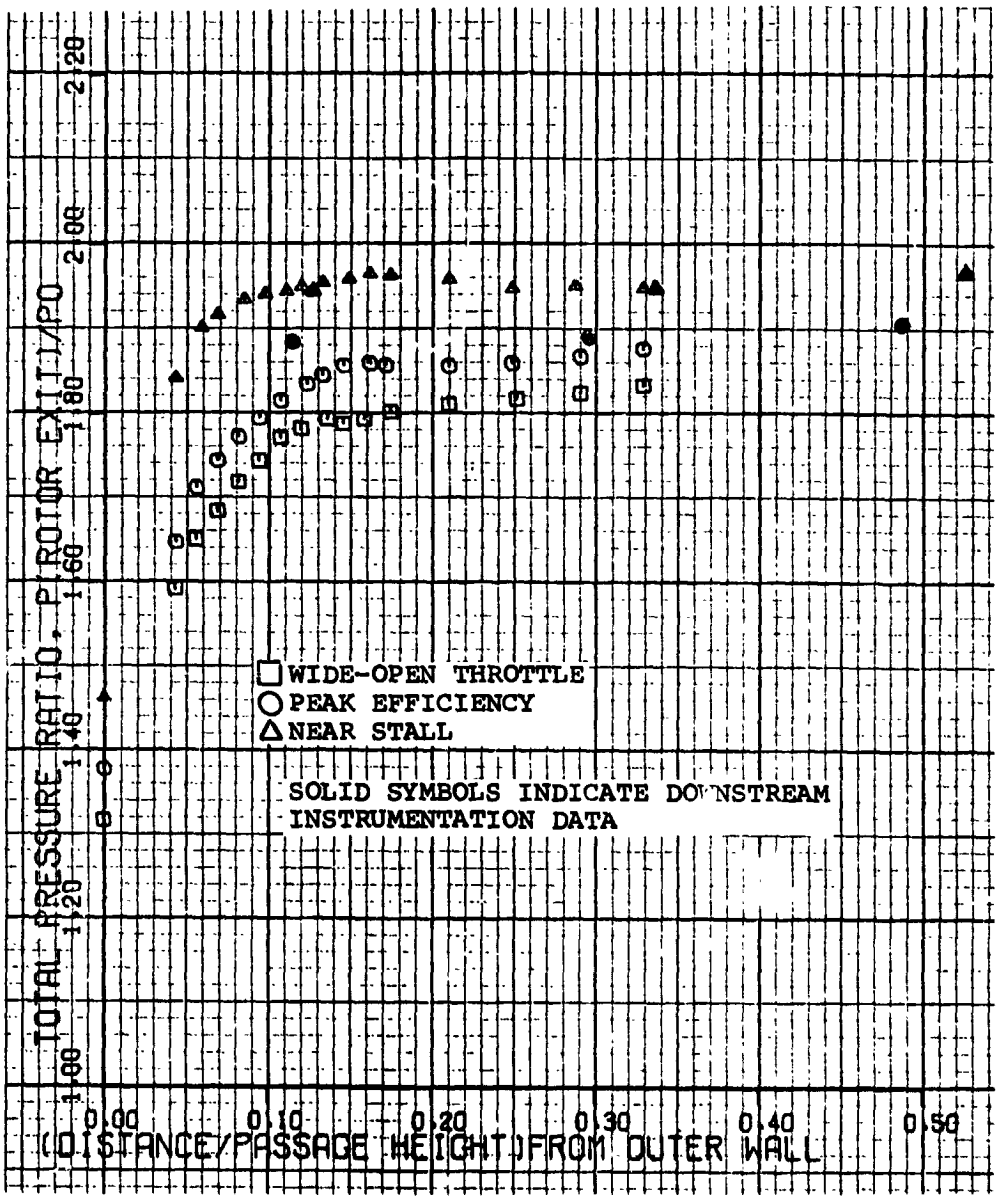

Figure 74. -Rotor exit outerwall boundary layer total pressure profile, 100 percent design speed, Test 2.

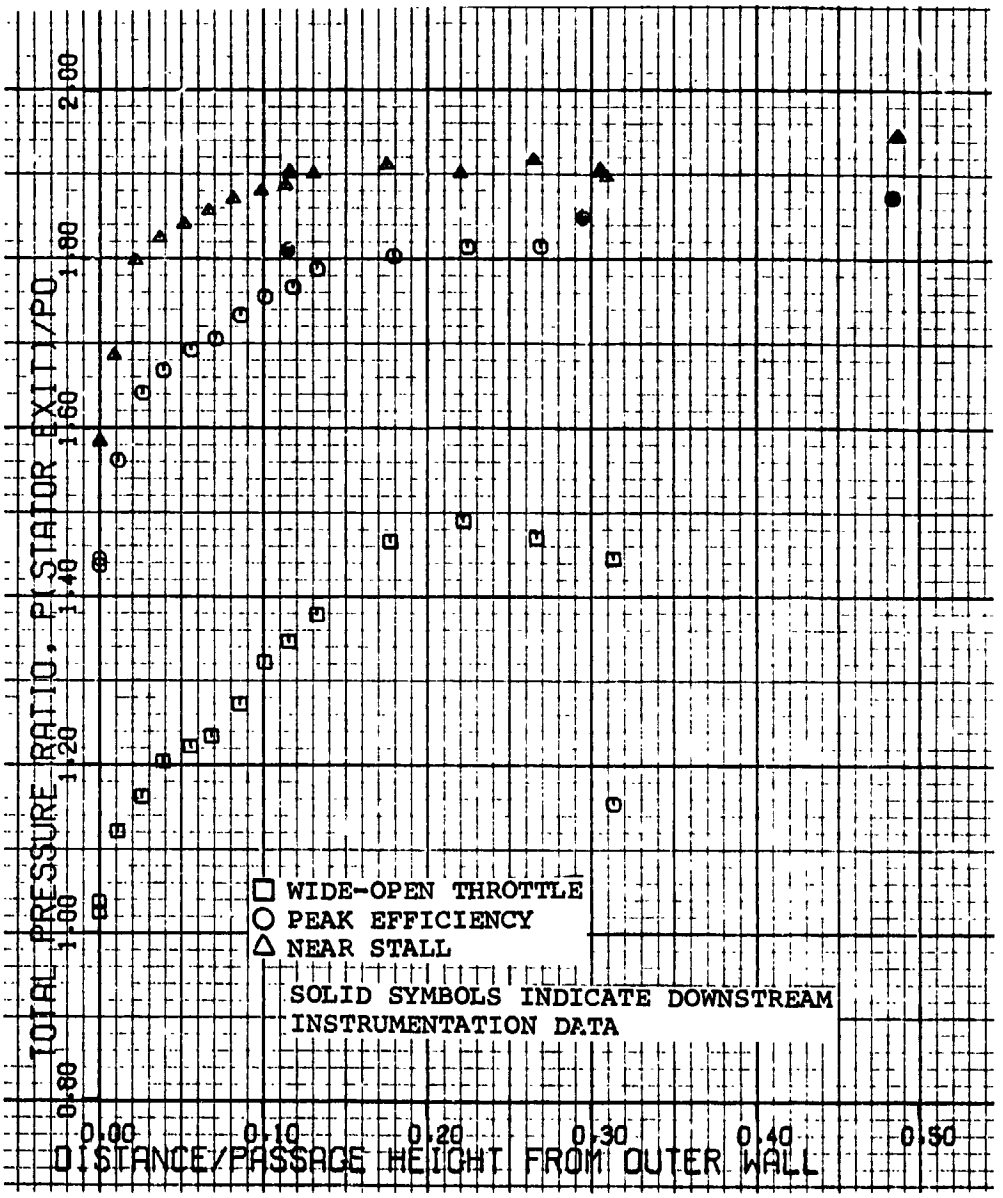

Figure 75. -Stator exit outerwall boundary layer total pressure profile, 100 percent design speed, Test 2.

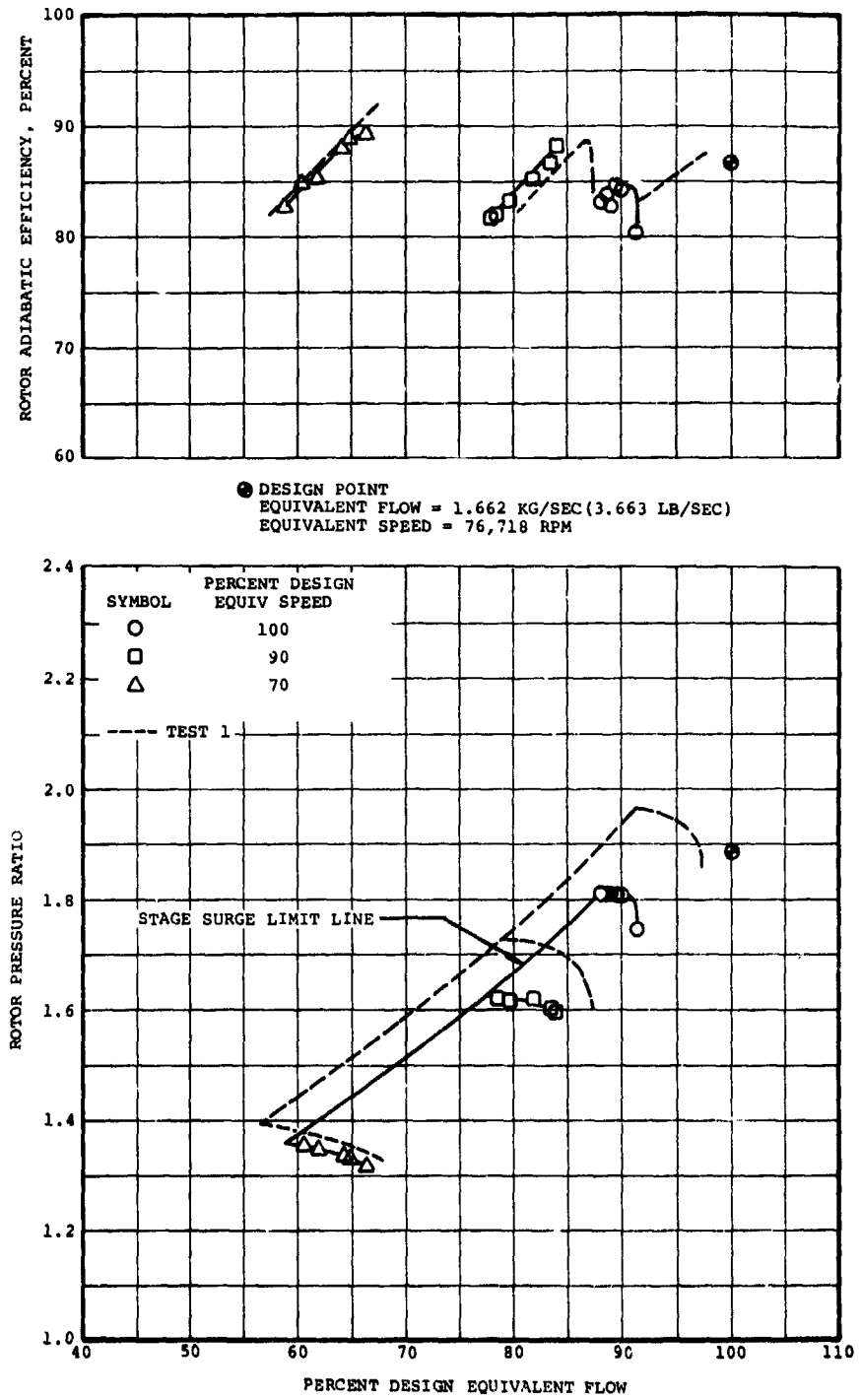

Figure 76. -Test 3 - rotor performance.

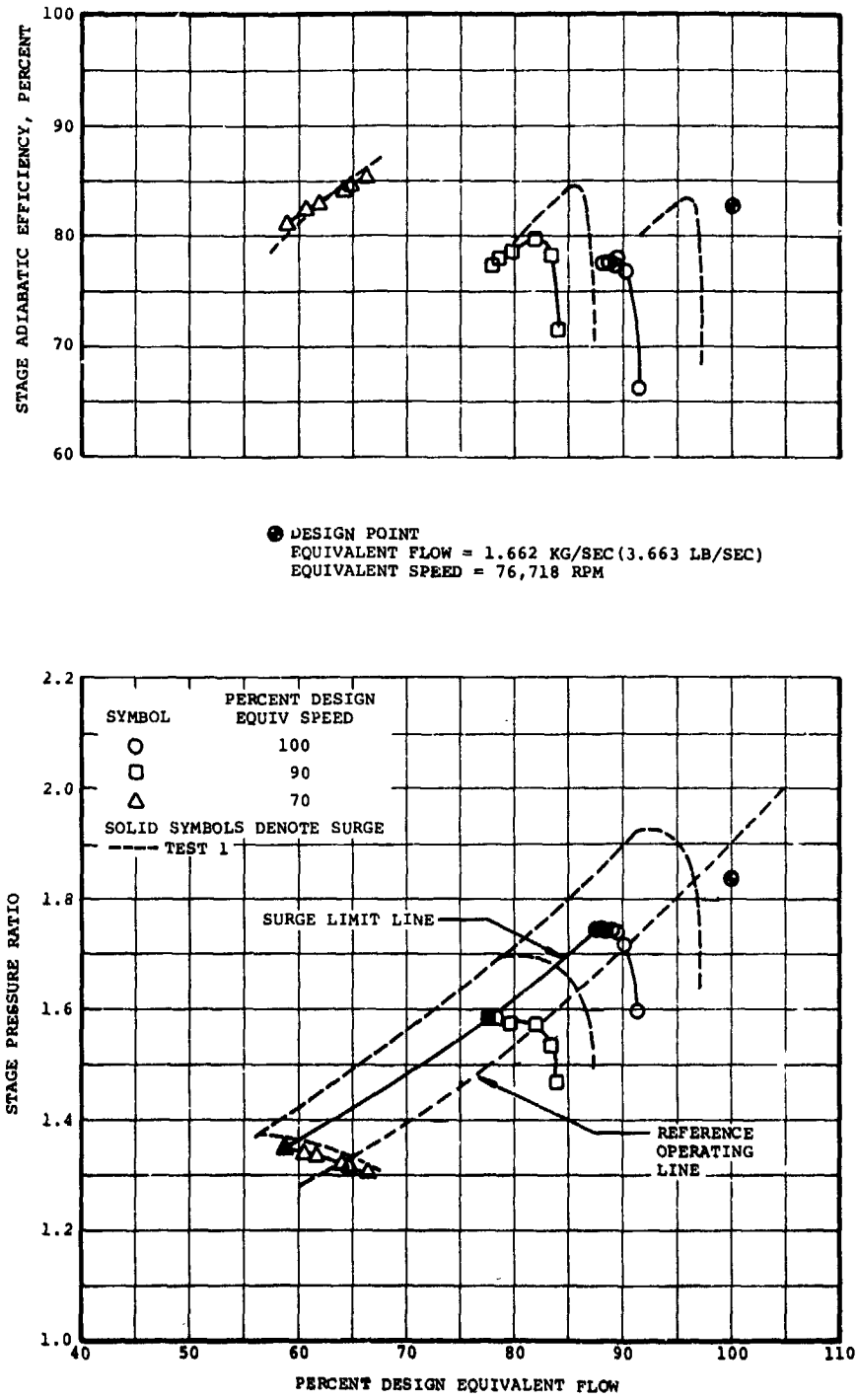

Figure 77. -Test 3 - stage performance.

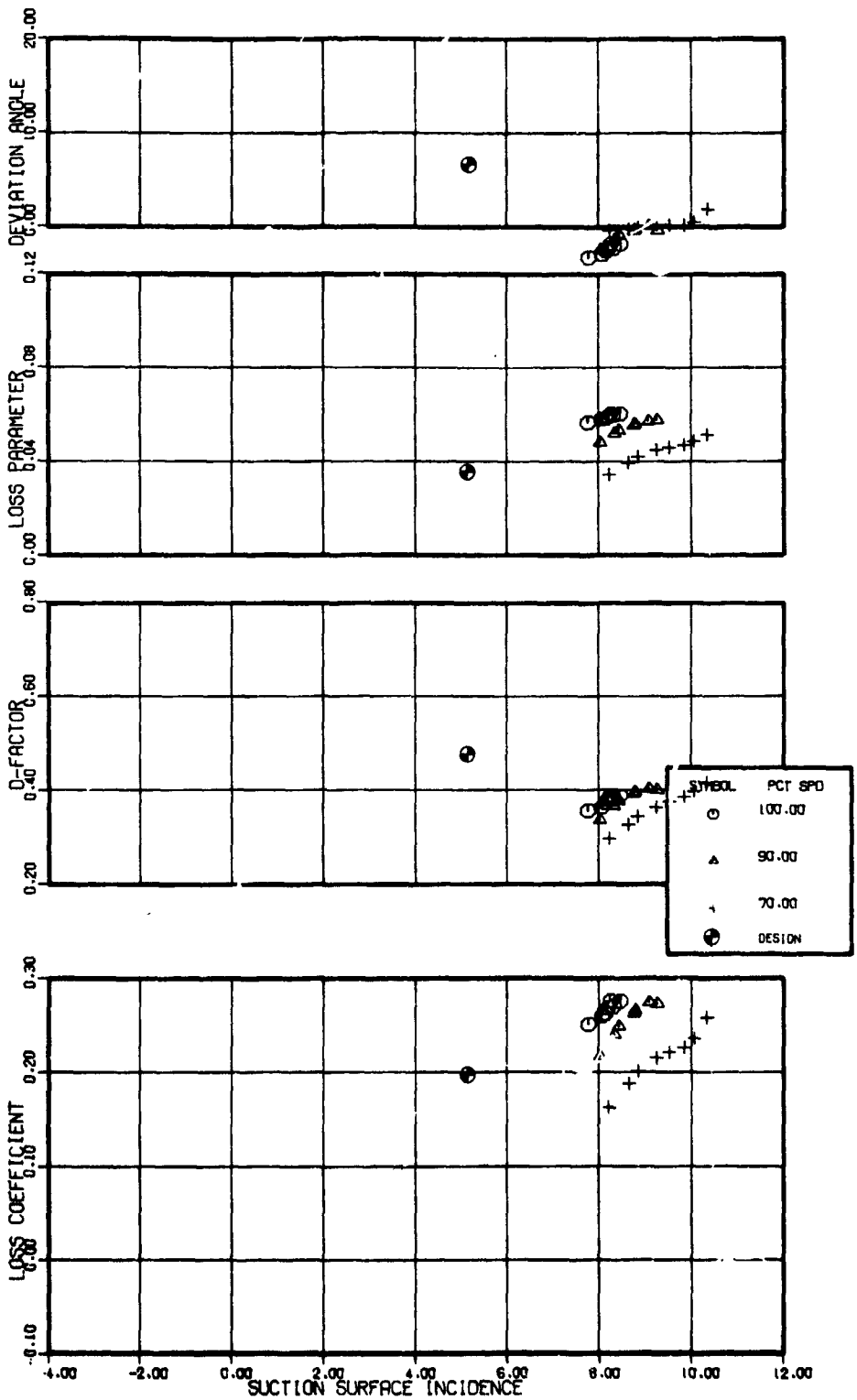

Figure 78. -Rotor blade element performance, 10 percent span from tip, Test 3.

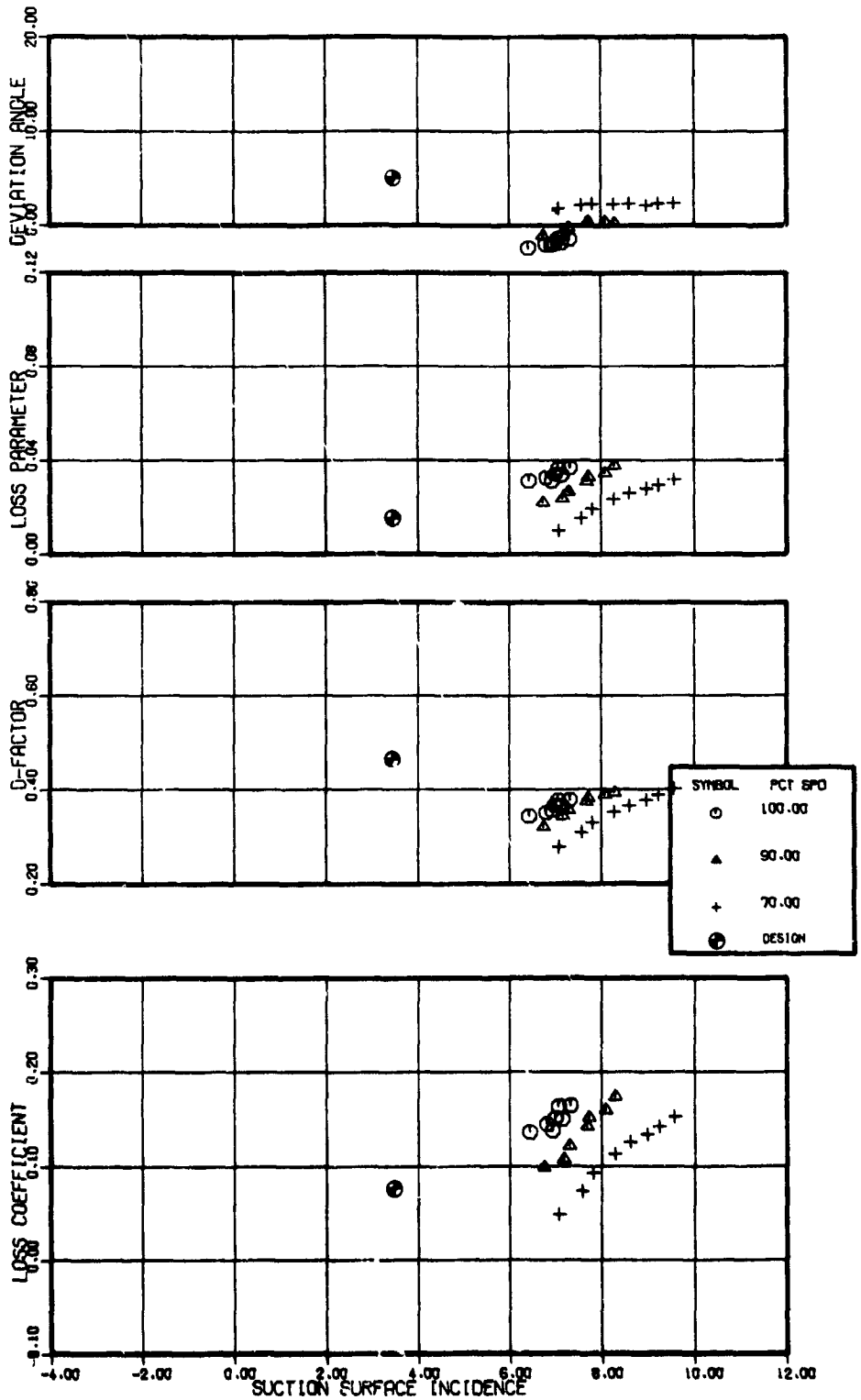

Figure 79. -Rotor blade element performance, 30 percent span from tip, Test 3.

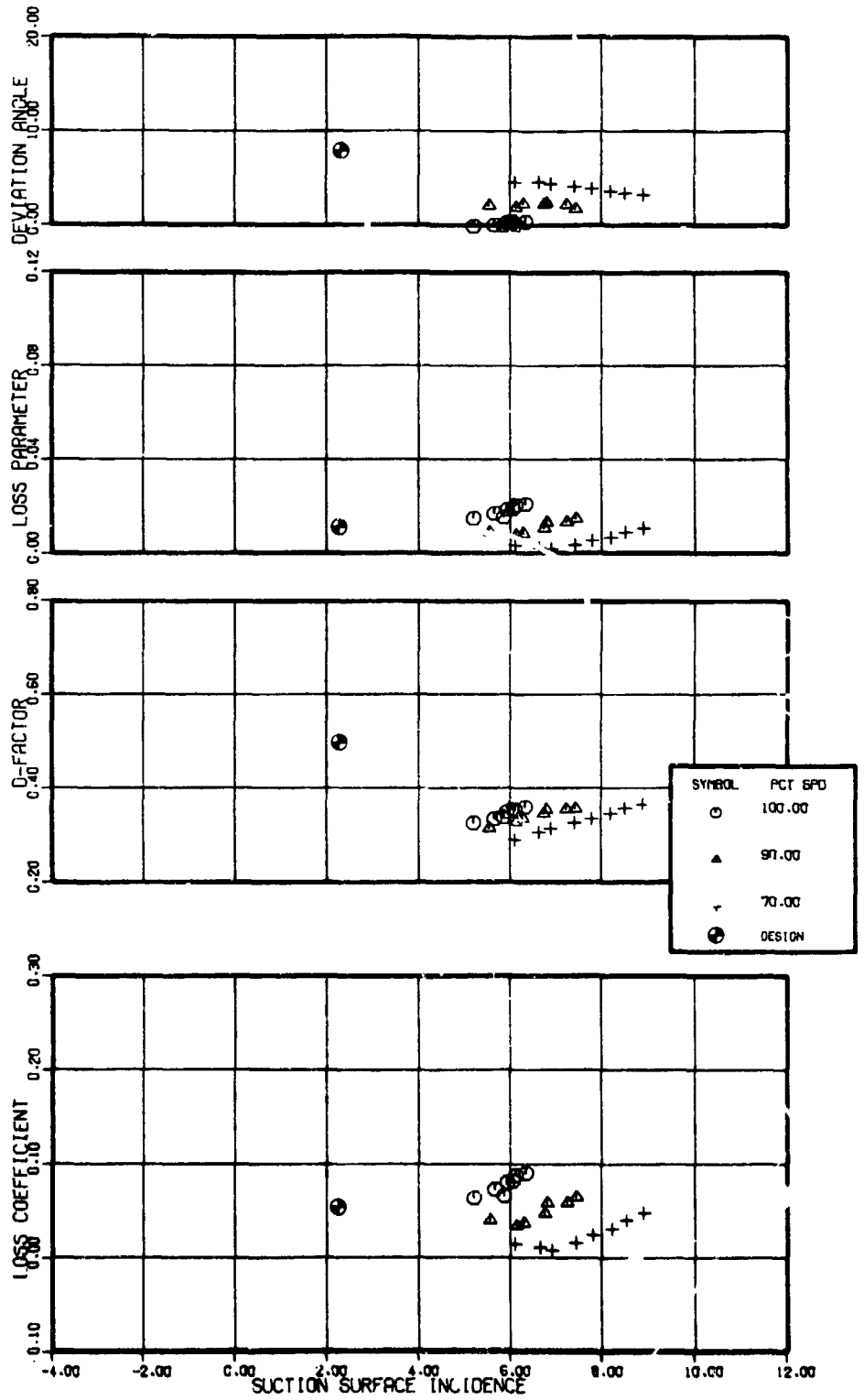

Figure 80. -Rotor blade element performance, 50 percent span from tip, Test 3.

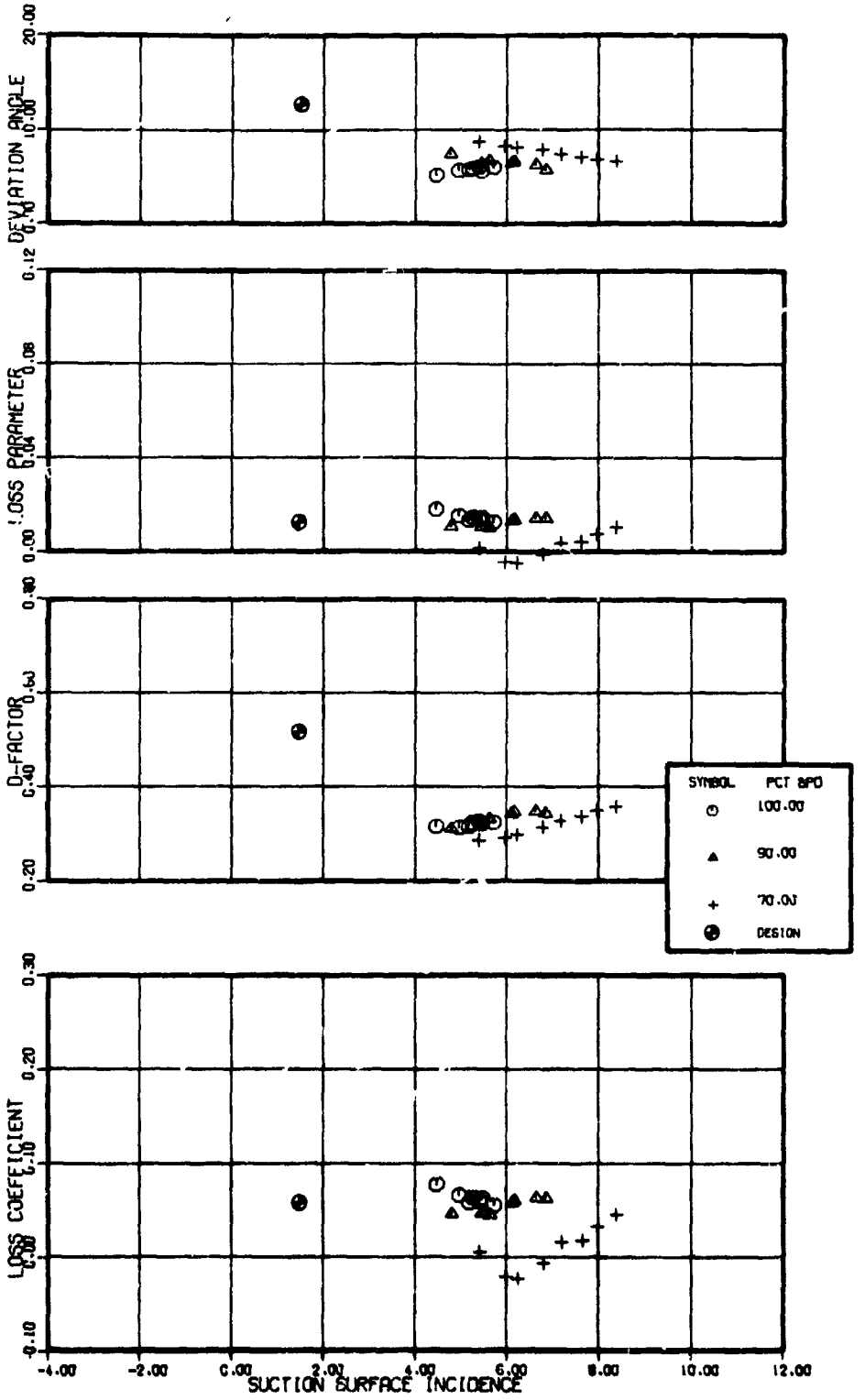

Figure 81. -Rotor blade element performance, 70 percent span from tip, Test 3.

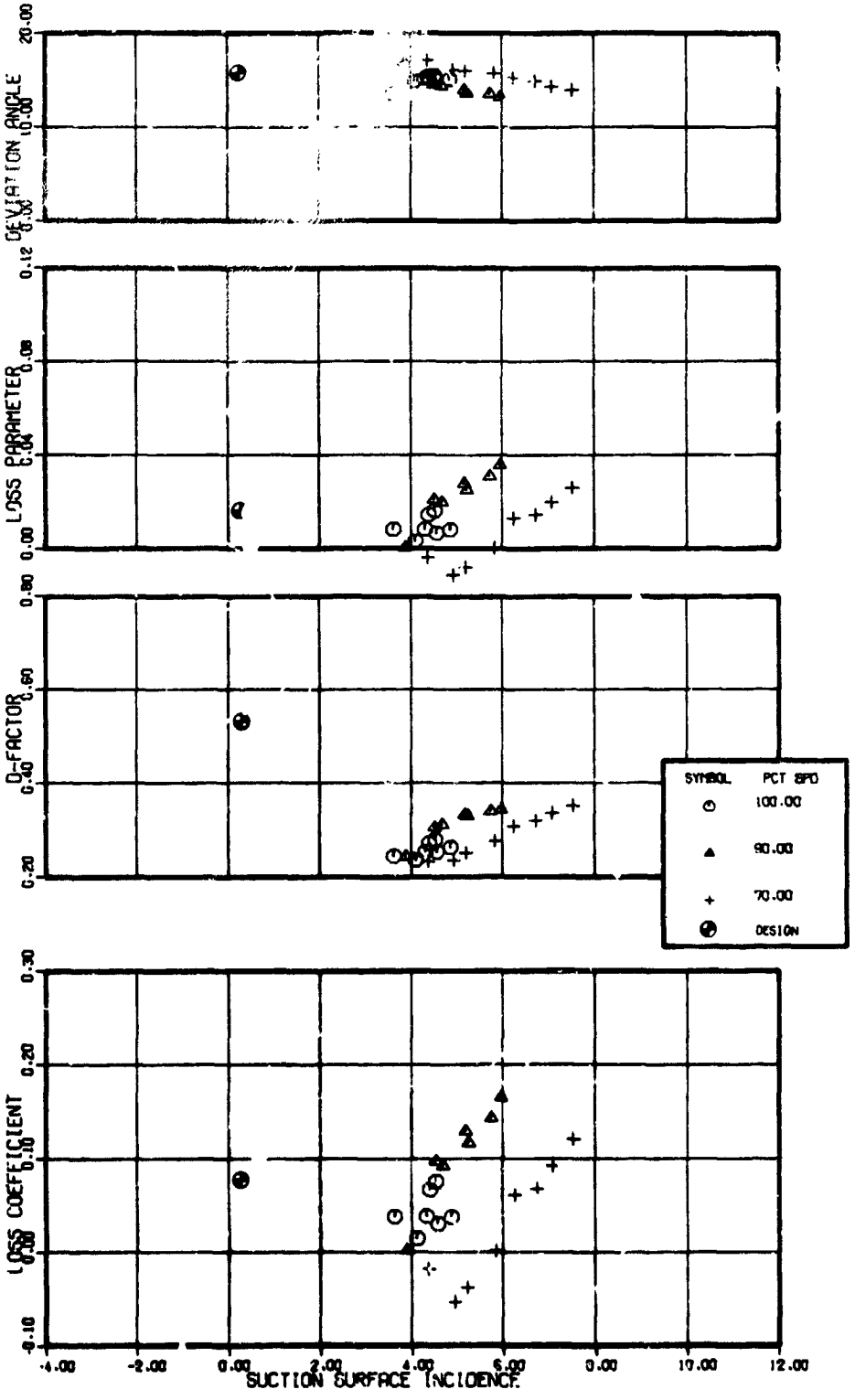

Figure 82. -Rotor blade element performance, 90 percent span from tip, Test 3.

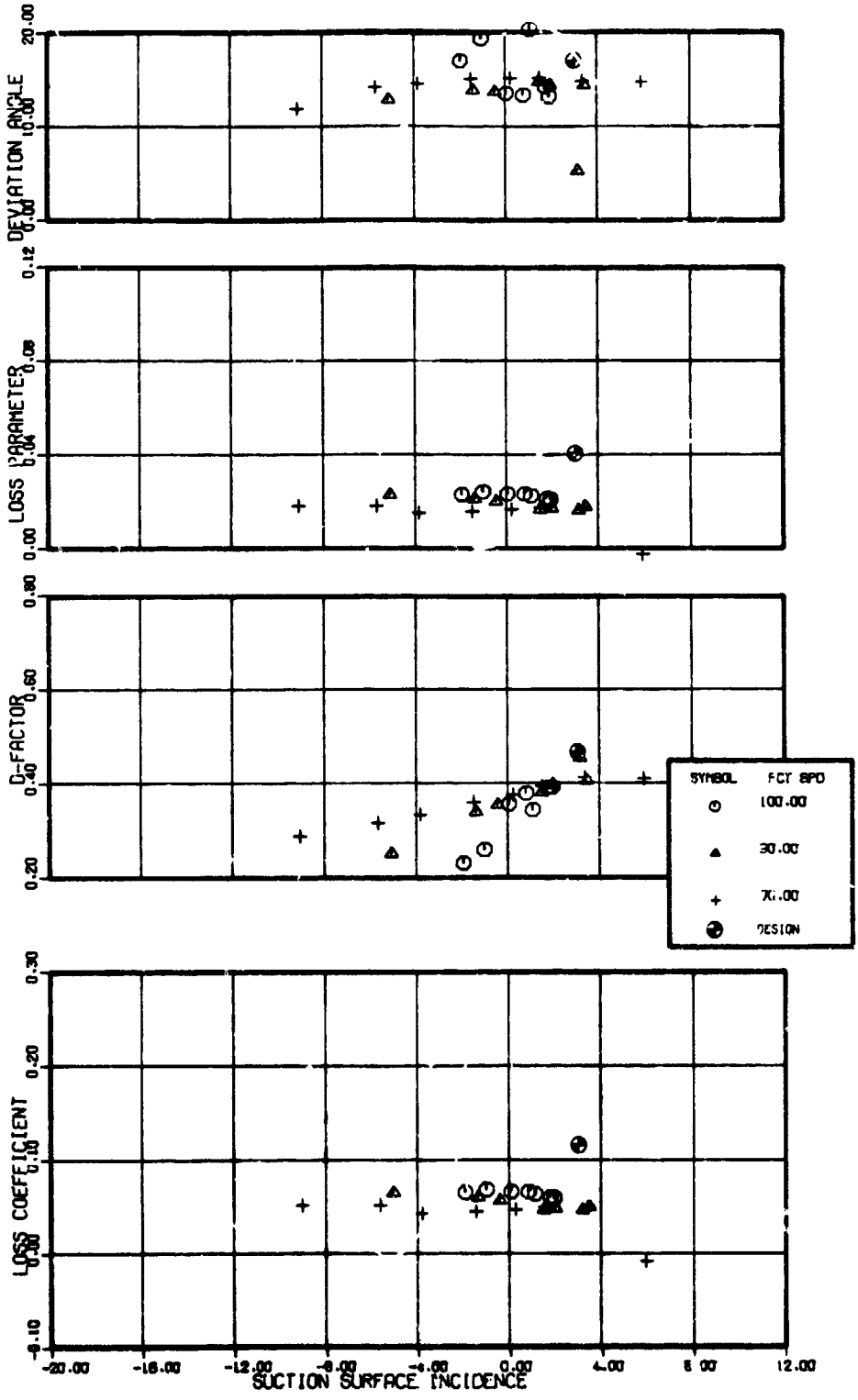

Figure 83. -Stator blade element performance, 10 percent span from tip, Test 3.

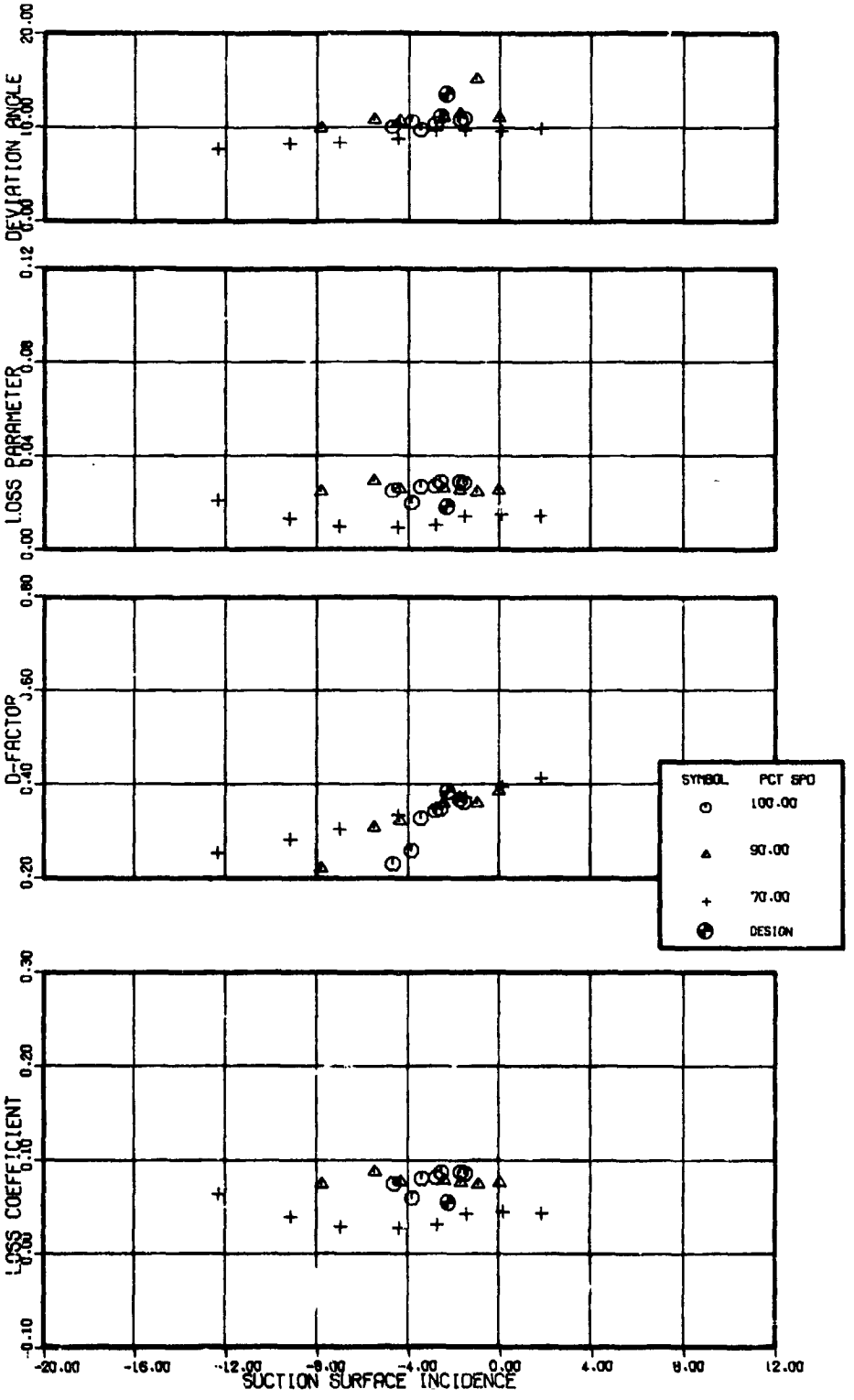

Figure 84. -Stator blade element performance, 30 percent span from tip, Test 3.

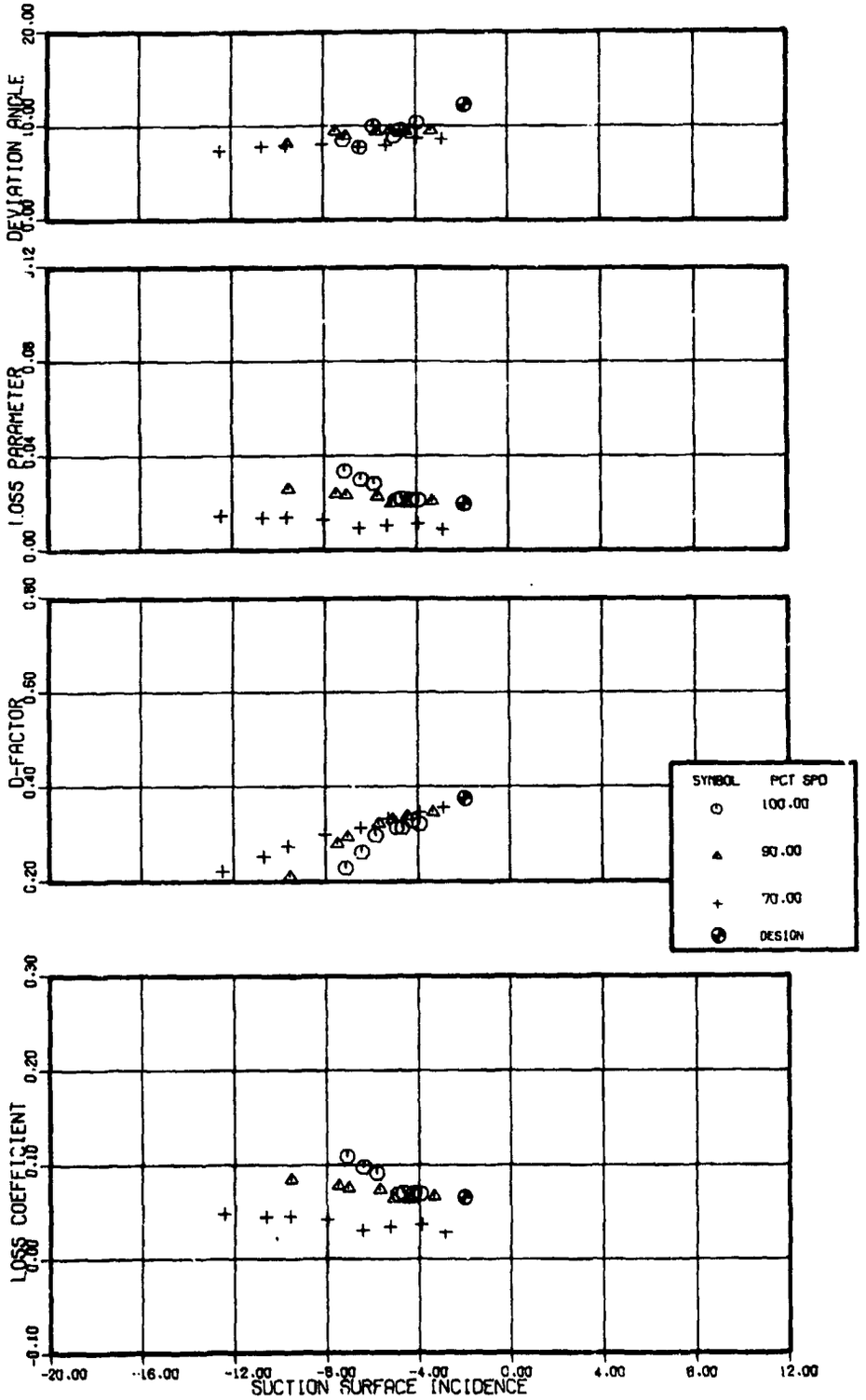

Figure 85. -Stator blade element performance, 50 percent span from tip, Test 3.

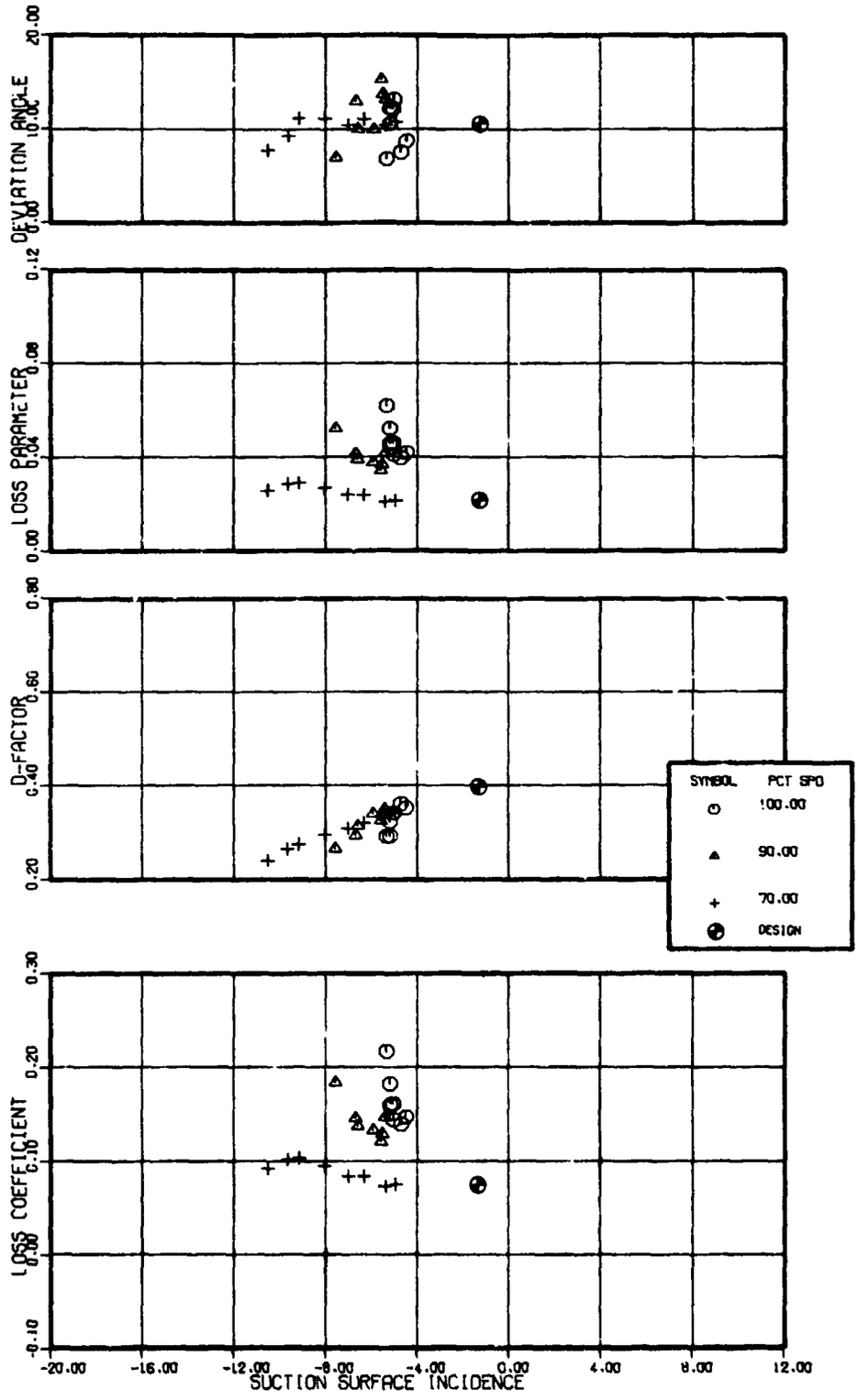

Figure 86. -Stator blade element performance, 70 percent span from tip, Test 3.

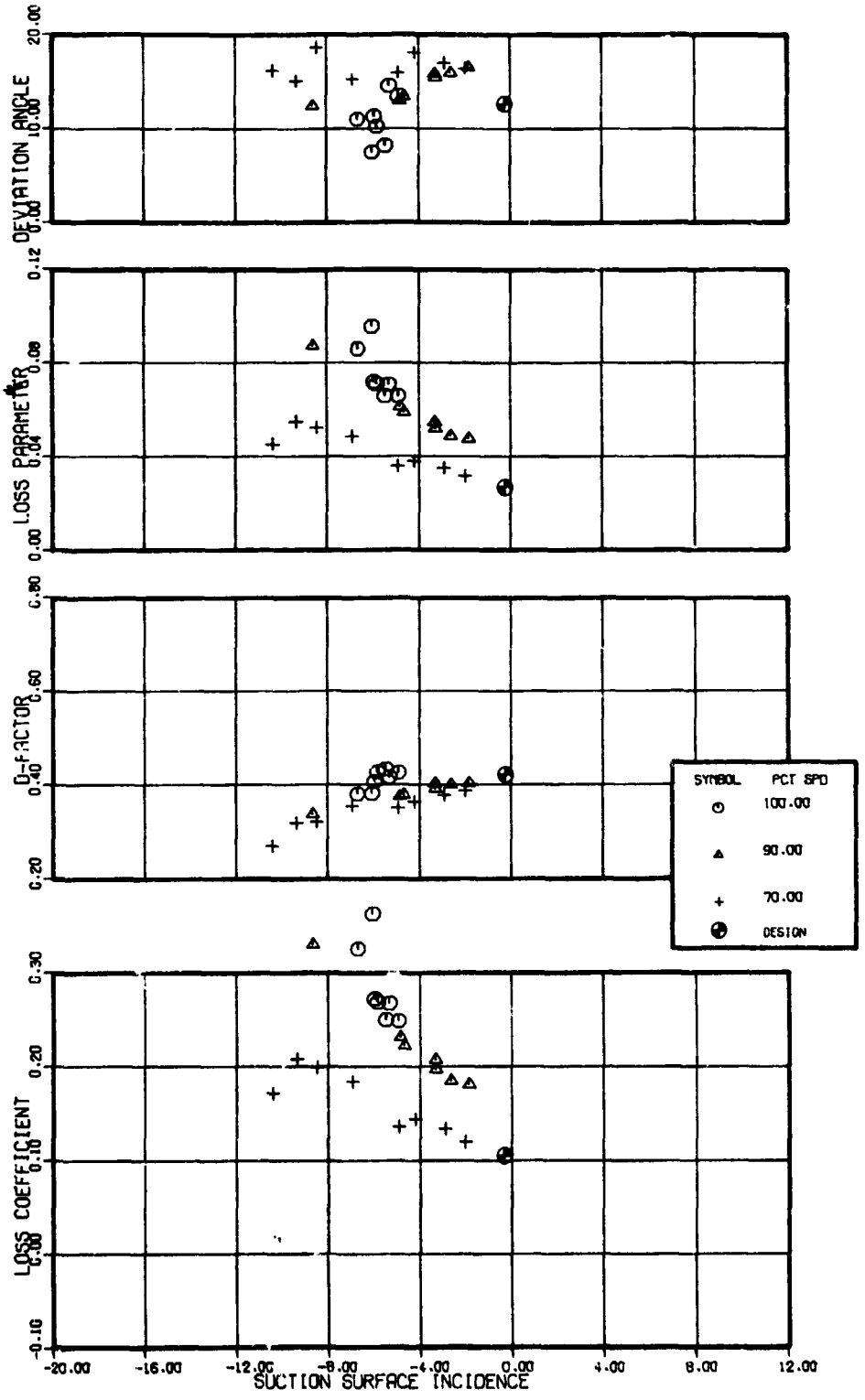

Figure 87. -Stator blade element performance, 90 percent span from tip, Test 3.

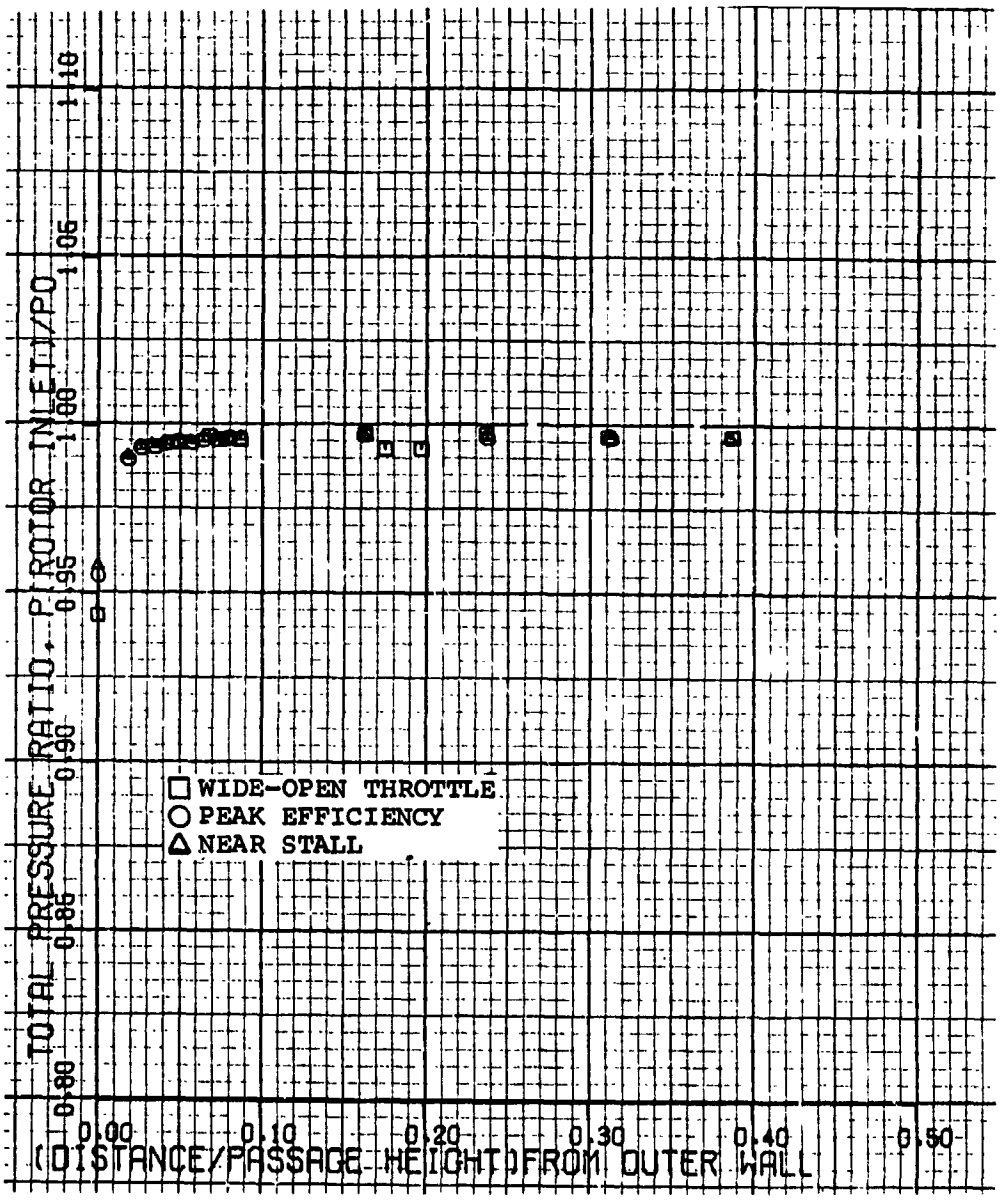

Figure 88. -Rotor inlet outerwall boundary layer total pressure profile, 70 percent design speed, Test 3.

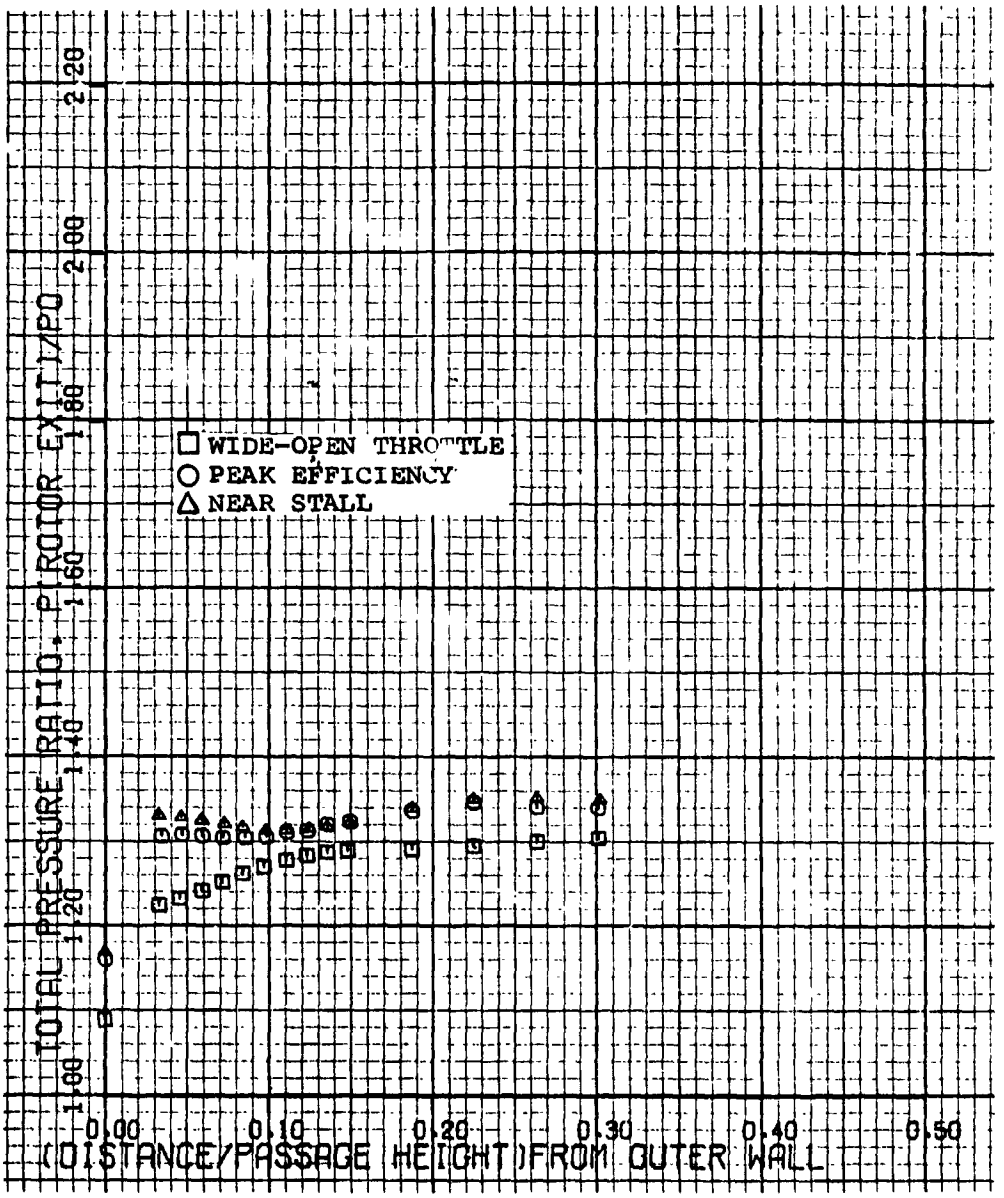

Figure 89. -Rotor exit outerwall boundary layer total pressure profile, 70 percent design speed, Test 3.

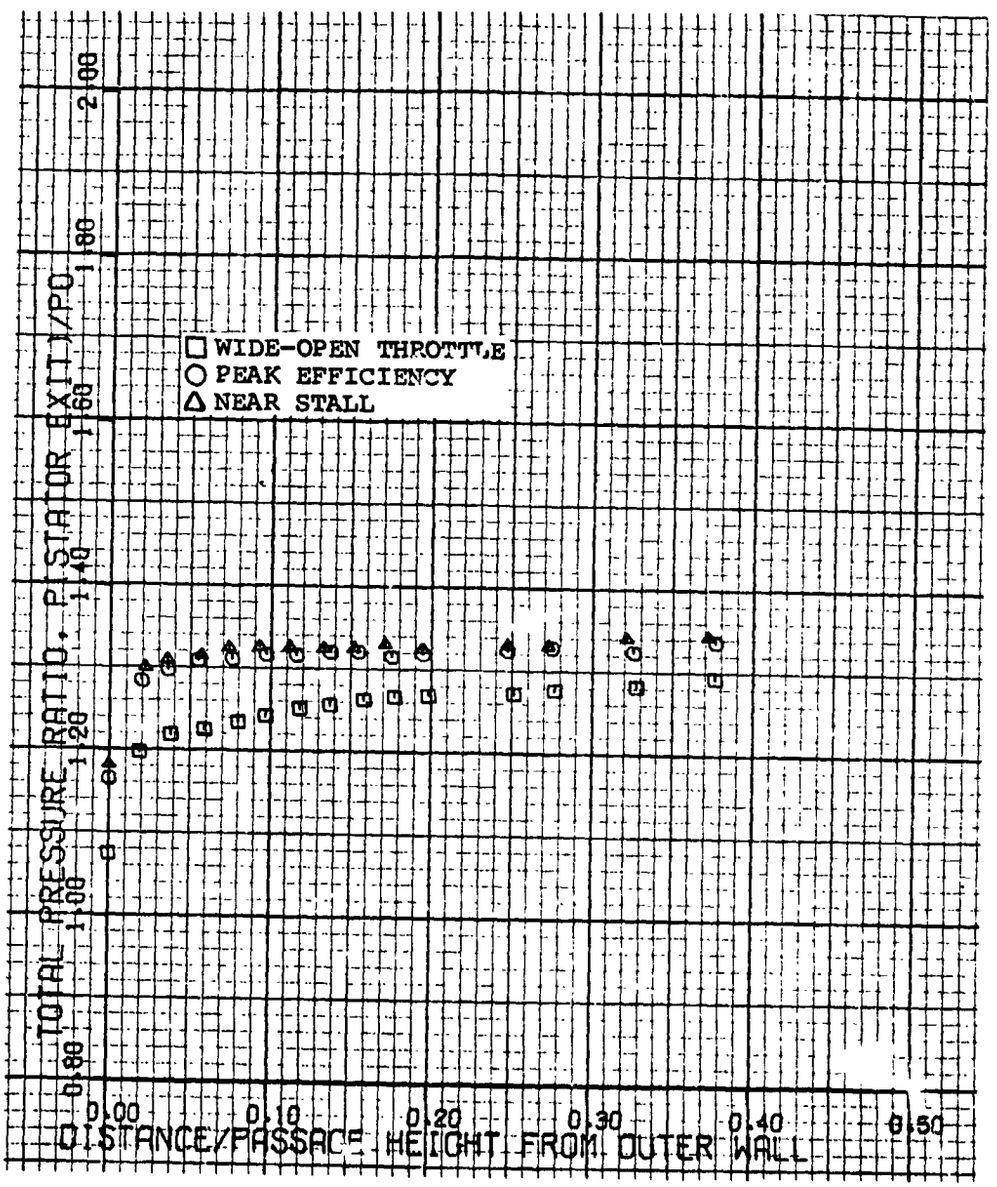

Figure 90. -Stator exit outerwall boundary layer total pressure profile, 70 percent design speed, Test 3.

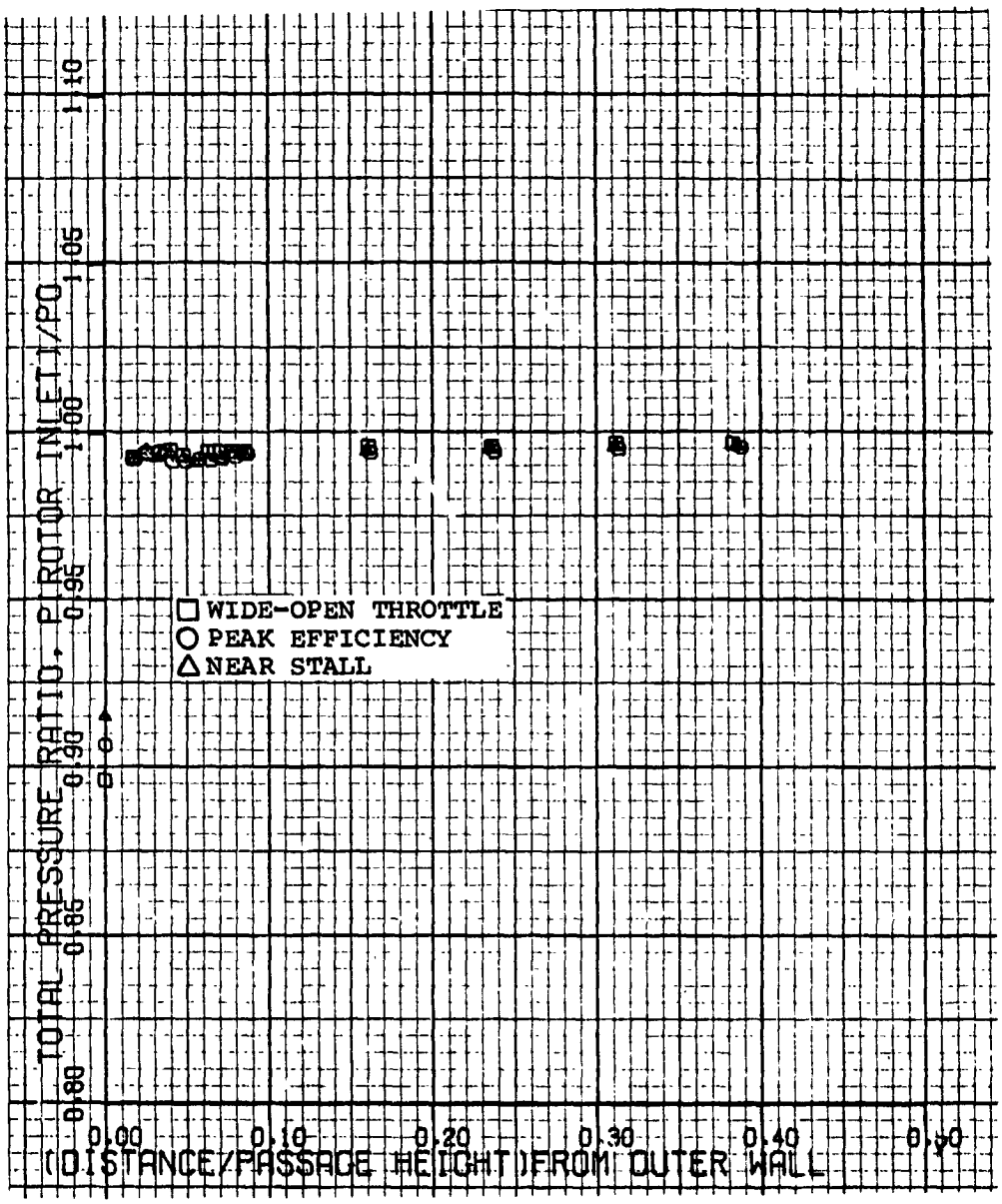

Figure 91. -Rotor inlet outerwall boundary layer total pressure profile, 90 percent design speed, Test 3.

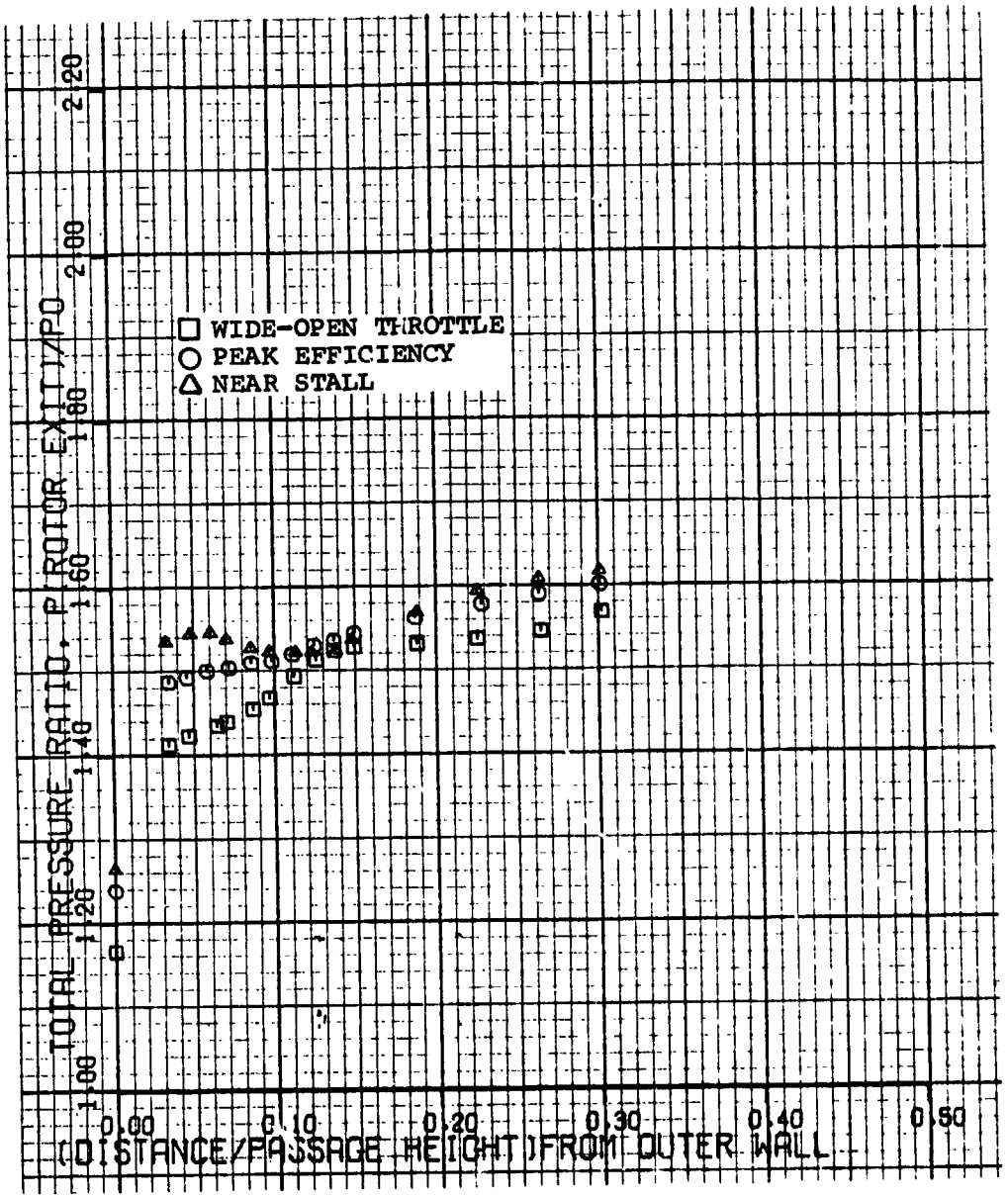

Figure 92. -Rotor exit outerwall boundary layer total pressure profile, 90 percent design speed, Test 3.

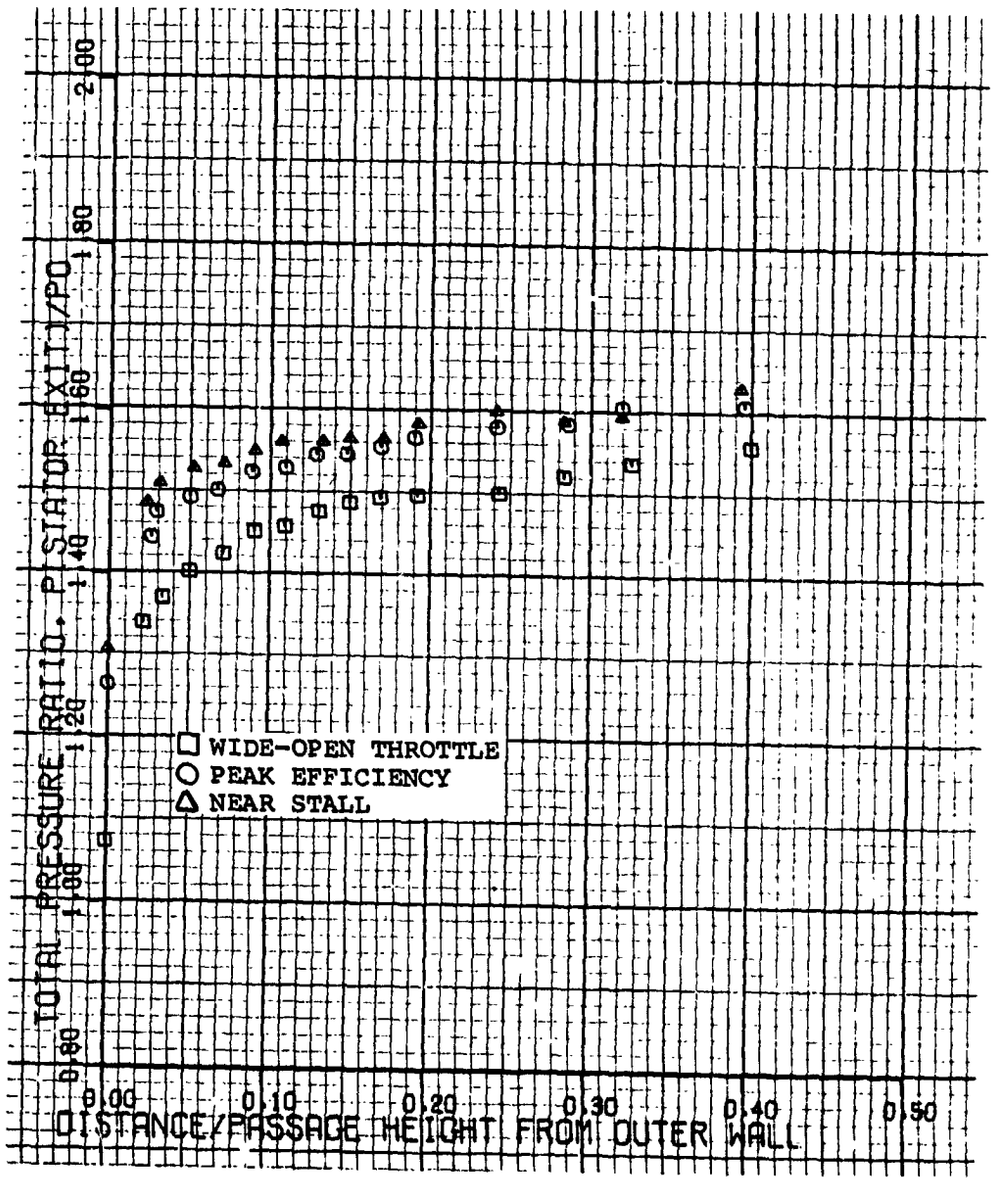

Figure 93. -Stator exit outerwall boundary layer total pressure profile, 90 percent design speed, Test 3.

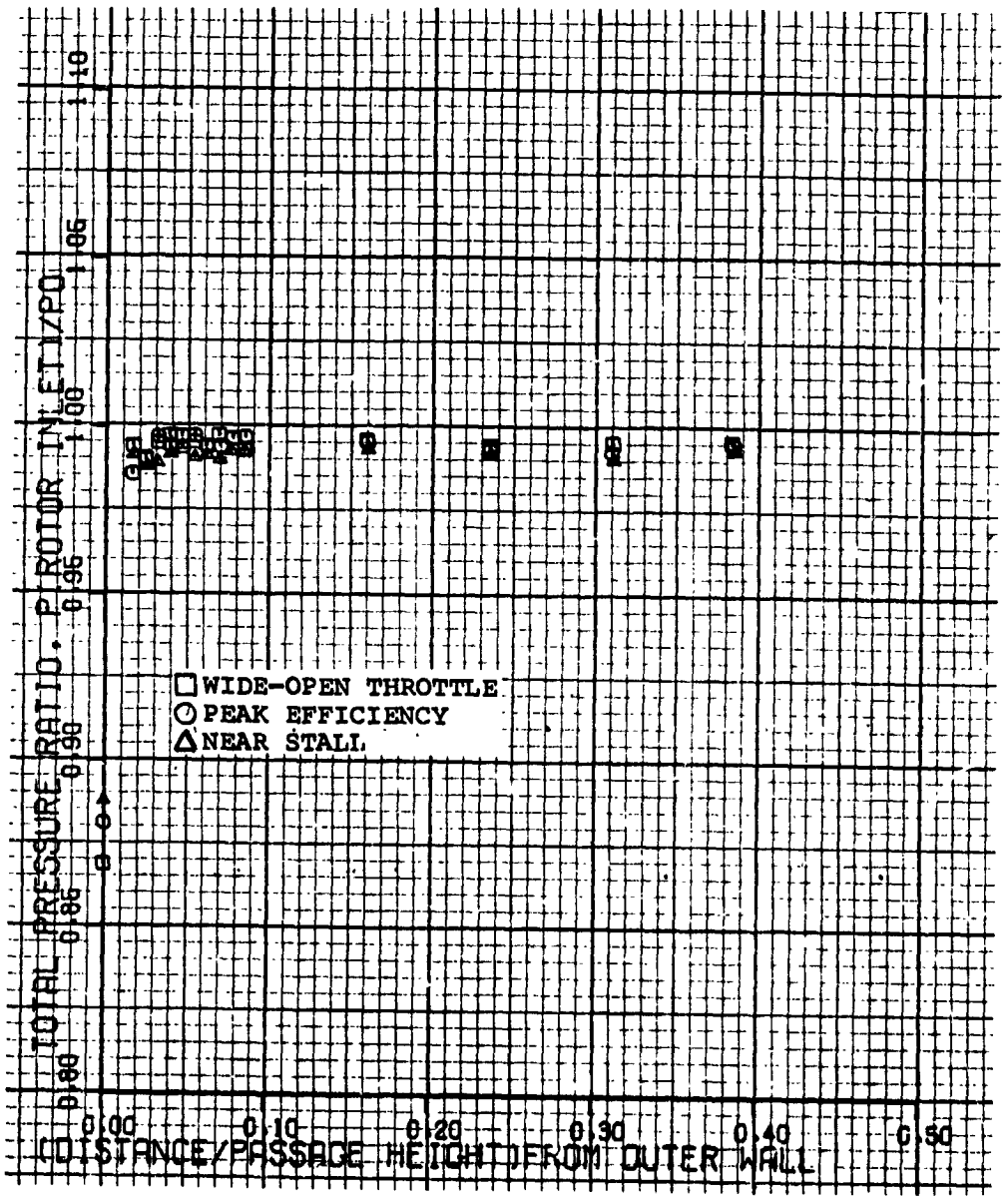

Figure 94. -Rotor inlet outerwall boundary layer total pressure profile, 100 percent design speed, Test 3.

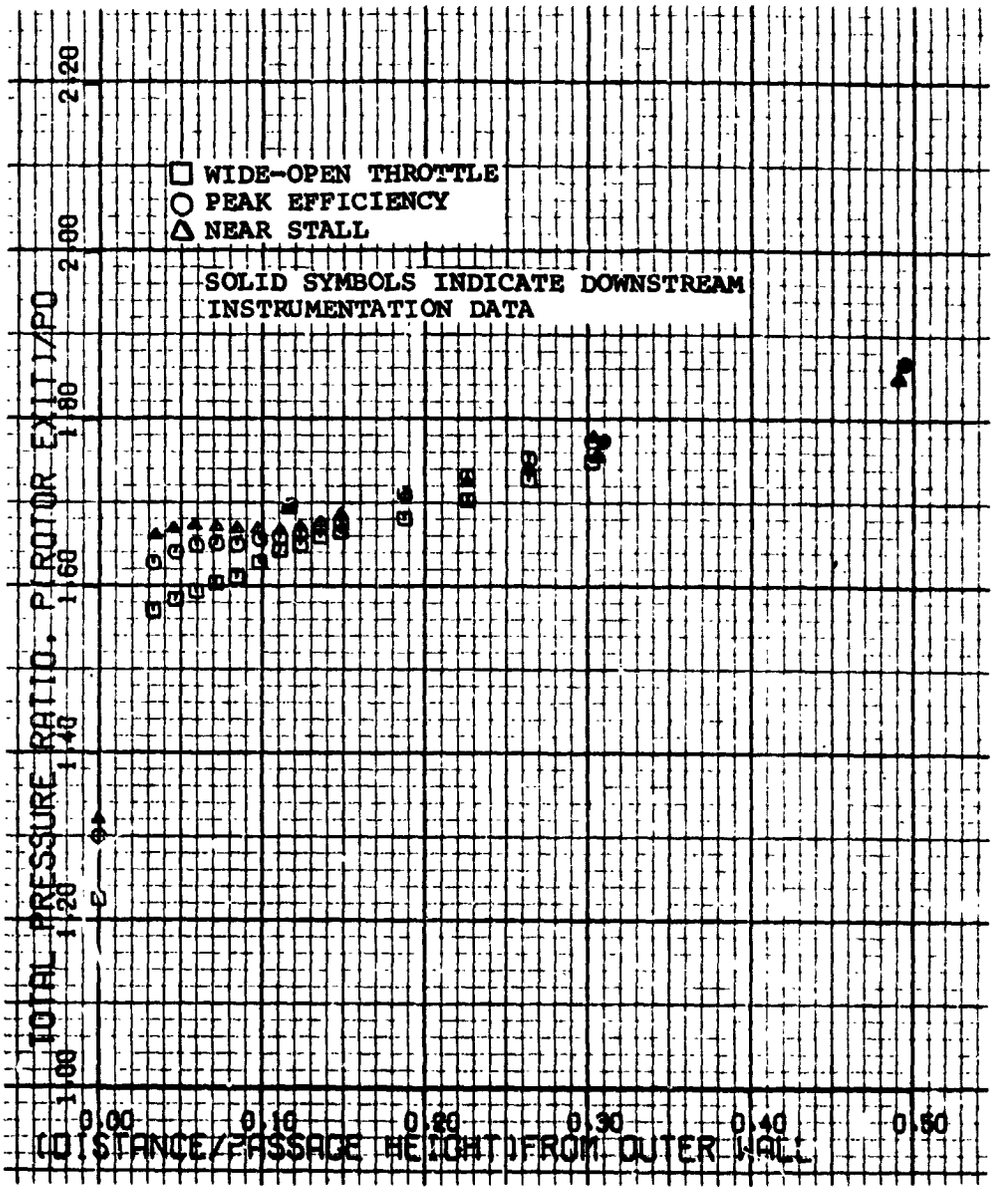

Figure 95. -Rotor exit outerwall boundary layer total pressure profile, 100 percent design speed, Test 3.

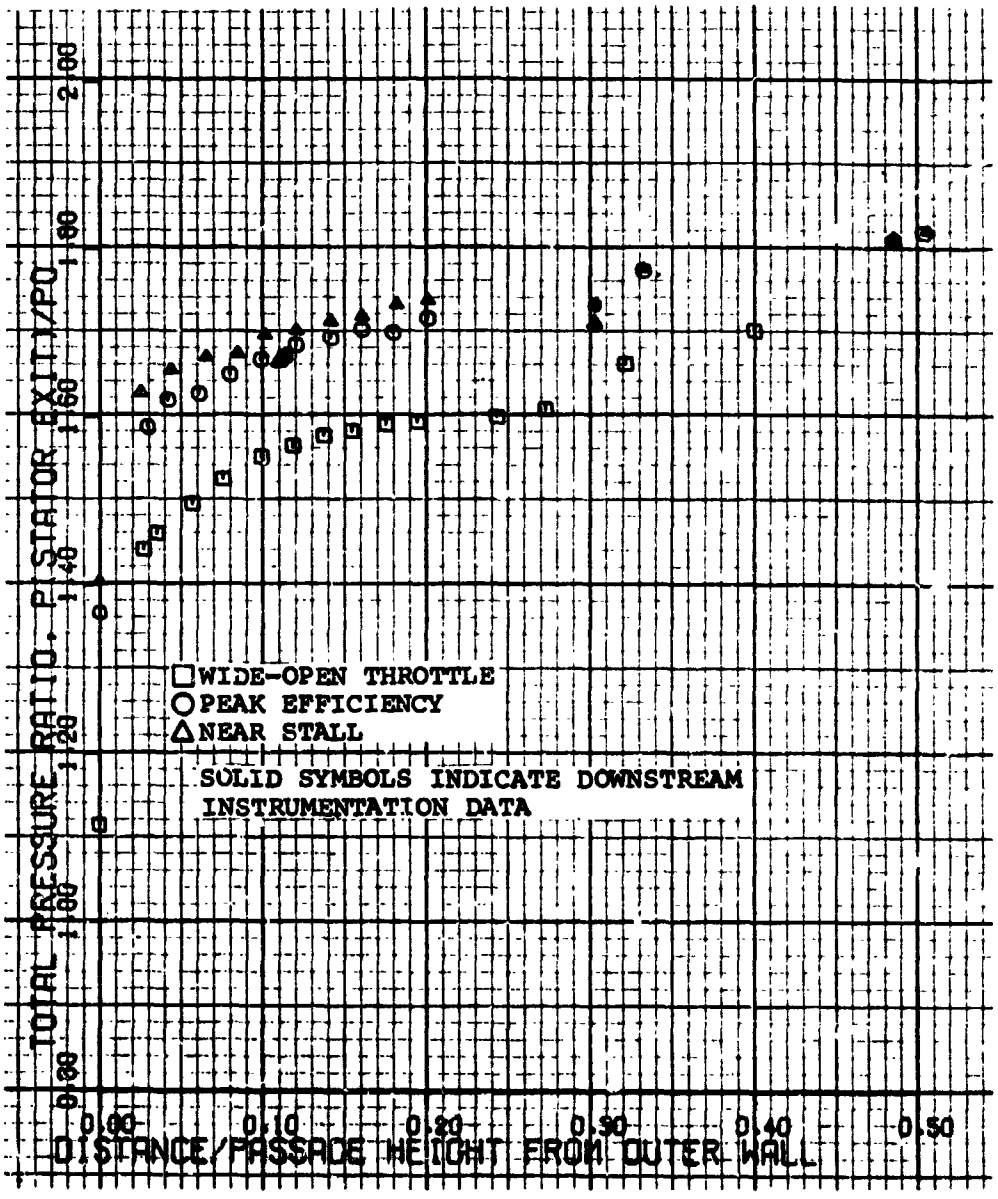

Figure 96. -Stator exit outerwall boundary layer total pressure profile, 100 percent design speed, Test 3.

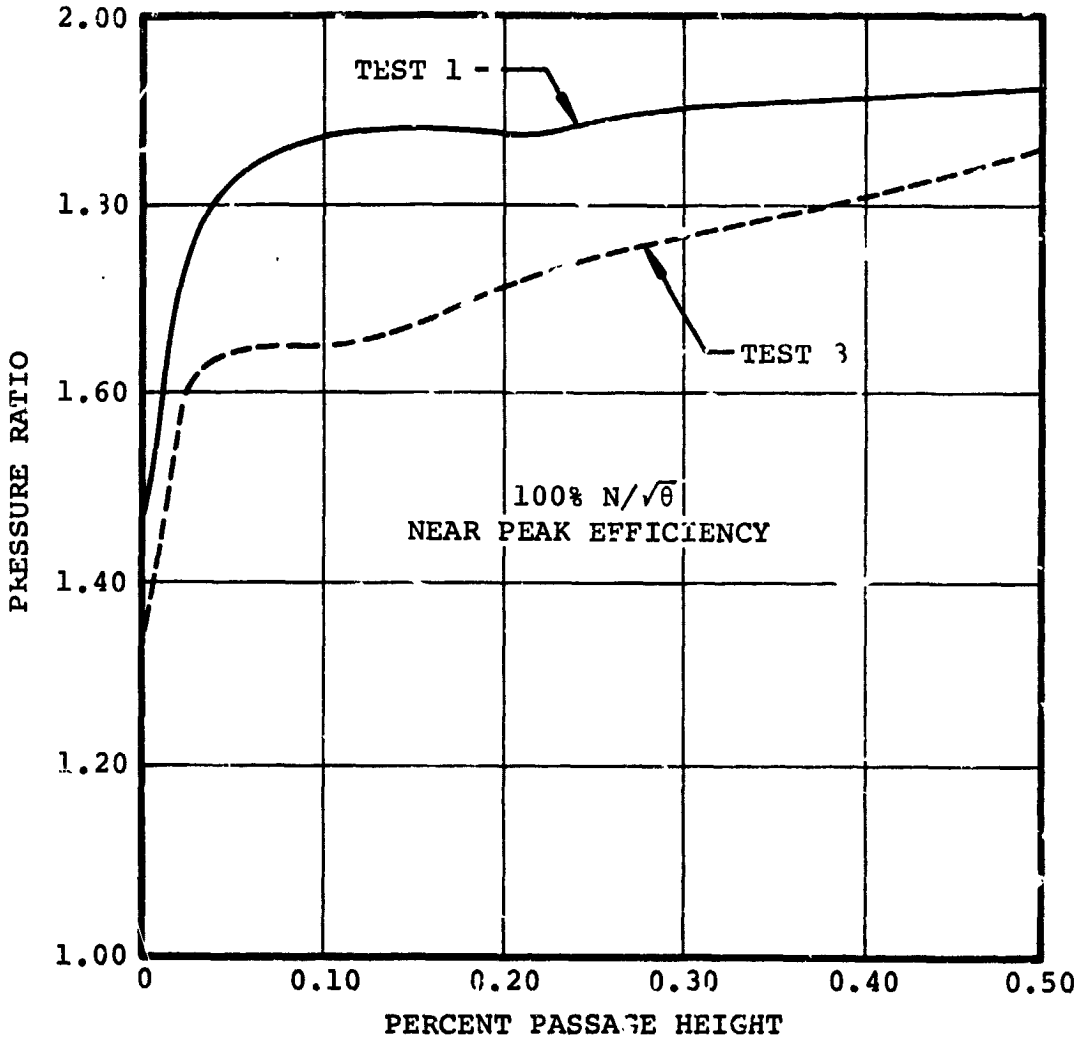

Figure 97. -Comparison of Test 1 and Test 3 rotor exit outerwall boundary layer total pressure profile, 100 percent design speed near peak efficiency.

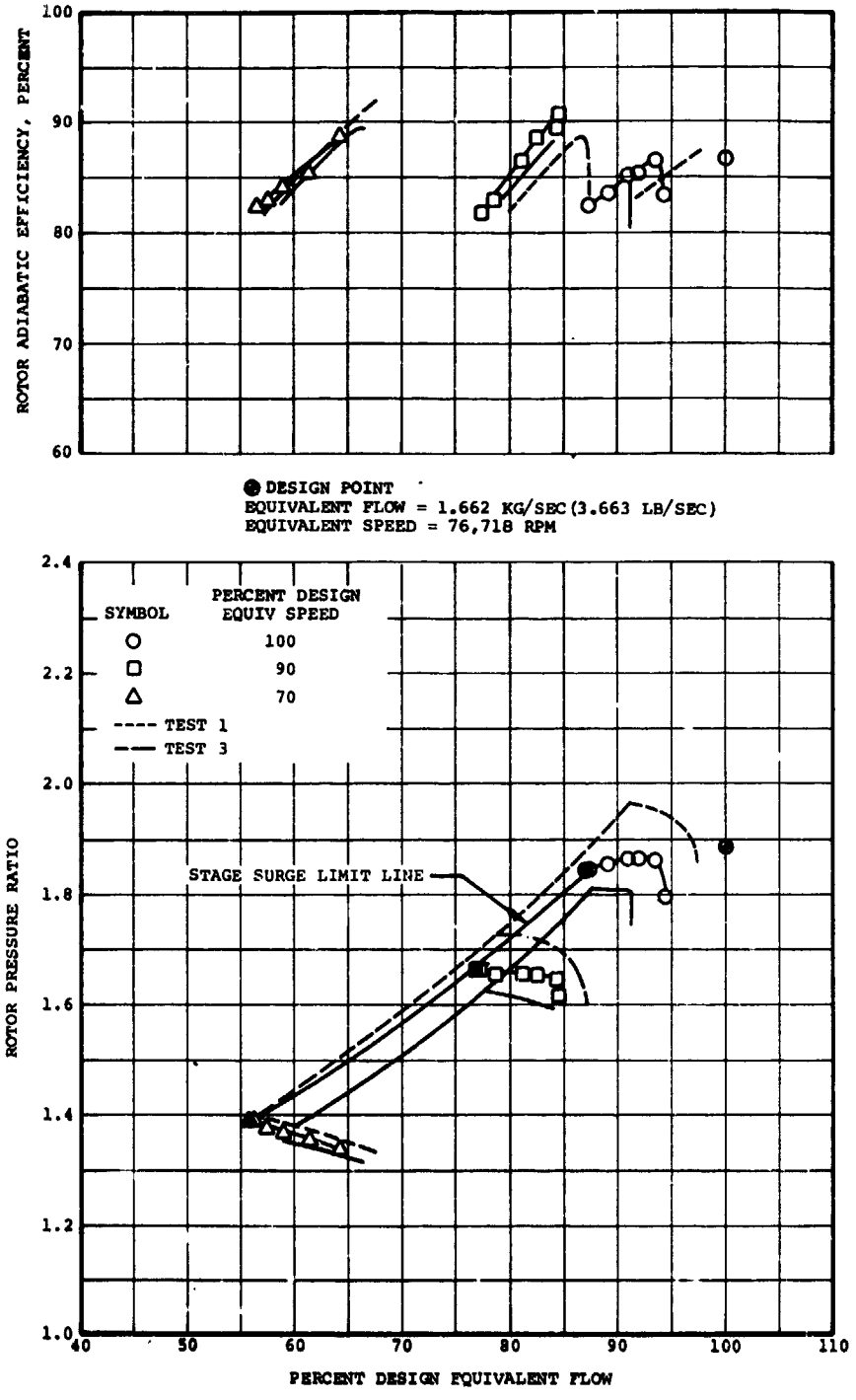

Figure 98. -Test 4 - rotor performance.

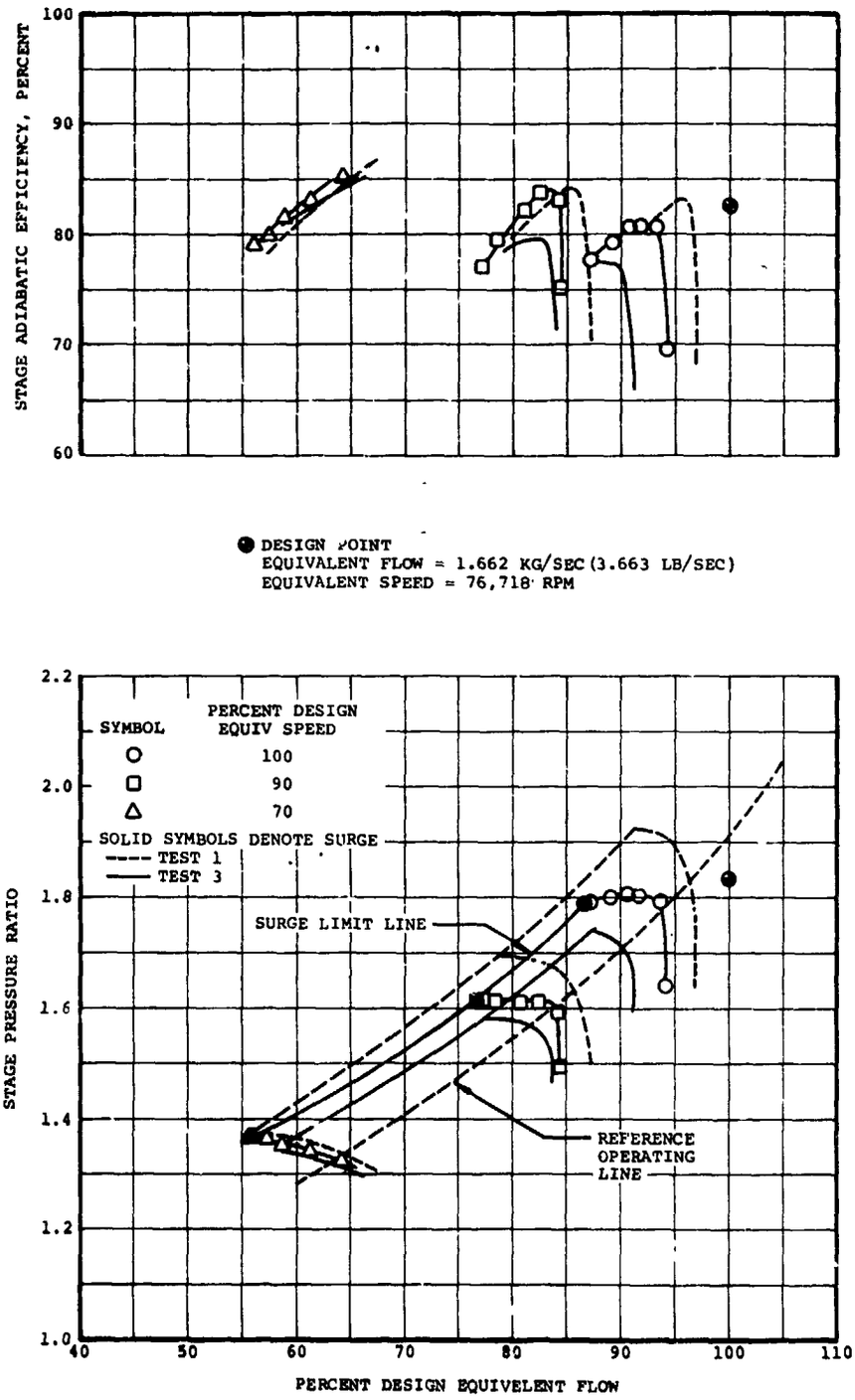

Figure 99. -Test 4 - stage performance.

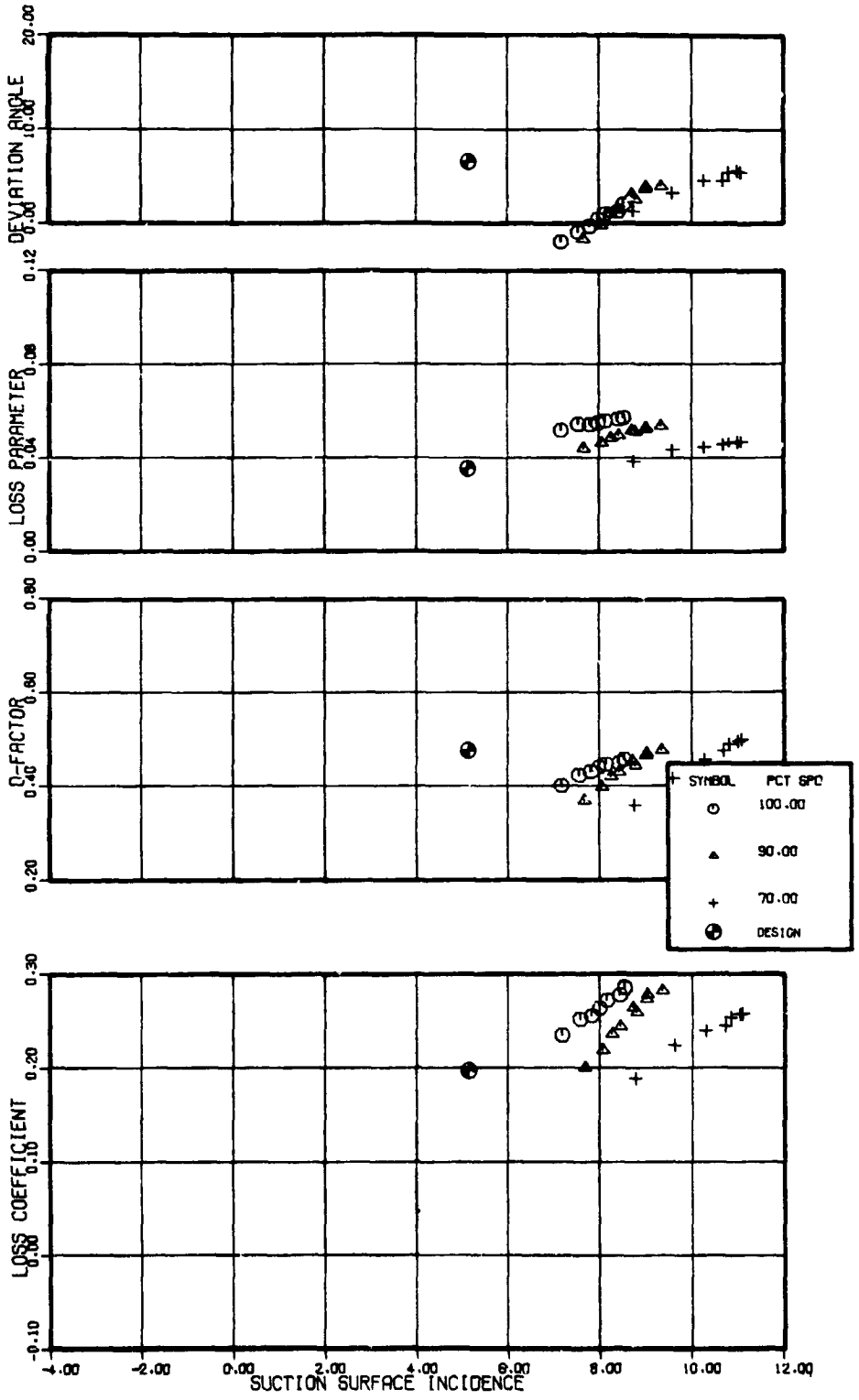

Figure 100. -Rotor blade element performance, 10 percent span from tip, Test 4.

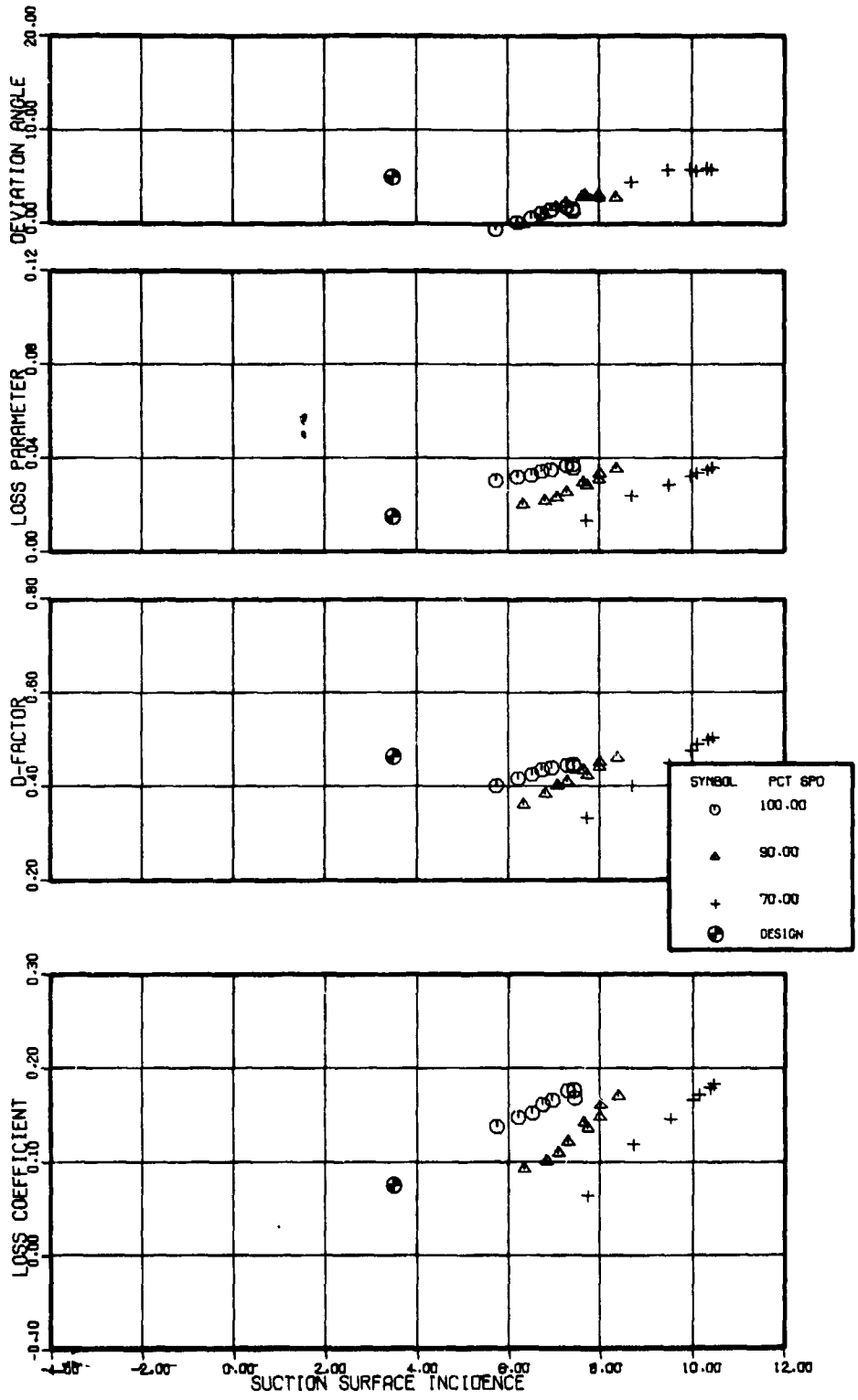

Figure 101. -Rotor blade element performance, 30 percent span from tip, Test 4.

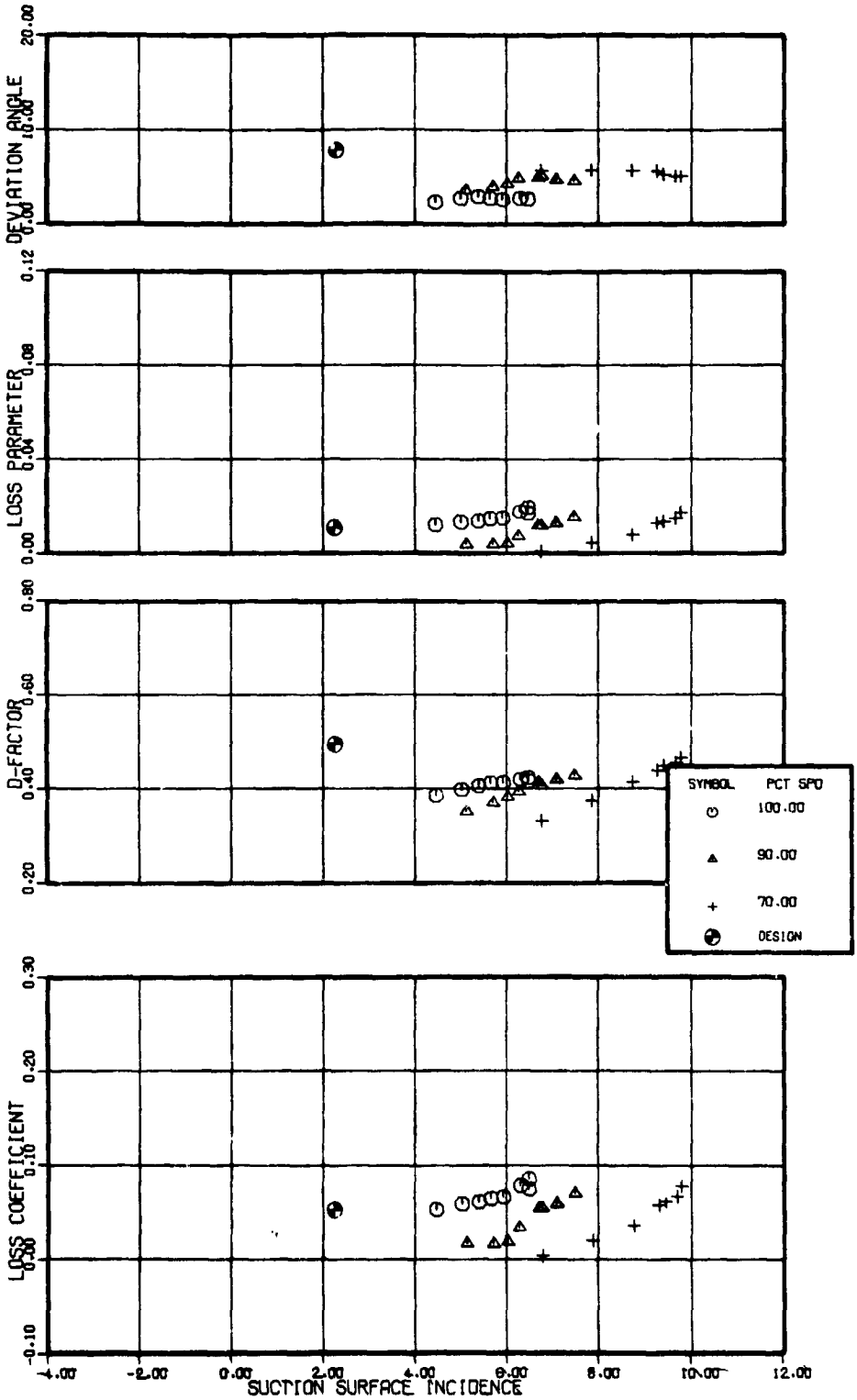

Figure 102. -Rotor blade element performance, 50 percent span from tip, Test 4.

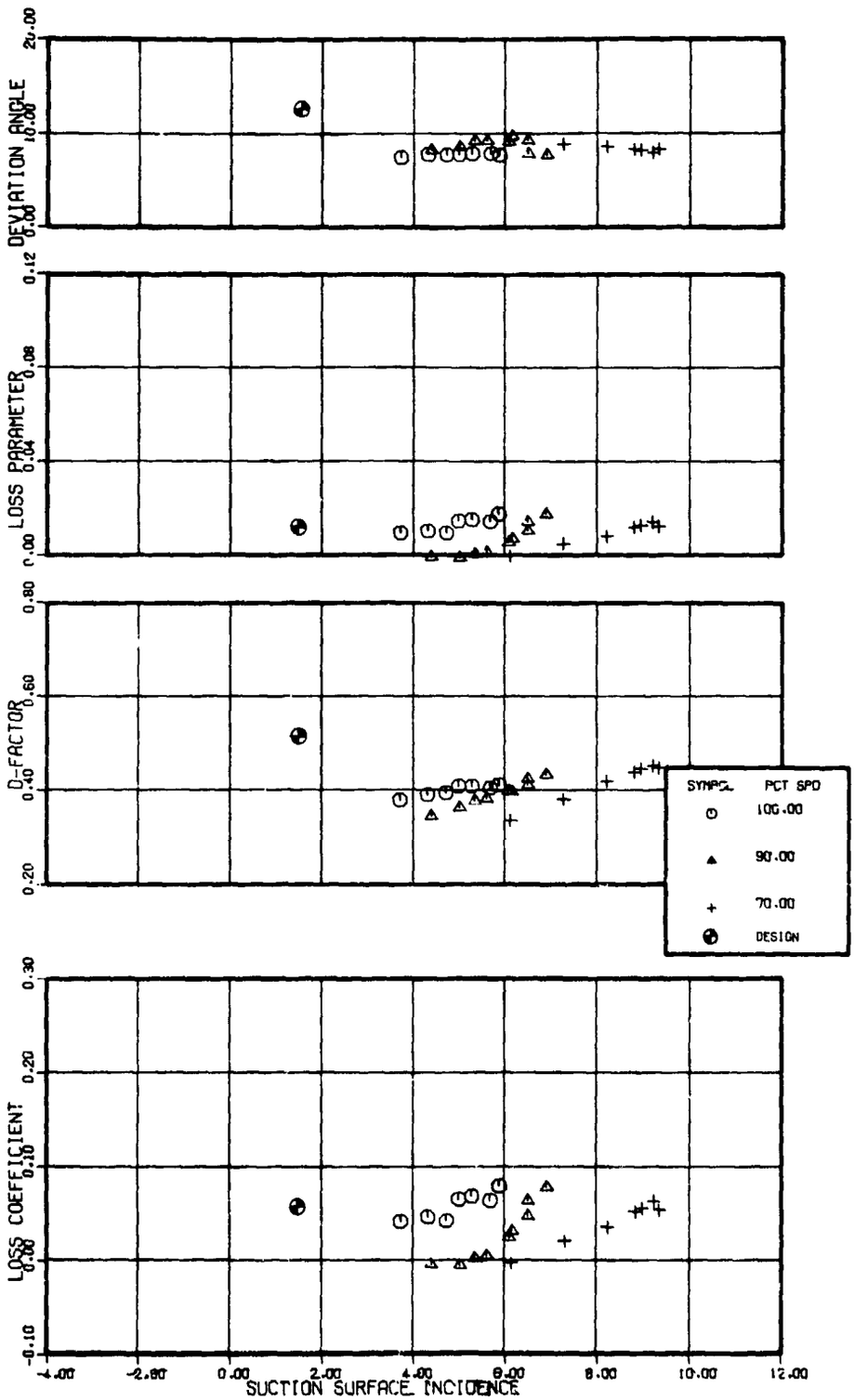

Figure 103. -Rotor blade element performance, 70 percent span from tip, Test 4.

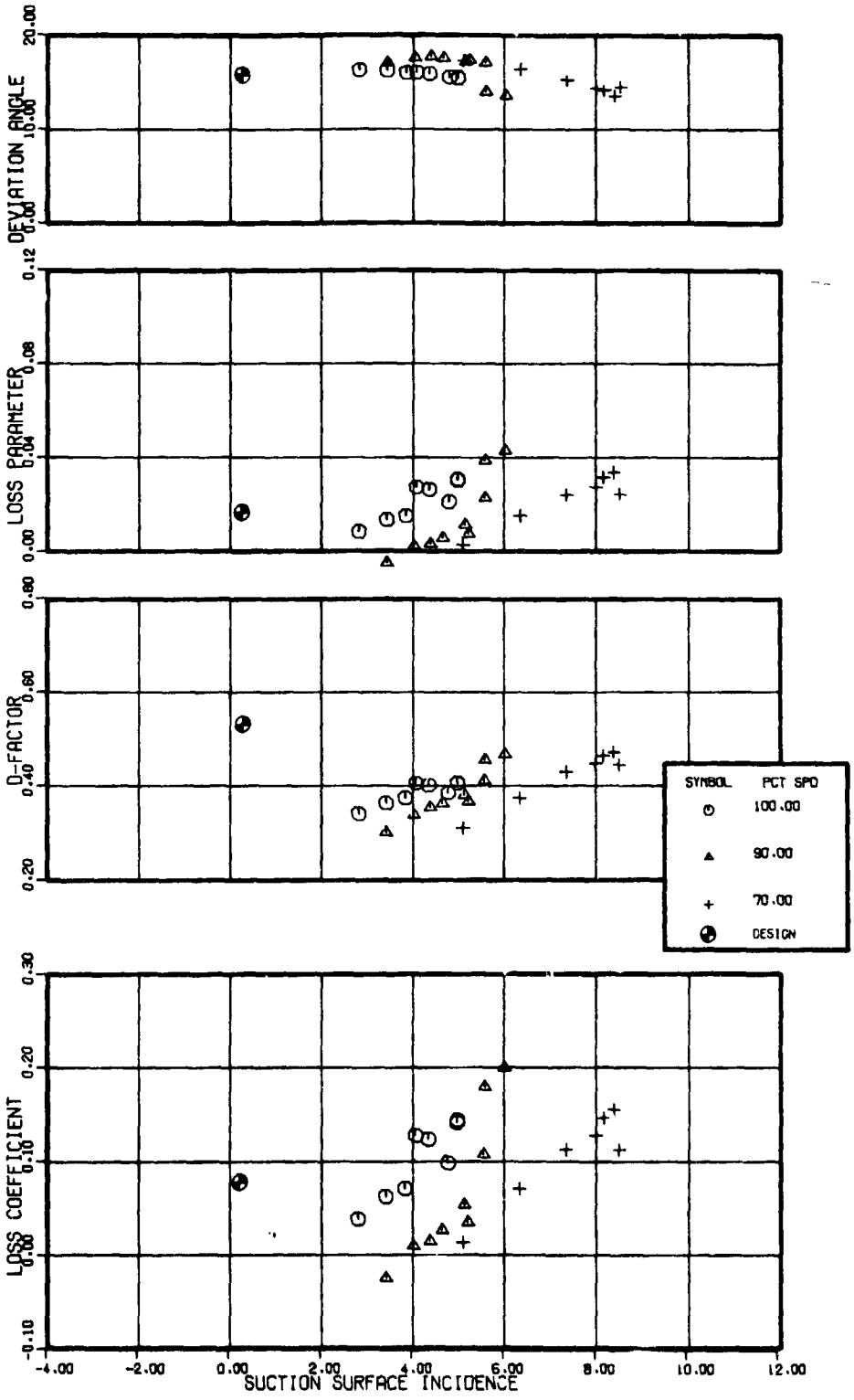

Figure 104. -Rotor blade element performance, 90 percent span from tip, Test 4.

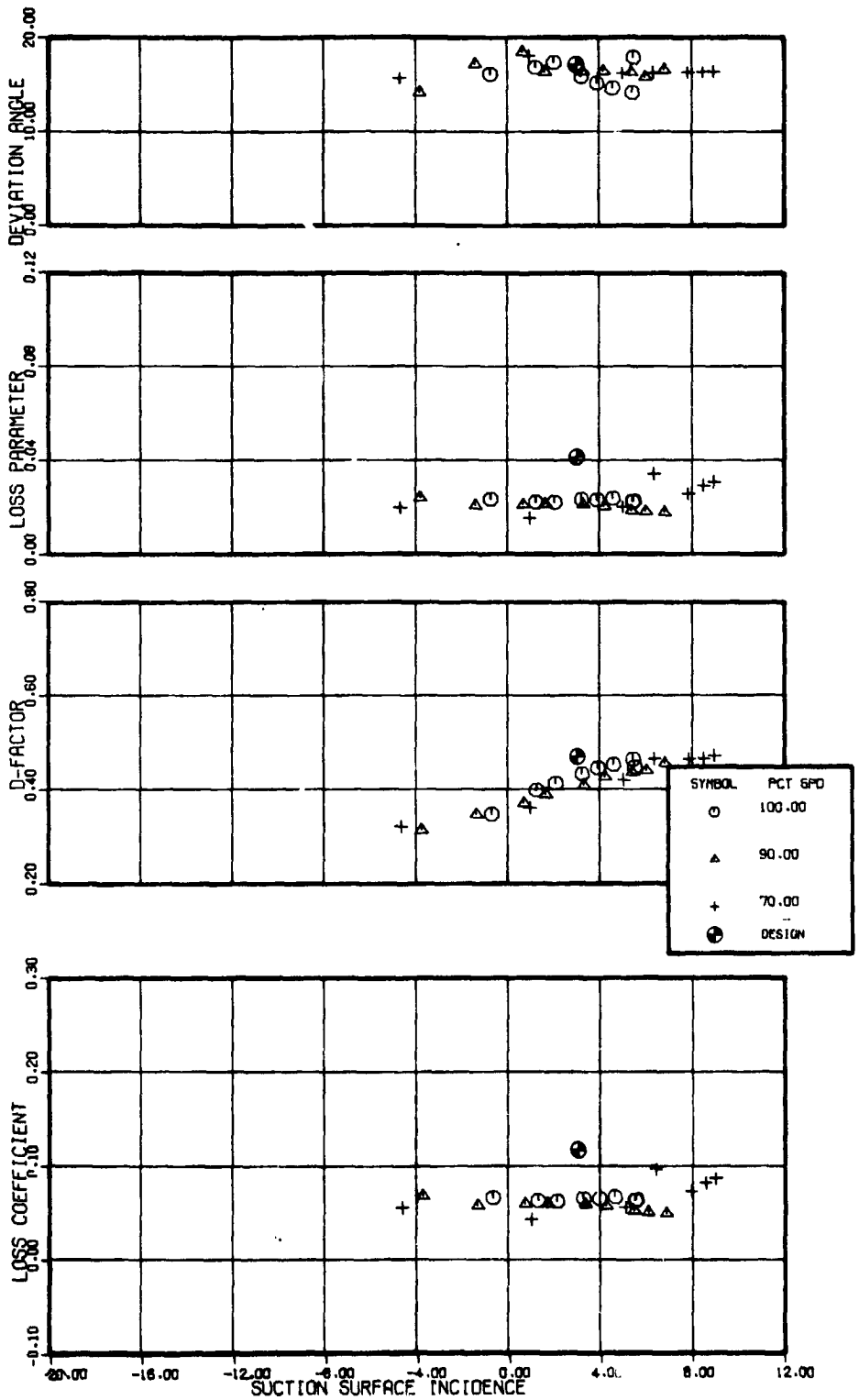

Figure 105. -Stator blade element performance, 10 percent span from tip, Test 4.

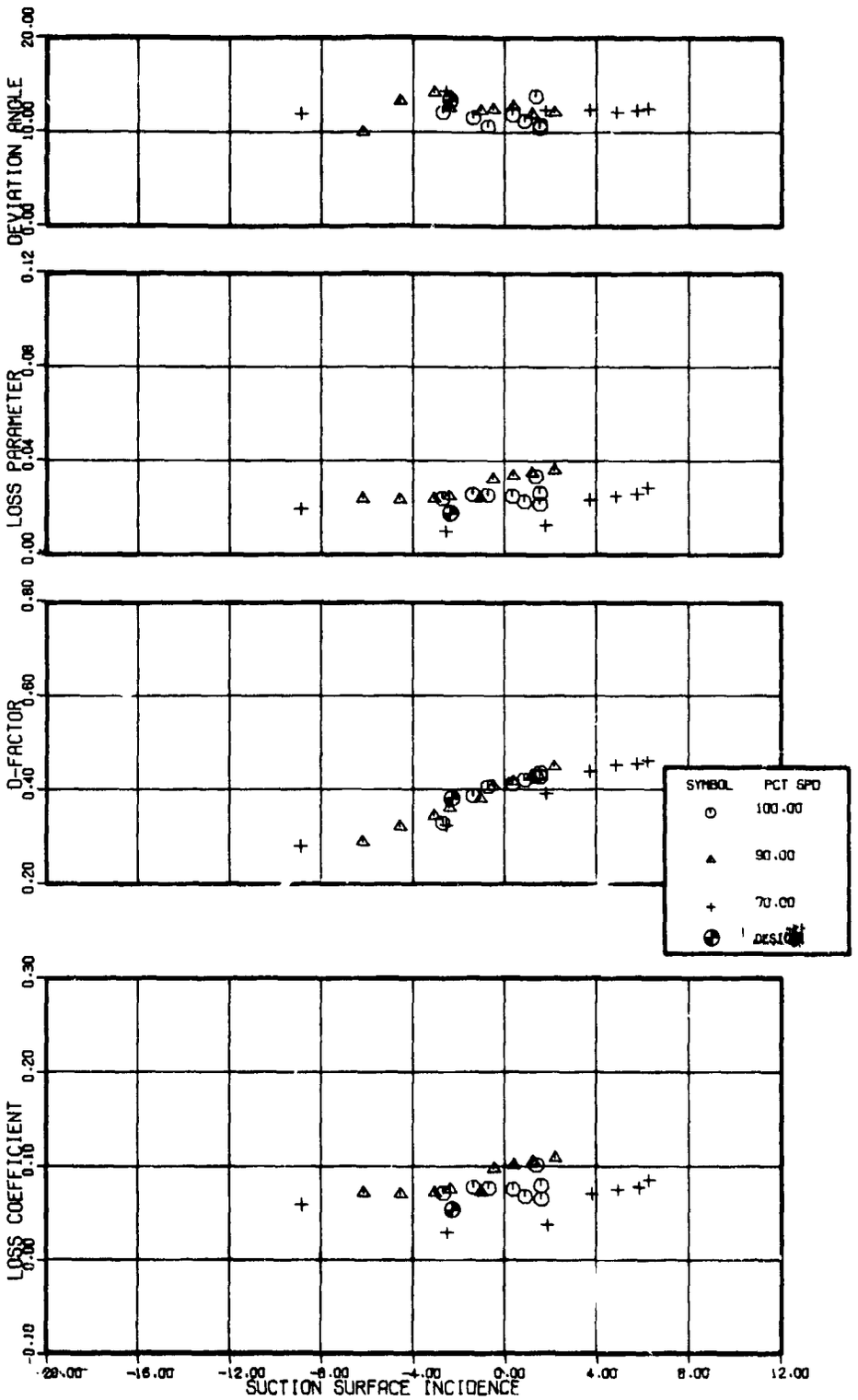

Figure 106. -Stator blade element performance, 30 percent span from tip, Test 4.

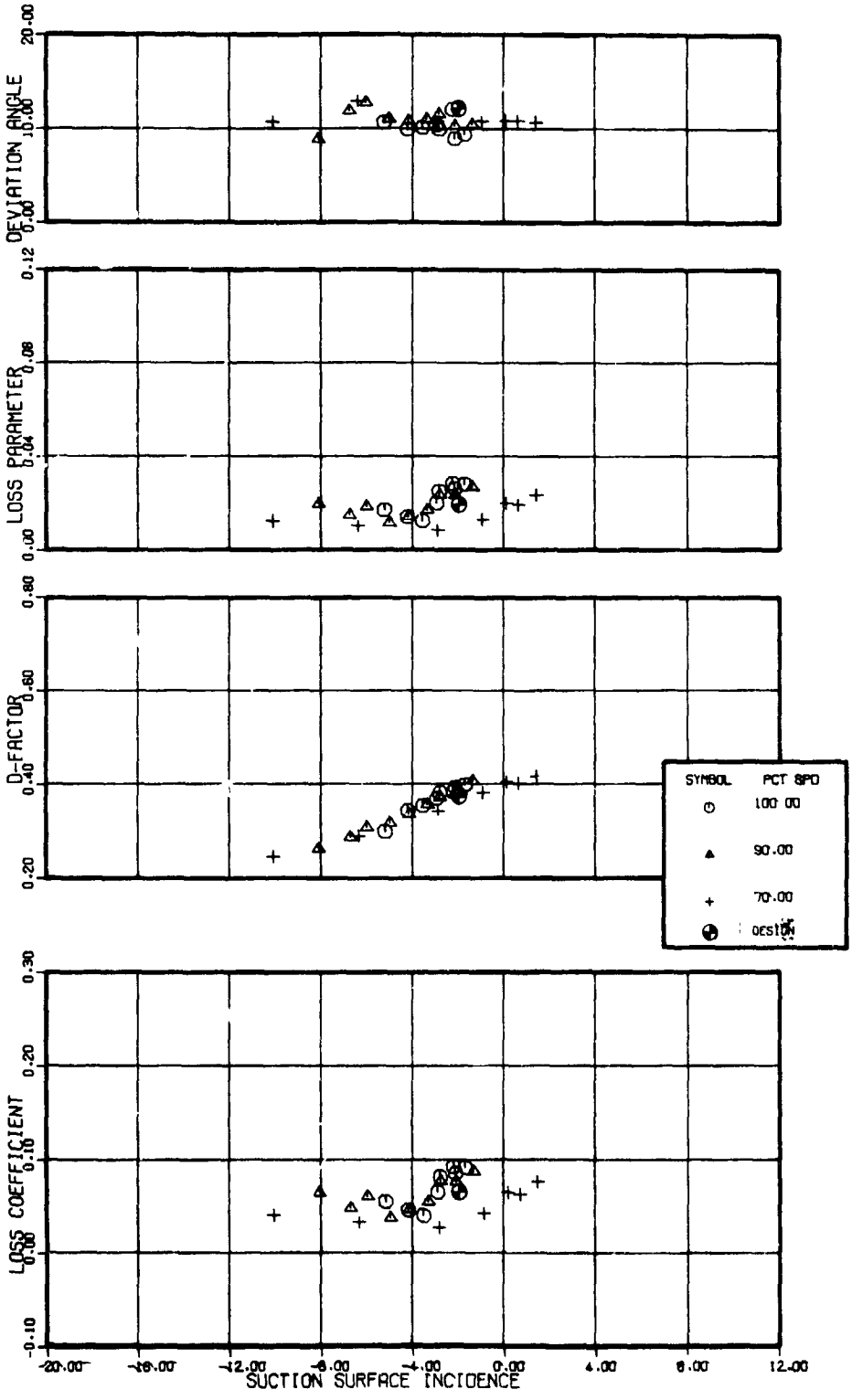

Figure 107. -Stator blade element performance, 50 percent span from tip, Test 4.

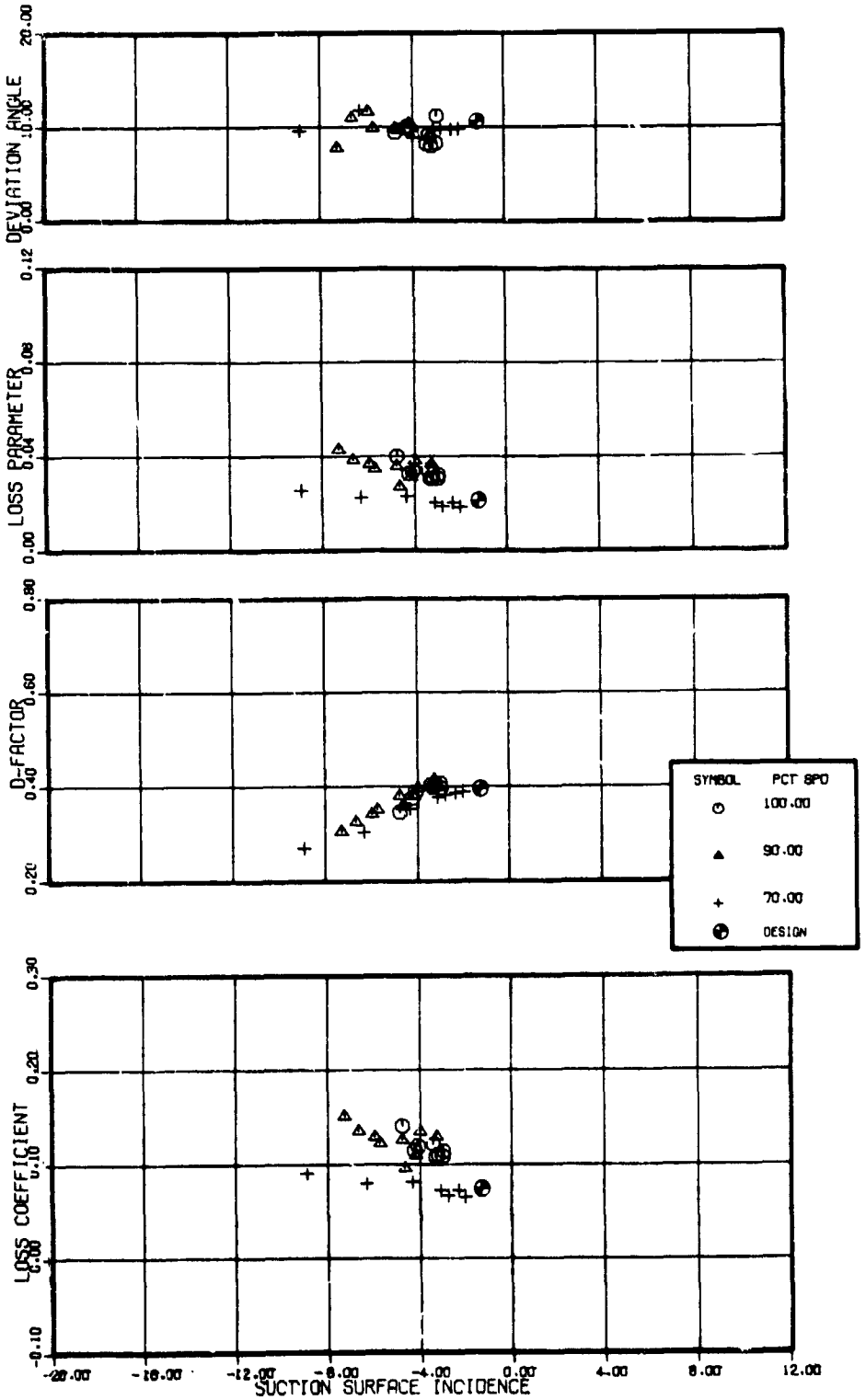

Figure 108. -Stator blade element performance, 70 percent span from tip, Test 4.

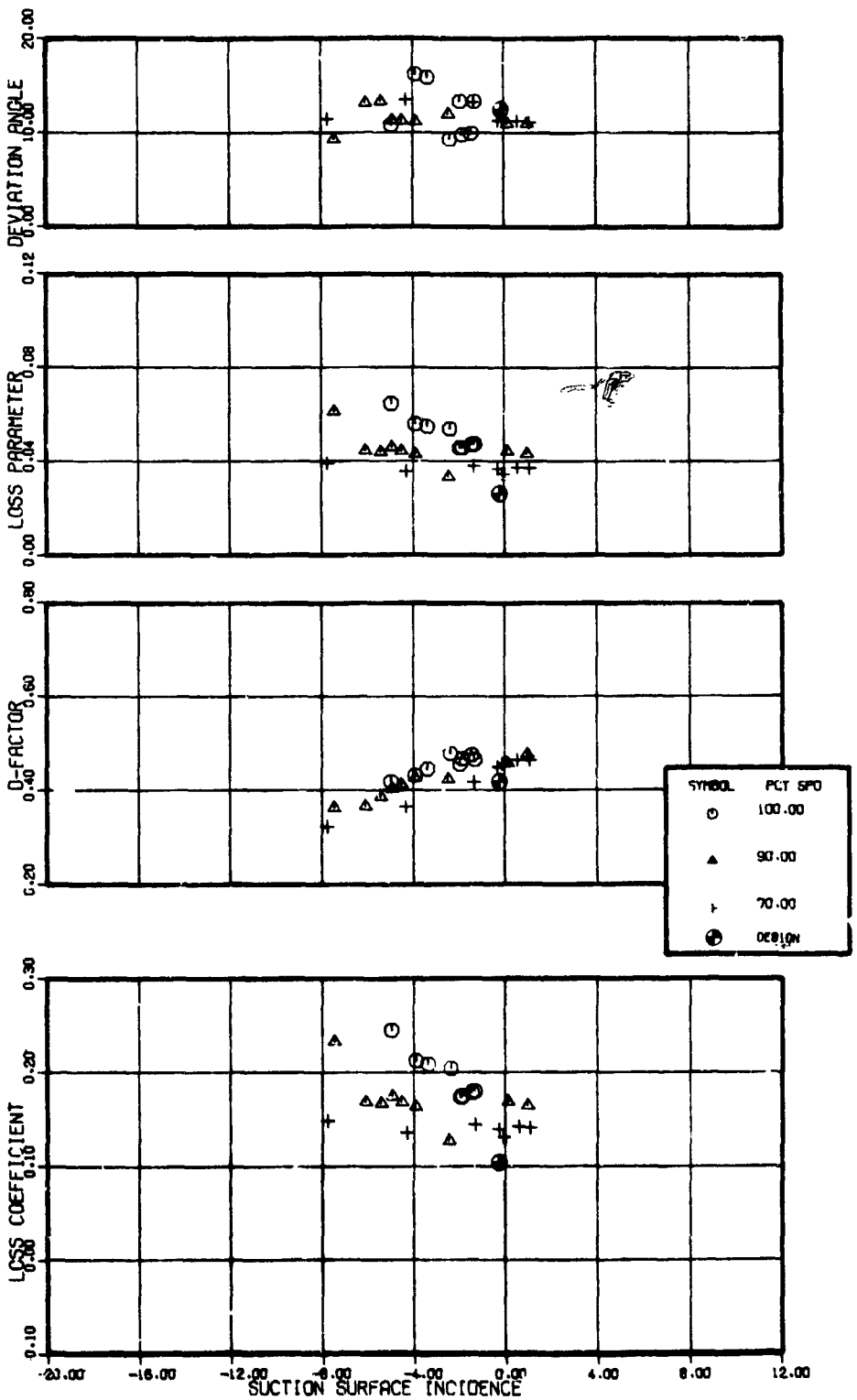

Figure 109. -Stator blade element performance, 90 percent span from tip, Test 4.

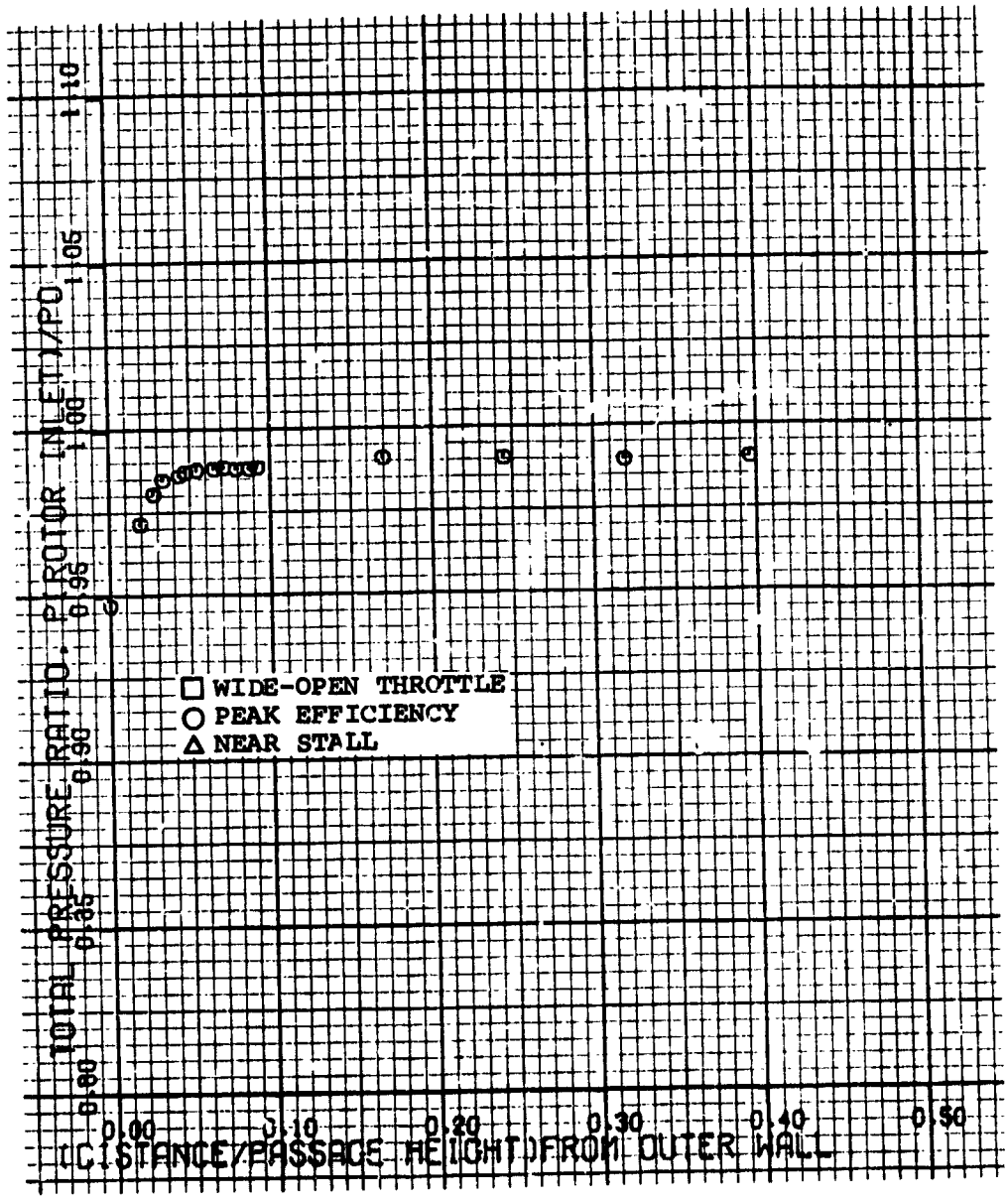

Figure 110. -Rotor inlet outerwall boundary layer total pressure profile, 70 percent design speed, Test 4.

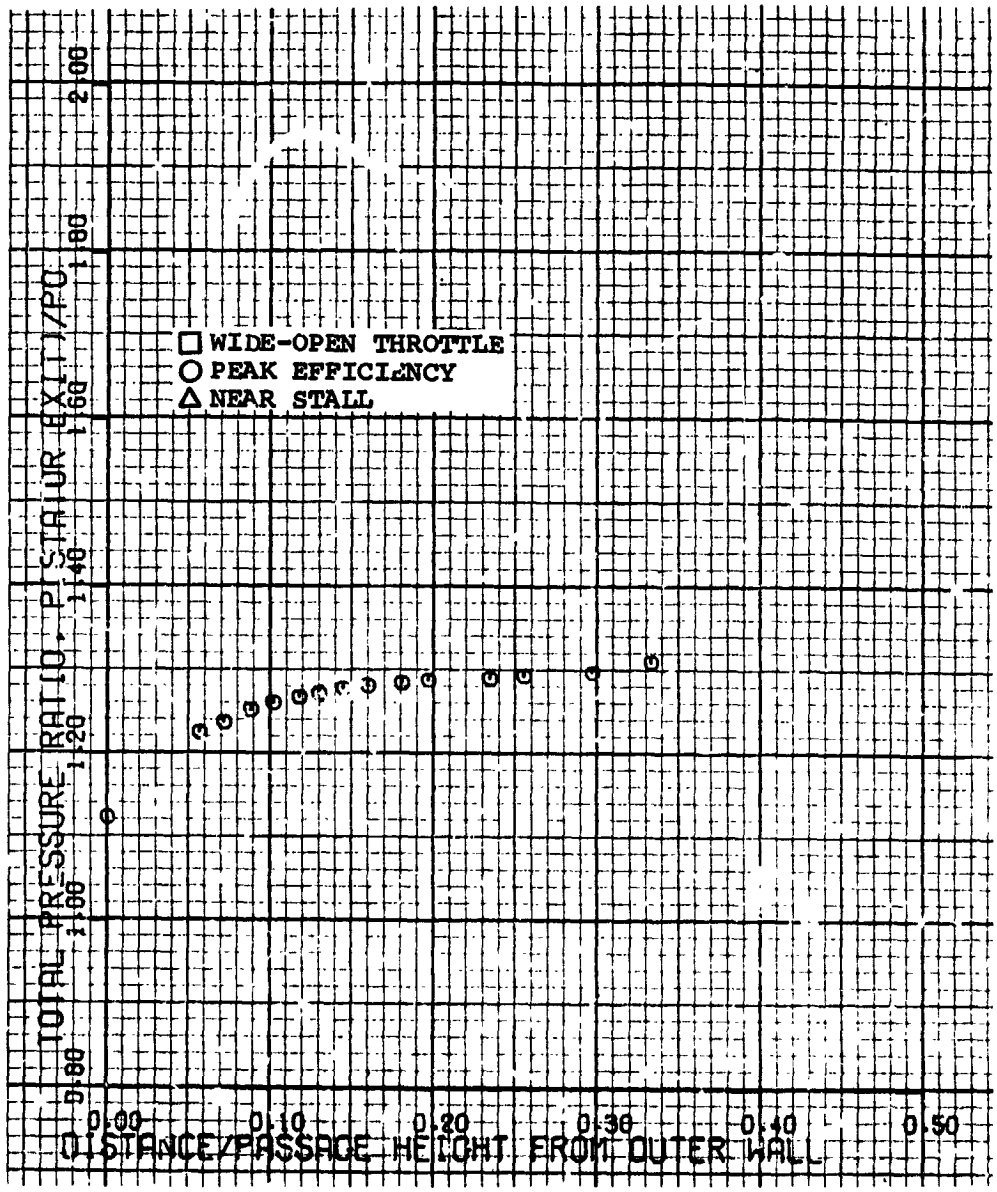

Figure 111. -Stator exit outerwall boundary layer total pressure profile, 70 percent design speed, Test 4.

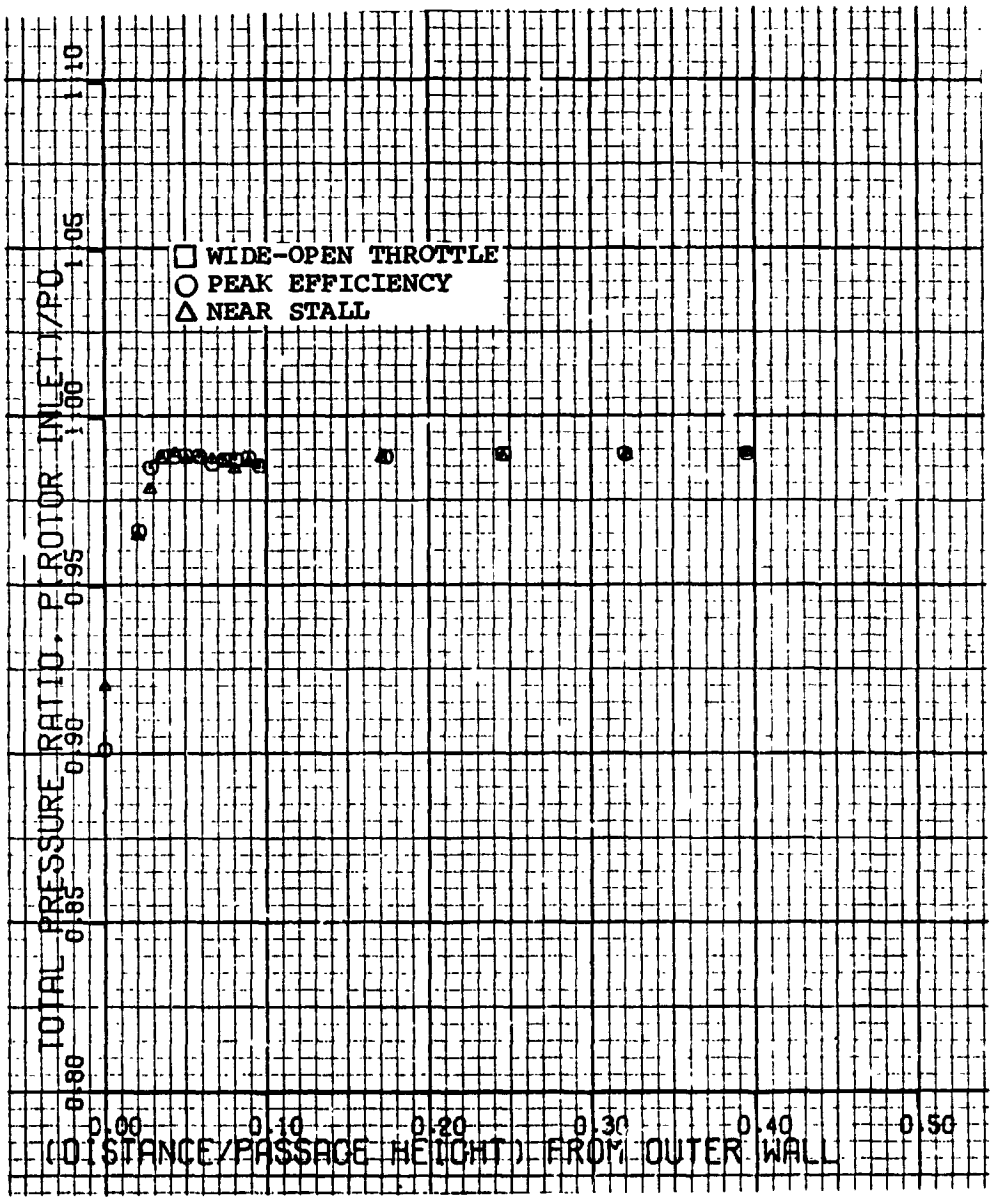

Figure 112. -Rotor inlet outerwall boundary layer total pressure profile, 90 percent design speed, Test 4.

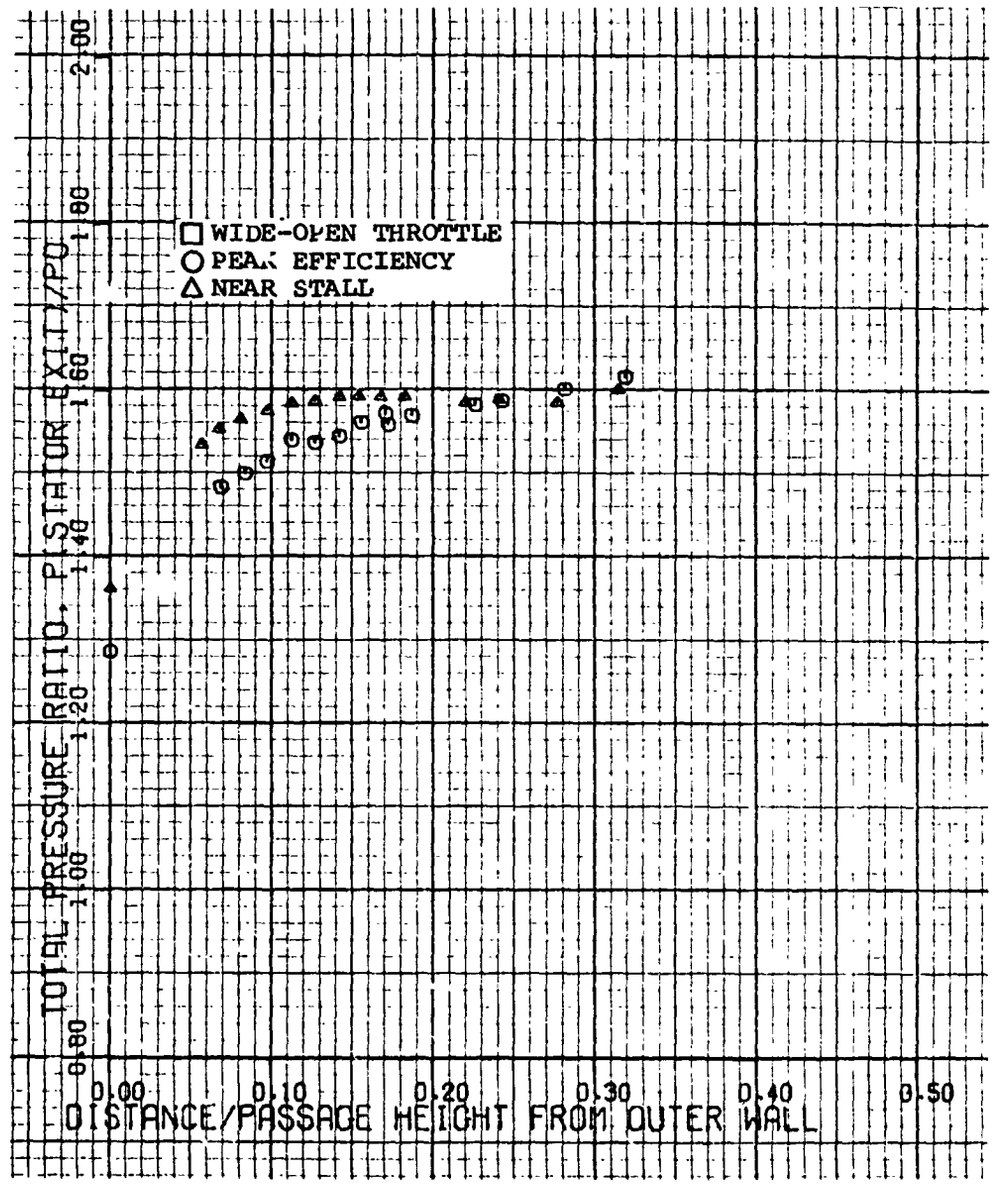

Figure 113. -Stator exit outerwall boundary layer total pressure profile, 90 percent design speed, Test 4.

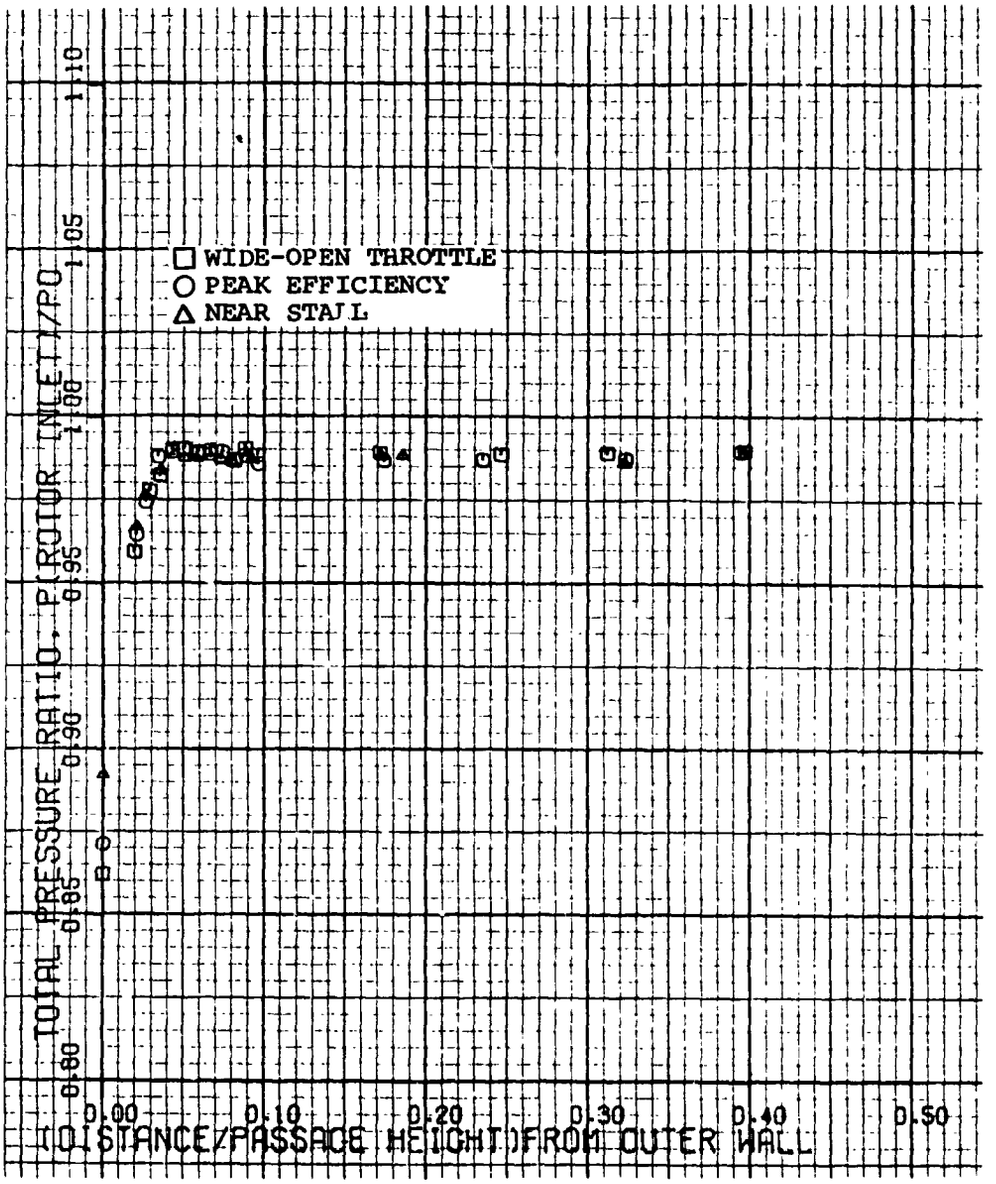

Figure 114. -Rotor inlet outerwall boundary layer total pressure profile, 100 percent design speed, Test 4.

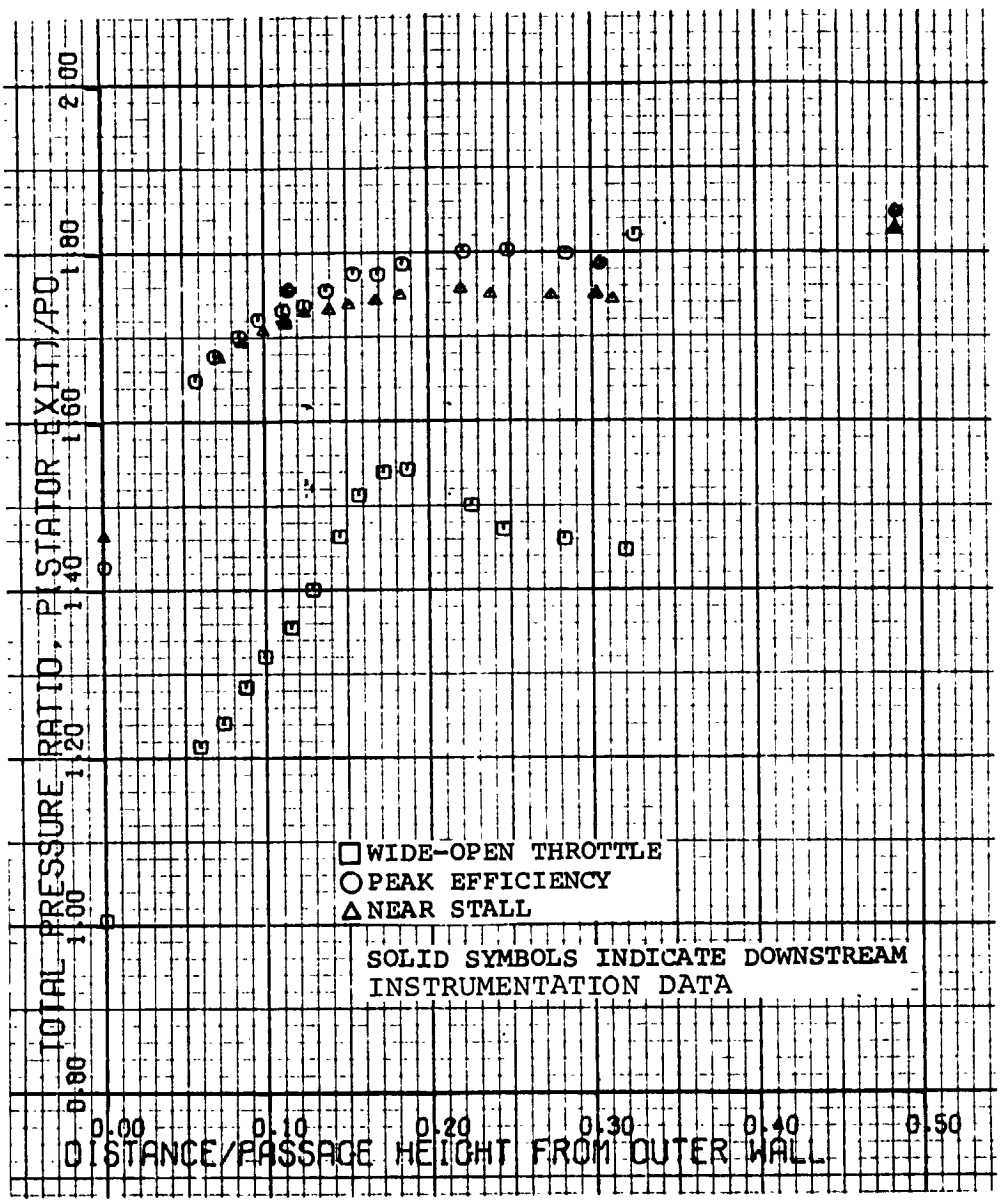

Figure 115. -Stator exit outerwall boundary layer total pressure profile, 100 percent design speed, Test 4.

TEST NO.	SYMBOL		
1	OPEN	○	CLOSE CLEARANCE UNTREATED
2	DARKENED	●	CLOSE CLEARANCE WITH TREATMENT
3	LEFT DARK	◐	OPEN CLEARANCE UNTREATED
4	TOP DARK	◒	OPEN CLEARANCE WITH TREATMENT
		◓	DESIGN

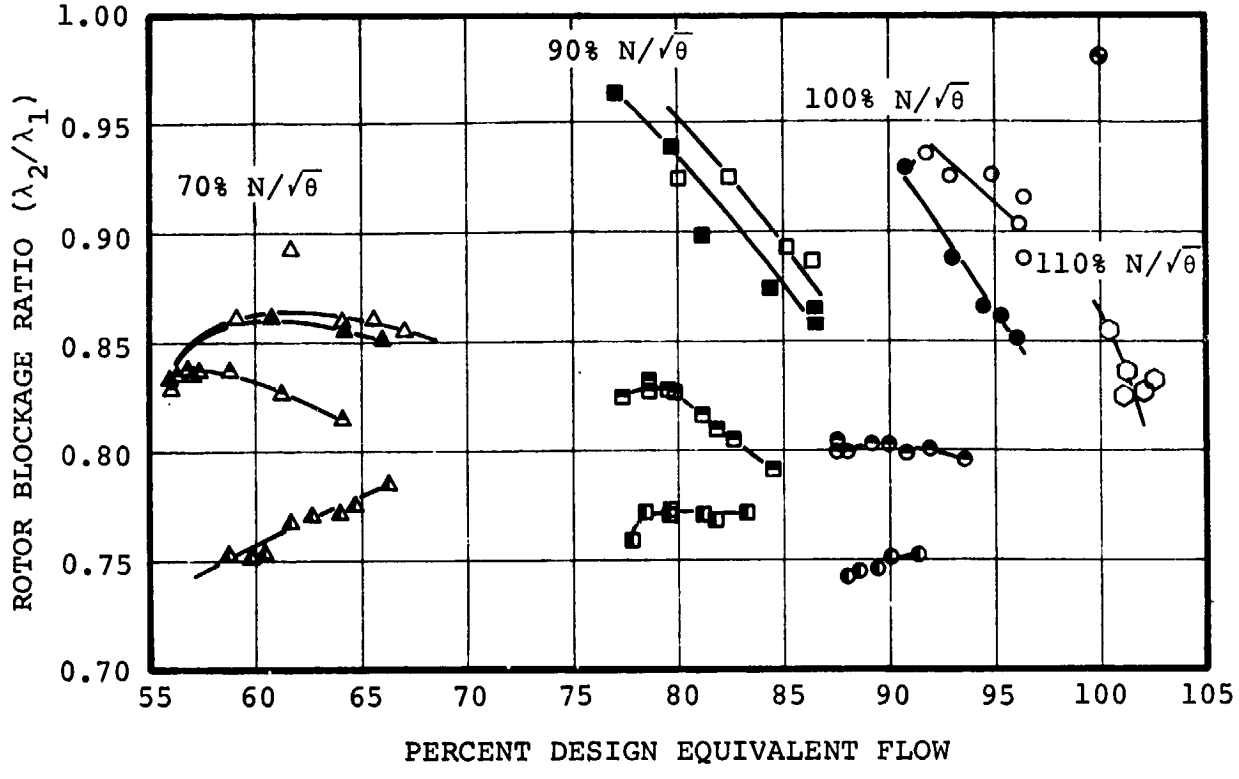

Figure 116. -Rotor blockage.

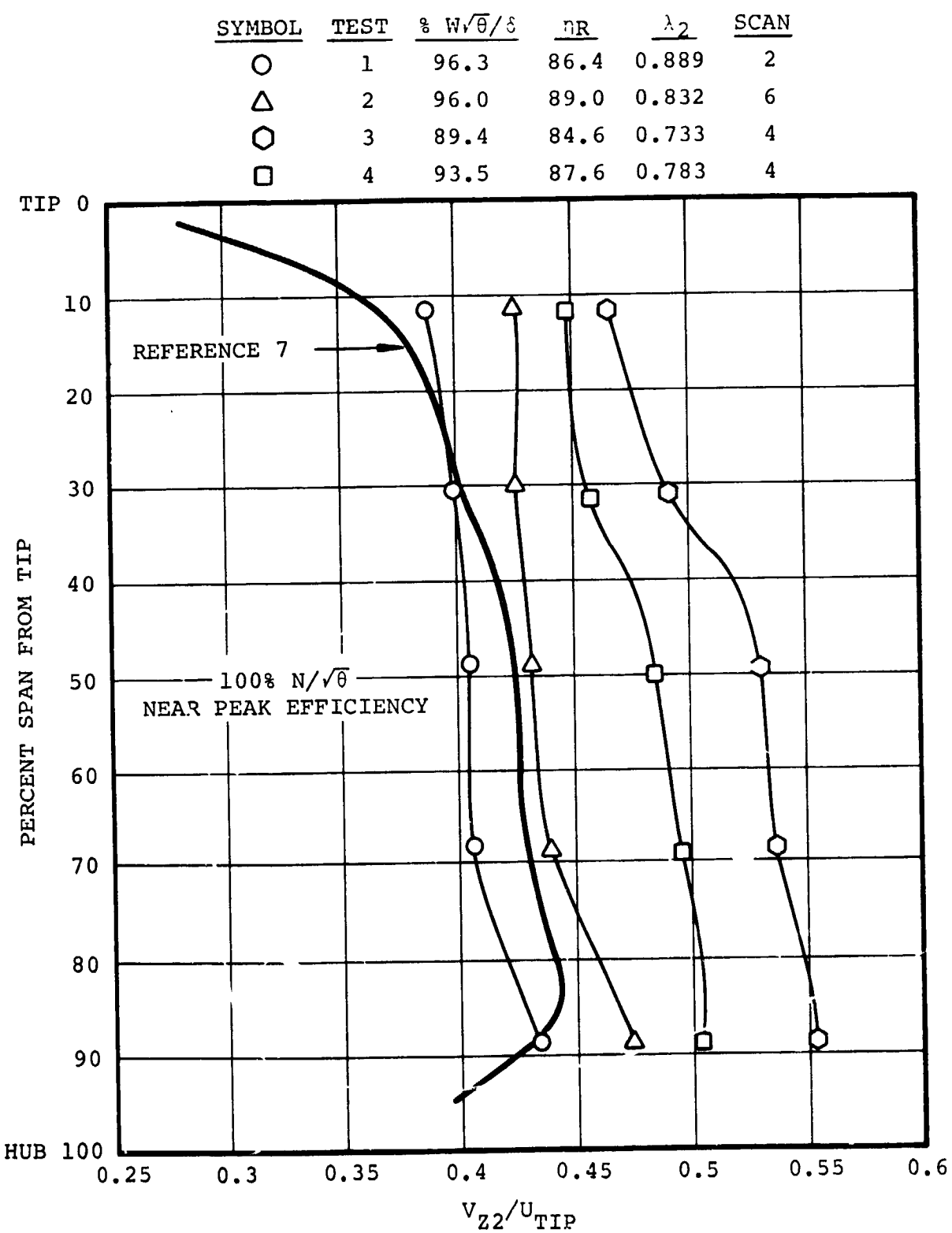

Figure 117. -Rotor discharge axial velocity, 100 percent design speed near peak efficiency.

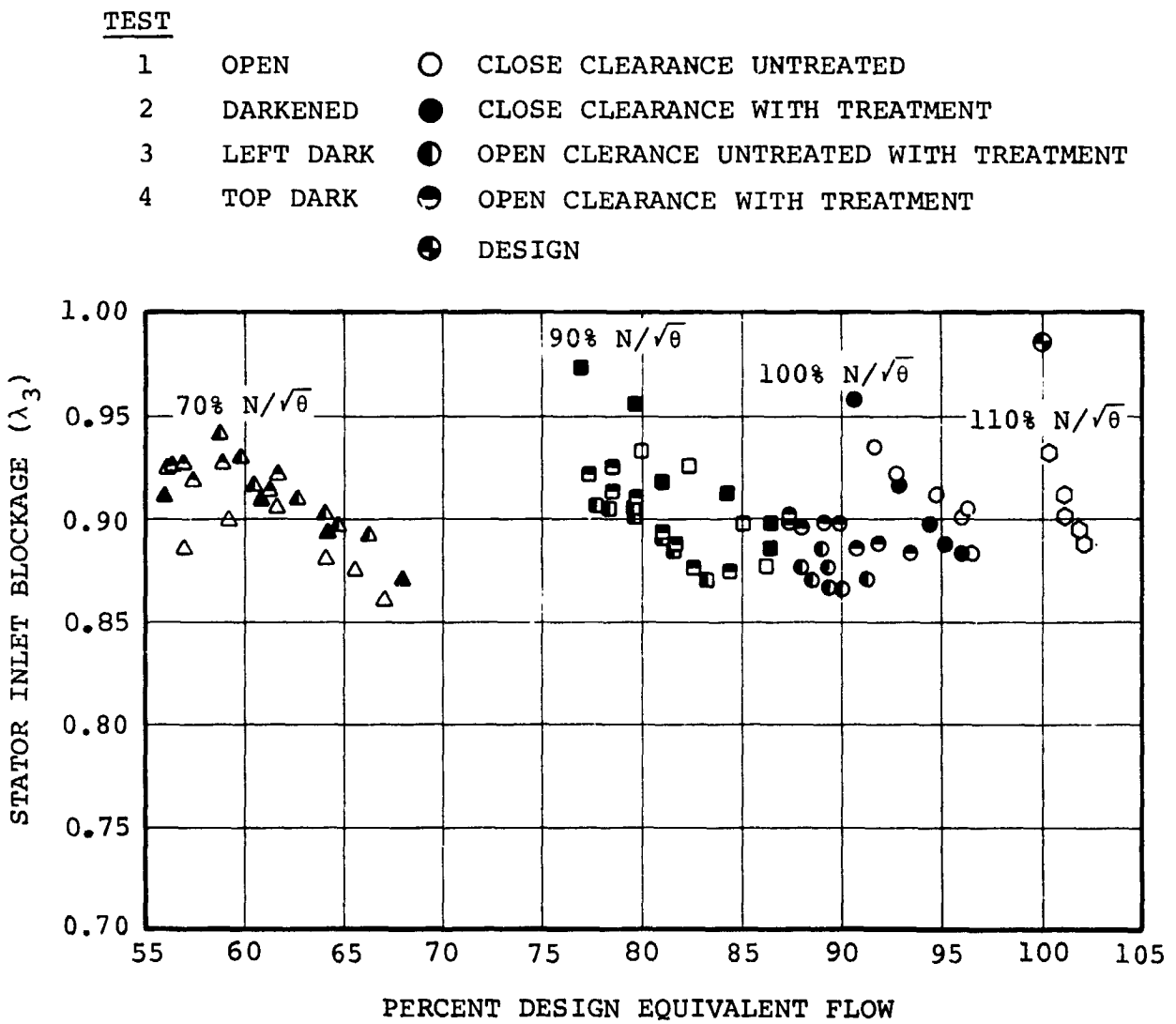

Figure 118. -Stator inlet blockage.

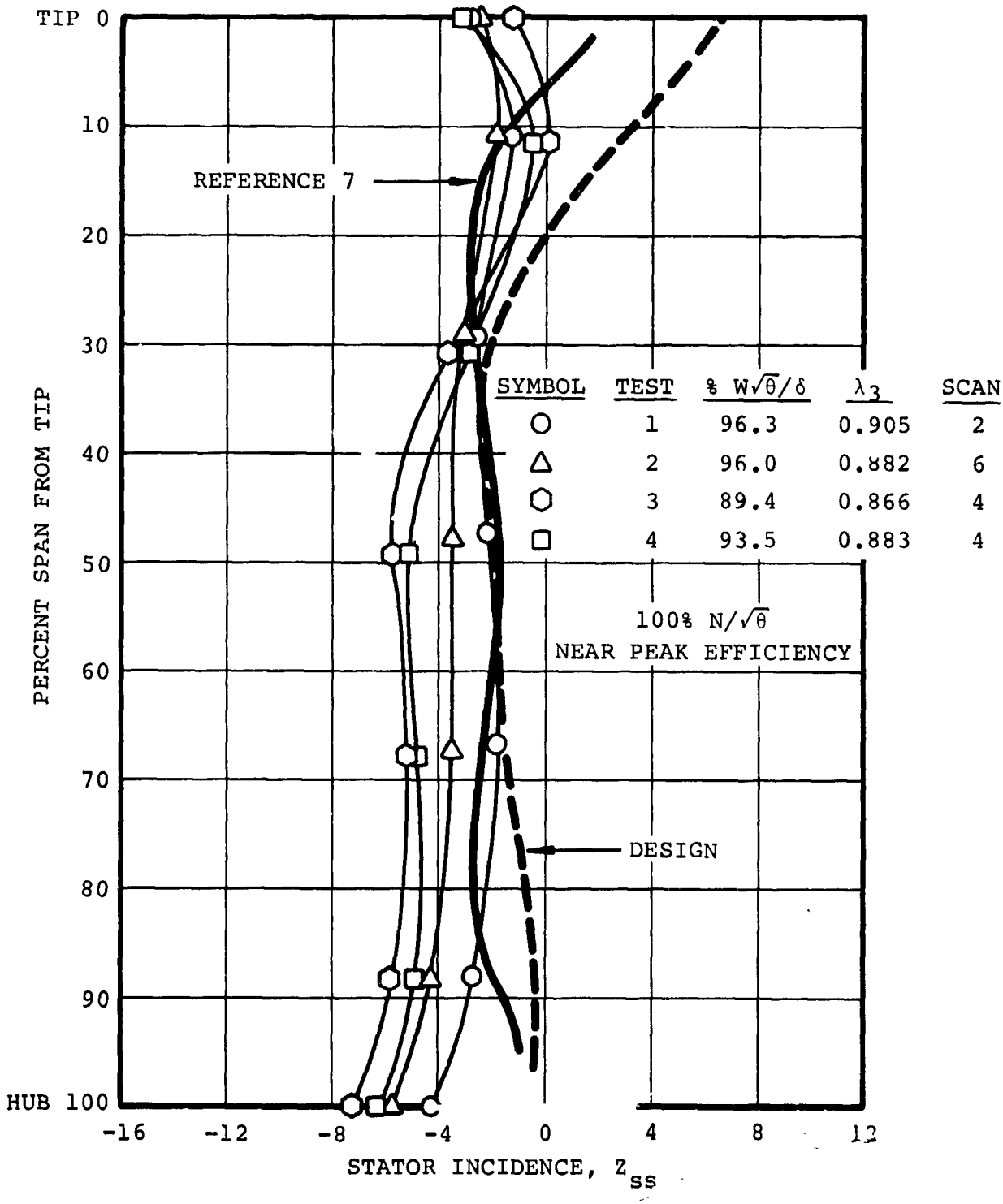

Figure 119. -Stator incidence, 100 percent design speed near peak efficiency.

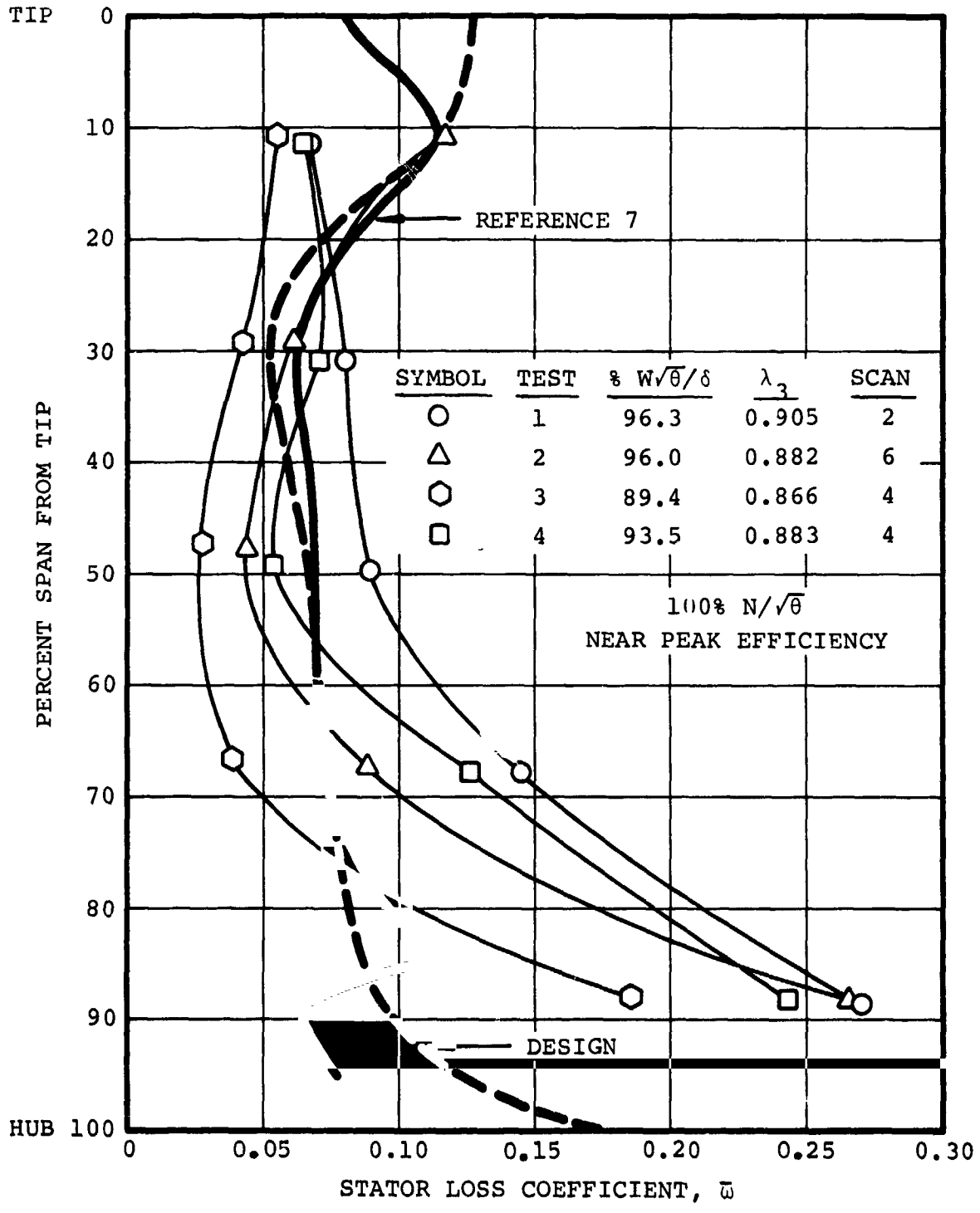

Figure 120. -Stator loss coefficient, 100 percent design speed near peak efficiency.

APPENDIX A

DEFINITION OF SYMBOLS AND PERFORMANCE PARAMETERS

A	area, m^2 (ft^2)
c	chord length, cm (in.)
C_p	specific heat at constant pressure, J/kg-°K (Btu/lb_m-°R)
d	diameter, cm (in.)
D	diffusion factor
g	gravitational constant, 9.8066 kg-m/N-sec^2 (32.174 lb_m-ft/lb_f-sec^2)
H	enthalpy, J/kg-°K (Btu/lb-°R)
i_s	incidence angle, angle between inlet air direction and blade leading edge, deg
J	mechanical equivalent of heat, 0.1019 m-kg/J (778.161 ft-lb_f/Btu)
m	distance along meridional projection of streamline, cm (in.)
$\dot{m}_s$	increment of mass flow, kg/sec (lb_m/sec)
M	Mach number
N	rotor speed, rpm
n	distance along meridional projection of station line, cm (in.)
P	total pressure, N/cm^2 (psia)
p	static pressure, N/cm^2 (psia)
Q	entropy function, $e^{-\Delta S/Cp}$
r	radius, cm (in.)
R_g	gas constant for air, 287.00 J/kg-°K (53.342 ft-lb_f/lb_m-°R)
r_c	streamline curvature in meridional projection, cm^{-1} ($in.^{-1}$)
S	entropy, J/kg-°K (Btu/lb-°R)
s	blade circumferential spacing, cm (in.)

t	blade maximum thickness, cm (in.)
T	total temperature, °K (°R)
t	static temperature, °K (°R)
t/c	thickness-to-chord ratio
U	rotor speed, m/sec (ft/sec)
V	velocity, m/sec (ft/sec)
α	streamline slope in meridional projection, deg
β	$\tan^{-1} V_\theta/V_m$, deg
β^*	$\tan^{-1} V_\theta/V_z$, deg
β_e	$\tan^{-1}\{(V_\theta/V_z + [(\tan \varepsilon)\ (\tan \gamma)]\}$, deg
γ	ratio of specific heats
$\gamma°$	blade-chord angle (from axial direction), deg
δ	ratio of inlet total pressure to NASA standard sea level pressure of 10.1325 N/cm^2 (14.6959 psia)
$\delta°$	deviation angle (based on mean camber line), deg
Δ	delta, finite difference
ε	angle between the radial direction and the stream surface in the t = constant plane $\left(\tan^{-1}\frac{-\delta(rd)}{\delta r}\ t = \text{constant}\right)$ plane and axial direction, deg
η	efficiency
θ	ratio of inlet total temperature to NASA standard sea level temperature of 288.16°K (518.69°R), or polar coordinate, radian
κ	blade metal angle from meridional direction
λ	fraction of annulus available for flow
ξ	angle between radial direction and meridional projection of station line, deg

ψ_S axial momentum, kg-m/sec^2 (lb-ft/sec^2)

ϕ blade camber angle, $\kappa_{le} - \kappa_{te}$, deg

ϕ_S tangential momentum, kg-m/sec^2 (lb-ft/sec^2)

$\bar{\omega}$ loss coefficient

$\bar{\omega} \cos \beta/2\sigma$ loss parameter

ρ fluid density, kg/m^3 (lb/ft^3)

σ solidity c/s

101-225 pressure instrumentation identification numbers

Subscripts:

0 compressor inlet (bellmouth)

0.9 upstream of rotor inlet

1 rotor inlet

2 rotor exit

3 stator inlet

4 stator exit

5 stage discharge

ad adiabatic

E equivalent parameter

i relating to immersion

id isentropic condition

m meridional component or mean camber

p polytropic

le leading edge

te trailing edge

s static condition

ss suction surface

z or X axial component

θ tangential component

Superscripts:

' relative to rotor blade

— mass or momentum average value

NOTE

All conversion factors based on NASA SP7012 Revised.

Pressure Ratio:

Rotor: $\frac{\overline{P}_2}{\overline{P}_o}$ Stage: $\frac{\overline{P}_5}{\overline{P}_o}$

Corrected Flow:

$$\frac{W\sqrt{\theta}}{\delta}$$

Equivalent Rotor Speed:

$$N/\sqrt{\theta}$$

Adiabatic Efficiency:

Rotor: $\eta_{ad} = \frac{H_{2_{id}} - H_1}{H_2 - H_1}$ Stage: $\eta_{ad} = \frac{H_{5_{id}} - H_1}{H_5 - H_1}$

Incidence Angle:

Rotor: $i_m = \beta_1' - \kappa_{le}$ Stator: $i_m = \beta_2 - \kappa_{le}$

$i_{ss} = \beta_1' - \kappa_{ss}$ $i_{ss} = \beta_2 - \kappa_{ss}$

Diffusion Factor:

Rotor: $D = 1 - \frac{V_2'}{V_1'} + \frac{d_2 V_{\theta 2} - d_1 V_{\theta 1}}{(d_1 + d_2) V_1' \sigma}$

Stator: $D = 1 - \frac{V_4}{V_3} + \frac{d_3 V_{\theta 3} - d_4 V_{\theta 4}}{(d_3 + d_4) V_3 \sigma}$

Deviation Angle:

Rotor: $\delta° = \beta_2' - \kappa_{te}$ Stator: $\delta° = \beta_4 - \kappa_{te}$

Loss Coefficient:

Rotor: $\bar{\omega}' = \frac{P_{2id}' - P_2'}{P_1' - p_1}$

where:

$$T_1' = t\left(1 + \frac{\gamma-1}{2} M_1'^2\right); \quad T_2' = T_1' + \frac{U_2^2 - U_1^2}{\frac{2\gamma}{\gamma-1} gR_g}$$

$$P_{2id}' = P_1' \left(\frac{T_2'}{T_1'}\right)^{\gamma/\gamma-1}$$

P' is found from $p/P' = \left(1 + \frac{\gamma-1}{2} M'^2\right)^{\frac{\gamma}{1-\gamma}}$

Where the relative Mach numbers are input from the velocity diagram program.

Stator: $\bar{\omega} = \frac{P_{3_1} - \bar{P}_4}{P_{3_1} - p_3}$

where:

P_{3_1} = the wake rake freestream total pressure

Loss parameter:

rotor $\dfrac{\bar{\omega}' \cos \beta_2'}{2\sigma}$

stator $\dfrac{\bar{\omega} \cos \beta_4}{2\sigma}$

Polytropic efficiency:

rotor $\eta_p = \dfrac{\frac{\gamma-1}{\gamma} \ln \frac{P_2}{P_0}}{\ln \frac{T_2}{T_0}}$

stator $\eta_p = \dfrac{\frac{\gamma-1}{\gamma} \ln \frac{P_4}{P_3}}{\ln \frac{t_4}{t_3}}$

SM - surge margin:

$$SM = \left\{ \left(\frac{\frac{\bar{P}_5}{P_0}}{\frac{W\sqrt{\theta}}{\delta}} \right)_{\text{at surge}} \cdot \left(\frac{\frac{W\sqrt{\theta}}{\delta}}{\frac{\bar{P}_5}{P_0}} \right)_{\text{at reference point}} - 1 \right\} \times 100, \text{ percent}$$

$N/\sqrt{\theta}$ = constant

For absolute values of surge margin, the reference point at any speed is defined as the intersection of that particular speed line with the constant throttle line passing through the design pressure ratio at design speed for the Test 1 configuration.

APPENDIX B
MOMENTUM AVERAGING PROCEDURE

By considering the equations of state, energy, continuity and momentum a set of equivalent parameters can be evaluated which can be considered representative of a uniform flow field with the same momentum and mass flow as the test field. The equivalent parameters of static pressure p_E, stagnation temperature T_E, swirl angle β_E, and stagnation pressure P_B, can be computed from the following procedure utilizing the listed assumptions.

$$\dot{m}_S = \cos\beta \int \rho V dA \tag{1}$$

This equation can be numerically evaluated once the equation of state has been employed and equation (1) is rewritten in the following form

$$\dot{m}_S = \cos\beta \; r\Delta r p_S \sum_{i=1}^{imax} \sqrt{\frac{\gamma g}{R_g t_i}} M_i \Delta\theta_i \tag{2}$$

using the energy equation

$$t = \frac{T}{1 + \frac{\gamma-1}{2} M^2} \tag{3}$$

yields the relation which can be evaluated from the measured parameters

$$\dot{m}_S = \cos\beta \; r\Delta r p_S \sqrt{\frac{\gamma g}{R_g}} \sum_{i=1}^{imax} \frac{M_i}{\sqrt{T_i}} \left(1 + \frac{\gamma-1}{2} M^2\right)^{1/2} \Delta\theta_i \tag{4}$$

The static pressure p_S is assumed to be a function of radius only and the value of the ratio of specific heats, γ, is based on the arithmetic average of the stagnation temperature at each immersion after being corrected for Mach number effects. The incremental height Δr is determined by the hub and tip flowpath radii and the arithmetic average radius between probe immersions. The Mach number is computed from the local static and total pressure and, hence, is a function of radius and circumferential location. The circumferential increment $\Delta\theta$ is the spacing between measuring elements on the wake rake and progresses until one blade pitch at a given immersion is traversed.

The continuity equation in equivalent form is written

$$\dot{m}_{SE} = \rho_E V_E \cos\beta_E \text{ arc} \tag{5}$$

or in terms of the axial Mach number

$$\dot{m}_{SE} = p_E \sqrt{\frac{\gamma g}{R_g t_E}} M_{XE} \tag{6}$$

Using the same technique, the axial and tangential momentum equations can be written. The axial momentum is

$$\psi_S = p_S A + \frac{\cos^2\beta}{g} \int \rho V^2 dA \tag{7}$$

or in the form used for numerical evaluation.

$$\psi_S = p_S r \Delta r \sum_{i=1}^{imax} (1 + \cos^2\beta \gamma M_i^2) \Delta\theta_i \tag{8}$$

The axial momentum in terms of equivalent parameters is

$$\psi_{SE} = \left(p_E + \frac{\cos^2\beta_E \rho_E V_E^2}{g}\right) arc \tag{9}$$

or in terms of Mach number function

$$\psi_{SE} = p_E(1 + \gamma M_{X_E}^2) arc \tag{10}$$

In a similar manner the tangential momentum can be written

$$\phi_S = \frac{\sin\beta \cos\beta}{g} \int \rho V^2 dA \tag{11}$$

or in the form for numerical evaluation

$$\phi_S = \sin\beta \cos\beta \gamma p_S r \Delta r \sum_{i=1}^{imax} M_i^2 \Delta\theta_i \tag{12}$$

The tangential momentum in terms of equivalent parameters is

$$\phi_{SE} = \frac{\sin\beta_E \cos\beta_E \rho_E V_E^2}{g} arc \tag{13}$$

or in terms of the Mach number functions with positive ϕ in the direction of rotor rotation

$$\phi_{SE} = p_E \gamma M_{XE} M_{\theta E} arc \tag{14}$$

If the equivalent functions are set identically equal to the integral values then there exists sufficient information to solve for the Mach numbers.

$$\dot{m}_S \equiv \dot{m}_{SE} \tag{15}$$

$$\psi_S \equiv \psi_{SE} \tag{16}$$

$$\phi_S \equiv \phi_{SE} \tag{17}$$

Combining equations (6) and (10) yields

$$\frac{\dot{m}_{SE}}{\psi_{SE}} = \frac{\sqrt{\frac{\gamma g}{R_g t_e}}\, M_{XE}}{[1 + \gamma M_{XE}^2]} \tag{18}$$

Using the energy equation

$$\frac{T_E}{t_E} = 1 + \frac{\gamma-1}{2}\,(M_{XE}^2 + M_{\theta E}^2) \tag{19}$$

to eliminate t_E from equation (18) yields

$$\frac{\dot{m}_{SE}}{\psi_{SE}}\sqrt{\frac{R_g T_E}{\gamma g}} = M_{XE}\,\frac{[1 + \frac{\gamma-1}{2}(M_{XE}^2 + M_{\theta E}^2)]^{1/2}}{(1 + \gamma M_{XE}^2)} \tag{20}$$

where the equivalent stagnation temperature T_E is evaluated at each radial immersion by converting the local circumferenctial value of stagnation temperature to an enthalpy value utilizing a polynomial curve fit of Keenan & Kay's Gas tables for the properties of air at low pressure. These local values of enthalpy are then mass averaged to obtain an equivalent stagnation enthalpy.

$$H_E = \frac{\int H d\dot{m}}{\dot{m}_S} \tag{21}$$

The value of H_E is used to compute T_E from a polynomial of temperature versus enthalpy.

By combining the axial and tangential momentum equations (10) and (14) two equations with two unknowns can be generated.

$$\frac{\phi_{SE}}{\psi_{SE}} = \frac{\gamma M_{XE} M_{\theta E}}{(1+\gamma M_{XE}^2)} \tag{22}$$

Equations (20) and (22) can be solved for M_{XE} as follows. Letting

$$A = \frac{\dot{m}_{SE}}{\psi_{SE}} \sqrt{\frac{R_g T_E}{\gamma g}} \tag{23}$$

and

$$M_{\theta E} = \frac{(1 + \gamma M_{XE}^2)\phi_{SE}}{\psi_{SE} \gamma M_{XE}} \tag{24}$$

then

$$\frac{\gamma-1}{2} \frac{M_{XE}^4}{(1 + \gamma M_{XE}^2)^2} + \frac{M_{XE}^2}{(1 + \gamma M_{XE}^2)^2} + \frac{\gamma-1}{2} \frac{\phi_{SE}^2}{\psi_{SE}^2 \gamma^2} - A^2 = 0 \tag{25}$$

with

$$B = \frac{\gamma-1}{2\gamma^2} \left(\frac{\phi_{SE}}{\psi_{SE}} \right)^2 \tag{26}$$

then

$$A^2\gamma^2 M_{XE}^4 - \frac{\gamma-1}{2} M_{XE}^4 - B\gamma^2 M_{XE}^4 + 2A^2\gamma M_{XE}^2 - M_{XE}^2 - 2B\gamma M_{XE}^2 + A^2 - B = 0 \tag{27}$$

Letting

$$X = M_{XE}^2 \qquad \text{then} \tag{28}$$

$$X^2 + \frac{(2A^2\gamma - 2B\gamma - 1)}{(A^2\gamma^2 - \frac{(\gamma-1)}{2} - B\gamma^2)} X + \frac{(A^2 - B)}{(A^2\gamma^2 - \frac{(\gamma-1)}{2} - B\gamma^2)} = 0 \qquad (29)$$

which is in the form of a quadratic equation with the solution

$$X = \frac{-b \pm \left(b^2 - 4ac\right)^{1/2}}{2a} \qquad (30)$$

where

$$a = 1 \qquad (31)$$

$$b = \frac{2A^2\gamma - 2B\gamma - 1}{A^2\gamma^2 - \frac{(\gamma-1)}{2} - B\gamma^2} \qquad (32)$$

$$c = \frac{A^2 - B}{A^2\gamma^2 - \frac{(\gamma-1)}{2} - B\gamma^2} \qquad (33)$$

Once the equivalent axial Mach number, M_{XE}, is known, then from equation (10), the equivalent static pressure, p_E, can be obtained. The tangential Mach number, $M_{\theta E}$, can then be solved from equation (14). The equivalent swirl angle, β_E, is

$$\beta_E = \tan^{-1}\left(\frac{M_{\theta E}}{M_{XE}}\right) \qquad (34)$$

and the momentum average stagnation pressure is

$$P_E = p_E \left[1 + \frac{\gamma-1}{2}\left(M_{XE}^2 + M_{\theta E}^2\right)\right]^{\gamma/\gamma-1} \qquad (35)$$

This process is repeated until equivalent parameters are determined at each immersion.

REFERENCES

1. Bailey, E. E.; and Voit, C. H.: Some Observations of Effects of Porous Casings on Operating Range of a Single Axial-Flow Compressor Rotor. NASA TMX-2120, 1970.

2. Oscarson, R. P. and Wright, D. L.: Experimental Evaluation of a Honeycomb Rotor Shroud Configuration to Improve the Stall Margin of a 0.5 Hub-Tip Ratio Single-Stage Compressor. NASA CR-72808, December 1970.

3. Moore, R. D.; Kovich, G.; and Blade, R.J.: Effect of Casing Treatment on Overall and Blade-Element Performance of a Compressor Rotor. NASA TN D-6538, November 1971.

4. Osborn, W. M.; Lewis, G. W.; and Heidelberg, L. J.: Effect of Several Porous Casing Treatments on Stall Limit and on Overall Performance of an Axial-Flow Compressor Rotor. NASA TN D-6537, 1971.

5. Bailey, E. E.: Effect of Grooved Casing Treatment on the Flow Range Capability of a Single-Stage Axial Flow Compressor. NASA TMX-2459, January 1972.

6. Monsarrat, N. T.; Keenan, M. J.; and Tramm, P. C.: Design Report Single-Stage Evaluation of a Highly Loaded High-Mach-Number Compressor Stages. NASA CR-72562, July 1969.

7. Sulam, D. H.; Keenan, M. J.; and Flynn, J. T.: Single-Stage Evaluation of a Highly-Loaded High-Mach-Number Compressor Stage. Data and Performance Multiple-Circular ACC Rotor. NASA CR-72694, July 1970.

8. Holman, F. F.; Kidwell, J. R.; and Ware, T. C.: Small Axial Compressor Technology Program (Volume II - Data Compilation). NASA CR-134827, AiResearch 74-310862, June 1976.

9. Smith, L. H., Jr.: The Radial Equilibrium Equation of Turbomachinery. ASME, Pages 65-WA/GTP-1, 1965.